



NONLINEAR DYNAMICS OF AN ORIGAMI TESSELLATION BASED ON
THE WATERBOMB PATTERN

Larissa Maciel da Fonseca

Tese de Doutorado apresentada ao Programa de Pós-graduação em Engenharia Mecânica, COPPE, da Universidade Federal do Rio de Janeiro, como parte dos requisitos necessários à obtenção do título de Doutor em Engenharia Mecânica.

Orientador: Marcelo Amorim Savi

Rio de Janeiro

Julho de 2021

NONLINEAR DYNAMICS OF AN ORIGAMI TESSELLATION BASED ON
THE WATERBOMB PATTERN

Larissa Maciel da Fonseca

TESE SUBMETIDA AO CORPO DOCENTE DO INSTITUTO ALBERTO
LUIZ COIMBRA DE PÓS-GRADUAÇÃO E PESQUISA DE ENGENHARIA (COPPE)
DA UNIVERSIDADE FEDERAL DO RIO DE JANEIRO COMO PARTE DOS
REQUISITOS NECESSÁRIOS PARA A OBTENÇÃO DO GRAU DE DOUTOR EM
CIÊNCIAS EM ENGENHARIA MECÂNICA.

Examinada por:

Prof. Marcelo Amorim Savi, D. Sc. – COPPE (UFRJ)

Prof. Gustavo R. dos Anjos, D. Sc. – COPPE (UFRJ)

Prof. Pedro M.C.L. Pacheco, D. Sc. – CEFET (RJ)

Prof. Arthur M. B. Braga, D. Sc. – PUC (RJ)

Prof. Davide Bernardini, D. Sc. – University of Rome

RIO DE JANEIRO, RJ - BRASIL

JULHO DE 2021

Fonseca, Larissa Maciel da

Nonlinear Dynamics of an Origami Tessellation Based on The Waterbomb Pattern / Larissa Maciel da Fonseca. – Rio de Janeiro: UFRJ/COPPE, 2021.

XXI, 195 p.: il.; 29,7 cm.

Orientador: Marcelo Amorim Savi

Tese (Doutorado) – UFRJ/ COPPE/ Programa de Engenharia Mecânica, 2021.

References: p. 172-183.

1. Waterbomb. 2. Origami tessellation. 3. Nonlinear Analysis. I. Savi, Marcelo Amorim II. Universidade Federal do Rio de Janeiro, COPPE, Programa de Engenharia Mecânica. III. Título.

*To my parents and siblings, whose support and love were
essential for the development of this work.*

*To my professor and advisor, for encouraging and guiding
a crazy student in the unfolding of a new path.*

*“You must unlearn what you have learned....Try not. Do.
Or do not. There is no try” – Yoda, The Empire Strikes Back*

Resumo da Tese apresentada à COPPE/UFRJ como parte dos requisitos necessários para a obtenção do grau de Doutor em Ciências (D. Sc.)

NONLINEAR DYNAMICS OF AN ORIGAMI TESSELLATION BASED ON
THE WATERBOMB PATTERN

Larissa Maciel da Fonseca

Julho/2021

Orientador: Marcelo Amorim Savi

Programa: Engenharia Mecânica

Origamis vêm inspirando novas estruturas adaptativas, como micro robôs, painéis solares e coletores de energia. Um dos desafios no projeto de estruturas origâmicas é o grande número de graus de liberdade (GdLs) associados a tais estruturas complexas, incluindo variáveis associadas às dobras vincadas e variáveis ocultas associadas à flexão e torção de painéis. As tesselações fechadas possuem um número reduzido de GdL quando comparadas às abertas, além de um comportamento periódico. Simetrias permitem a descrição da estrutura a partir de modelos de ordem reduzida. Este trabalho apresenta uma visão geral de estruturas origâmicas, em especial o padrão *waterbomb* e tesselações relacionadas. A ideia é estudar uma célula unitária estabelecendo uma comparação entre as formulações cinemática e mecânica. O estudo é expandido para tesselações, considerando casos abertos e fechados. Propõem-se modelos de ordem reduzida para descrever o comportamento mecânico dos origamis, verificando a sua validade a partir de uma comparação com modelos mais sofisticados. A dinâmica não linear de estruturas origâmicas é investigada considerando uma roda-origami, uma tesselação *waterbomb* fechada modificada. Finalmente, analisa-se um robô autônomo equipado com duas rodas-origami, investigando a manobrabilidade e capacidade de resposta a partir da deformação das rodas.

Abstract of Thesis presented to COPPE/UFRJ as a partial fulfillment of the requirements for the degree of Doctor of Science (D.Sc.)

NONLINEAR DYNAMICS OF AN ORIGAMI TESSELLATION BASED ON
THE WATERBOMB PATTERN

Larissa Maciel da Fonseca

July/2021

Advisor: Marcelo Amorim Savi

Department: Mechanical Engineering

Origamis have been inspiring new adaptive structures, such as micro robots, solar panels and energy harvesting. One of the challenges of the design of origami structures is the large number of degrees of freedom (DoF) associated with such complex structures, including variables associated with creased folds and hidden variables associated with the bending and twisting of panels. Closed tessellations have a reduced number of DoF when compared to open ones. Symmetries allow the description of the structure from reduced-order models. This work presents an overview of origami structures, with special interest on waterbomb pattern and related tessellations. A unit cell is studied establishing a comparison with kinematic and mechanical formulations. The study is expanded to tessellations, considering open and closed cases. Reduced-order models are proposed in order to describe the mechanical behavior of the origamis, verifying their validity from a comparison with more sophisticated models. Nonlinear dynamics of origamis is explored by investigating an origami wheel, a modified closed waterbomb tessellation. Finally, a two-wheel autonomous robot with origami wheel is analyzed, investigating the maneuverability and responsiveness from the deformation of the wheels. Numerical simulations related to operational conditions are performed for different thermal and mechanical loads, showing rich behaviors with periodic and chaotic responses.

Content

1	Introduction	1
2	Theoretical Fundamentals	4
2.1.	Origami concept.....	6
2.2.	Developable surface.....	11
2.3.	Tessellation	12
2.4.	Rigid foldability	16
2.5.	Origami applications	16
3	Origami Modeling	24
3.1.	Kinematic approach	24
3.2.	Spherical trigonometry	27
3.3.	Finite Element Method	29
3.3.1.	Modified displacement-based method.....	33
4	Waterbomb Cell	36
4.1.	Kinematic analysis	37
4.2.	Workspace analysis.....	39
4.3.	Symmetry analysis	42
4.4.	Closed-form trigonometric description.....	45
4.5.	Finite Element Analysis (FEA).....	49
5	Waterbomb Tessellation	59
5.1.	Poisson’s ratio	60
5.2.	Opened tessellation	67
5.3.	Closed tessellation	81
6	Origami-Wheel	96
6.1.	Mechanical evaluation of the origami-wheel.....	96
6.2.	Reduced-order model.....	109

7	Origami-Wheel Dynamics	114
7.1.	Dynamical formulation	116
7.2.	Quasi-static analysis	118
7.3.	Dynamical analysis	120
8	Origami-Wheel Robot.....	132
8.1.	Kinematics	133
8.1.1.	Constraints	137
8.2.	Dynamical formulation	139
8.3.	Dynamical analysis	144
8.3.1.	Different driven cases	144
8.3.2.	Free vibration system – definition of a preferred path	146
8.3.3.	Forced vibration system – origami-soil interaction and temperature variation 150	
9	Final Remarks and Future Works.....	167
10	References.....	171
	APPENDIX	183
A.1.	SMA Constitutive Models	183
A.1.1.	Thermomechanical aspects of SMA.....	183
A.1.2.	Overview of constitutive models.....	186
A.2.	Polynomial constitutive model	187
A.3.	Hyperelastic constitutive model.....	190
A.4.	Elastic constitutive model	192

List of Figures

Figure 2-1: Traditional paper crane (<i>Orizuru</i>). (a) Simplified representation of the basic folding process; (b) Picture by 2006 Martin Bailey of the red-crowned crane, the inspiration for the <i>Orizuru</i> origami.	5
Figure 2-2: Representations of the seven basic origami types. (a) Action Origami (Jumping frog); (b) Origami tessellation; (c) Wet-folded origami; (d) Pureland Origami (simple version of the Jumping frog); (e) General forms obtained from the same origami tessellation; (f) Kirigami; (g) Strip folding origami.	7
Figure 2-3: <i>Flapping bird</i> origami (top left) and the bottom view of the crease pattern (bottom right).....	9
Figure 2-4: Fold state or definition as mountain or valley crease type. (a) Waterbomb cell with the fold definition; (b) Top view; (c) Bottom view.....	10
Figure 2-5: “An impossible fold”, presented first by Thomas Hull in the <i>Congressus Numerantium</i> , 1994.	11
Figure 2-6: Origami tessellations generating developable surfaces: (a) Whirlpool pattern (cone); (b) Huffman Stars-Triangles (cylinder).....	12
Figure 2-7: Directions for tessellation pattern Huffman Rect Wave and folded pattern	13
Figure 2-8: Regular tessellation. (a) Yoshimura; (b) Miura-Ori	15
Figure 2-9: Flower tower tessellation based on the design by Chris K. Palmer. On the left, the pattern is in the fully opened state. On the right, the pattern is in a partially folded state.....	15
Figure 2-10: Miura-Ori pattern with a high (a) and a low (b) ratio between panels and creases’ stiffness, with mechanical description provided by a displacement-based method, and panel flexibility represented by a virtual fold.....	16

Figure 2-11: Starshade deployment sequence, from the launch configuration (fully folded) to the deployed state (fully unfolded). (Image credit: www.nasa.gov)..... 17

Figure 2-12: Self-folding wireless actuated robotic arm. a) Simplified illustration of the kinematic design and components. The natural spherical movement of the waterbomb pattern is represented by spherical joints; b) A micro-robotic arm prototype with a permanent magnet for anchoring, with a panel highlighting one SMA coil actuator attached at the side of the waterbomb pattern; c) On the left, a three-dimensional rendering of the folding laminate containing a rigid sheet -a-, and adhesive layer -b- and a flexure film -c-. On the right, a folding joint with a coil SMA actuator with a moment arm that also serves as a fold stop (Image credit: Boyvat *et al.*, 2017). 18

Figure 2-13: CAD drawing and printed outcome. (a) CAD model of TWISTER with embedded holes for routing cables; (b) Printed structure with cables routed diagonally; (c) Structure with cables routed in a zigzag pattern; (d) Main chassis contains a microprocessor, battery, power switch, mini-USB port, XBee module, servo motor, pulley mechanism, and docks for the fingers and cables (Image credit: Lee *et al.*, 2020) 19

Figure 2-14: (a) Photo of a fabricated origami structure after the direct laser-write MCG patterning process (black color areas) on a paper substrate (white color areas); (b) Schematic illustration of the simplified MCG process from fibrous paper, soaked with the gelatin-mediated ink containing Mo5+ ions, laser conversion process, to the resulting MCG composites; (c) Two partially folded, four 2 × 2 cm² electrodes on a paper substrate: (top) after the laser conversion process, and (bottom) before the conversion process. (inset) A fully folded device with two electrodes on top and two electrodes at the bottom for a two-capacitor in sandwich structure to be connected in series or parallel as supercapacitors; (d) Recorded relative conductivity of an electrical connector made of MCG composites during the 750 cycles of 180° mechanical folding tests. (inset) Use of the mechanical folding and touching of electrodes made of MCG composites as an electrical switch to turn on/off a red light-emitting diode (Image credit: Zang *et al.*, 2018) 20

Figure 2-15: Self-foldable miniature origami robot. (a) Miniature robot that walks, swims, carry loads and degrades; (b) Miniature robot for patching stomach wounds and retrieving swallowed batteries (Image credit: Miyashita *et al.*, 2015;2016)..... 21

Figure 2-16: Stent graft developed with a Nitinol sheet, using waterbomb tessellation (Image credit: Kuribayashi, 2006).....	22
Figure 2-17: Robot with an origami gripping arm and origami wheels. (Image credit: Lee <i>et al.</i> , 2016).....	23
Figure 2-18: Application of a waterbomb tessellation as an inflatable drone landing gear for water landing (Image credit: Le <i>et al.</i> , 2014).....	23
Figure 3-1: Mechanism movement representation for joint type identification. (a) Planar; (b) Spherical and (c) Spatial.	25
Figure 3-2: D-H parameters' setup.....	26
Figure 3-3: Schematic of a waterbomb spherical mechanism. The links are projected onto the sphere surface, and the joints' rotation axis intersect at the sphere center.	28
Figure 3-4: Spherical triangle on the sphere surface, formed through the connection of the arcs described on the sphere surface.....	29
Figure 3-5: Bar-and-hinge description of an origami.....	29
Figure 3-6: Bar element and its local referential axis.....	31
Figure 3-7: Unified incremental-iterative scheme to solve nonlinear problems for N+1 dimensional space.....	32
Figure 3-8: (a) Original Input method, with the Input being applied to the Referential Frame (x, y, z)// (X, Y, Z); (b) Modification proposed, where the Input is applied to the Referential frame (x, y, z) that follows the Node movement. In the example shown, axis $z \perp Face237$ and plane xy is contained within <i>Face237</i>	34
Figure 3-9: Overview of simulation framework. The initial configuration is inserted in a combination of Nodes and Bars, and the external forces and constraints are carefully considered. At each iteration, a convergence is performed on each node displacement using MGDCM, and, after converging, a new input is generated with the reevaluation of the forces based on the new Nodes (Nodes considering the displacement).	35
Figure 4-1: Typical waterbomb base crease pattern, where full line means a mountain fold and dashed line means a valley fold.	36
Figure 4-2: Equivalent mechanism for the 6-creased waterbomb pattern.....	37

Figure 4-3: From (a) to (i): Different representations of the unit cell shape configurations for distinct values of the input angles $\theta_1, \theta_2, \theta_3$. The waterbomb cell is represented through the connective of the position of each vertex on the workspace where vertices A, C, D and F belong to the outer sphere with radius $b\sqrt{2}$, wherein $OA = OC = OD = OF = b\sqrt{2}$, and vertices B and E belong to the inner sphere with radius b , wherein $OB = OE = b$ 40

Figure 4-4: Workspace for each joint-linkage pair of the waterbomb cell, considering the referential frame at joint A (crease OA)..... 42

Figure 4-5: Symmetry conditions on a waterbomb unit cell: (a) planes of symmetry; (b) configuration related to Case Π_1 , with mobility 2; (c) configuration related to Case Π_2 , with mobility 2; (d) symmetric configuration related to Case Π_3 , with mobility 1..... 43

Figure 4-6: Workspaces for the plane-symmetry cases Π_1 and Π_2 and the symmetry case Π_3 (a). The symmetric case Π_3 is showed superposed to only the plane-symmetric case Π_1 in (b), while it is superposed to only the plane-symmetric case Π_2 in (c)..... 44

Figure 4-7: Spherical representation of the origami unit cell: (a) top view; (b) side view; (c) tridimensional view; (d) schematic view of a waterbomb spherical mechanism..... 46

Figure 4-8: Spherical triangle sides' definition. 46

Figure 4-9: Spherical triangles used to define geometric relations of the unit cell, computing angles α and θ 47

Figure 4-10: Definition of vectors for the waterbomb cell..... 48

Figure 4-11: Origami waterbomb pattern unit cell with boundary conditions and Input as a Force type. 49

Figure 4-12: Closure process of a waterbomb cell with and without the force decomposition procedure. Waterbomb final configurations (a) and (d), spatial location of the vertices during the closure (b) and (e), and true strain (c) and (f) of each bar of the waterbomb cell. 50

Figure 4-13: Final configuration of the waterbomb cell considering the activation of a single crease at a time, for the boundary conditions of clamped Nodes 5, 6 and 7, including the dual cases for creases 2 – 7 and 3 – 7..... 52

Figure 4-14: Configuration of the waterbomb cell considering activated creases 3 – 7, 4 – 7 and 5 – 7.	53
Figure 4-15: Workspace for cases Π_1 and Π_2 and simulations for a generic case (asymmetric), plane-symmetric behavior (Π_1 , Π_2) and symmetric behavior (Π_3). The correspondent deformation of each origami face is shown for cases Π_3 (b), Π_2 (c), Π_1 (d) and asymmetric (e).	55
Figure 4-16: Evolution of the inner angles of the waterbomb cell with the increment during the folding process, for a folding occurring according to cases Π_3 (a), Π_2 (b) and Π_1 (c), and according to an asymmetric actuation (d). The final configuration is also shown in evidence in each case.	57
Figure 4-17: Asymmetric behavior of the waterbomb cell described by the kinematic formulation (using D-H parameters) and the FEA formulation (using bar-and-hinge description). (a) Tridimensional movement of the cell on folding process; (b) Difference between the inner angles evaluated by kinematics method and by FEA method.	58
Figure 5-1: Target 3D surface and approximation using waterbomb tessellation. (a) Target surface and coordinates in parametric u - v plane; (b) Quad surface; (c) to (f): Target surface approximated using waterbomb tessellation, with increasing resolution. [Image source: Zhao <i>et al.</i> (2018)]	60
Figure 5-2: Poisson’s ratio explained in two dimensions.	61
Figure 5-3: Waterbomb unit cell, selected points for Poisson’s ratio evaluation and variables for the 8-creased (a, b) and the 6-creased (c, d) patterns.	63
Figure 5-4: Poisson’s ratio representation for the 6-creased and the 8-creased waterbomb patterns. (a) and (b): Input force/ displacement and output result for the in-plane case; (c) and (d): Final configuration reached for 8-creased and 6-creased respectively; (e) and (f): Overlap between final and initial configurations.	65
Figure 5-5: Effective volume of 6-creased and 8-creased waterbomb unit cells as a function of the deployable angle.	66
Figure 5-6: 5×9 waterbomb tessellation generated from a squared waterbomb unit cell. The cells $C1$, $C2$ and $C3$ are highlighted.	68

Figure 5-7: Waterbomb tessellation in a fully closed (a) and in an opened (b) configuration.....	69
Figure 5-8: Waterbomb tessellation under bending. (a) Case I-A: 2-points boundary condition; (b) Case II-A: 3-points boundary condition; (c): Case III-A: 4-points boundary condition; (d) Case I-B: 2-points boundary condition; (e) Case II-B: 3-points boundary condition; (f): Case III-B: 4-points boundary condition.....	72
Figure 5-9: Top view of the waterbomb tessellation's folding process over time for an A-type bending actuation, for Cases I, II and III.	73
Figure 5-10: Top view of the waterbomb tessellation's folding process over time for a B-type bending actuation, for Cases I, II and III.	74
Figure 5-11: Time evolution of inner angle D of unitary cells C_1 , C_2 and C_3 for folding A-type cases I (a), II (b) and III (c); and for B-type cases I (d), II (e) and III (f).....	75
Figure 5-12: Front view (top) and side view (bottom) of the final configuration of the waterbomb tessellation for Case III-B (green), compared to the initial configuration (gray).	76
Figure 5-13: Waterbomb tessellation under uniaxial loading. (a) Uniaxial load inducing the unfolding of the waterbomb tessellation (traction); (b) uniaxial load inducing the folding of the waterbomb tessellation (compression).....	77
Figure 5-14: Side view of the waterbomb tessellation's folding process over time for a uniaxial actuation, for Cases I and II.	78
Figure 5-15: Time evolution of the Load factor for an asymmetric folding process of the waterbomb tessellation.	80
Figure 5-16: Time evolution of inner angles A to F of unit cells C_1 , C_2 and C_3	81
Figure 5-17: Three different configurations assumed by a closed waterbomb tessellation. (a) The RVE is the symmetric unit cell, and, in this case, the structure has both local and global symmetries; (b) The RVE is a set of cells, where the set is composed by two cells from consecutive lines for (i) case and by a single plane-symmetric unit cell for (ii) case. The (ii) case has global symmetry; (c) A RVE is not identified, resulting in a structure with neither local nor global symmetry.	83

Figure 5-18: Waterbomb pattern and natural way of folding. (a) 6-creased waterbomb unitary cell; (b) Illustration of the geometric relationship between natural force and waterbomb fold pattern; (c) Illustration of a closed waterbomb tessellation with a double-curved surface; (d) Illustration of a closed waterbomb tessellation with a single-curved surface..... 84

Figure 5-19: Closed waterbomb tessellation generated with the 6 creased waterbomb unit cell. The tessellation is defined by the number of lines (m) and the number of cells on each line (n)..... 85

Figure 5-20: Load factor λ evolution during the symmetric folding process of a closed 3×6 waterbomb tessellation. The panels (i) to (vi) show, sequentially, a closer look into the origami configuration for each remarkable variation in the load factor evolution... 86

Figure 5-21: Top view of the closed waterbomb tessellation during the folding process. On each view from (i) to (vi), the gray line represents the initial configuration, and the green panels are the tessellation. 87

Figure 5-22: Closed waterbomb tessellation formed by m lines, with each line composed by $n=6$ squared cells. (a) $m=3$; (b) $m=4$; (c) $m=7$; (d) $m=8$ 88

Figure 5-23: Relation between the inner angles of each one of the $6m$ cells of the tessellation, where m is the number of lines of that tessellation. (a) Relation for the case $m = 3$; (b) Relation for the case $m = 4$; (c) Relation for the case $m = 7$; and (d) Relation for the case $m = 8$. For all four cases, the bisector line represents the symmetric behavior (case Π_3). 89

Figure 5-24: Maximum deviation of each inner angle with the increasing of the number of cells per line, considering a tessellation with m lines. (a) Maximum deviation for a tessellation with an odd number of lines, with $m = 5$; (b) Maximum deviation for a tessellation with an even number of lines, with $m = 6$ 91

Figure 5-25: Folding process of a tessellation with $m = 5$ lines (a) and $m = 6$ lines (b), with each remarkable phase highlighted. The strangulation that happens in the middle of the tessellation is highlighted by red arrows. 93

Figure 5-26: Strangulation (Δ) evaluation for an even and an odd tessellation, as a function of the ratio between the number of cells on each line (n) and the number of lines (m)..... 94

Figure 5-27: Strangulation (Δ) evaluation for both even and odd tessellations as a function of the number cells on each line (n), with a color map on the number of lines (m)...... 95

Figure 6-1: Representation of an opened waterbomb tessellation in an opened configuration, showing the colored-defined folds (mountain in blue and valley in red). The inserted tips are also present, with a dashed mark for regions that will be glued. ... 97

Figure 6-2: Folding process of a 3×8 closed waterbomb tessellation starting in an unfolded configuration and reaching a half-folded configuration..... 98

Figure 6-3: Folding process of a 3×8 modified closed waterbomb tessellation starting in an unfolded configuration and reaching a half-folded configuration..... 99

Figure 6-4: Unfolding process of a 3×8 modified closed waterbomb tessellation starting as a half-folded configuration and reaching an unfolded configuration..... 100

Figure 6-5: Highlight of one cell of an odd parity line for the modified closed waterbomb tessellation. (a) Pop-in behavior happening during the folding process; (b) Pop-out behavior happening during the unfolding process..... 101

Figure 6-6: Axis definition for the closed waterbomb tessellation, where the longitudinal direction is defined as Y axis. The rigid plate is highlighted in gray..... 103

Figure 6-7: Load factor over time for the folding process of the closed waterbomb tessellation with rigid elements on both endings, and final configurations. (a) Time evolution of the Load factor, with a highlight for the bifurcation region; (b) to (e) Final configuration (at time 100) achieved for each case..... 104

Figure 6-8: Time evolution of inner angles relation for each cell for the case with an increasing of 24% on the external load. From (a) to (d), respectively, the difference between angles A and C, A and D, C and D, and B and E..... 105

Figure 6-9: Time evolution of inner angles relation for each cell for the case with an increasing of 20% on the external load. From (a) to (d), respectively, the difference between angles A and C, A and D, C and D, and B and E..... 106

Figure 6-10: Load factor over time for the folding process of the closed waterbomb tessellation with a rigid element on one end..... 107

Figure 6-11: Time evolution of inner angles for the ‘popped out’ unit cell, with a zoom for inner angles A, C, D and F after the inversion of crease. 108

Figure 6-12: Time evolution of inner angles relation for each cell for the case with an increasing of 24% on the external load. From (a) to (d), respectively, the difference between angles A and C, A and D, C and D, and B and E.....	109
Figure 6-13: Plane views of the origami-wheel.	110
Figure 6-14: Trapezoidal pyramid (a) used to obtain the relation between β and γ (b).	110
Figure 6-15: Origami-wheel and symmetric plane views. (a) Radial symmetry –XZ plan; (b) Simplified view; (c) Longitudinal symmetry –YZ plan; (d) Simplified view.....	112
Figure 6-16: Origami-wheel geometric relations. (a) Curve of the distance between the acrylic plates ($L2$) as a function of the middle row opening ($L1$); (b) Curve of the inner ($R1$) and outer ($R2$) radii of the origami-wheel as a function of the middle row opening ($L1$).	113
Figure 7-1: Origami-wheel with SMAs placed along the middle row to promote the folding process (left) and a cut exposing the elastic passive spring, connecting the acrylic plates, to promote the BIAS effect (right).	115
Figure 7-2: Quasi-static analysis of the origami wheel, considering the sum of the efforts of the SMA and elastic springs.....	119
Figure 7-3: Origami structure quasi-static behavior due to temperature changes. (a) Thermal load; (b) External and internal radii evolution during heating/cooling process; (c) Displacements on elastic spring and on each SMA actuator; (d) Actuators' length.	120
Figure 7-4: Representation of the external excitation represented by the force $Ft = F1t + F2t$, where the contribution of each Fit is highlighted on the right, being (a) for $F1t$ and (b) for $F2t$	121
Figure 7-5: Origami-wheel basins of attraction. (a) Shape configuration for the three stable positions and its color representation; (b) Basin of attraction for $T < TM$; (c) Basin of attraction for $TM < T < TA$; (d) Basin of attraction for $T > TA$	122
Figure 7-6: Origami bifurcation diagrams varying perturbation forcing amplitudes: (a) $T = 288 K (T < TM)$; (b) $T = 315 K (TM < T < TA)$; (c) $T = 327 K (T > TA)$	123

Figure 7-7: Bifurcation diagram for an intermediate temperature ($T_M < T = 300 K < T_A$).....	124
Figure 7-8: Origami response subjected to mechanical forcing ($\delta_1=10 N, \omega_1=200 \text{ rad/s}$) at $T=288 K$. (a) Mechanical load $F(t)$; (b) phase space and Poincaré section.	125
Figure 7-9: Origami response to a perturbed mechanical load at $T=288 K$. (a) Mechanical loading process (without and with a small perturbation); (b) Phase space and strange attractor; (c) Origami configurations.....	126
Figure 7-10: Different periodic orbits for different external mechanical forces at $T=288 K$. (a) Phase portraits; (b) External radius variation.....	127
Figure 7-11: Frequency response of the origami for $T = 288 K (T < T_M)$ in a run-up and run-down simulation. Some phase spaces positioned in high dynamic regions are highlighted.....	128
Figure 7-12: Frequency response of the origami for $T = 315K (T_M < T < T_A)$ in a run-up and run-down simulation. Some phase spaces positioned in high dynamic regions are highlighted.....	129
Figure 7-13: Origami frequency response for $T = 320K T_A < T$ in a run-up and run-down simulation.	130
Figure 7-14: Origami response subjected to thermal fluctuation. Transient response is represented by a red line, while stabilized response is represented by a blue line. (a) SMA displacement time history; (b) phase space; (c) Poincaré section associated with transient chaos (chaotic saddle); (d) steady state periodic phase space.	131
Figure 8-1: Origami-wheel robot of two deformable wheels. (a) Isometric view with indications of the mass centers for the wheels, G_A and G_B , and mass center of the chassis, G ; (b) Superior view, with cuttings on the wheels, for details of the attachment of the wheels to the axes.....	133
Figure 8-2: Representation of the referential frames to describe the origami-wheel trajectory. (a) indication of the yaw motion (Φ); (b) indication of the roll movement (θ); (c) and (d) indication of the referential frame attached to each wheel for spinning (Φ_A, Φ_B).....	135

Figure 8-3: Driven situations of the robot: (a) driven torques at each wheel; (b) robot linear velocity. 144

Figure 8-4: Origami wheel robot movement for different driven conditions. (a) Thermal load; (b) Path; (c) velocity driven motion: time evolution of the velocities of the chassis and wheels and time evolution of the torques; (d) torque driven motion: time evolution of the linear velocities of the chassis and wheels and time evolution of the torques. 146

Figure 8-5: Representation for an arbitrary desired path of the origami wheel robot. (a) Thermal load applied to each wheel individually, promoting a turn counterclockwise and then clockwise; (b) desired arbitrary path, starting with a straight line and ending on a straight line, shifted vertically from the original one; (c) zoom on the region I pointed at (b), where the car follows a straight line; (d) zoom on the region II, where the car turns left (counterclockwise turn from wheel *B* to wheel *A*). 147

Figure 8-6: Thermal cycles (a) to (d) and path (e) described by the projection of G point on the fixed frame (*X, Y, Z*). 149

Figure 8-7: Representation of the external mechanical excitation shaped as a force $Ft = F1t + F2t$, where the contribution of each Fit is highlighted on the right, being (a) for $F1t$ and (b) for $F2t$ 151

Figure 8-8: Path followed by the origami-wheel robot when passing through different soils, represented by hatched regions and described by an external stimulus. A zoom from the first dashed region is also presented. 152

Figure 8-9: Binary representation of the wheels related to the dashed region in Figure 8-8. 153

Figure 8-10: Time evolution of the wheels' radius for the cases (a) $\delta_2 = 0$ N; (b) $\delta_2 = 0.5$ N; (c) $\delta_2 = 1$ N and (d) $\delta_2 = 1.5$ N. 155

Figure 8-11: Phase portrait and Poincaré section of wheel A for $mG=0.1$ kg subjected to $F(t)$ for the cases (a) $\delta_2 = 0$ N; (b) $\delta_2 = 0.5$ N; (c) $\delta_2 = 1$ N and (d) $\delta_2 = 1.5$ N. 156

Figure 8-12: Phase portrait and Poincaré section of wheel B for $mG=0.1$ kg subjected to $F(t)$ for the cases (a) $\delta_2=0$ N; (b) $\delta_2=0.5$ N; (c) $\delta_2=1$ N and (d) $\delta_2=1.5$ N. 156

Figure 8-13: Path followed by the origami-wheel robot when passing through different soils considering $mG=0.2$ kg. 157

Figure 8-14: Time evolution of the wheels' radius considering $mG=0.2$ kg for the cases: (a) $\delta 2 = 0$ N; (b) $\delta 2 = 0.5$ N; (c) $\delta 2 = 1$ N and (d) $\delta 2 = 1.5$ N..... 158

Figure 8-15: Phase portrait and Poincare section of wheel A considering $mG=0.2$ kg for the cases: (a) $\delta 2 = 0$ N; (b) $\delta 2 = 0.5$ N; (c) $\delta 2 = 1$ N and (d) $\delta 2 = 1.5$ N..... 159

Figure 8-16: Phase portrait and Poincare section of wheel B considering $mG=0.2$ kg for the cases: (a) $\delta 2 = 0$ N; (b) $\delta 2 = 0.5$ N; (c) $\delta 2 = 1$ N and (d) $\delta 2 = 1.5$ N..... 160

Figure 8-17: Dynamic response of the system when subjected to the force $F(t)$. (a) Force on time with a selection of one period (T) with the phase going from 0 to 2π ; (b) Spectrum diagram for R_A evaluated on ρ 162

Figure 8-18: Path described by the G point for the chaotic and the periodic responses. 163

Figure 8-19: Synchronization between wheels A and B. (a) Time evolution of wheels' radius with a zoom at the permanent regime; (b) phase portrait of wheels A and B at the synchronized configuration; (c) path described by the origami-wheel robot; (d) radius manifold showing the synchronization..... 164

Figure 8-20: Chaotic behavior of wheels A and B. (a) Time evolution of wheels' radius with a zoom at the permanent regime; (b) phase portrait of wheels A and B at the synchronized configuration; (c) path described by the origami-wheel robot; (d) radius manifold..... 166

Figure A-1: SMA thermoelastic (a), pseudo elastic (b) and partial pseudo elastic, for $AS < T < AF$, or shape memory effect, for $T < AS$ behavior. 185

Figure A-2: Typical Stress-Strain-Temperature curves for SMA springs: (a) shape memory effect (SME); (b) SME on a bias system..... 186

Figure A-3: Polynomial constitutive model describing SMA behavior for $T = 283$ K $T < TM$, $T = 298$ K $TM < T < TA$ and $T = 323$ K $T > TA$. (a) Free energy; (b) Stress-strain relations 188

Figure A-4: Four different materials represented by the Ogden model considering different sets of $\alpha 1, \alpha 2$ 192

Figure A-5: Relationship between the resisting moment per unit length and the dihedral angle θ , considering the additional kinematic restrictions 193

List of Tables

Table 7-1: Configurations of the origami-wheel for $b = 0.04$ m and $r = 0.065$ m....	115
Table 7-2: Material and system parameters.....	118

1 Introduction

Origami, from Japanese words *Oru* – fold and *kami* – paper, is the art of paperfolding that creates general 3D structures and forms from a flat sheet of paper (2D element) following a sequence of folding creases, without stretching, cutting, or gluing other pieces of paper to it. Since it can be flattened onto a plane without distortion (it has a zero Gaussian curvature) and the 3D form is generated by a bending process without stretching or shrinking (Struik, 1961), origami is a developable surface. Therefore, the concept of origami can be applied to the manufacturing of various complex 3D forms by out-of-plane deformation (bending and folding), from a watertight sheet of materials such as paper, fabric, plastic and metal.

Engineering has an increasing need for reduced size mechanisms without reducing their ability to complete complex tasks. As a matter of fact, the need for more efficient yet smaller and weightless devices boost the study of origami structures and origami-like elements. One way to reach the performance requirements without losing sight on the size restriction is the use of “developable mechanisms”, a class of mechanism that address the origami concept, the theory of compliant mechanisms and the concept of developable surfaces. Shapes emerging from cylindrical or spherical configurations, as the combination of morphing capable elements, can be applied on architecture (Sorguç *et al.*, 2009), robotic (Felton *et al.*, 2014), spatial systems (Nishiyama, 2012) and biomedical devices (Salerno *et al.*, 2014).

The description of origami structures can be made considering either kinematic or mechanical approaches. The kinematic approach considers the shape changing of an origami element neglecting any deformation on panels, focusing on the angle variation and the tridimensional configuration associated to a set of angles. The mechanical description of the folding process is essentially based on forces and movements, or work and energy, which captures the actual behavior of such slender structures. It mostly considers bending and torsion of panels and their effect on the origami behavior and

configuration. The folding process usually involves significant geometric nonlinearity, which promotes additional nonlinear behaviors related to the deformation of the panels.

The combination of origami concepts with smart material elements, such as shape memory alloys (SMAs), piezoelectric, magnetostrictive and magnetorheological materials, allows the developing of complex and low-weight self-foldable structures, which can permeate between geometric configurations through the folding process promoted by the origami pattern. Since origami systems are slender structures, they are usually close to stability limits with important dynamical issues to be investigated. The combination of geometric and constitutive nonlinearities is responsible for a rich dynamic behavior and, therefore, external excitations and perturbations can be critical to the system response, being a problem in several applications.

This work presents an analysis of the complex behavior of origami structures, with a focus on the waterbomb pattern and related tessellations. As can be observed through this work, the literature is mainly dedicated to analyzing symmetric behaviors, quasi-static analysis and dynamic of folding, without considering the folding motion, distortion of panels and their influence to hidden variables and degrees of freedom (DoFs). Dynamical and nonlinear behaviors of the folding process are usually neglected.

In this regard, this work fills this literature gap dealing with the nonlinear dynamics of origami structures. An analysis of asymmetries is of concern establishing a proper investigation about the reduction of the number of DoFs allowing to build reduced-order models based on mechanical restrictions of the origami pattern. Kinematic and mechanical analyses are of concern. Concerning kinematic analysis, equivalent mechanisms are employed allowing the identification of symmetry planes. Besides, the spherical trigonometry is employed to develop reduced order models. Mechanical investigation is based on the finite element analysis (FEA).

Kinematic analysis considers a unit cell based on the folding pattern defining an equivalent mechanism. Symmetry conditions are identified allowing to build a 1 DoF reduced-order model. Mechanical analysis allows one to explore the influence of hidden variables on the shape prediction. The rigidity hypothesis is evaluated and verified establishing a comparison between kinematic and mechanical formulations. The work evolves to the mechanical analysis of a waterbomb tessellation, investigating the influence of asymmetries on the tessellation. Thereafter, closed waterbomb tessellations are treated. A particular closed-form configuration, henceforth called origami-wheel, is

investigated from a reduced-order model. The dynamical behavior of the origami-wheel actuated by shape memory alloy (SMA) actuators is evaluated and, afterward, an origami-robot with origami-wheels is investigated, evaluating the maneuverability and responsiveness due to deformable wheels. Numerical simulations related to operational conditions are carried out considering different thermal and mechanical loads, presenting periodic, quasi-periodic and chaotic dynamic behaviors.

This work is organized as follows: the next chapter presents the general idea of origamis, with a brief description and explanation of the main topics and concepts on this work (sections 2.1 to 2.4) and some origami applications (section 2.5); chapter 3 brings the formulations considered for this work; chapter 4 contains the studies related to the waterbomb unit cell, including the kinematic formulation and mechanical analysis; the behavior analysis of the waterbomb tessellation, for both opened and closed cases, are undertaken in chapter 5; chapter 6 depicts the origami-wheel study, considering a mechanical analysis and finishing with a reduced-order formulation; chapter 7 brings the dynamical analysis of the origami-wheel actuated by shape memory alloys. In the sequence, the kinematic and dynamical formulations for the origami-car are presented in chapter 8, followed by the dynamical study; and chapter 9 summarizes this work conclusions and suggests future work. The references cited in this work are organized in chapter 10. At the end, there is an appendix with the constitutive models.

2 Theoretical Fundamentals

One of the most traditional and classic origamis is the *Orizuru* or crane (Figure 2-1-a), a tridimensional structure folded from a single flat sheet of paper. In Japanese culture, it is believed that these paper craft symbolize good health, luck and longevity being a representation of the red-crowned crane (Figure 2-1-b). Beyond arts, origami applications started to be employed on educational (Andreass, 2011) and mathematical (Alperin, 2000; Glassner, 1996; Xi & Lien, 2015) fields of knowledge. Besides, origami concept is already being widely applied on architecture and decoration (Sorguç *et al.*, 2009) due to the structure beauty.

In addition, there is an increasing need on engineering reduced size mechanisms without reducing their ability to complete complex tasks. One example is the developable elements on minimally invasive surgery, where a highly precise and sophisticated mechanical function is essential for the procedure, allowing the reduction of the size of the incisions due to the smaller instruments. Another promising area is on electronic devices, where the demand of performance increases while the size and weight of the equipment must not enlarge with it. On this basis, it is important to highlight the growing research efforts on robotics (Felton *et al.*, 2014), spatial systems (Nishiyama, 2012), biomedical devices (Salerno *et al.*, 2014) and MEMS (microelectromechanical systems).

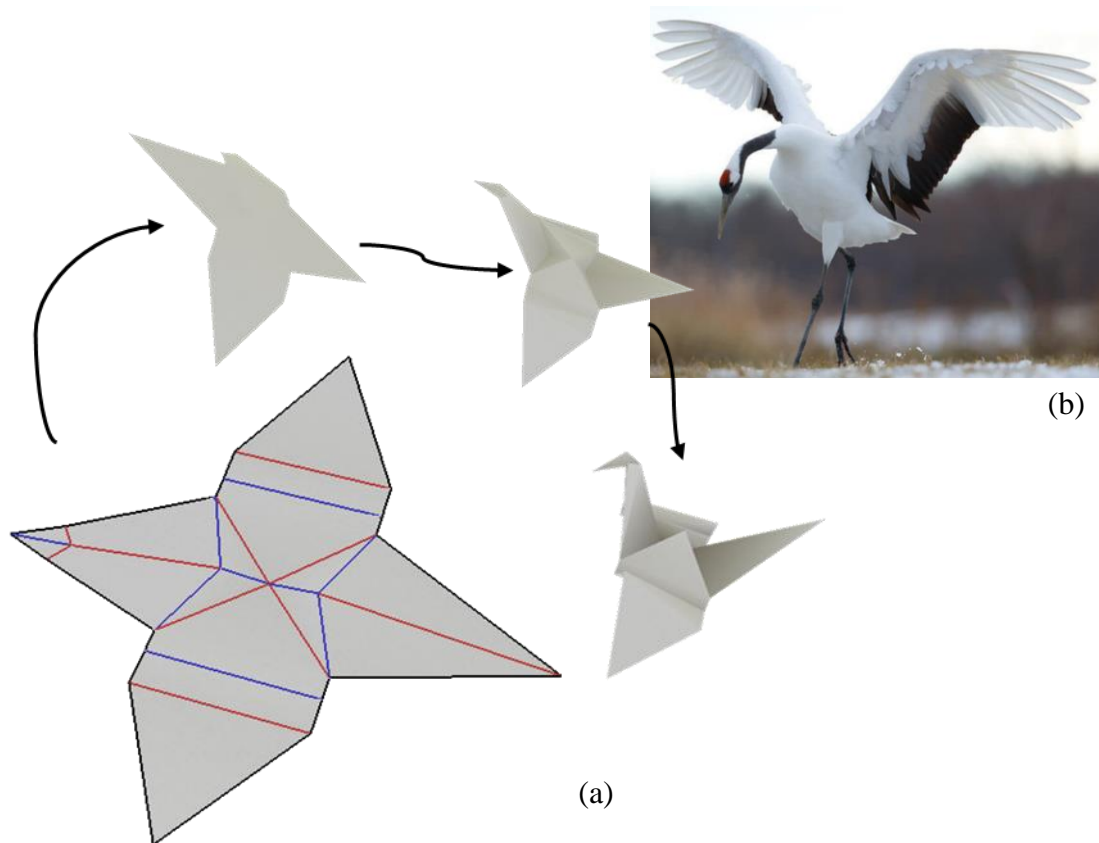


Figure 2-1: Traditional paper crane (*Orizuru*). (a) Simplified representation of the basic folding process; (b) Picture by 2006 Martin Bailey of the red-crowned crane, the inspiration for the *Orizuru* origami.

The combination of origami concepts with smart material elements allows the developing of complex and low-weight self-foldable structures, that can permeate between geometric configurations through the folding process promoted by the origami pattern. Shape memory alloys (SMAs) are smart or responsive materials being applied in different situations and with special interest for origami structures (Savi *et al.*, 2016). Dynamical applications of SMA systems constitute a rich research field that can be explored in different situations. Savi (2015) presented a review of dynamical applications of smart systems, or systems actuated by smart materials, including oscillators, adaptative tuned vibration absorbers (ATVA), adaptative structures and rotordynamic systems.

Among the combined SMA-origami applications, it should be pointed out the minimally invasive surgery actuator with 4 degrees of freedom (DoF) (Salerno *et al.*, 2014); a NiTi stent generated by a closed origami tessellation (Kuribayashi *et al.*, 2006); and an origami-wheel that has the inherent ability of radius variation (Lee *et al.*, 2013).

A robot with a variable diameter wheel can drive through different soils, climb or deviate from different objects with a reduced number of actuators. Even though the engineering application of origami-inspired concepts is a growing field, there are few works related to the dynamics of these complex devices, as shown along this work.

2.1. Origami concept

Origami is a three-dimensional structure generated from a two-dimensional source by a sequence of folding. In general, origamis can be categorized in three major classes, widely known as *origami*, *kirigami* and *modular origami*. The definition of these classes is based on the required combination of actions to generate the desired structure and does not take into consideration the fold but the general process.

The *origami* class is related to the simple folding process as popularly spread, corresponding to the continuously folding process of a flat and continuous paper sheet, and no cuts or glued elements are allowed. The *kirigami* class corresponds to the process of cutting the folded paper to generate the desired structure. Alternatively, it is possible to fold a pre-cut paper sheet, resulting in the well-known *pop-up cards*.

The *modular origami* class corresponds to an assemble of a number of either the first or the second-class origamis. In this class, each part to be assembled is known as a module, and the structure is generated by gluing or simply connecting each module.

Different folding patterns and strategies can be employed to obtain an origami element. Instead of being classified by the general process, the origami element can be classified according to the folding type. This classification allows an origami to be categorized in seven basic groups (Figure 2-2): action origami; modular origami; wet folding; purelanding origami; origami tessellation; kirigami; and strip folding. A brief description of each one of these groups is presented in the sequence.



Figure 2-2: Representations of the seven basic origami types. (a) Action Origami (Jumping frog); (b) Origami tessellation; (c) Wet-folded origami; (d) Pureland Origami (simple version of the Jumping frog); (e) General forms obtained from the same origami tessellation; (f) Kirigami; (g) Strip folding origami.

Action Origami: once the folding sequence is complete, the origami has the capability of preset motion between the panels, around the creases. One example is the origami called *jumping frog*, where, at the final configuration, a group of folds take advantage of the material elasticity and low stiffness, which results in a jumping motion once a force is applied on those creases (Figure 2-2a).

Modular Origami: this category relates to a 3D structure built from stacking identical pieces (modules) to form a complex shape. The module itself is usually simple, but the final structure may have a high complexity and the stacking process might be tricky (Figure 2-2b).

Wet-folding: it is possible to generate origamis without hardly- folding the creases. In this technique, the paper sheet is damped to allow light curving, and the final shape is obtained once it is dry. This is a highly complex technique, and it is usually applied to the folding process of complex figures, such as the wet-folded *Greater Kodu* by Robert Lang (Figure 2-2c).

Pureland Origami: it was developed by a British paper folding named John Smith with the purpose to help those with limited motor skills or inexperienced folders. In this technique, only simple mountain/valley folds are allowed, and the usual folding inversions present in most origami patterns are not allowed (Figure 2-2d).

Origami Tessellations: this category has increasing its popularity among researchers on the last few years, due to some interesting aspects such as a negative Poisson and the high compaction allied to the morphing ability. Tessellations are also generated by a repetition of a single module or pattern but, differently from *modular origami*, they are obtained from a single paper sheet. This type of origami it will be further explored in section 2.3 (Figure 2-2e).

Kirigami: as previously described, it is generated through cuts on paper sheet, and the final form is obtained by bending or slightly folding the cut paper (Figure 2-2f).

Strip folding: it is the technique of generating an origami shape by using just strips of papers by weaving them. It is mostly artistic, but there are some applications as zigzag-folded strips generating tubes with increased stiffness and folding capability (Figure 2-2g).

Origami nomenclature is based on artistic, mathematical and engineering terms (Lang, 2017; Greenberg *et al.*, 2011; Tachi, 2010), where most of them are well defined and self-explanatory. However, it is interesting to clarify the origami terms employed in this work, their meanings and situations related to their use, which is presented in the sequence. In order to start the presentation, consider Figure 2-3 that presents the flapping bird origami, a variation of the Tsuru folding, showing some of the elements described in the sequence.

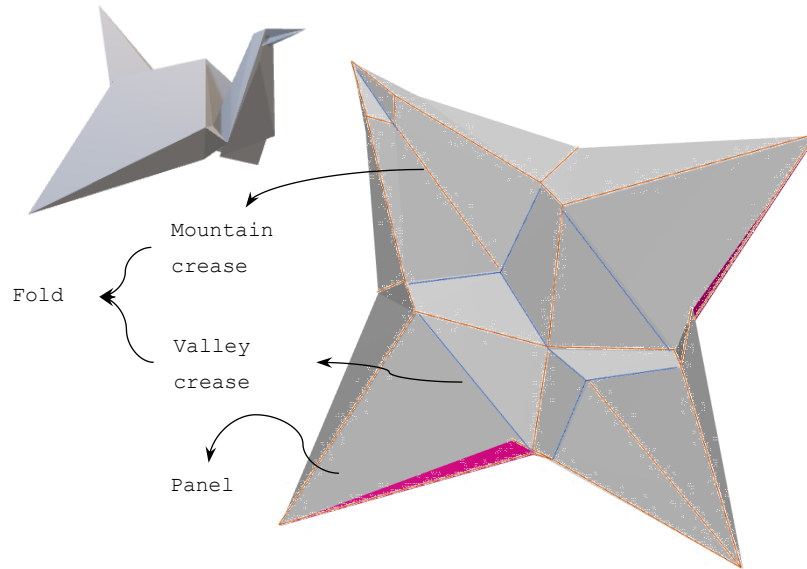


Figure 2-3: *Flapping bird* origami (top left) and the bottom view of the crease pattern (bottom right)

A *crease* is a straight line along which a fold takes place, and this crease can be *unfolded*, *partially folded* or *fully folded* (Lang, 2017), and it is usually associated to a revolute joint. In this work, the *unfolded* state is associated to a revolute joint angle θ of 0 degrees, while the *fully folded* state is associated to a revolute joint angle θ of 180 degrees, and the *partially folded* state belongs to the range $]0,180[$ degrees.

A *fold* is the type of the origami crease, and it can be classified as mountain or valley, as can be seen at Figure 2-4-a. The crease type receives those names since it visually resembles a mountain or a valley. It is worth noticing that the definition of the fold type is dependent on the observer, since the same origami, when viewed from the bottom, presents an inversion on the crease type (Figure 2-4-b and Figure 2-4-c).

A *fold angle* is the angular opening of a crease, and it is usually measured as the angle between the normal vectors of two consecutive faces connected through a crease. In this work, the fold angle has also an associated direction, meaning that the evaluation of this angle can be associated with either an opening or a closure motion of that fold.

A *panel* or *face* is the closed area defined by a set of creases and boundaries, such that this set does not contain any crease or vertex. Triangular panels or faces, for origamis as the example in Figure 2-4, are defined by two creases and a boundary or three creases. Squared panels or faces are usually defined by three creases and a boundary or four creases, such as the example in Figure 2-2g.

An *origami pattern* or simply *pattern* is a set of creases, among valley and mountain folds, that define an origami element. Different patterns generate different structures, and it can be formed by a set of different creases or by a repetition of a specific group of creases. This second case generates the tessellations, and this concept is further explained in section 2.3.

A *single vertex origami* is an origami where all creases converge to the same vertex, and it is the case of the waterbomb pattern (Figure 2-4).

A *rigidly foldable* origami is an origami pattern in which the panels remain flat and undeformed during all the folding/ unfolding process, and this concept is further explained in section 2.4.

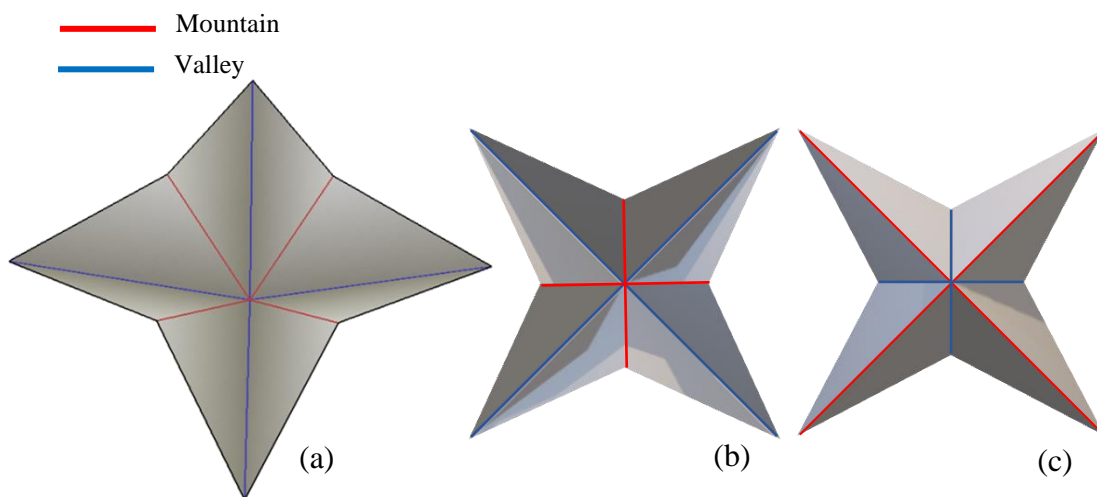


Figure 2-4: Fold state or definition as mountain or valley crease type. (a) Waterbomb cell with the fold definition; (b) Top view; (c) Bottom view.

A crease pattern is defined as *flat-foldable* if, once all folds are activated, the final form can be considered as flat. A *flat-foldable* origami must at least attend to Maekawa's and Kawasaki's Theorems, as follow:

Maekawa's Theorem: At any given vertex of a flat-foldable origami pattern, the amount of mountain folds differs by two from the amount of valley folds.

Kawasaki's Theorem: At any given vertex of a flat-foldable origami pattern, the sum of every other angle about said vertex is always 180 degrees.

Note that if an origami pattern is *flat-foldable*, then it attends to Kawasaki's and Maekawa's Theorems. The opposite is not necessarily true, as shown in Figure 2-5. This

pattern suffices both theorems, but it is not *flat-foldable*. This happens because extending globally the *flat-foldability* concept is not that easy and simple. In fact, identifying a *flat-foldability* aspect is characterized as a *Complete NP Problem* (complete nondeterministic polynomial problem), meaning that the *flat-foldability* condition can be verified in a NDTM (nondeterministic Turing's machine) but not solved.

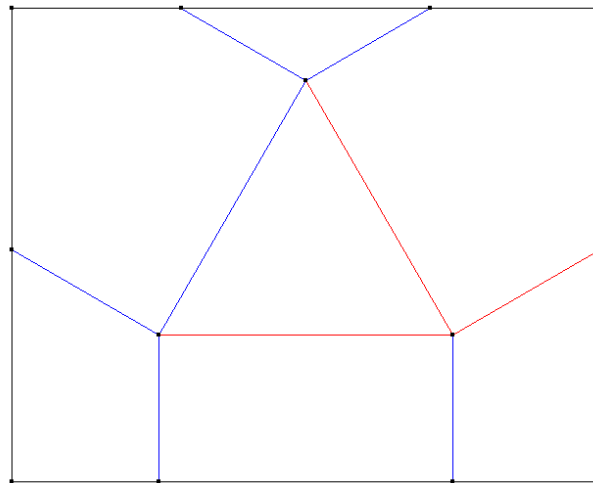


Figure 2-5: “An impossible fold”, presented first by Thomas Hull in the *Congressus Numerantium*, 1994.

2.2. Developable surface

A developable surface is defined as the one that can be flattened onto a plane without deformations or bending. In other words, it is a surface that has *zero Gaussian curvature* everywhere. Based on that, since the Gaussian curvature, K , is evaluated as the product between two principal curvatures, κ_1 and κ_2 , at least one of them must be zero. On this basis, developable surfaces include planes ($\kappa_1 = \kappa_2 = 0$), cylinders, elliptic cones or cones ($\kappa_1 > 0, \kappa_2 = 0$), and hyperbolic cylinders ($\kappa_1 = 0, \kappa_2 < 0$). An interesting property of these surfaces is that they can be made from a metal sheet, and therefore, they can be obtained by transformation from a plane. Figure 2-6 shows origami tessellations generating two developable surfaces.

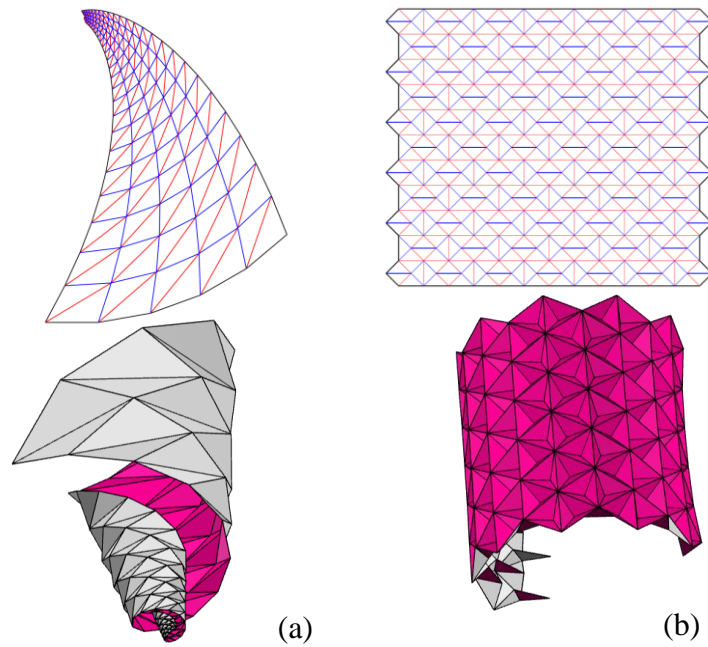


Figure 2-6: Origami tessellations generating developable surfaces: (a) Whirlpool pattern (cone); (b) Huffman Stars-Triangles (cylinder).

Origami tessellations generate developable surfaces allowing the design of 3D structures obtained through folding patterns of a 2D element such as a sheet of paper. Origami mechanisms are designed based on the developable behavior, which allows the compactness without losing range of action and effectiveness.

2.3. Tessellation

A tessellation is built from a repetition of a pattern or containing some identifiable periodicity, without gaps or holes, covering a flat surface. Tessellations generated with origami-based concepts are a complex developable structure composed by foldable shapes with the capability to map 3D structures onto 2D flat surfaces without stretching.

This developable characteristic of origami tessellations has been widely studied. Tachi (2010; 2011; 2012; 2013) developed a kinematic analysis on waterbomb tessellations built from regular basis (6-creased squared waterbomb pattern) to achieve adaptive freeform surfaces using an open-source software. Kuribayashi *et al.* (2006) explored a closed form of the waterbomb tessellation in a biomechanical application, developing a shape memory alloy stent. The structure is self-developable and is capable

of achieving large deployable ratio. Rodrigues *et al.* (2017) performed a dynamical investigation of the stent, evaluating shape morphing and stability behavior for different external actuations, assuming a perfectly symmetric description. Lee *et al.* (2013) and Felton *et al.* (2014) fabricated a deformable wheel robot, exploring the shape changing of the closed form tessellation for the wheel radius variation. Fonseca *et al.* (2019) investigated the nonlinear dynamics of the origami wheel using mirror-symmetry, exploring the shape morphing and the influence of external loads over the structure behavior. Fonseca & Savi (2020) explored this shape morphing as a two wheeled robot with deformable wheels, dealing with its nonlinear dynamics.

Part of the challenge in designing tessellations is the large number of variables and degrees of freedom (DoFs) associated with such complex structures. Zhao *et al.* (2018) explored this complexity, designing generalized waterbomb tessellations to describe several 3D shapes going from spherical and cylindrical elements to hyperbolic paraboloids and torus, exploring asymmetries on both the pattern design and its shape configuration.

The tessellation is characterized by the identifiable repeated pattern over a $m \times n$ sheet and the repetition directions \mathbf{v}_1 and \mathbf{v}_2 (Figure 2-7). The direction \mathbf{v}_1 provides the pattern repetition along the row (with dimension m) while the direction \mathbf{v}_2 provides the pattern repetition along the column (with dimension n).

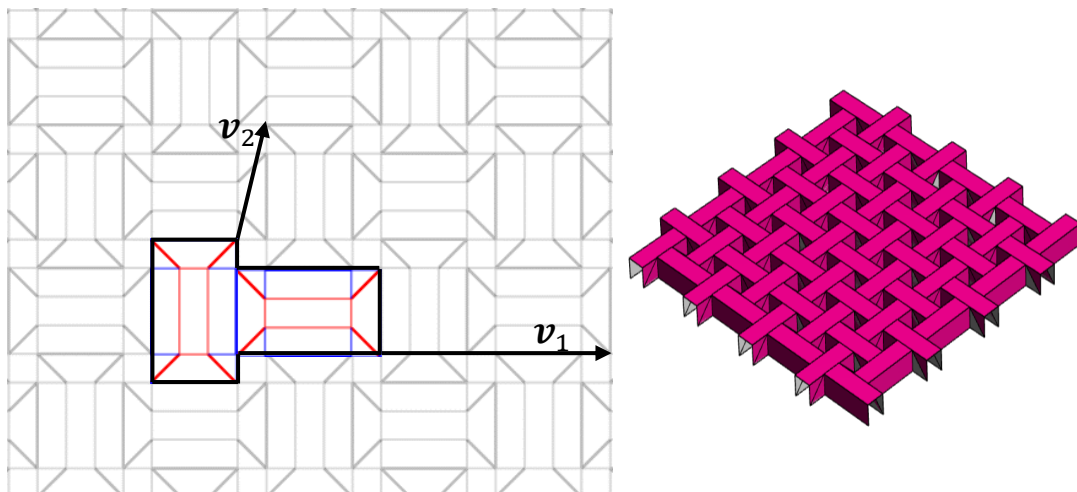


Figure 2-7: Directions for tessellation pattern Huffman Rect Wave and folded pattern

Tessellations can be classified as *regular*, *semi-regular* and *demi-regular*. The first group refers to tessellations generated by a repetition of a regular polygon, and it can be identified by looking into each vertex. In a regular tessellation, the pattern is identical on every vertex. There are only three regular tessellations: generated by triangles, squares or hexagons.

The *semi-regular* group refers to tessellations generated by two or more regular polygons, where it is possible to identify sets of vertexes belonging to different groups, depending on the polygons that surround it. There are eight plane semi-regular tessellations, composed by a mix among triangles, squares, hexagons, octagons and dodecagons (Ghyka, 1977; Williams, 1979; Steinhaus, 1999; Wells, 1991).

The definition of the *demi-regular* tessellations is controversial. Some authors define this group as composed by a mix of regular and semi-regular tessellations. More precisely, three regular and eight semi-regular. Other authors define demi-regular tessellations as a general tessellation presenting more than one transitivity class of vertex, which means more than one type of vertex.

Origami tessellations have a visual similarity to the tessellations, not necessarily following the mathematical classification and description, but keeping the general repetition-like aspect. Yoshimura tessellation is a triangular origami tessellation generated by the repetition of the Yoshimura or diamond pattern (1995), which repetition directions and chosen base pattern are represented at Figure 2-8-a. A squared origami tessellation is generated by the repetition of the Miura-Ori pattern, represented at Figure 2-8-b. Note that the repetition directions change depending on the tessellation. Besides, it might vary depending on the chosen base pattern.

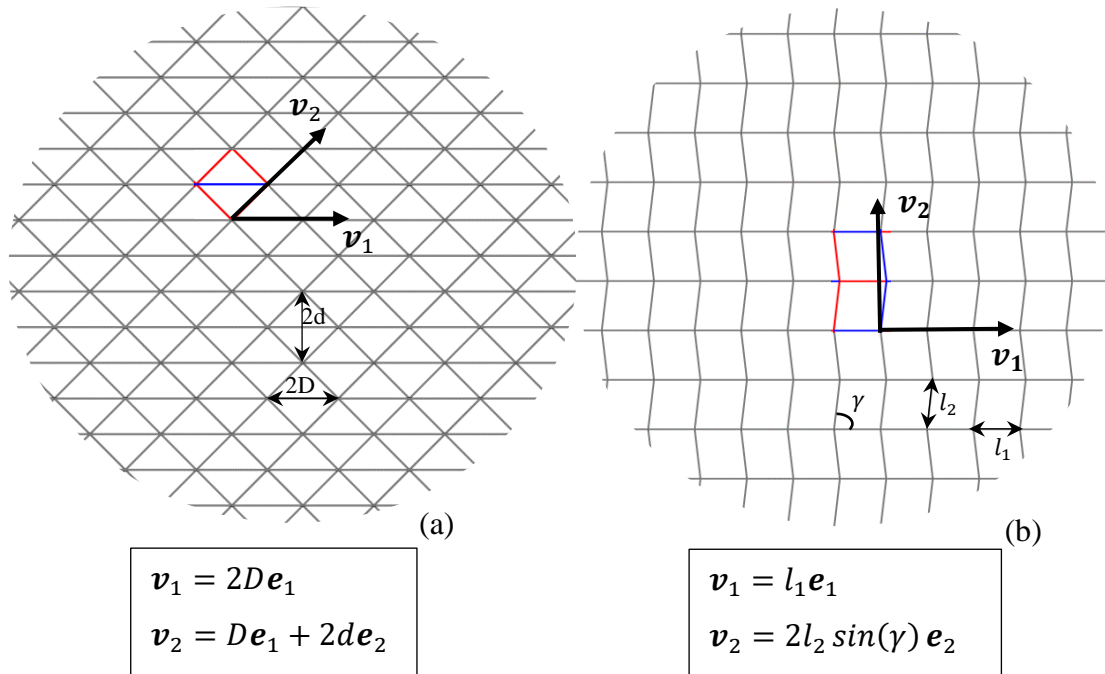


Figure 2-8: Regular tessellation. (a) Yoshimura; (b) Miura-Ori

The waterbomb tessellations are generated by a 6-creased waterbomb pattern, and further explanations of this tessellation are presented in chapter 5 . As an example of a general origami tessellation, the flower tower is represented at Figure 2-9.

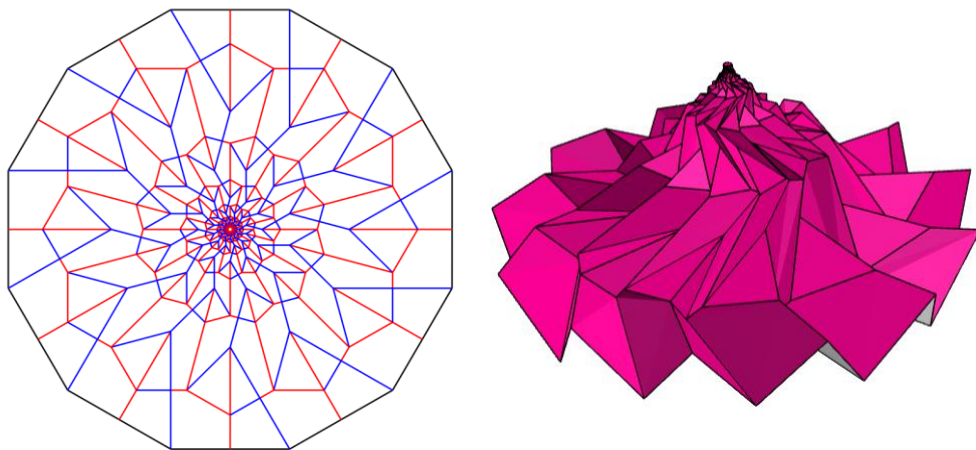


Figure 2-9: Flower tower tessellation based on the design by Chris K. Palmer. On the left, the pattern is in the fully opened state. On the right, the pattern is in a partially folded state.

2.4. Rigid foldability

The mechanical description of the origami structure is essentially related to the fold rigidity. If the panels or faces are conceived by elements of high stiffness while the creases have a low stiffness, it is reasonable to assume that the deformation is prominent on the crease area and the origami is assumed to be rigid or *rigidly foldable* (Figure 2-10a). If the ratio between the panels and the creases stiffness decreases, the deformation area increases, and the rigid foldability hypothesis fails (Figure 2-10b).

The folding process description must be chosen according to the nonlinearity of the structure, related to both geometrical and mechanical parameters. If the origami is rigidly foldable, it can be evaluated through an equivalent mechanism, and its motion is fully described by purely geometric, arithmetic or kinematic models (Lang, 1996; 2011; Belcastro and Hull, 2002; Lee *et al.*, 2013; Song *et al.*, 2013; Chiang, 2000; Chen *et al.*, 2016; Pesenti *et al.*, 2015). On the other hand, if the panel deformation is such that the origami cannot be assumed as rigidly foldable, mechanical properties must be taken into account, so these hidden degrees of freedom are considered and properly described (Lv, 2014; Gattas and You, 2014; Liu & Paulino, 2017).

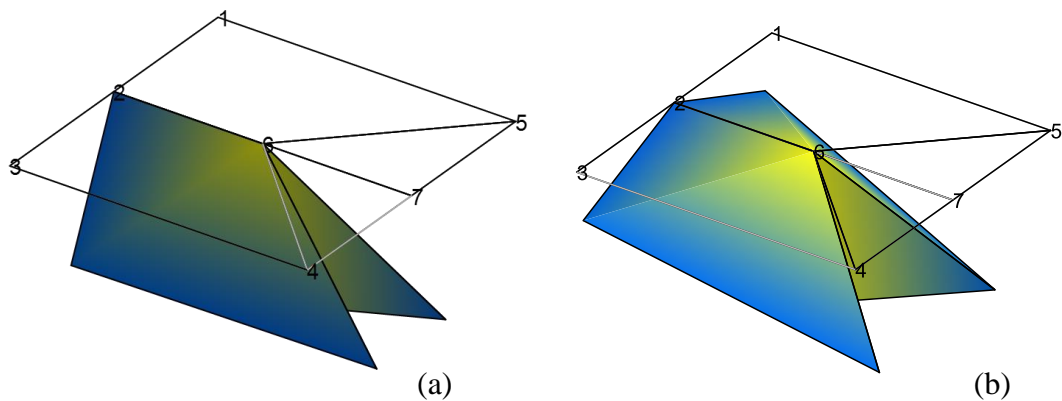


Figure 2-10: Miura-Ori pattern with a high (a) and a low (b) ratio between panels and creases' stiffness, with mechanical description provided by a displacement-based method, and panel flexibility represented by a virtual fold.

2.5. Origami applications

Origami elements and concepts have inspired the design of self-foldable, compact and adaptive systems and devices for several science and technological fields of knowledge (Peraza-Hernandez *et al.*, 2014; Fei & Sujan, 2013). Shapes such as spheres and cylinders or elements with morphing ability can be applied to architecture (Sorguç *et al.*, 2009), robotics (Felton *et al.*, 2014; Miyashita *et al.*, 2015), aerospace systems (Nishiyama, 2012; Webb *et al.*, 2016) and biomedical devices (Salerno *et al.*, 2014; Miyashita *et al.*, 2016).

The compact inherent ability of origamis allows the development of structures such as the *starshade*, an external occulter with the purpose to detect and directly characterize exoplanets, by blocking the light emitted by nearby stars and focusing only the light emitted from orbiting planets onto a telescope (Webb *et al.*, 2016). The structure is launched in a fully folded state, in the maximum compact capacity of the *starshade* (Figure 2-11) and, once it is in orbit, it is deployed and fully opened, until it reaches the maximum covered area in the fully unfolded state.

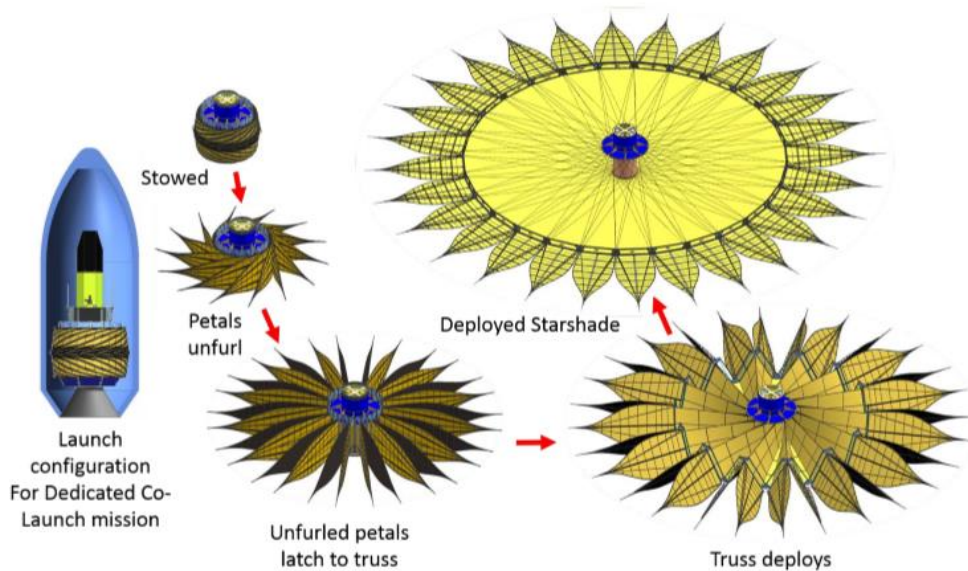


Figure 2-11: Starshade deployment sequence, from the launch configuration (fully folded) to the deployed state (fully unfolded). (Image credit: www.nasa.gov)

The self-foldability allows the development of structures that can have from millimeters to hundreds of meters, considering its largest dimension. The coupling between self-foldable structures and smart materials, such as Shape Memory Alloys

(SMA), allow a wireless actuation of said devices using potential fields, such as electro-magnetic, and thermal variations.

Boyvat *et al.* (2017) developed a scalable self-folding multijoint robot actuated with SMA through the application of an external magnetic field. This device allows the development of micro-robotic arms with a tridimensional movement, low weight, low wiring and no-contact actuation and control (Figure 2-12).

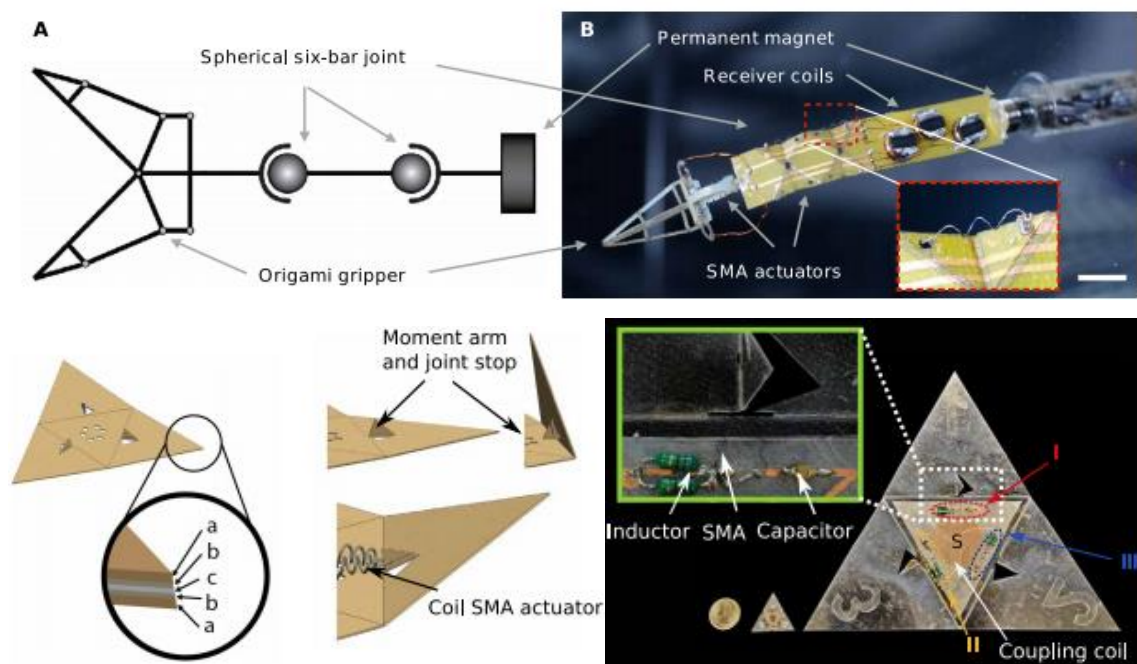


Figure 2-12: Self-folding wireless actuated robotic arm. a) Simplified illustration of the kinematic design and components. The natural spherical movement of the waterbomb pattern is represented by spherical joints; b) A micro-robotic arm prototype with a permanent magnet for anchoring, with a panel highlighting one SMA coil actuator attached at the side of the waterbomb pattern; c) On the left, a three-dimensional rendering of the folding laminate containing a rigid sheet -a-, and adhesive layer -b- and a flexure film -c-. On the right, a folding joint with a coil SMA actuator with a moment arm that also serves as a fold stop (Image credit: Boyvat *et al.*, 2017).

Another interesting origami-inspired robot is proposed by Lee *et al.* (2020). Using a different origami pattern and a cable driven actuation, the device, named TWISTER, is an adaptive hand-like for grasping of objects in different shapes, weights, sizes, and textures. Each ‘finger’ is actuated by a cable passing through the entire structure and attached to servo motors located at the base (‘palm’). By pulling the cable, the structure folds in a twisting motion until it reaches the object. The major advantage of this device is its underactuated ability of grasping objects, which reduces considerably the weight and necessary devices to obtain a claw.

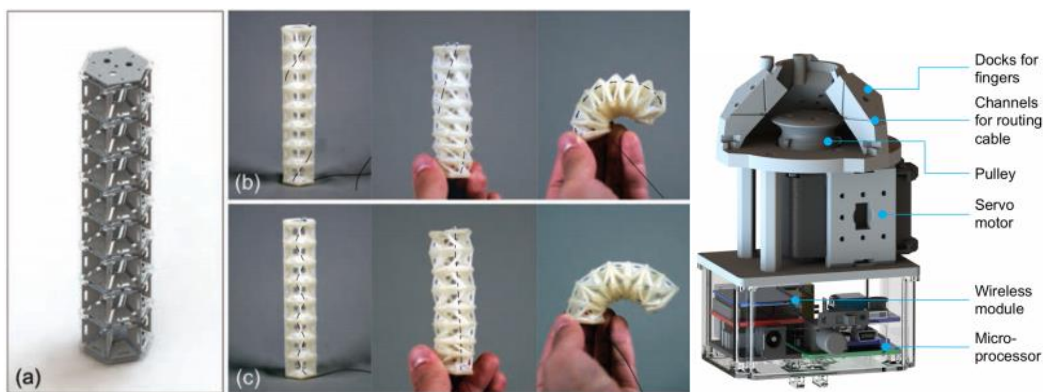


Figure 2-13: CAD drawing and printed outcome. (a) CAD model of TWISTER with embedded holes for routing cables; (b) Printed structure with cables routed diagonally; (c) Structure with cables routed in a zigzag pattern; (d) Main chassis contains a microprocessor, battery, power switch, mini-USB port, XBee module, servo motor, pulley mechanism, and docks for the fingers and cables (Image credit: Lee *et al.*, 2020)

On a different approach, Zang *et al.* (2018) developed a direct-write laser-patterning technology to make metal-carbide-graphene (MCG) composites directly on paper substrates through engraving the surface (Figure 2-14). This technology allows the design of low cost, low weight, easily scalable and compactable electronic devices, such as supercapacitors, paper-based piezoelectric generator, electrochemical sensors, and actuators.

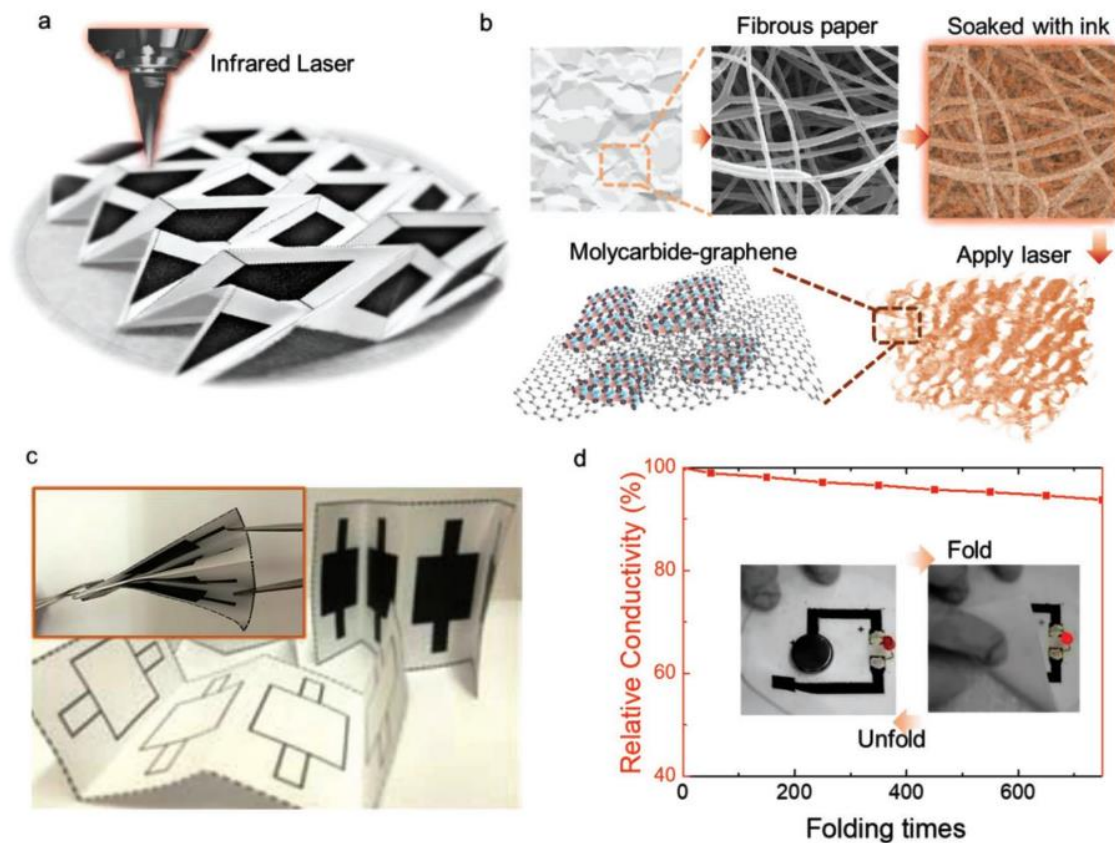


Figure 2-14: (a) Photo of a fabricated origami structure after the direct laser-write MCG patterning process (black color areas) on a paper substrate (white color areas); (b) Schematic illustration of the simplified MCG process from fibrous paper, soaked with the gelatin-mediated ink containing Mo^{5+} ions, laser conversion process, to the resulting MCG composites; (c) Two partially folded, four $2 \times 2 \text{ cm}^2$ electrodes on a paper substrate: (top) after the laser conversion process, and (bottom) before the conversion process. (inset) A fully folded device with two electrodes on top and two electrodes at the bottom for a two-capacitor in sandwich structure to be connected in series or parallel as supercapacitors; (d) Recorded relative conductivity of an electrical connector made of MCG composites during the 750 cycles of 180° mechanical folding tests. (inset) Use of the mechanical folding and touching of electrodes made of MCG composites as an electrical switch to turn on/off a red light-emitting diode (Image credit: Zang *et al.*, 2018)

The self-folding characteristic attributed to some origami patterns, combined to the compactness, allow the design of miniature origami robots that can complete complex tasks, such as swim, walk and carry particles or pieces many times heavier than its own

weight (Miyashita *et al.*, 2015). The miniature robot (Figure 2-15a) is conceived with different materials, allowing its degradation on different solvents, such as acetone. A further development on the miniature robot led to the design of a miniature robot for patching stomach wounds (Miyashita *et al.*, 2016). The origami is collapsed onto a cylindrical shape and inserted into an ice capsule to be swallowed (Figure 2-15b). Once that the capsule melts in the stomach, the robot is released and self-folds. The robot is controlled from the outside, and it can be used to patch stomach wounds or even for the retrieval of batteries and other small components swallowed by kids.

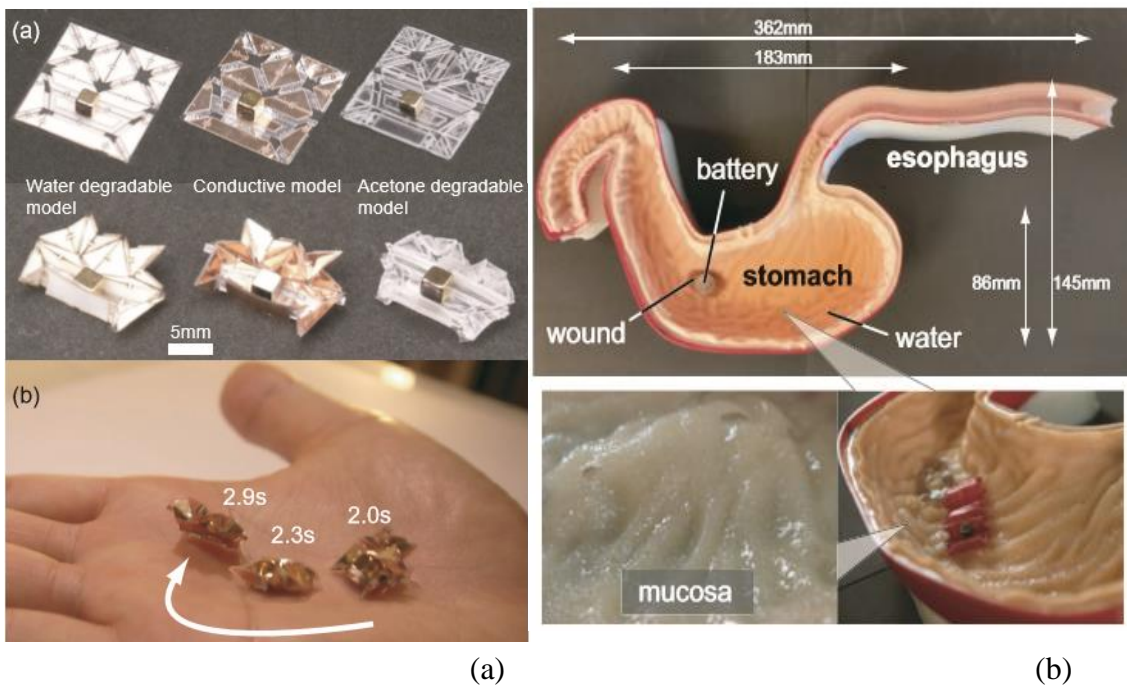


Figure 2-15: Self-foldable miniature origami robot. (a) Miniature robot that walks, swims, carry loads and degrades; (b) Miniature robot for patching stomach wounds and retrieving swallowed batteries (Image credit: Miyashita *et al.*, 2015;2016)

Another biomedical application of origami structure is the Nitinol stent graft proposed by Kuribayashi *et al.* (2006), that has the purpose to reduce the occurrence of restenosis. The stent with a membrane cover avoids the accumulation of fat tissue on the stent area through the holes and spaces of the stent (Figure 2-16).



Figure 2-16: Stent graft developed with a Nitinol sheet, using waterbomb tessellation (Image credit: Kuribayashi, 2006).

Besides, the stent graft is designed with a Nitinol sheet, different from the original stent produced with Nitinol wires, for shape recovery without permanent damage to the device. The origami pattern used on the stent graft is the waterbomb tessellation further exploited in Chapter 5 .

Waterbomb pattern is employed to build the origami-wheel (Lee *et al.*, 2013; Lee *et al.*, 2016), a structure based on the magic-ball closed tessellation. The structure has degrees of freedom (DoFs) associated with the creases of the tessellation, allowing the shape changing from a flat circular tube to a cylindrical shape. This shape changing can be translated as a wheel's radius variation, reducing the height of the robot, and allowing it to pass under obstacles. This shape changing also gives the robot an additional ability to bypass obstacles and to follow a curved path with a reduced number of required actuators (Figure 2-17).

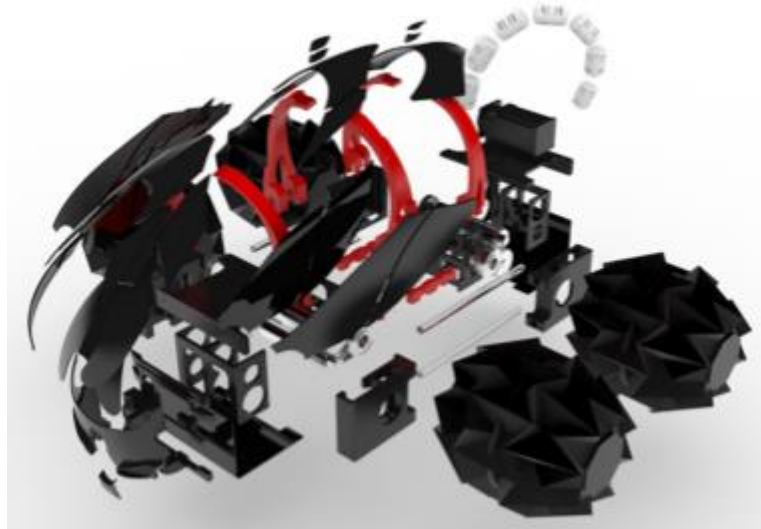


Figure 2-17: Robot with an origami gripping arm and origami wheels. (Image credit: Lee *et al.*, 2016).

This closed tessellation can also be used as an easily controllable water landing gear for drones, that is inflated for landing (kept in an opened configuration) and deflated on cruise (kept in a closed configuration). This device, shown in Figure 2-18, allows a smooth water landing while keeping the flight stability (Le *et al.*, 2014).



Figure 2-18: Application of a waterbomb tessellation as an inflatable drone landing gear for water landing (Image credit: Le *et al.*, 2014).

3 Origami Modeling

This chapter presents the modeling alternatives to describe the origami structure behavior. The chapter starts with the kinematic formulation, where the origami is described by an equivalent mechanism and its kinematic behavior is evaluated through its workspace. It is followed by the trigonometric formulation employed for the description of the symmetric behaviors. Kinematic formulations define reduced-order models that can be employed for different purposes, and the trigonometric description allows a reduced-order algebraic formulation. Finally, a mechanical approach is carried out considering the finite element analysis (FEA). This approach allows one the analysis of panel deformation.

3.1. Kinematic approach

Origami description can be carried out by considering a unit cell, whose kinematics description uses an equivalent mechanism treated as a linkage mechanism. Its shape can be completely defined by a required number of inputs or angles between the links, and the number of inputs is defined by the mobility of the mechanism. Chebyshev-Grübler-Kutzbach (C-G-K) equation can be employed for this aim as follows (Gogu, 2004),

$$M_{ob} = \Lambda(N_L - J - 1) + \sum_{i=1}^J f_i \quad (3.1)$$

The mobility, M_{ob} , is a function of the number of links, N_L , the number of joints, J , and the joint type (planar, spherical, cylindrical). The joint type influences two variables: the generalized displacement of the i th joint, f_i ($i= 1 \dots J$), and the constraint parameter related to the mechanism movement, Λ . A unit cell of the waterbomb pattern

is typically a spherical mechanism ($\Lambda = 3$) with 6 faces or links ($N_L = 6$) and 6 creases or joints ($J = 6$). Since all the joints are R-type (revolute joints), each one has only one DoF ($f_i=1$), the rotation around its axis. Therefore, C-G-C equation establishes that $M_{ob} = 3$, which means that each cell is completely described by three angles, each angle defined between two consecutive links.

The definition of joint type considers three basic forms described in the sequence. A planar mechanism has its motion restricted to the plane, allowing two translational movements and a rotation $\{x, y, \theta_z\}$ (Figure 3-1a), which provides a constraint parameter $\Lambda = 3$. A spherical mechanism has rigid connections with movements restricted to a sphere $\{\theta_x, \theta_y, \theta_z\}$ (Figure 3-1b), providing a constraint parameter $\Lambda = 3$. Finally, a spatial mechanism can translate and rotate in any direction, leading to a constraint parameter $\Lambda = 6$ (Figure 3-1c).

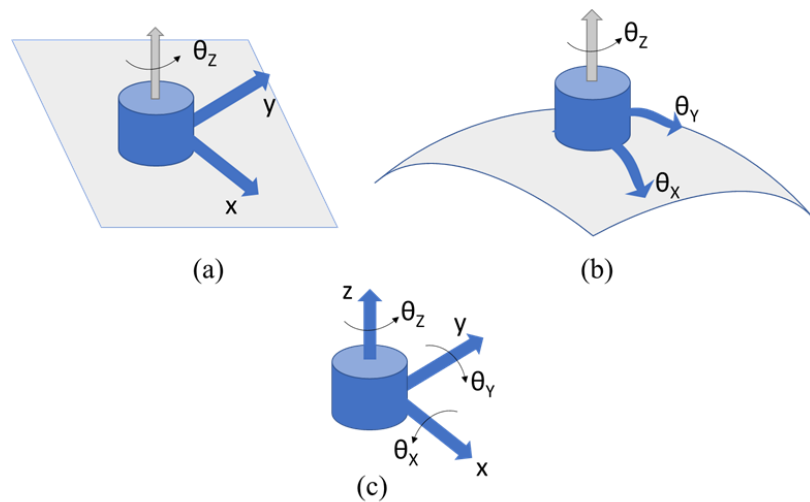


Figure 3-1: Mechanism movement representation for joint type identification. (a) Planar; (b) Spherical and (c) Spatial.

The objective of forward kinematic analysis is to determine the cumulative effect of the entire set of joint variables, while the objective of the inverse kinematics is to determine the individual values for each joint that result in a specific configuration. This work uses a forward kinematics formulation to evaluate the mechanism configuration. A proper formulation is chosen to avoid singularities that would cause the inverse problem to be ill-posed. One way to address the problem is the use of dual quaternion method (Figueredo *et al.*, 2013), a robust technique that allows to unify the translation and the

rotation into one single invariant state. Another formulation involves the use of screw theory applied to the joints, or even the definition of screw polygons (Mavroidis *et al.*, 1997) and screw triangles (Huang & Chen, 1995). The screw triangles theory, applied by Huang & Chen (1995), is focused on the unification of finite and infinitesimal kinematics, which proved to be relevant since the motion of rigid bodies can be described as a serial chain of screws.

In this work, the Denavit-Hartenberg (D-H) formulation is employed (Denavit & Hartenberg, 1955), and the transformation between two consecutive joints i and $i + 1$ is a consequence of two rotations and two translations, resulting in a 4 parameters description for each joint-link pair. Therefore, the transformation matrix from joint i and to joint $i + 1$ is given by

$${}^i T_{i+1} = \begin{bmatrix} \cos(\theta_i) & -\sin(\theta_i) \cos(\alpha_i) & \sin(\theta_i) \sin(\alpha_i) & a_i \cos(\theta_i) \\ \sin(\theta_i) & \cos(\theta_i) \cos(\alpha_i) & -\cos(\theta_i) \sin(\alpha_i) & a_i \sin(\theta_i) \\ 0 & \sin(\alpha_i) & \cos(\alpha_i) & R_i \\ 0 & 0 & 0 & 1 \end{bmatrix} \quad (3.2)$$

where α_i is the angular distance between two consecutive joints, from z_i to z_{i+1} axis about the x_{i+1} axis; θ_i is the rotation of the i -th joint, from x_i to x_{i+1} axis about the z_i axis; a_i is the offset distance measured from the origin O_i to the intersection of axes z_i and x_{i+1} , along the x_{i+1} axis; and R_i is the joint offset, measured as the distance from the i frame to the intersection of axes z_i and x_{i+1} , along the z_i axis (Figure 3-2).

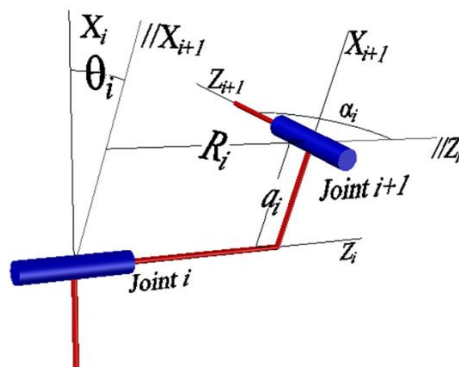


Figure 3-2: D-H parameters' setup.

The D-H convention requires an additional restriction or constraint equation to accurately describe the end-effector, that is the last linkage. In the case of origami

patterns, the equivalent mechanism is usually a closed chain, which means that the last joint connects to the first one. In this regard, there is no sense in talking about the end-effector, instead it is necessary to evaluate the loop closure equation that, for a chain with n joints, is given as follows

$$\mathbf{P}(\boldsymbol{\theta}) = {}^1\mathbf{T}^2 {}^2\mathbf{T}^3 \dots {}^i\mathbf{T}^{i+1} \dots {}^n\mathbf{T}^1 \quad (3.3)$$

where $\boldsymbol{\theta} = [\theta_1 \dots \theta_6]^T$ is the vector of θ_i . Besides, once that the first and last joints are connected by a link, the loop-closure equation must satisfy $\mathbf{P}(\boldsymbol{\theta}) - \mathbf{I} = \mathbf{0}$.

The system (3.3) can be written as $f_i(\boldsymbol{\theta}) = [\mathbf{P}(\boldsymbol{\theta}) - \mathbf{I}]_{mn}$, where $i = 4(m - 1) + n$, for $m, n = 1..4$. The parameters attributed to each origami case will dictate the number of degrees of freedom (DoF) for that case. In a general condition, the system results in 16 equations in the form $f_i(\boldsymbol{\theta}) = 0$, $i = 1..16$.

The system is solved in this work using nonlinear least-square solver, where the system solutions are obtained as the minimization of the vector $\mathbf{F}(\boldsymbol{\theta})$, for a vector input $\boldsymbol{\theta}$, given by

$$\begin{aligned} \mathbf{F}(\boldsymbol{\theta}) &= [f_1(\boldsymbol{\theta}) \ f_2(\boldsymbol{\theta}) \ \dots \ f_{16}(\boldsymbol{\theta})]^T \\ \min_{\boldsymbol{\theta}} \|\mathbf{F}(\boldsymbol{\theta})\|^2 &= \min_{\boldsymbol{\theta}} (\sum_{i=1}^{16} f_i(\boldsymbol{\theta})^2) \end{aligned} \quad (3.4)$$

The system is solved within the lower and upper boundaries that define each θ_i range that, in a general case, is $[-\pi, \pi]$, with a central method to estimate gradients for the finite difference estimation. The boundaries are used here to avoid superposition or penetration of panels, because even though some configurations are allowed in the equivalent mechanism, they are not achievable by the origami itself, due to these superpositions/ penetrations. The solution is considered converged for a threshold of 10^{-15} for both the function, satisfying $f_i(\boldsymbol{\theta}) = [\mathbf{P}(\boldsymbol{\theta}) - \mathbf{I}]_{mn} \approx 0$, and the variables (θ_i).

3.2. Spherical trigonometry

Spherical linkage mechanisms have the property that every link in the system rotates around the same fixed point. Based on that, it is possible to describe the

mechanism motion using spherical trigonometry. Therefore, an analysis is developed assuming that the waterbomb cell has a symmetric motion, and the spherical trigonometry formulation provides a reduced-form analytical description of the origami motion.

This formulation is developed for a waterbomb unit cell, inscribed in a unitary radius sphere, where the waterbomb vertex O is located at the center of the sphere, as can be seen at Figure 3-3.

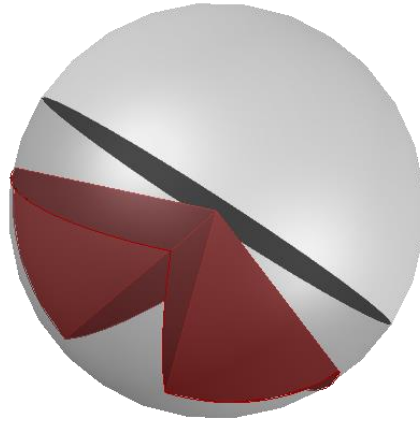


Figure 3-3: Schematic of a waterbomb spherical mechanism. The links are projected onto the sphere surface, and the joints' rotation axis intersect at the sphere center.

It is possible to describe relations among the arcs and the angle arcs through trigonometric functions applied to the spherical triangles described on the sphere surface (Figure 3-4). Note that for spherical triangles, sides a , b and c are given in angular units. Besides, uppercase letters are related to inner angles or angles between the arcs, and lowercase letters are related to arcs length, and, by definition, the angle between arcs is the smaller one. Among the trigonometric spherical relations, cosine and sine rules are employed and, given the spherical triangle in Figure 3-4, the sides and the inner angles relate as follows:

$$\begin{aligned} \cos(a) &= \cos(b) \cos(c) + \sin(b) \sin(c) \cos(A) \\ \frac{\sin(A)}{\sin(a)} &= \frac{\sin(B)}{\sin(b)} = \frac{\sin(C)}{\sin(c)} \end{aligned} \tag{3.5}$$

$$\Phi = U_{bar} + U_{spr} - V_{ext} \quad (3.6)$$

where U_{bar} is the strain energy stored in bars, U_{spr} is the strain energy stored in folding (torsional springs on the creases) and bending (torsional springs as virtual folds), and V_{ext} is the work done by external loads. By assuming quasi-static equilibrium,

$$\frac{\partial \Phi}{\partial \mathbf{u}} = \frac{\partial U_{bar}}{\partial \mathbf{u}} + \frac{\partial U_{spr}}{\partial \mathbf{u}} - \frac{\partial V_{ext}}{\partial \mathbf{u}} = \mathbf{T}_{bar} + \mathbf{T}_{spr} - \mathbf{F}_{ext} = 0 \quad (3.7)$$

where \mathbf{u} is the nodal displacement vector, \mathbf{T}_{bar} and \mathbf{T}_{spr} are internal forces and \mathbf{F}_{ext} is the external load. The analysis of internal forces needs to be evaluated considering a proper constitutive equation for both bars and springs. A small perturbation of the externally applied load corresponds to a perturbation in the nodal DoF displacements, such that

$$\mathbf{T}_{bar}(\mathbf{u}_0) + \mathbf{T}_{spr}(\mathbf{u}_0) + \left. \frac{\partial(\mathbf{T}_{bar} + \mathbf{T}_{spr})}{\partial \mathbf{u}} \right|_{\mathbf{u}=\mathbf{u}_0} d\mathbf{u} = \mathbf{F}_{ext} + d\mathbf{F}_{ext} \quad (3.8)$$

Since Equation (3.7) is satisfied by the solution \mathbf{u}_0 , Equation (3.8) reduces to

$$d\mathbf{F}_{ext} = \left. \frac{\partial(\mathbf{T}_{bar} + \mathbf{T}_{spr})}{\partial \mathbf{u}} \right|_{\mathbf{u}=\mathbf{u}_0} d\mathbf{u} = [\mathbf{K}_T(\mathbf{u}_0)] d\mathbf{u} = [\mathbf{K}_{bar}(\mathbf{u}_0) + \mathbf{K}_{spr}(\mathbf{u}_0)] d\mathbf{u} \quad (3.9)$$

where \mathbf{K}_T is the tangent stiffness matrix.

Each bar element is assumed as one-dimensional and is modeled as a hyper elastic material which constitutive relation is governed by a strain energy density function W . The mechanical behavior of the bars is described by the hyperelastic constitutive relation presented at the appendix (A.3). Thus, for the i -th bar element showed in Figure 3-6,

$$\begin{aligned} \mathbf{T}_{bar}^i &= A_i L_i S_x \frac{\partial E_x}{\partial \mathbf{u}_i} \\ \mathbf{K}_{bar}^i &= A_i L_i \left[S_x \frac{\partial^2 E_x}{\partial \mathbf{u}_i^2} + C_t \frac{\partial E_x}{\partial \mathbf{u}_i} \left(\frac{\partial E_x}{\partial \mathbf{u}_i} \right)^T \right] \end{aligned} \quad (3.10)$$

where E_x is the Green-Lagrange one-dimensional strain along the bar axis, S_x is the one-dimensional component of the second Piola-Kirchhoff (P-K) tensor (A.7, A.8), A_i is the

transversal section area of the bar element, L_i is the length of the bar element and C_t is the tangent modulus (A.6).

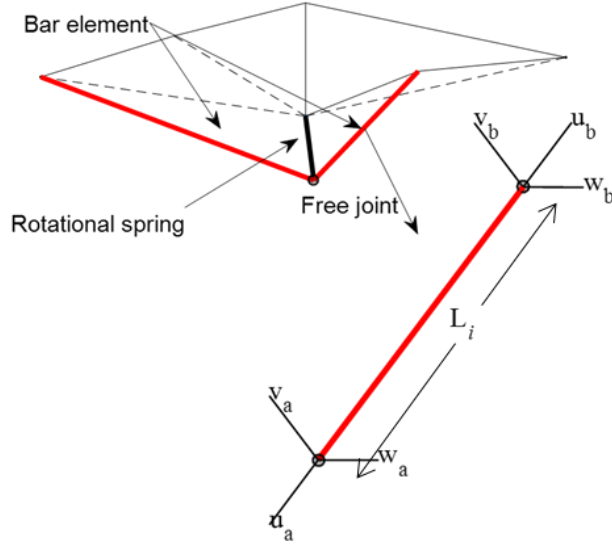


Figure 3-6: Bar element and its local referential axis

Now that the bar elements are fully described, we might develop the constitutive formulation of the torsional springs. The degree of freedom that describe the torsional spring (its rotation) is given by the dihedral angle between the panels and can be obtained straight from the displacements and the original coordinates of the vertices. Besides, the torsional spring has its behavior assumed as linear elastic. Thus, for the j -th torsional spring,

$$\begin{aligned} \mathbf{T}_{spr}^j &= L_j \frac{\partial \Psi}{\partial \theta} \frac{\partial \theta}{\partial \mathbf{u}_j} L_j M_{res} \frac{\partial \theta}{\partial \mathbf{u}_j} \\ \mathbf{K}_{spr}^j &= L_j \left[M_{res} \frac{\partial^2 \theta}{\partial \mathbf{u}_j^2} + k \frac{\partial \theta}{\partial \mathbf{u}_j} \left(\frac{\partial \theta}{\partial \mathbf{u}_j} \right)^T \right] \end{aligned} \quad (3.11)$$

Where M_{res} is the resisting moment per unit length, k is the rotational stiffness modulus per unit length and θ is the dihedral angle. The linear formulation of the moment M_{res} does not detect local penetration of origami panels and, to avoid that, additional kinematic constraints are considered. The constitutive model is presented at the appendix (A.4).

This formulation is a nonlinear analysis of the origami, and the solution scheme can be summarized as shown in Figure 3-7.

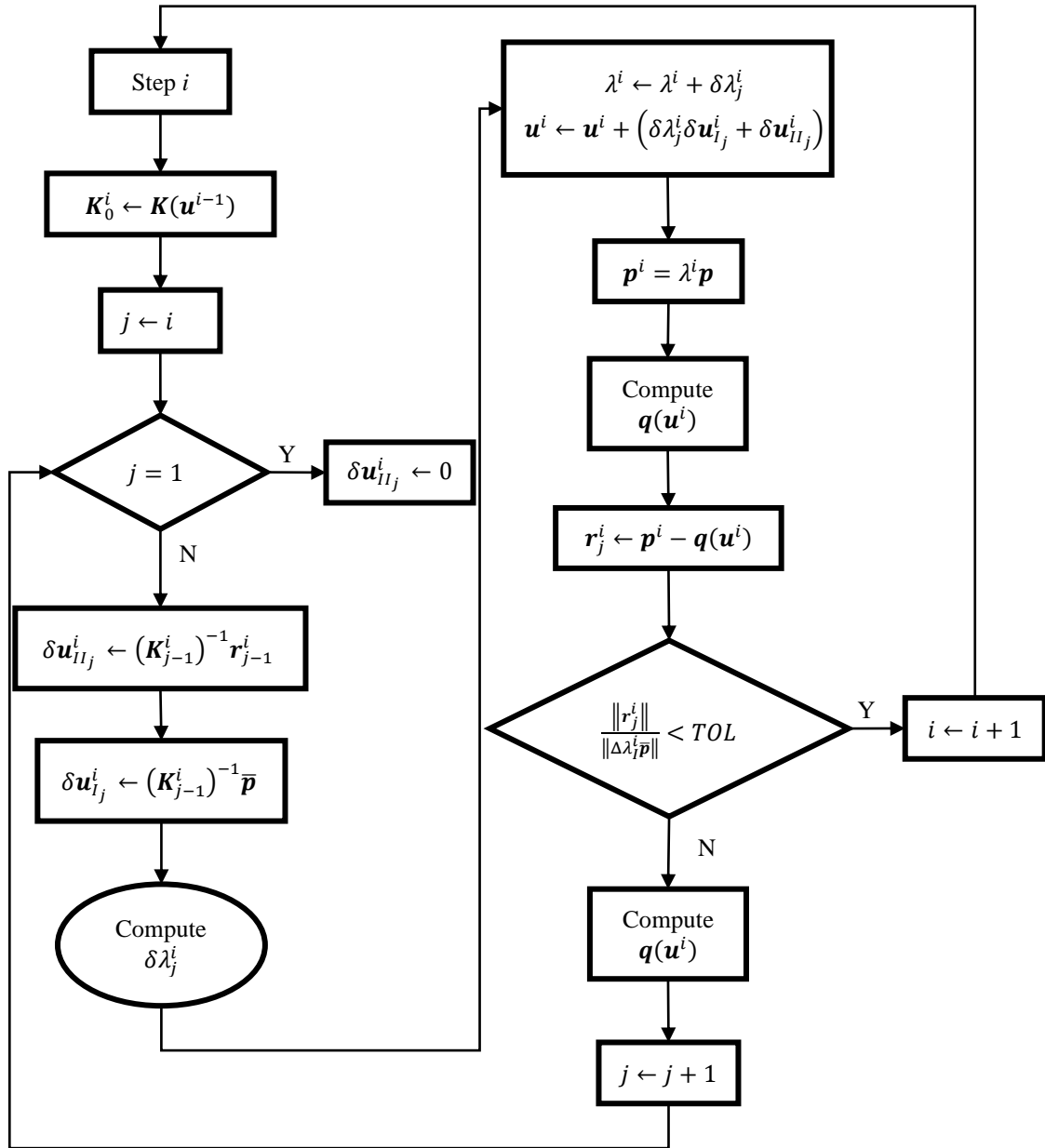


Figure 3-7: Unified incremental-iterative scheme to solve nonlinear problems for N+1 dimensional space.

There are multiple algorithms to solve nonlinear problems and the difference among these approaches is on the computation of the load factor ($\delta\lambda_j^i$) showed in Figure 3-7. This load factor is computed differently for each nonlinear solution scheme based on

its unique characteristics (Leon *et al.*, 2011). The displacement-based method from this work uses a modified generalized displacement control method (MGDCM), a robust and powerful solution method that avoids singularities, present in methods like load (LCM) and regular displacement (DCM) control method. This method was proposed by Leon *et al.* (2014), and its main feature is to converge the solution even for high values of initial load factor. The load factor on the MGDCM is modified such that instead of relying on previous values of the increment to define its magnitude, it only considers their sign. This way, for large load factor values and for regions of high gradients near load limit points, the generalized stiffness parameter (GSP) of the MGDCM will correctly reflect the stiffness of the structure.

The load factor for the method is evaluated as follows

$$\Delta\lambda_j^i = \begin{cases} \overline{\Delta\lambda} & j = 1 \\ -\frac{\Delta u_{p_1}^1 \cdot \Delta u_{r_j}^1}{\Delta u_{p_1}^1 \cdot \Delta u_{p_j}^1} & j > 1 \quad i = 1 \\ \pm \overline{\Delta\lambda} \sqrt{\frac{|\Delta u_{p_1}^1 \cdot \Delta u_{p_1}^1|}{\Delta u_{p_1}^i \cdot \Delta u_{p_1}^i}} & j = 1 \quad i > 1 \\ -\frac{\Delta u_{p_1}^i \cdot \Delta u_{r_j}^i}{\Delta u_{p_1}^i \cdot \Delta u_{p_j}^i} & j > 1 \end{cases} \quad (3.12)$$

3.3.1. Modified displacement-based method

The original formulation of Input used by the displacement-based method proposed by Liu & Paulino (2017) assumes that the Input is applied to the undeformed configuration, and at every step the initial Input is kept (Figure 3-8-a). A modification is proposed here on the Input description, where the Input now follows the deformed configuration (Figure 3-8-b). This approach allows a proper description of the origami that does not present any incorrect extra stretching.

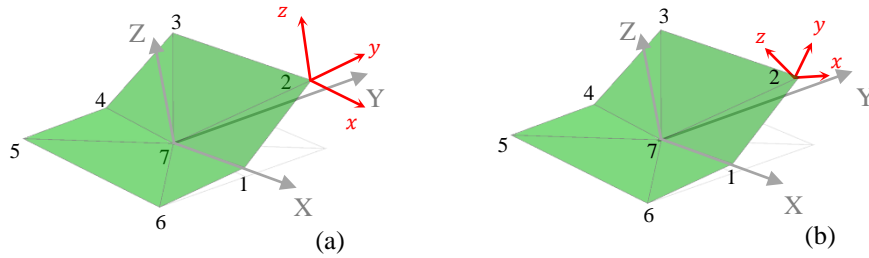


Figure 3-8: (a) Original Input method, with the Input being applied to the Referential Frame $(x, y, z) // (X, Y, Z)$; (b) Modification proposed, where the Input is applied to the Referential frame (x, y, z) that follows the Node movement. In the example shown, axis $z \perp Face_{237}$ and plane xy is contained within $Face_{237}$.

A workflow for the modified FEA is presented in Figure 3-9, illustrated by a single cell. The XYZ coordinates of each node of the origami is used as input, being reshaped as a combination of nodes and panels, and the creases are properly identified and stored as bars in a trussed-like structure. Additionally, the boundary conditions and the actuation are defined as inputs, being either force or displacement type. This set of inputs are fed to the solver that, using an iteration method and with the formulation previously presented, converge the solution through a quasi-static analysis of the unbalanced system, until it reaches the equilibrium. When the Input is of Force type, for example, the modification is applied as an adaptative load that keeps its norm but change the direction at each iteration, following the node movement.

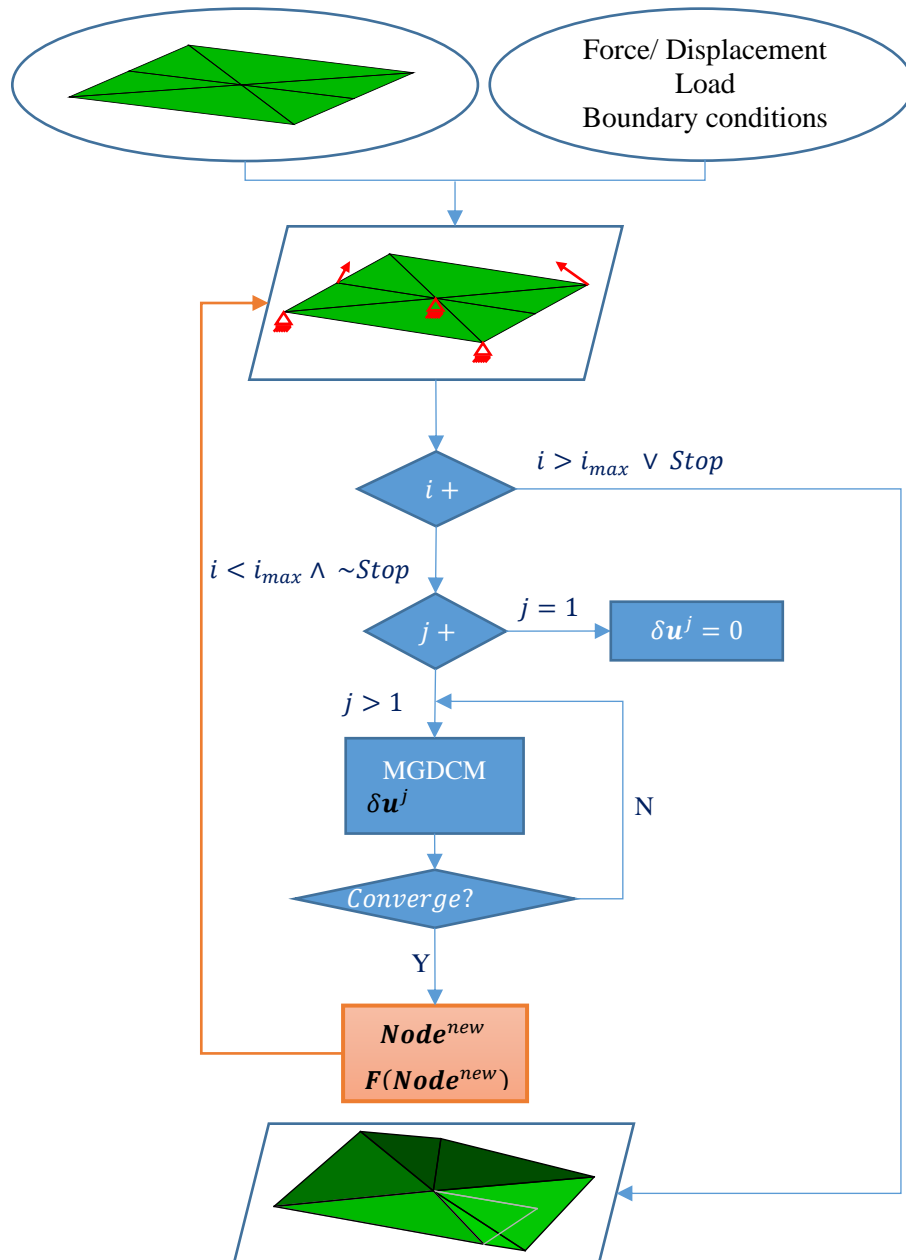


Figure 3-9: Overview of simulation framework. The initial configuration is inserted in a combination of Nodes and Bars, and the external forces and constraints are carefully considered. At each iteration, a convergence is performed on each node displacement using MGDCM, and, after converging, a new input is generated with the reevaluation of the forces based on the new Nodes (Nodes considering the displacement).

4 Waterbomb Cell

The waterbomb base is a well-known single vertex bi-stable origami pattern (Hanna *et al.*, 2014; Ma and You, 2014) that has some interesting properties, such as a negative Poisson ration. It also has a natural mirror-symmetry behavior that is thoroughly explored in this chapter. The crease pattern for a typical waterbomb base is shown at Figure 4-1a. Typically, this origami is conceived with 8 creases, intercepting each other at their middle points, equally spaced by a 45 degrees angle. Some variations can be observed such as the 6-creased pattern (Figure 4-1b), where 2 folds are inactive, and the triangle waterbomb unit (Figure 4-1c), where a 6-creased pattern has its folds alternated and separated by a 60 degrees angle. This chapter starts with the kinematic analysis of the 6-creased origami pattern, followed by a study through its equivalent mechanism workspace. A plane-symmetry study is developed in sequence, and a closed-form reduced order is presented for the symmetric case. Section 4.5 brings the mechanical analysis of the pattern considering the displacement-based method.

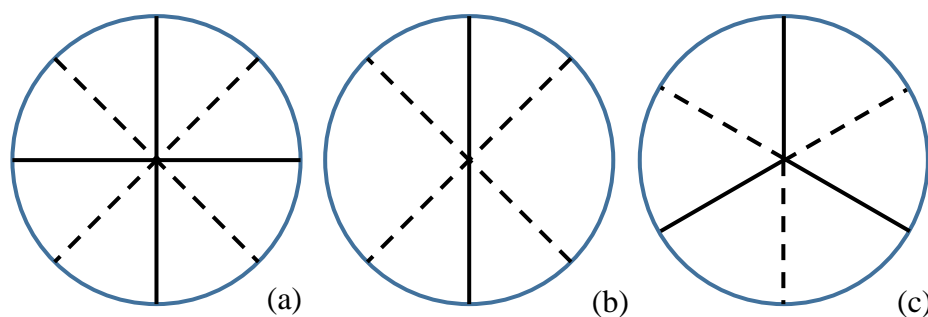


Figure 4-1: Typical waterbomb base crease pattern, where full line means a mountain fold and dashed line means a valley fold.

4.1. Kinematic analysis

The kinematic analysis of a 6-creased waterbomb starts with the equivalent mechanism definition. This pattern is composed by 2 mountain folds and 4 valley folds. In a bi-stable configuration, the pattern presents 2 valley folds and 4 mountain folds. The equivalent mechanism for the waterbomb unit cell is showed in Figure 4-2.

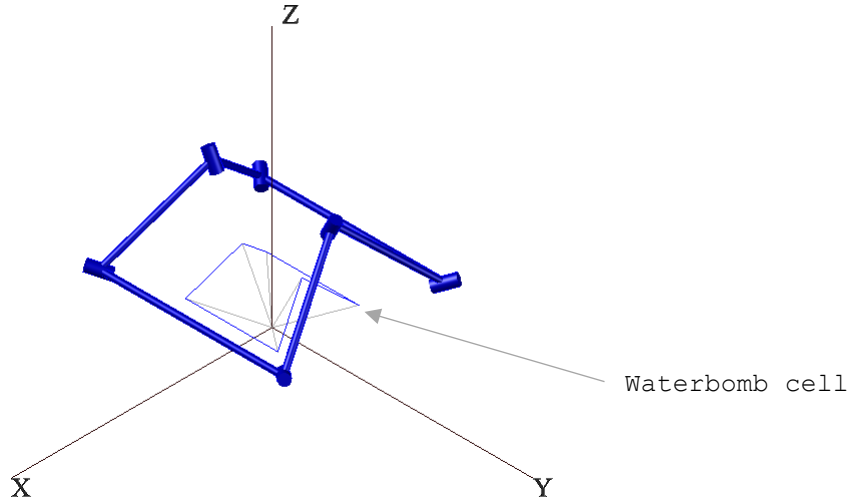


Figure 4-2: Equivalent mechanism for the 6-creased waterbomb pattern.

Waterbomb pattern has a characteristic that all joints intercept at a common point, resulting in $a_i = R_i = 0$ ($i = 1 \dots 6$). In addition, α_i is fixed for each pair of consecutive joints, being associated with the angle λ that defines the shape of the waterbomb cell. For a squared waterbomb cell, $\lambda = \pi/4$.

Note that the waterbomb cell is a closed-loop mechanism. For the formulation, it is assumed that the first linkage ($i = 1$) is associated with the crease OB , being numbered counterclockwise. Therefore, the last linkage ($i = 6$) is associated to the crease OA (see Figure 4-2). The frame definition is summarized as:

1. The first frame ($i = 1$) is defined as the crease OB .
2. Frames are disposed following a counterclockwise sequence, following the vertex order B, C, D, E, F and A , starting from ($i = 1$) at vertex B and ending at ($i = 6$) at vertex A .

3. The z_i axis of each i frame is aligned with the crease, with its origin at O (see Figure 4-2).
4. The y_i axis of each frame is coplanar with the origami face delimited by the joints i and $i - 1$, and the y_1 frame is coplanar with the origami face delimited by frames 1 and 6.
5. The x_i axis of each i frame is the normal of the face delimited by joints i and $i - 1$, and the x_1 frame is the normal to the face delimited by frames 1 and 6.
6. The waterbomb defines an inner region and an outer region, where the inner region is contained within the waterbomb edges AB, BC, CD, DE, EF and FA . Each x_i axis points outwards the inner region.

Each z_i axis is defined such that every θ_i angle belongs to the range $[0, \pi]$. With this consideration, z_i axis associated with valley folds (creases OA, OC, OD and OF) are positioned along the crease, pointing from O_i to the correspondent vertex (A, C, D or F), while z_i axis associated with mountain folds (OB and OE) are positioned along the crease, pointing to the opposite direction of the correspondent vertex (B or E). The values of the D-H parameters for a generic waterbomb cell are given in Table 4-1.

Table 4-1: D-H parameters and its correspondence to each vertex of the unit cell

vertex	B	C	D	E	F	A
i	1	2	3	4	5	6
α_i	$\pi - \lambda$	$\pi + 2\lambda$	$\pi - \lambda$	$\pi - \lambda$	$\pi + 2\lambda$	$\pi - \lambda$
θ_i	θ_1	θ_2	θ_3	θ_4	θ_5	θ_6
R_i	0	0	0	0	0	0
a_i	0	0	0	0	0	0

The D-H formulation allows the description of each $i \rightarrow i + 1$ joint pair through just four parameters, and since three of them are constant values, each joint can be represented by one degree of freedom, θ_i , resulting in 6 free variables. Note that the waterbomb pattern is related to a closed chain, which means that the last joint connects to the first one. In this regard, there is no sense in talking about the end-effector, instead it is necessary to evaluate the loop closure equation. It acts as a restriction to the system,

reducing the number of degrees of freedoms that results in the mobility 3 mechanism previously analyzed.

The system (3.4) is solved using the parameters from Table 4-1. Note that the system can be simplified and reduced from 16 to 9 equations, once that the parameters from Table 4-1 applied to Equation (3.4) result in $P_{m4} = 0$ and $P_{4n} = 0$ for every $m, n = 1 \dots 3$, and $P_{44} = 1$. Therefore, the system of equations is conceived without the last row and the last column of matrix $\mathbf{P}(\boldsymbol{\theta})$, resulting in $f_i(\boldsymbol{\theta}) = [\mathbf{P}(\boldsymbol{\theta}) - \mathbf{I}]_{mn}$, where $i = 3(m - 1) + n$, for $m, n = 1 \dots 3$.

The system is solved within the lower and upper boundaries that define the θ range, $[0, \pi]$. Besides, the unit cell is built as a square of side length $2l$. Thus, D-H parameters are $a_i = 0$ and $R_i = 0$, for $i = 1 \dots 6$, $\alpha_1 = \alpha_3 = \alpha_4 = \alpha_6 = 3\pi/4$ and $\alpha_2 = \alpha_5 = 3\pi/2$, and θ_i are the mechanism variables. With these known parameters and the closure equation (3.6), it is possible to fully describe the 6-creased waterbomb equivalent mechanism with only 3 inputs.

4.2. Workspace analysis

The mechanism workspace represents a region of movement of the end-effector relative to a referential frame, usually attached to the frame associated with the first linkage. In this subsection, a workspace analysis is carried out considering the motion of the waterbomb unit cell related to the frame attached to the crease OA .

The origami analysis considers a subset of angles $(\theta_1, \theta_2, \theta_3)$ that, if physically attainable without stretching, twisting, or compressing the links and without penetration of panels, is identified in a feasible region of the 3D space named as workspace. Figure 4-3-a to Figure 4-3-i presents the waterbomb unit cell workspace, defined by the feasible region generated by giving $(\theta_1, \theta_2, \theta_3)$ in a range $[0, \pi]$. The workspace assumes a spherical configuration, centered at $(0,0,0)$. Note that it is composed by two spheres: an inner sphere, associated with the motion of vertices B and E , and an outer sphere, associated with motion of vertices C, D and F , being vertex A an inertial point located in the outer sphere.

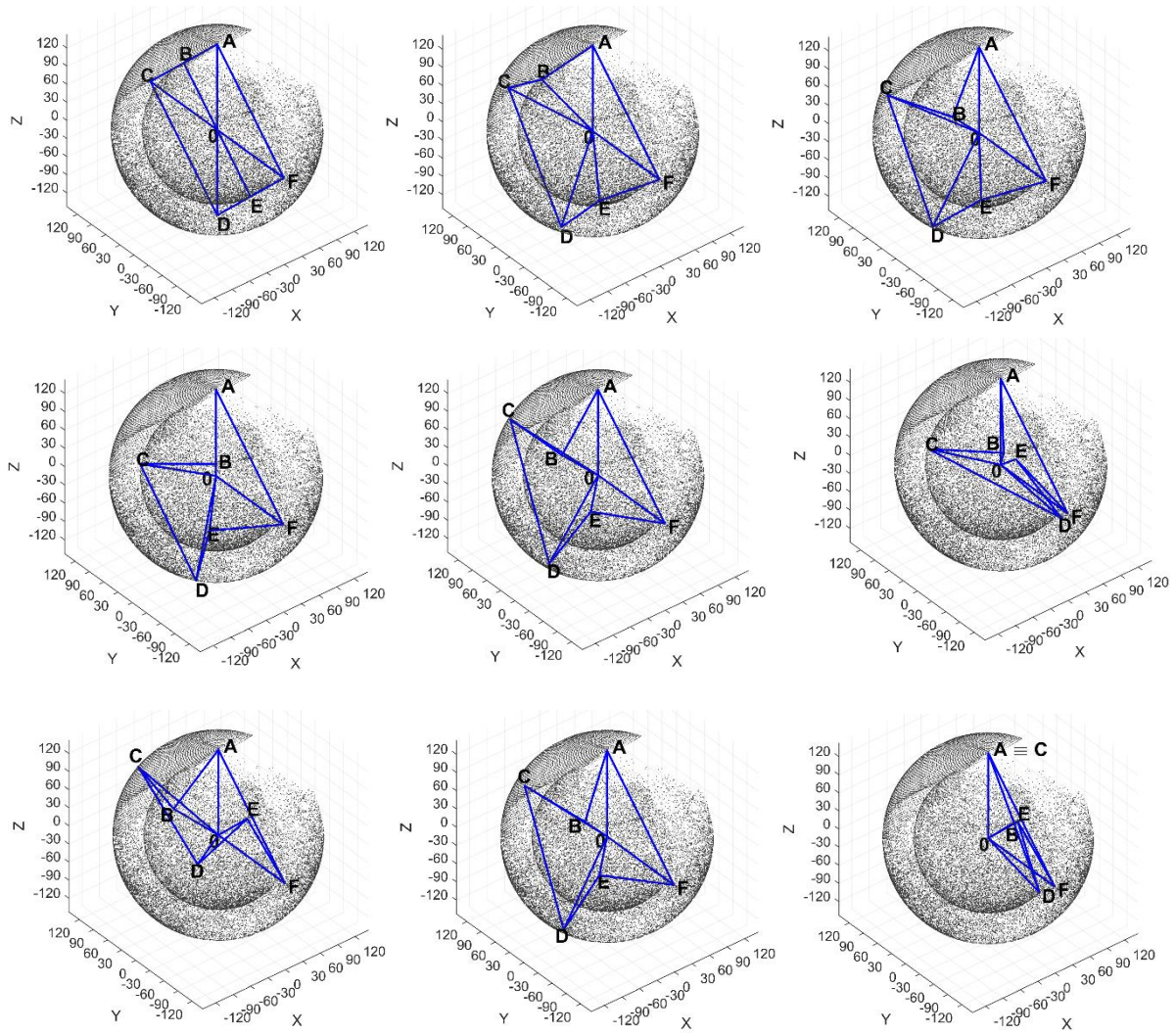


Figure 4-3: From (a) to (i): Different representations of the unit cell shape configurations for distinct values of the input angles $(\theta_1, \theta_2, \theta_3)$. The waterbomb cell is represented through the connective of the position of each vertex on the workspace where vertices A, C, D and F belong to the outer sphere with radius $b\sqrt{2}$, wherein $OA = OC = OD = OF = b\sqrt{2}$, and vertices B and E belong to the inner sphere with radius b , wherein $OB = OE = b$.

The workspace contained in Figure 4-3 corresponds to the gray dots, and it is formed through a contribution of the combined motion of vertices B to F of the waterbomb cell, where vertex A is assumed as the inertial one. The points in the workspace should not be considered individually, but as a set of 6 points. As examples, we selected 9 sets, where each set corresponds to a subset of angles $(\theta_1, \theta_2, \theta_3)$ given as an input and a subset of angles $(\theta_4, \theta_5, \theta_6)$ that corresponds to the output. The subset for

each case in Figure 4-3-*a* to Figure 4-3-*i* is shown in Table 4-3, along with the converted remaining three angles, rounded in the Table 4-3 to the second decimal number. Figure 4-3-*a* shows the case where the waterbomb is fully unfolded.

Table 4-2: Subset of input angles ($\theta_1, \theta_2, \theta_3$) and numerically converged remaining three angles ($\theta_4, \theta_5, \theta_6$)

	(a)	(b)	(c)	(d)	(e)	(f)	(g)	(h)	(i)
θ_1	0	30	90	90	95	95	95	105	180
θ_2	0	45	75	75	110	145	170	105	180
θ_3	0	30	75	130	90	145	80	105	175
θ_4	0	22.70	19.51	68.00	63.52	174.04	100.90	66.60	165.90
θ_5	0	48.28	49.30	74.86	99.44	153.67	173.72	96.64	175.00
θ_6	0	34.56	111.11	140.73	98.11	144.33	83.09	116.49	170.04

A different perspective of the workspace is now of concern highlighting the vertices on the workspace. Figure 4-4 highlights each joint-linkage pair, considering a referential frame at crease OA (joint A). Some isolated groups of points on the workspace are more visible on the workspace for vertex D . These isolated groups represent a peculiar set of tridimensional configurations achieved by the waterbomb cell, where the structure has an inversion of crease type or is on the verge of a panel penetration. Any configuration that would be in between these isolated components results in a cell with a superposition and/or penetration of panels and, therefore, are not contemplated in the workspace. A connection between these isolated components requires a deformation on at least one panel that is not feasible for the equivalent mechanism description due to geometrical restrictions. It is important to highlight that even though a few components are more evident in one panel than in another one, each component of one panel has a connection with one component on another panel.

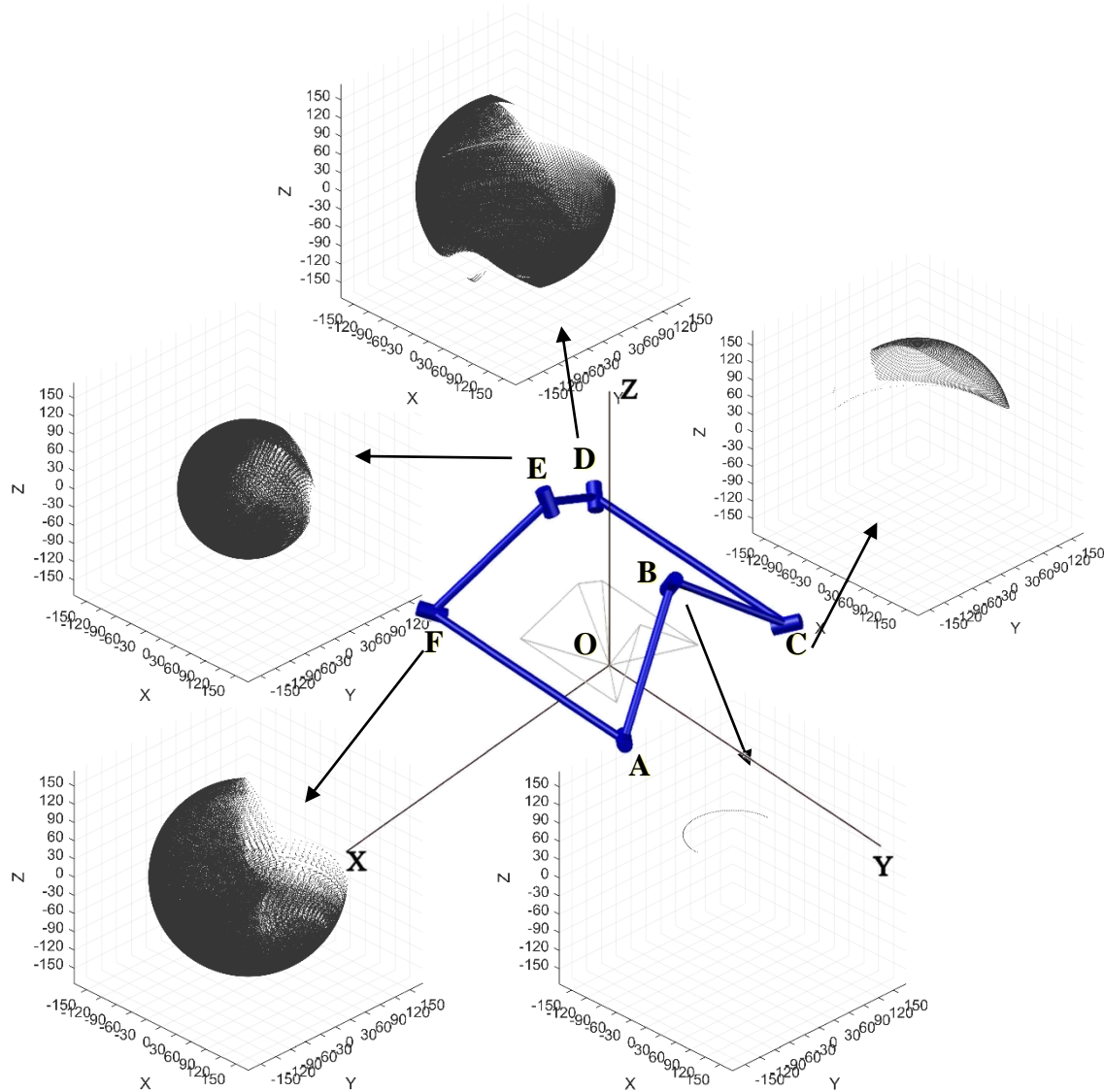


Figure 4-4: Workspace for each joint-linkage pair of the waterbomb cell, considering the referential frame at joint A (crease OA).

4.3. Symmetry analysis

The mobility of the mechanism can be reduced by imposing symmetry conditions on the origami, which can be associated with either the actuation or some mechanical restriction imposed to the origami. The actuation providing symmetric responses is related to external forces that are applied in such a way that preserves the symmetry. The mechanical restriction can be achieved by considering some displacement constraint.

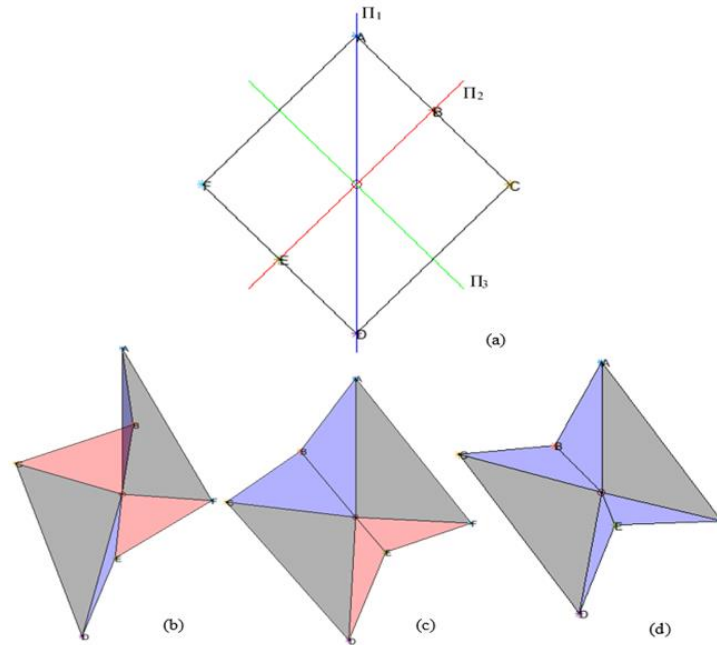


Figure 4-5: Symmetry conditions on a waterbomb unit cell: (a) planes of symmetry; (b) configuration related to Case Π_1 , with mobility 2; (c) configuration related to Case Π_2 , with mobility 2; (d) symmetric configuration related to Case Π_3 , with mobility 1.

By observing the unit cell in Figure 4-5-a, three symmetry planes can be defined, where two of them lead to a partial symmetry (with mobility 2) and the third one represents the cell with a symmetric behavior (with mobility 1). The first symmetry plane is obtained through a diagonal of the unit cell, either AD or CF (Π_1), resulting in $\theta_i = \theta_{i+3}$ ($i = 1 \dots 3$). The second symmetry plane is obtained through the cut BE (Π_2), resulting in $\theta_3 = \theta_5$ and $\theta_2 = \theta_6$. The third symmetry plane is obtained by connecting the middle points of the links CD and AF such that $AF // CD$ (Π_3), resulting in $\theta_2 = \theta_3 = \theta_5 = \theta_6$ and $\theta_1 = \theta_4$. Note that this third case has a shape that can be fully described by only one angle, since the origami is fully symmetric (mobility 1). In addition, the shapes resulting from Π_3 can be considered as a subset of the shapes resulting from both Π_1 and Π_2 , as can be observed in Figure 4-6, where the intersection between the workspaces considering Π_1 and Π_2 is the workspace considering Π_3 .

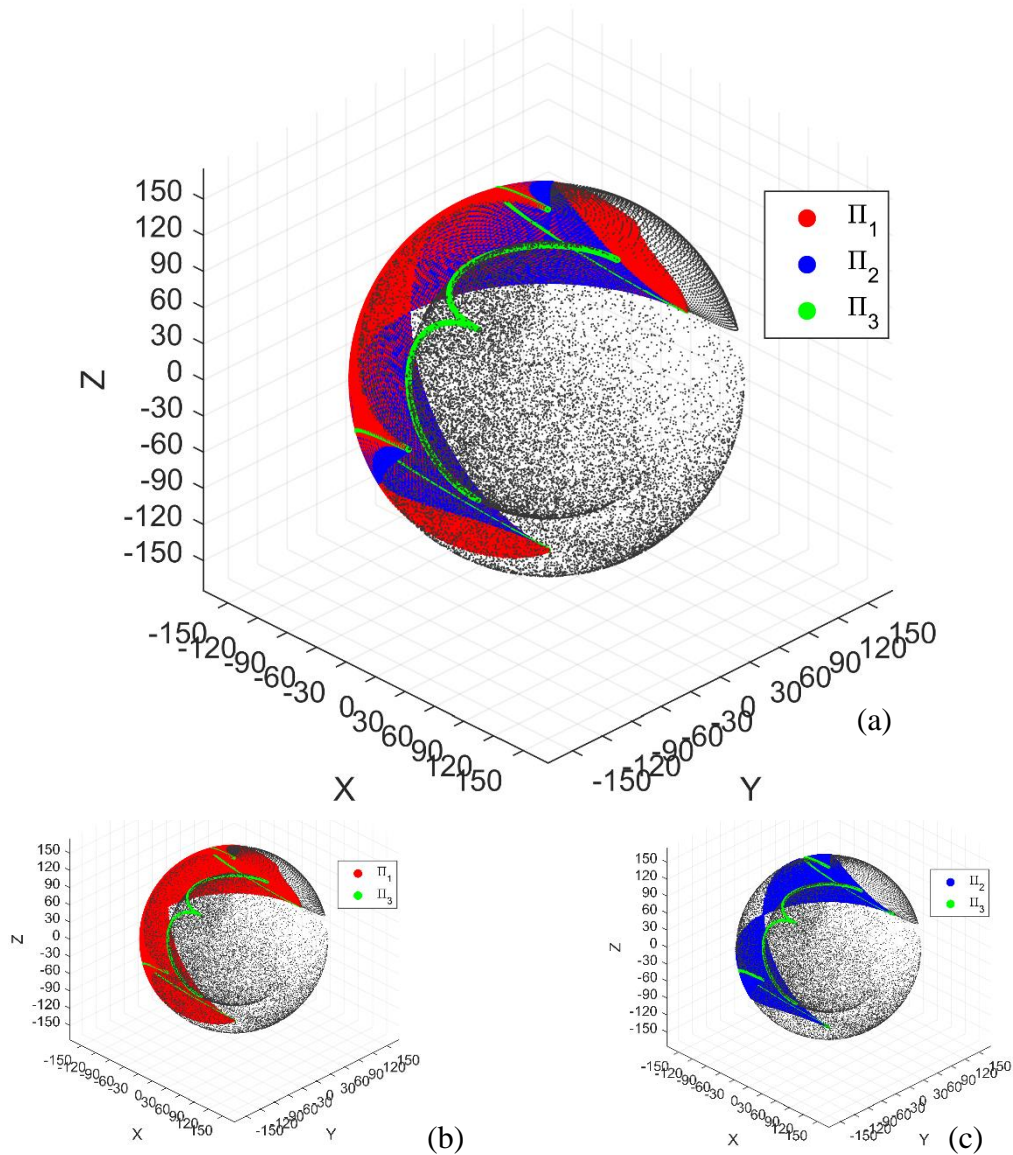


Figure 4-6: Workspaces for the plane-symmetry cases Π_1 and Π_2 and the symmetry case Π_3 (a). The symmetric case Π_3 is showed superposed to only the plane-symmetric case Π_1 in (b), while it is superposed to only the plane-symmetric case Π_2 in (c).

Plane-symmetry constrains mostly the workspace of the joint 4, associated with the crease OE . The original spherical surface covered by the motion of crease OE (see Figure 4-4) is now reduced to a single spherical arc for all three cases, Π_1 , Π_2 and Π_3 . It is important to remember that the referential frame associated to the crease OA is considered as the inertial frame. The study of the symmetry cases is an interesting strategy to intelligently design the actuation of the origami in applied cases. This advantage is clear when observing the change on the workspace of Node E from a general case (Figure

4-4) to the plane-symmetric cases (Figure 4-6). If the objective is to constrain the waterbomb to a symmetric or quasi-symmetric motion, it suffices to control the motion of Node E, keeping it in a spherical arc, as shown in Figure 4-4. Additionally, it is possible to notice that for all three plane-symmetric and symmetric cases, the workspace of Node F is confined within a single dot in space. This immovability of Node F is the main reason why Node E behaves the same way as Node B, describing just a single arc in space.

It is important to highlight that these observations are made here considering that there is no inversion on the creases, so creases 1 – 7 and 4 – 7 (creases *OB* and *OE*) are always a mountain type fold while the other four (2 – 7, 3 – 7, 5 – 7, 6 – 7) are always a valley type fold.

Symmetry assumptions can be employed to reduce the necessary equations for the origami description, leading to a simplified formulation. Another way to obtain the equations for the symmetric case is the use of other formulations such as spherical trigonometry, since the waterbomb is a spherical mechanism (Bowen *et al.*, 2014; Evans *et al.*, 2015; Chen & Santangelo, 2018; Fonseca *et al.*, 2019; Fonseca & Savi, 2020). The next section presents a discussion about this subject considering only the case Π_3 , where the origami has mobility 1, and therefore can be represented by a single degree of freedom system (DoF).

4.4. Closed-form trigonometric description

This section has the objective to present the kinematics analysis of a waterbomb unit cell based on spherical trigonometry formulation. This formulation is widely explored in the literature (Bowen *et al.*, 2014; Evans *et al.*, 2015; Chen & Santangelo, 2018; Fonseca *et al.*, 2019), and is represented here in details. Hence, consider a symmetric unit cell inserted into a sphere of unitary radius such that the vertex *O* matches with the sphere center. Figure 4-7 shows the top view (Figure 4-7-a) and side view (Figure 4-7-b) of the unit cell, respectively.

Figure 4-7-c shows a tridimensional view of the cell inserted in the sphere while Figure 4-7-d presents a tridimensional view of a general rectangular waterbomb cell with sides $2a$ and $2b$ and internal acute angle λ , such that $a = b \tan(\lambda)$. Each side of the spherical triangle is defined by its correspondent internal angle, as shown in Figure 4-8.

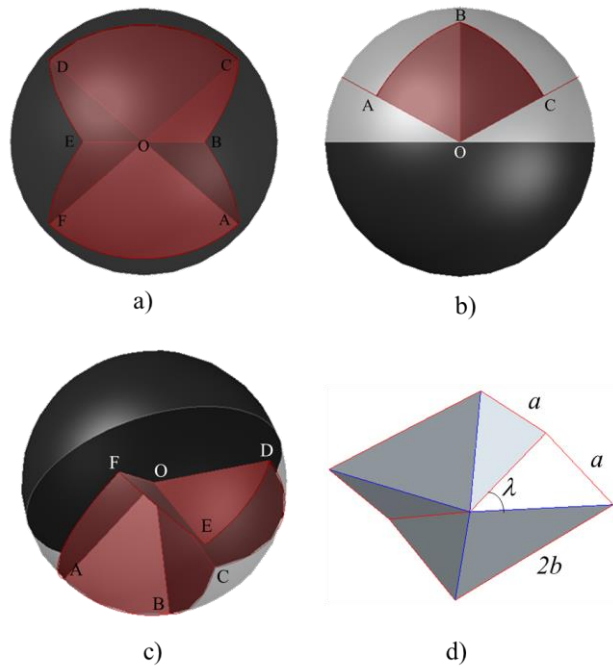


Figure 4-7: Spherical representation of the origami unit cell: (a) top view; (b) side view; (c) tridimensional view; (d) schematic view of a waterbomb spherical mechanism

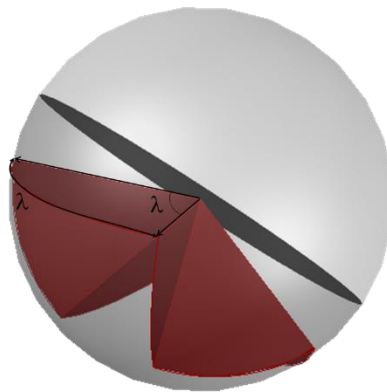


Figure 4-8: Spherical triangle sides' definition.

Based on that and knowing the unit cell inner angles (λ and $\pi-2\lambda$), the following arcs are obtained: $\widehat{AB} = \widehat{BC} = \widehat{DE} = \widehat{EF} = \lambda$ and $\widehat{CD} = \widehat{FA} = \pi - 2\lambda$, and the angle between these arcs are defined as ϕ_1 and ϕ_2 . The cell configuration is described by angles θ and α that are coupled by trigonometric relations and assuming symmetry conditions. Figure 4-9 shows the triangles inside the sphere employed to obtain the unit cell geometric relations.

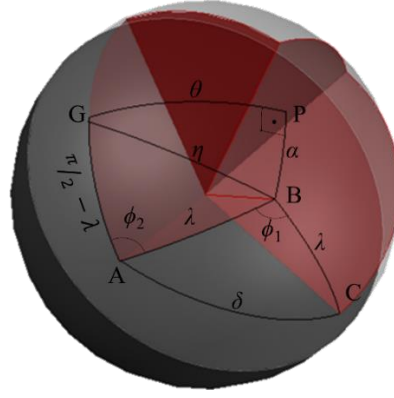


Figure 4-9: Spherical triangles used to define geometric relations of the unit cell, computing angles α and θ .

Three intermediate relations can be obtained by considering cosine and sine formulas for right and general spherical triangles:

$$\phi_1 = 2\theta \quad (4.1)$$

$$\cos(\phi_2) = \frac{\cos(\theta) \cos(\alpha)}{\sin(\lambda) \cos(\lambda)} - 1 \quad (4.2)$$

$$\sin(\phi_2) = \frac{\sin(\theta) \cos(\alpha)}{\sin(\lambda)} \quad (4.3)$$

By employing trigonometric fundamental law on Equations (4.2) and (4.3), it is possible to establish relations between θ and α , as follows:

$$\cos(\theta) \cos(\alpha) \tan(\lambda) + |\sin(\alpha)| = 1 \quad (4.4)$$

Afterward, it is necessary to establish the relation between the angles described by the D-H parameters and the angles described by the spherical trigonometry formulation. Note that the angles θ_i from D-H formulation can be interpreted as the angle between the normal vectors of two consecutive faces (Figure 4-10). It is assumed that the positive direction is outwards, which means that they are pointing to the external region of the waterbomb unit cell. Therefore, the following expressions are defined

$$\begin{aligned} \cos(\theta_1) &= \mathbf{n}_{AB} \cdot \mathbf{n}_{BC} \\ \cos(\theta_2) &= \mathbf{n}_{CD} \cdot \mathbf{n}_{BC} \end{aligned} \quad (4.5)$$

where $\theta_2 = \theta_3 = \theta_5 = \theta_6$ and $\theta_1 = \theta_4$; $\mathbf{n}_{AB} = \mathbf{n}_B \times \mathbf{n}_A$, $\mathbf{n}_{BC} = \mathbf{n}_C \times \mathbf{n}_B$ and $\mathbf{n}_{CD} = \mathbf{n}_D \times \mathbf{n}_C$, with \mathbf{n}_B being the unitary vector for the position of vertex B , \mathbf{n}_A being the unitary vector for the position of vertex A , and \mathbf{n}_{AB} being the normal unitary vector of face AOB , considering a referential frame attached to the vertex O (see Figure 4-10). Thus, equation (4.5) results in the following expressions

$$\begin{aligned}\cos(\theta_1) &= \frac{(\tan(\lambda) \sin(\theta))^2 - (\cos(\alpha) - \tan(\lambda) \cos(\theta) \sin(\alpha))^2}{(\tan(\lambda) \sin(\theta))^2 + (\cos(\alpha) - \tan(\lambda) \cos(\theta) \sin(\alpha))^2} \\ \cos(\theta_2) &= \frac{\tan(\lambda)^2 \sin(\alpha) - \tan(\lambda) \cos(\theta) \cos(\alpha)}{\sqrt{(\tan(\lambda) \sin(\theta))^2 + (\cos(\alpha) - \tan(\lambda) \cos(\theta) \sin(\alpha))^2}}\end{aligned}\quad (4.6)$$

For a symmetric 6-creased waterbomb cell, equation (4.6) is rewritten as:

$$\begin{aligned}\cos(\theta_1) &= \frac{\sin^2(\theta) - (\cos(\alpha) - \cos(\theta) \sin(\alpha))^2}{\sin^2(\theta) + (\cos(\alpha) - \cos(\theta) \sin(\alpha))^2} \\ \cos(\theta_2) &= \frac{\tan(\lambda)^2 \sin(\alpha) - \tan(\lambda) \cos(\theta) \cos(\alpha)}{\sqrt{(\tan(\lambda) \sin(\theta))^2 + (\cos(\alpha) - \tan(\lambda) \cos(\theta) \sin(\alpha))^2}}\end{aligned}\quad (4.7)$$

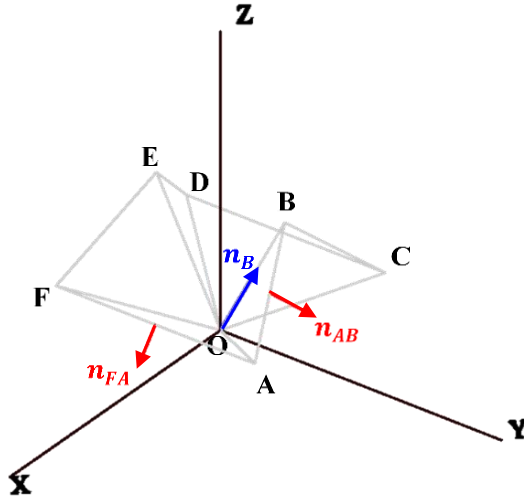


Figure 4-10: Definition of vectors for the waterbomb cell.

The spherical trigonometry formulation offers a reduced-order description of the waterbomb cell behaving under Π_3 condition (symmetric behavior), resulting in a low computational cost while evaluating complex behaviors such as dynamical aspects of origami structures applied to mechanical devices (Fonseca *et al.*, 2019; Fonseca & Savi, 2020). Closed tessellations, for example, present reduced DoF when compared to the opened tessellations formed by the same $m \times n$ unit cell distribution. Besides, quasi-

symmetric or symmetric actuation constrains the behavior of the unit cells to plane-symmetric or symmetric workspaces, as presented at the workspaces in Figure 4-6.

4.5. Finite Element Analysis (FEA)

As an example, boundary conditions are applied to the face 567 such that its node displacements (nodes 5, 6 and 7; or vertex F, A and O, respectively) are restrict in all directions (Figure 4-11). In a general situation, all creases might be actuated.

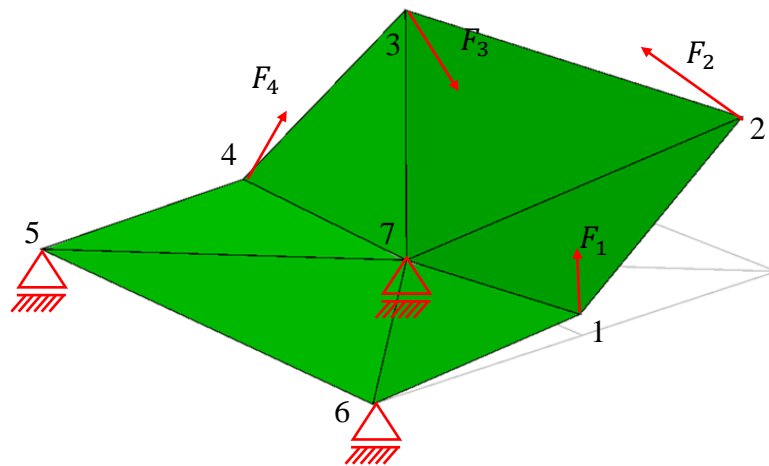


Figure 4-11: Origami waterbomb pattern unit cell with boundary conditions and Input as a Force type.

Initially, we present a comparative example (Figure 4-12) between the original result of a simulation using the displacement-based method, presented in Section 3.3, and the result after the modification (Section 3.3.1) is implemented, using the force application as Input presented at Figure 3-8-b, where the Inputs are applied as Force type to Nodes 3 and 4, being $\mathbf{F}_3 = 0.056 [0 \quad -1 \quad 1]^T$ and $\mathbf{F}_4 = 0.056 [1 \quad 1 \quad 1]^T$.

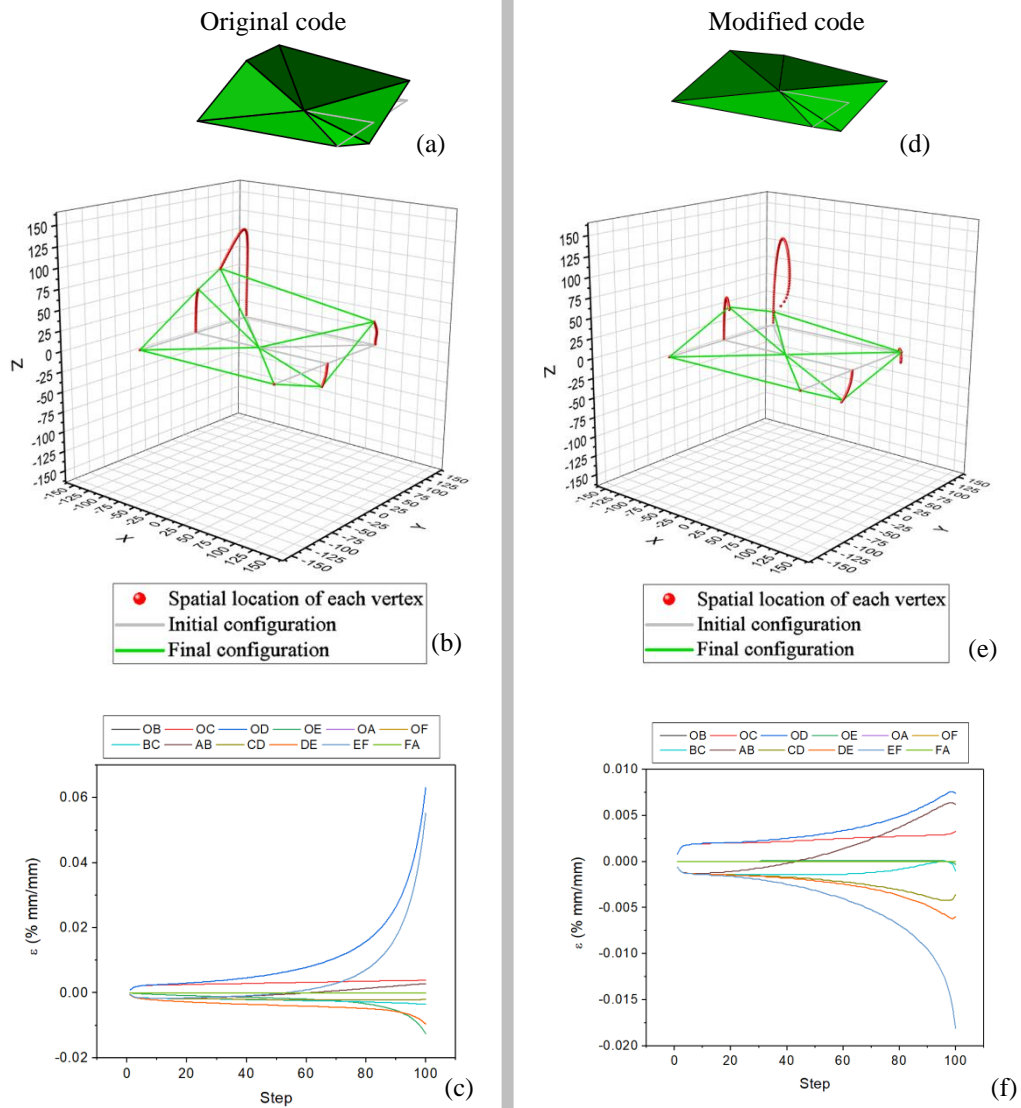


Figure 4-12: Closure process of a waterbomb cell with and without the force decomposition procedure. Waterbomb final configurations (a) and (d), spatial location of the vertices during the closure (b) and (e), and true strain (c) and (f) of each bar of the waterbomb cell.

For the original code, the forces F_3 and F_4 are described on the undeformed referential frame, while on the modified code they follow the Nodes movement. Thus, the absolute values of the forces ($\|F_3\|$ and $\|F_4\|$) is kept, but their direction changes with the Nodes' motion. Note that the modification reduces considerably the deformation presented by each bar, preserving the general aspect of the motion. Besides, it reduces the occurrence of an unadvised crease inversion due to an inadequate force actuation. Also, once that this modification allows a revaluation of the external effort for each iteration, it

makes it possible to generate a cyclic opening/closure process along the same simulation, with the proper modification of the force decomposition process.

The purpose of this modification is to make a considerably accurate representation of the folding process without imposing an extreme incorrect deformation on the bars of the bar-and-hinge representation, and, even so, consider a possible deformation on the origami. The simulations carried out along this paper use the modified method from Section 3.3.1.

The modified method uses not only the Node at which the Input is being applied to, but also an identifier as the direction of that Input, in the case of a Force type. In this work, we use the crease as the identifier. The relation between the node for applying the external force and the activated fold can be seen at Table 4-3. Note that the same fold can be activated by different nodes, depending on the chosen crease for the force decomposition. Besides, the order of the nodes for the chosen crease is important, once that it defines if it is a mountain or a valley fold, through the cross product. This table shows a general formulation, including activation through nodes 5 and 6. Note that creases 1 – 7 and 4 – 7 are mountain folds and the other creases are valley folds.

Table 4-3: Activated crease representation: Force applied at a Node and decomposed related to a predefined direction ($\text{Node}_{\text{direction}}$)

	$\text{Node}_{\text{direction}}$	
Crease	Case I	Case II
1 – 7	$2_{1 \rightarrow 7}$	$6_{7 \rightarrow 1}$
2 – 7	$1_{2 \rightarrow 7}$	$3_{7 \rightarrow 2}$
3 – 7	$2_{3 \rightarrow 7}$	$4_{7 \rightarrow 3}$
4 – 7	$5_{4 \rightarrow 7}$	$3_{7 \rightarrow 4}$
5 – 7	$4_{5 \rightarrow 7}$	$6_{7 \rightarrow 5}$
6 – 7	$5_{6 \rightarrow 7}$	$1_{7 \rightarrow 6}$

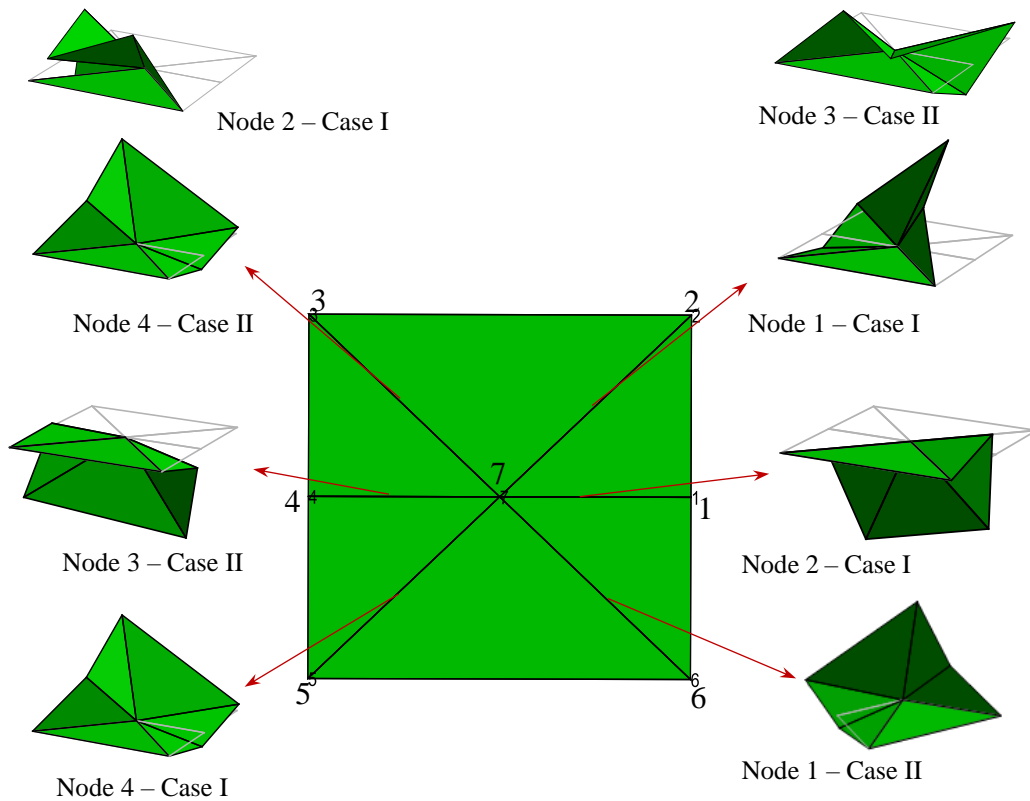


Figure 4-13: Final configuration of the waterbomb cell considering the activation of a single crease at a time, for the boundary conditions of clamped Nodes 5, 6 and 7, including the dual cases for creases 2 – 7 and 3 – 7.

An initial evaluation is made considering that only one crease is activated at each time, according to the relation presented at Table 4-3. The final configuration for each case is shown at Figure 4-13. It is important to highlight that due to the mirror-symmetry property of the waterbomb cell, the final configuration for creases 3 – 7, 4 – 7 and 5 – 7 are a mirrored-like image of cases 2 – 7, 1 – 7 and 6 – 7, respectively. The input of each case is the node and crease, according to Table 4-3, and a force with absolute value of 0.136 N.

Once that we know the behavior of each activated crease, it is noticeable the influence of each one in the final configuration of a waterbomb cell. A configuration promoted by the actuation of creases 3 – 7, 4 – 7 and 5 – 7 is shown in Figure 4-14, and the crease 3 – 7 is activated through the node 2 – Case I.

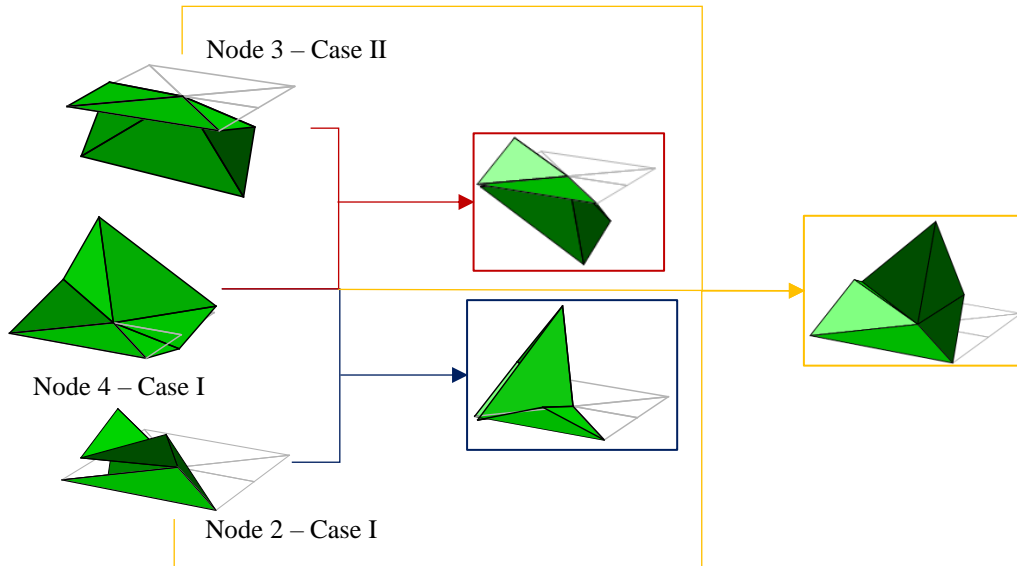


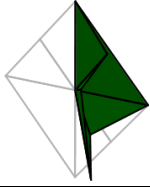
Figure 4-14: Configuration of the waterbomb cell considering activated creases 3 – 7, 4 – 7 and 5 – 7.

A mechanical analysis of the waterbomb unit cell is now in focus considering numerical simulations using ‘MERLIN’. The study starts with a general visualization of the waterbomb movement under external forces, with evaluation on the deformation of the creases. For all simulations presented here, boundary conditions and Inputs as Force type are defined as the example presented at Figure 4-11, where the face AFO (face formed by Nodes 5, 6 and 7) is fixed in space and the Nodes 1, 2, 3 and 4 (vertexes B, C, D and E, respectively) are subjected to external forces.

The folding process of the waterbomb cell is evaluated using FEA for four cases: the plane-symmetric (Π_1 , Π_2) and symmetric (Π_3) cases, presented at Section 4.3, and an asymmetric case. These four cases are evaluated with the inputs shown in Table 4-4, where the input is described by the Node where the Force is being applied and a crease. The crease as an input has two purposes: the first one is to define the Face to which the Force remains perpendicular, following the Node movement. The second one is the direction of the Force applied. Thus, a Force applied to Node 1 with Crease identification 7 – 6 results in a Force normal to Face *ABO* (face 167) following the motion of Node 1, folding the origami along the crease *OA* such that *OA* is a valley type fold. On the other hand, a Force applied to Node 1 with Crease identification 6 – 7 results in a Force normal

to Face ABO (face 167) following the motion of Node 1, folding the origami along the crease OA such that OA is a mountain type fold.

Table 4-4: Input and final configuration for each one of the four cases: quasi-symmetric (Π_1 and Π_2), symmetric (Π_3) and asymmetric

Case	Π_1			Π_2			Π_3		Asymmetric		
Node	1	4	3	1	4	2	1	4	1	4	2
Crease	7-6	7-3	7-4	7-6	5-7	7-3	7-6	5-7	7-6	5-7	3-7
Folded shape											

At this point, it is important to define the symmetric characteristics and their deviations of the symmetric case. From mechanical point of view, a symmetric behavior of the unit cell can be defined as the case where the creases have identical behaviors, and all mountain type folds present the same absolute deformation along the entire folding process (creases OA, OC, OD and OF) and all valley type folds present the same absolute deformation along the entire folding process (creases OB and OE). A similar observation is made for the angle variation. For the waterbomb unit cell under symmetric behavior, the angle variation of all mountain type folds is the same (angles A, C, D and F) along the entire folding process, just as the angle variation of all valley type folds (angles B and E). Discrepancies along the folding process on both deformation and angle variation are understood as deviation of the symmetric case. This deviated case is identified as a plane-symmetric case if the angle relation is according to either Π_1 or Π_2 . Otherwise, it is defined as an asymmetric case.

The bar-and-hinge formulation considers a simplified model of the origami face, where the face deformation is represented by the sum of the contribution of each edge and/or crease deformation. Therefore, a deformation on face OAF is represented by the cumulative effect of the deformation on creases OA and OF and edge AF .

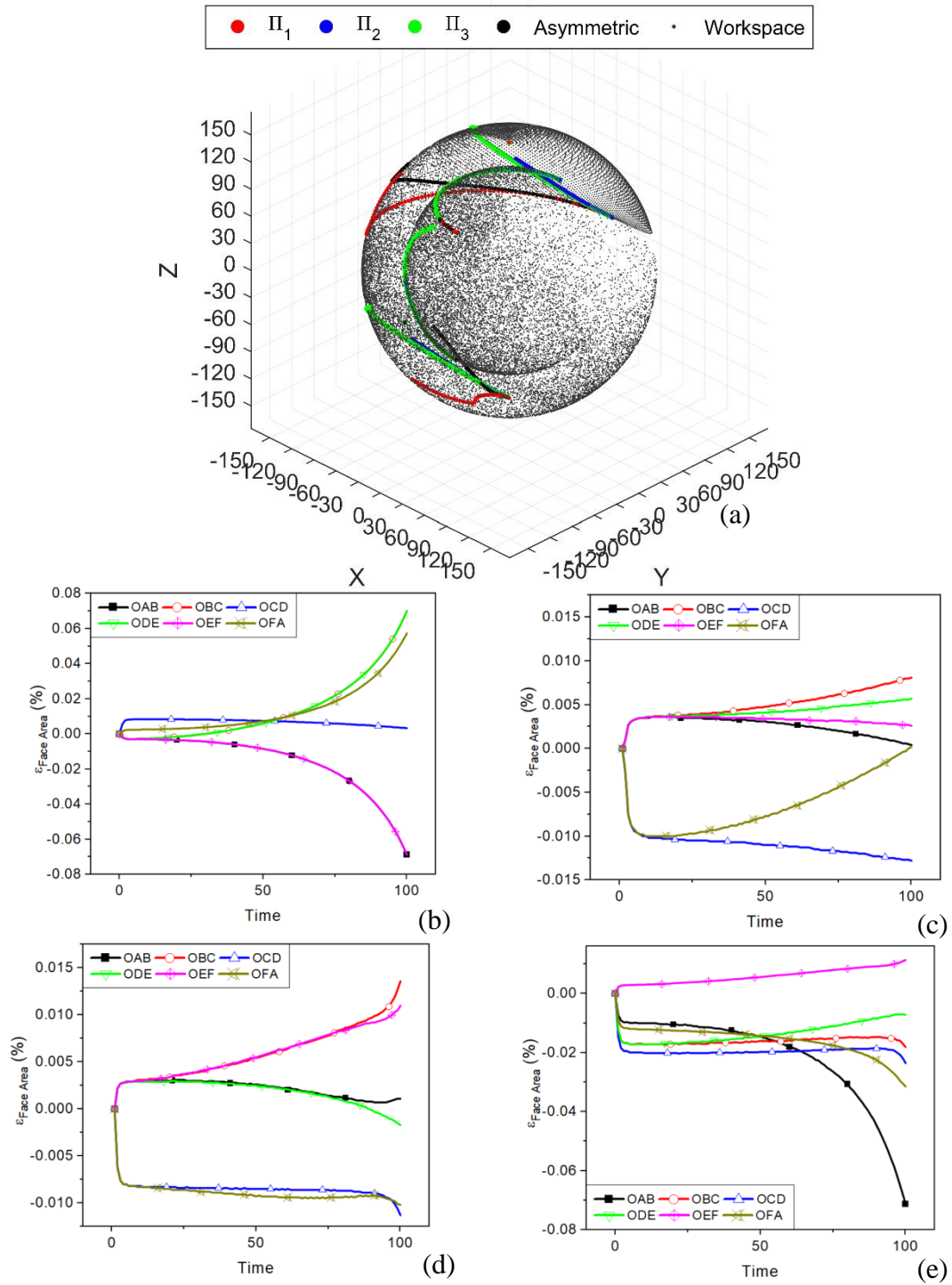


Figure 4-15: Workspace for cases Π_1 and Π_2 and simulations for a generic case (asymmetric), plane-symmetric behavior (Π_1 , Π_2) and symmetric behavior (Π_3). The correspondent deformation of each origami face is shown for cases Π_3 (b), Π_2 (c), Π_1 (d) and asymmetric (e).

Figure 4-15 (a) shows the motion in space of the four cases presented at Table 4-4. As a reference, the workspace for the plane-symmetric cases (Π_1 and Π_2) are also plotted. Figure 4-15 (b) shows the deformation evolution for the waterbomb origami under symmetric behavior of type Π_3 . It is possible to note that faces OBC and ODE have the same deformation, just as faces OAB and OEF . More than that, faces OAB , OBC , ODE and OEF have the same absolute deformation. Face OAF presents a larger deformation related to face OCD due to the boundary conditions applied to the origami, where nodes A and F have their motion restricted on two out of three directions.

One deviation from the symmetric case is observed in Figure 4-15 (c), where the waterbomb behaves according to the plane-symmetric case of type Π_2 . Note that there is a divergence on the deformation of faces OBC and ODE , just as for faces OAB and OEF . An interesting behavior is observed in Figure 4-15 (d), where the waterbomb unit cell behaves according to plane-symmetric case of type Π_1 . For this configuration, diagonally opposed faces present the same deformation, by pairs: faces OAB and ODE , faces OBC and OEF and faces OAF and OCD . Finally, for the asymmetric case, shown in Figure 4-15 (e), no symmetry is observed among the deformation of origami unit cell faces.

The folding process can also be evaluated through the inner angles of the origami unit cell, as can be seen at Figure 4-16. Note that for the case Π_3 , the kinematics formulation can precisely describe the increasing of the angles, even with the creases and edges presenting a larger deformation, showed in Figure 4-15 (b), and $A = C = D = F$ and $B = E$ along the entire folding process (Figure 4-16 (a)). A similar analysis is performed for the case Π_2 , showed in Figure 4-16 (b), where $A = C$ and $D = F$.

As evaluated through the kinematics formulation, when the waterbomb is folding according to case Π_1 , the inner angles relate as $\theta_i = \theta_{i+3}$, for $i = 1,2,3$. By observing the vertices, this can be translated as $A = D$, $C = F$ and $B = E$. Figure 4-16 (c) shows the angles evolving with the increment, and it can be noticed that $A \cong D$, $C \cong F$ and $B \cong E$. The deviation can be considered a result of the deformation that happens on the creases (Figure 4-15 (d)).

The fourth case, with inner angles showed in Figure 4-16 (d) and faces deformation showed in Figure 4-15 (e), represent a general asymmetric motion, with no relation among the angles. Note that in the asymmetric case, the continuous folding of an angle (angle A , for example) might occur in a sequential folding – unfolding – folding of

another angle (angle E , for example). This behavior can be seen between time 50 and 100 of Figure 4-16 (d).

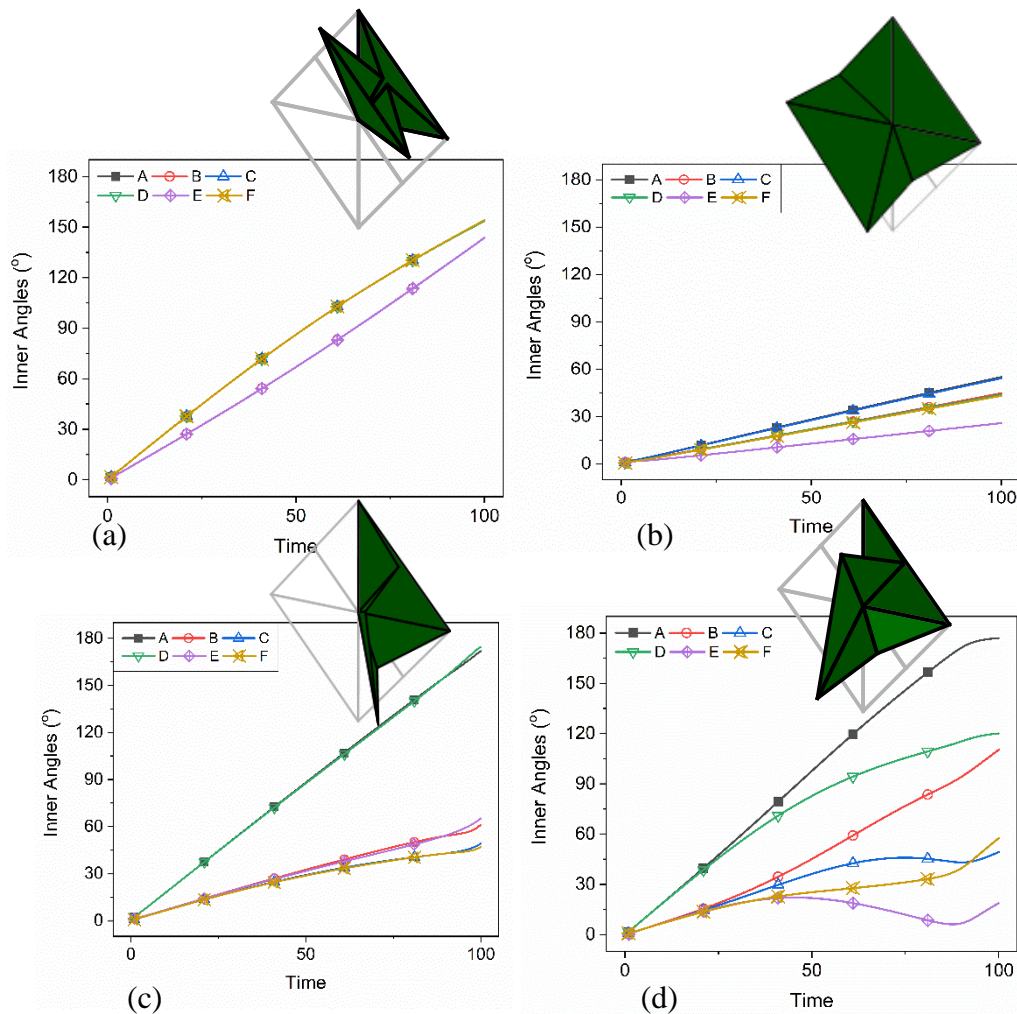


Figure 4-16: Evolution of the inner angles of the waterbomb cell with the increment during the folding process, for a folding occurring according to cases Π_3 (a), Π_2 (b) and Π_1 (c), and according to an asymmetric actuation (d). The final configuration is also shown in evidence in each case.

A closer observation of the asymmetric case is now performed comparing the path described through kinematics formulation with the path obtained by FEA. Figure 4-17 establishes a comparison between both formulations. Figure 4-17 (a) presents the superposed trajectories followed by both cases, showing a good match. This evaluation is ensured by observing the difference on the inner angles for each increment (Figure 4-17 (b)). For the kinematics formulation, the input is given by the set of angles $(\theta_1, \theta_2, \theta_3)$,

corresponding to the inner angles of vertices B , C and D , respectively. Note that the deviance is smaller than 1 degree (approximately 0.017 rad), meaning that the kinematics formulation can represent the folding process of the waterbomb origami. In other words, the rigid foldability hypothesis is valid.

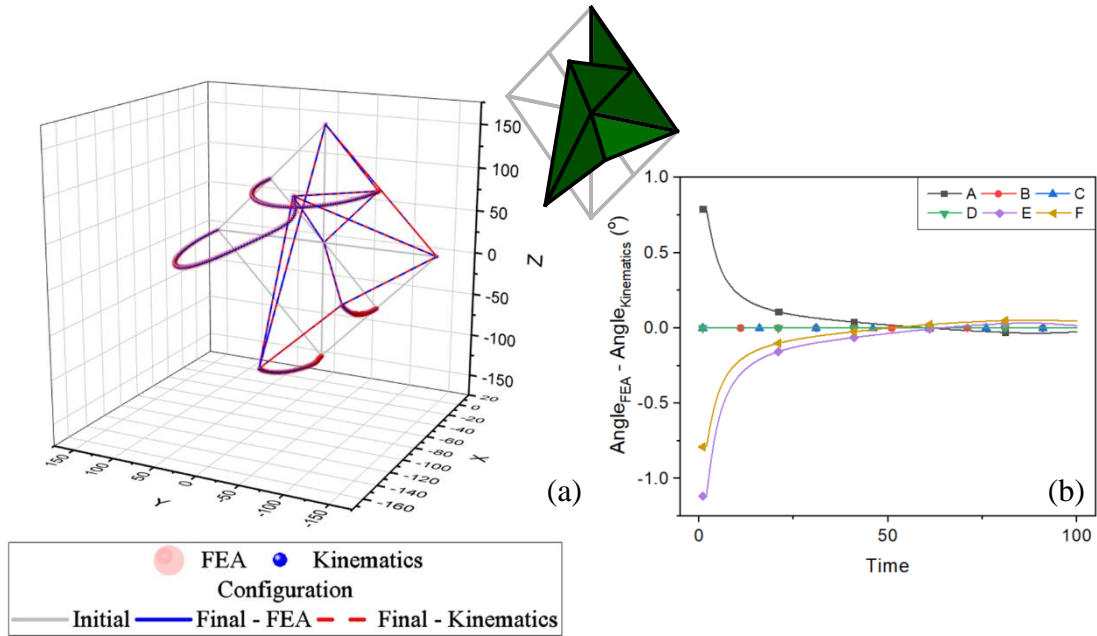


Figure 4-17: Asymmetric behavior of the waterbomb cell described by the kinematic formulation (using D-H parameters) and the FEA formulation (using bar-and-hinge description). (a) Tridimensional movement of the cell on folding process; (b) Difference between the inner angles evaluated by kinematics method and by FEA method.

5 Waterbomb Tessellation

A tessellation is a highly symmetric, edge-to-edge tiling surface, constructed through the arrangement of regular polygons. Zhao *et al.* (2018) explored the complexity of waterbomb tessellations, designing generalized tessellations to describe several 3D shapes going from spherical and cylindrical elements to hyperbolic paraboloids and torus, exploring asymmetries on both the pattern design and its shape configuration. In their work, Zhao *et al.* (2018) approximated 3D surfaces by modeling their curvatures with adapted waterbomb patterns, with variations in its unit cell. One example is the vase-like structure from Figure 5-1. Figure 5-1-a presents the target surface, where u and v are coordinates in the parametric u - v plane. With these coordinates, the structure is mapped into a quad surface (Figure 5-1-b), and each square is replaced by a waterbomb pattern half-folded. Depending on the resolution or the level of approximation desired, the number of waterbomb cells can increase substantially (Figure 5-1-c to Figure 5-1-f). The increasing in the resolution comes with a substantial increasing in the complexity and the number of degrees of freedom, apart from the level of variation input to the waterbomb unit cells.

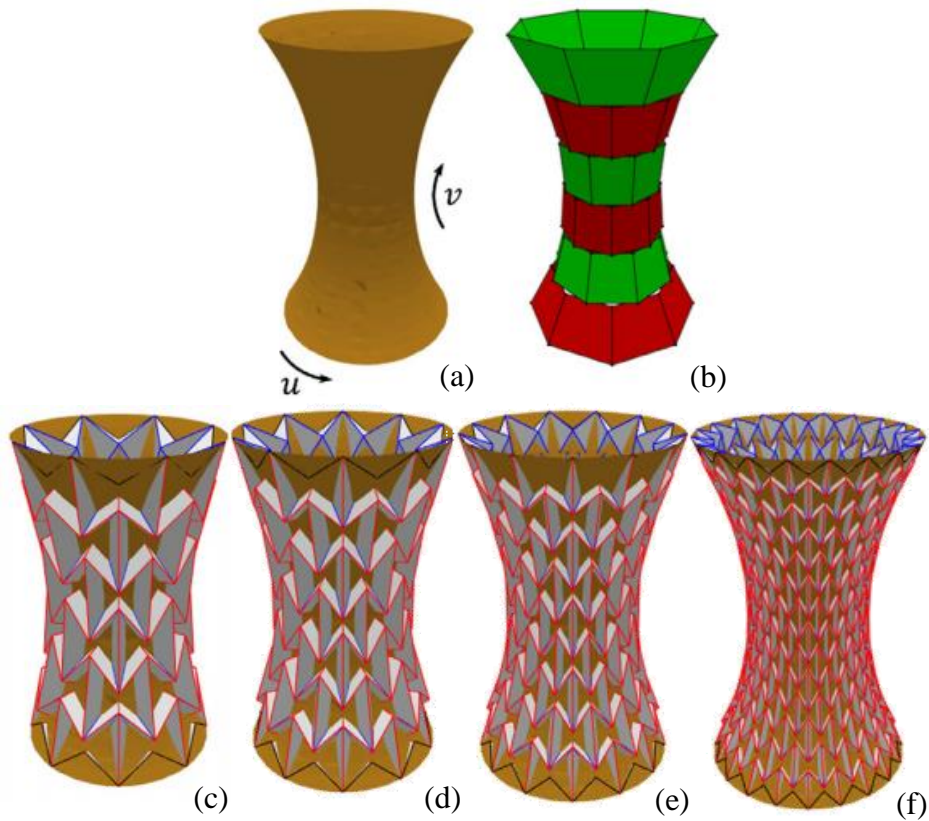


Figure 5-1: Target 3D surface and approximation using waterbomb tessellation. (a) Target surface and coordinates in parametric u - v plane; (b) Quad surface; (c) to (f): Target surface approximated using waterbomb tessellation, with increasing resolution.

[Image source: Zhao *et al.* (2018)]

5.1. Poisson's ratio

The Poisson's ratio of an element is a measurement of the dual effect subjected to an element by a compression load (Poisson's effect). In other words, the Poisson's ratio is a comparative numerical representation of the effect that a load applied in one direction has on a transversal direction of said element.

Assume that, for example, a tractive load is applied in the Y direction of a material, with two perpendicular directions X and Z, and the material's behavior regarding expansion/ contraction is described by the Poisson's ratio. In a bi-dimensional representation, the Poisson's ratio can be easily interpreted (Figure 5-2). A positive Poisson's ratio (PPR) indicates that by applying a tractive load in Y direction, the material

will contract in X and Z directions. If instead of contracting the material's cross-section expands in X and/ or Z directions, it has a negative Poisson's ratio (NPR). A peculiar case occurs for a material with zero Poisson's ratio (ZPR), where directions X and/ or Z are not affected by the loading on direction Y. This last category satisfies the morphing structure requirements.

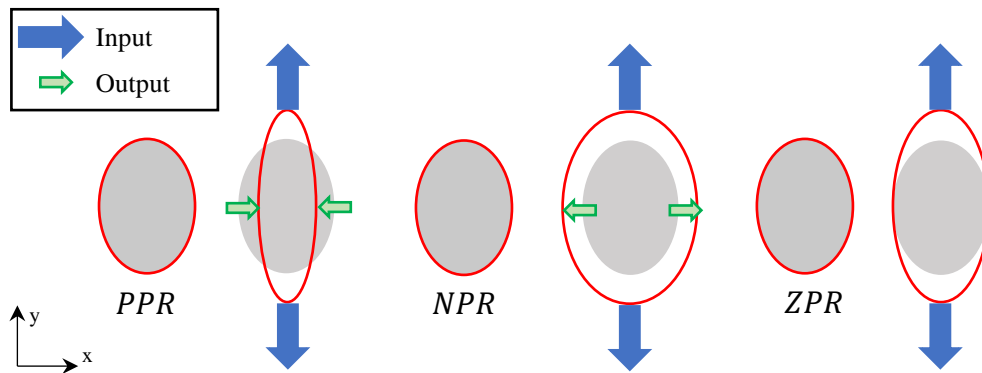


Figure 5-2: Poisson's ratio explained in two dimensions.

Based on this definition, the geometric particularities of origami unit cells and tessellations result in interesting characteristics related to the Poisson's ratio. In this regard, this parameter can be exploited in different applications, allowing engineers to design tessellation patterns for optimized desired mechanical properties. Findley (2013) presented an experimental study of several tessellations evaluating their properties applied in sandwich structures, acting as the sandwich core. Due to the negative Poisson's ratio of some origami tessellations, the application of said tessellations as sandwich cores present an interesting hardening-like behavior when loaded, once that the origami sandwich behaves as an auxetic structure. Findley (2013) studied sandwich cores made with Miura-Ori, Waterbomb, Square Twist and Honeycomb patterns.

Wei *et al.* (2013) developed an extensive work on the Miura-Ori tessellation, characterizing its geometry and planar and nonplanar effective elastic response. They verified that the Miura-Ori tessellation has an unusual emergent property, such as a negative Poisson's ratio. Origami Poisson's ratio evaluation was confirmed by Wei *et al.* (2013), for the Miura-Ori tessellation. This method, however, can be easily extended to other origami patterns, such as the waterbomb pattern studied here.

Wei *et al.* (2013) considered that the tessellation can be represented by a single cell, implicitly indicating a symmetric behavior. By definition, the Poisson's ratio is evaluated through the input/output relation of transversal principal directions, regarding the deformation. The Poisson's ratio can be evaluated for origami structures if the analyzed transversal directions are perpendicular through the entire deployment movement. Therefore, it is applicable mainly to symmetrical folding/unfolding process of unit cells. Even though, determining Poisson's ratio for the origami structure provides an optimization to the design method regarding the deployment motion, once it increases the understanding of a pattern's motion at any point in the deployment.

$$\nu_{wl} = -\frac{dw/w}{dl/l} \quad (5.1)$$

Length and width of an expanding and collapsing structure is properly defined by corner points, rather than edges, knowing that the selected corner points must define lines that remain perpendicular during the entire range of deployment. For the waterbomb patterns shown in Figure 5-3, three points are considered: points P_{L_1} and P_{L_2} , placed along the diagonal, and point P_{L_3} . The distance between the first two points is defined as R , and the deployment angle is defined as ϖ . For both waterbomb patterns shown in Figure 5-3, the distance R is defined as $R = \frac{2l \sin \frac{\varpi}{2}}{\cos \lambda}$. Variable R is used to evaluate W , L and H , indicated in Figure 5-3 for each waterbomb pattern, where W is the width, L is the length and H is the height.

Another interesting parameter for origami tessellations is the volumetric packing, that is characterized as the effective volume of the structure at a given folded state. When analyzing a single unit, the volumetric packing is evaluated as the effective volume of that unit $V = W \times H \times L$, where W is the width, H is the height and L is the length. Note that W , H and L not necessarily represent the edges, but instead are obtained as a relation between the cell geometry (edge's length) and the deployment angle.

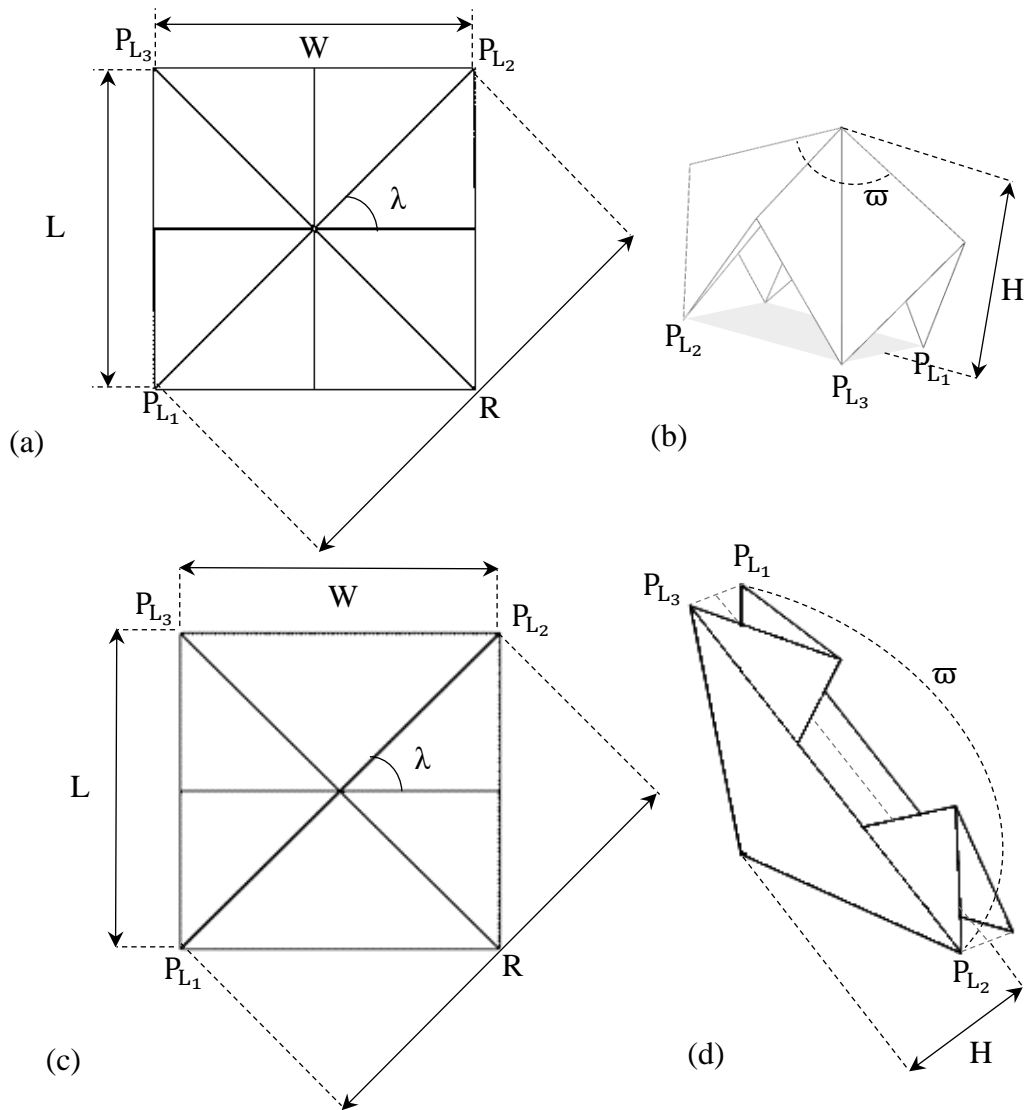


Figure 5-3: Waterbomb unit cell, selected points for Poisson's ratio evaluation and variables for the 8-creased (a, b) and the 6-creased (c, d) patterns.

Table 5-1 shows the variables W , L and H for each waterbomb pattern. Additionally, it presents the volumetric packing of each waterbomb pattern and the in-plane (ν_{wl}) and out-of-plane (ν_{wh} , ν_{lh}) Poisson's ratios.

Table 5-1: Characteristic length (L), height (H) and width (W), effective volume (V) and in-plane (ν_{wl}) and out-of-plane (ν_{wh} , ν_{lh}) Poisson's ratio of a 6-creased and an 8-creased waterbomb pattern

	8-creased	6-creased
W	$2l \sin \frac{\varpi}{2}$	$2l$
H	$l \cos \frac{\varpi}{2} / \cos \lambda$	$l \cos \frac{\varpi}{2} / \cos \lambda$
L	$2l \tan \lambda \sin \frac{\varpi}{2}$	$2l \tan \lambda \sin \frac{\varpi}{2}$
V	$2l^3 \frac{\tan \lambda}{\cos \lambda} \sin \frac{\varpi}{2} \sin \varpi$	$2l^3 \frac{\tan \lambda}{\cos \lambda} \sin \varpi$
ν_{wl}	-1	0
ν_{wh}	$(\sin \frac{\varpi}{2})^{-2} - 1$	0
ν_{lh}	$(\sin \frac{\varpi}{2})^{-2} - 1$	$(\sin \frac{\varpi}{2})^{-2} - 1$

It is interesting to notice that the 6-creased waterbomb has a zero Poisson's ratio in-plane, while the 8-creased waterbomb has a negative in-plane Poisson's ratio. Besides, the out-of-plane Poisson's ratio for the 8-creased waterbomb pattern decreases with the increasing of the deployment angle, being zero for a fully deployed cell (opened configuration) and -1 for a fully undeployed cell (closed configuration). This difference is clear when analyzing the deployment of each cell, as shown in Figure 5-4. Both cells are pushed in Y direction (red arrows in Figure 5-4 (a) and (b)) with a normal in-plane force. The result for the 8-creased cell is a reduction on both X and Y directions (Figure 5-4 (c)), while the result for the 6-creased waterbomb pattern is a reduction only on Y direction (Figure 5-4 (d)) and no change on X direction. Figure 5-4 (e) and (f) shows the superposition of XY projection of initial and final configurations for both waterbomb patterns.

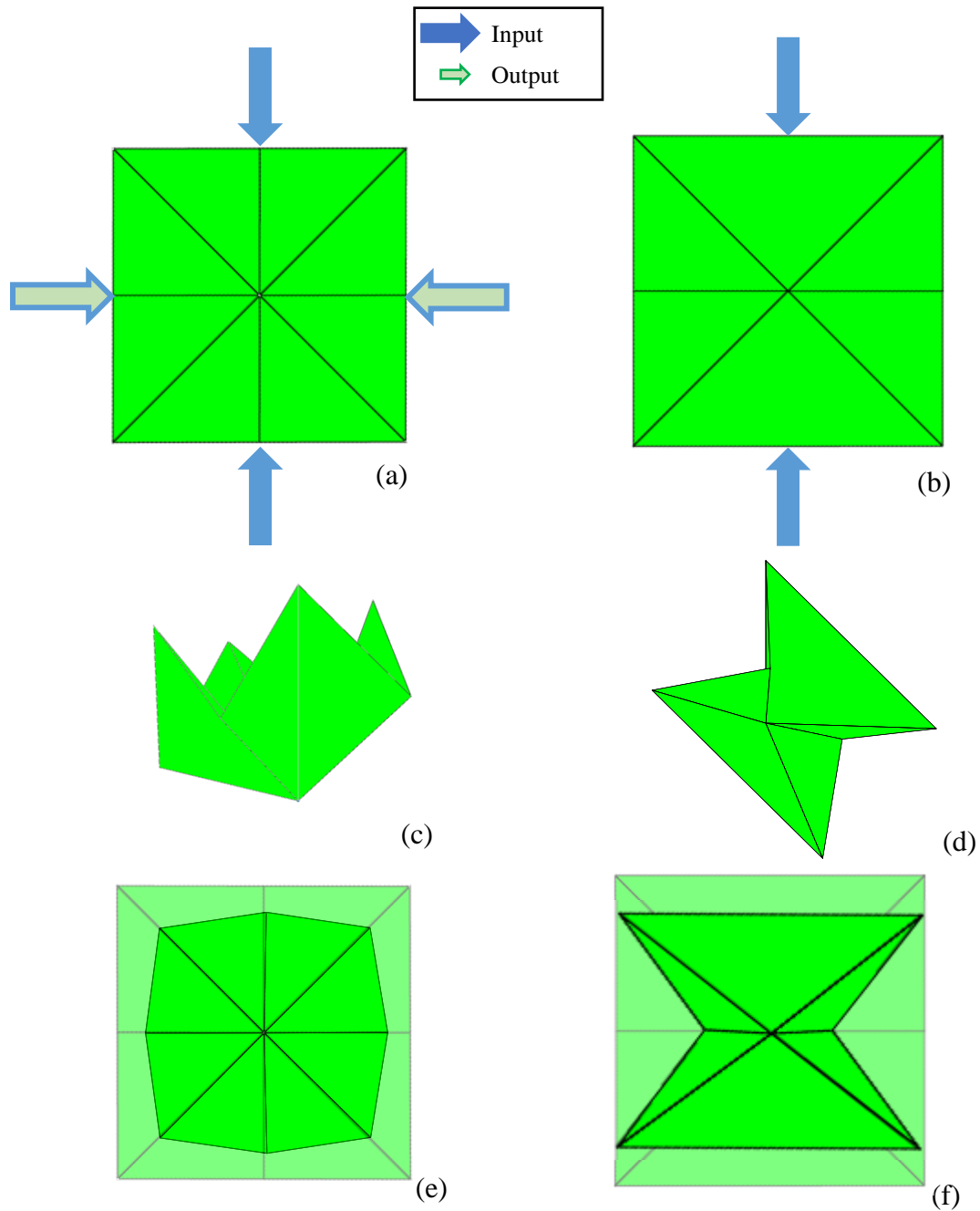


Figure 5-4: Poisson's ratio representation for the 6-creased and the 8-creased waterbomb patterns. (a) and (b): Input force/ displacement and output result for the in-plane case; (c) and (d): Final configuration reached for 8-creased and 6-creased respectively; (e) and (f): Overlap between final and initial configurations.

Comparatively, the effective volume of the 6-creased and the 8-creased waterbomb patterns are shown in Figure 5-5. It is interesting to notice that the effective volume of the 6-creased squared pattern has a perfectly symmetric shape, reaching its

maximum value for $\varpi = 90^\circ$, while the 8-creased squared pattern reaches its maximum at $\varpi \approx 110^\circ$. Also, it is possible to see that the 8-creased pattern is more compact than the 6-creased pattern for every deployable stage.

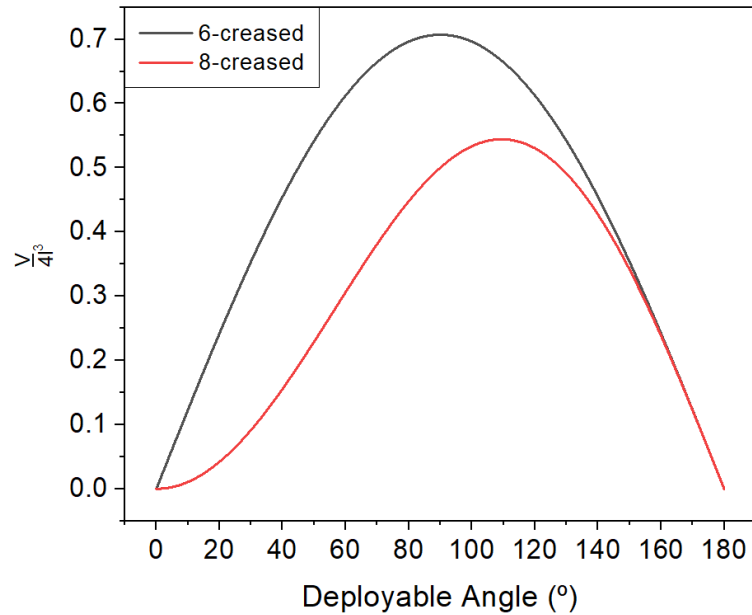


Figure 5-5: Effective volume of 6-creased and 8-creased waterbomb unit cells as a function of the deployable angle.

Therefore, considering a single waterbomb cell, the 6-creased pattern presents a higher maximum effective volume related to the 8-creased pattern. Extending this analysis to their tessellations, a waterbomb tessellation generated from a 6-creased pattern will generate a higher maximum effective volume than a tessellation generated from the 8-creased pattern. Since our focus here is to exploit the applicability and dynamical behavior of a closed waterbomb tessellation as a replacement for a robot wheel, and we are not focused on compactability but on morphing, the next analysis will be performed exclusively on the 6-creased tessellation.

This work is focused on the complexity related to the number of degrees of freedom and the identification of symmetry planes for engineering application purposes. This chapter presents a study on tessellations obtained through the regular distribution of a 6-creased waterbomb pattern through a surface. A general study is developed, starting with the opened tessellation, passing through a closed configuration and analysis of the structure.

5.2. Opened tessellation

Usually, origami tessellations are applied in situations where they are subjected to a symmetric actuation, presenting a reduced number of controlled variables and a considerably small number of degrees of freedom (DoF). However, slight asymmetries might influence substantially the origami behavior during opening/ folding process. Besides that, small actuations such as perturbations promoted to a crease that is near a bi-stable condition might affect significantly the origami configuration, its stability and the actuation.

Considering these possible situations, a general study is developed on the waterbomb opened tessellation, exploring its number of DoF, the variety of shapes and motions. David Huffman (1976) pioneered the study of origami tessellations by presenting a study on the behavior of surfaces with zero-Gaussian curvature (developable surfaces) near creases and apices of cones. He presented an interesting analysis of fundamentals of both straight and curved creases, using a dual diagram to analyze both local behavior and interactions among creases.

Tachi (2010) uses a perturbation-based approach for obtaining design variations of flat-foldable meshes. He develops a necessary and sufficient condition for existence of finite rigid motion of general flat-foldable quadrilateral mesh origami, using perturbations on a known stable configuration and reaching a subsequent stable configuration.

The analysis developed in this chapter use the deformation-based formulation from Liu & Paulino (2017) with the intent to evaluate the variety of configurations and degrees of freedom presented by a $m \times n$ waterbomb tessellation, with m lines and n cells on each line.

The tessellation configuration can be divided into three classifications: folded, unfolded and half-folded or semi-folded. The folded case is associated to a flat condition, where all creases are completely folded, meaning that $\theta_i = \pi$, for $i = 1..N_{creases}$. The unfolded case is also associated to a flat condition. But in this case, the origami is completely opened, in a flat sheet shape, meaning that $\theta_i = 0$, for $i = 1..N_{creases}$. Any configuration that is neither folded nor unfolded ($0 < \theta_i < \pi$, for $i = 1..N_{creases}$) is classified as half-folded or semi-folded. For the analysis developed here, it is considered the 5×9 waterbomb tessellation shown at Figure 5-6, with nodes indexes indicated. For

further local analysis, three cells are chosen for inner angles and deformation evaluation: cell C_1 , with vertex node 129, cell C_2 , with vertex node 53, and cell C_3 , with vertex node 21. These cells are also highlighted in Figure 5-6.

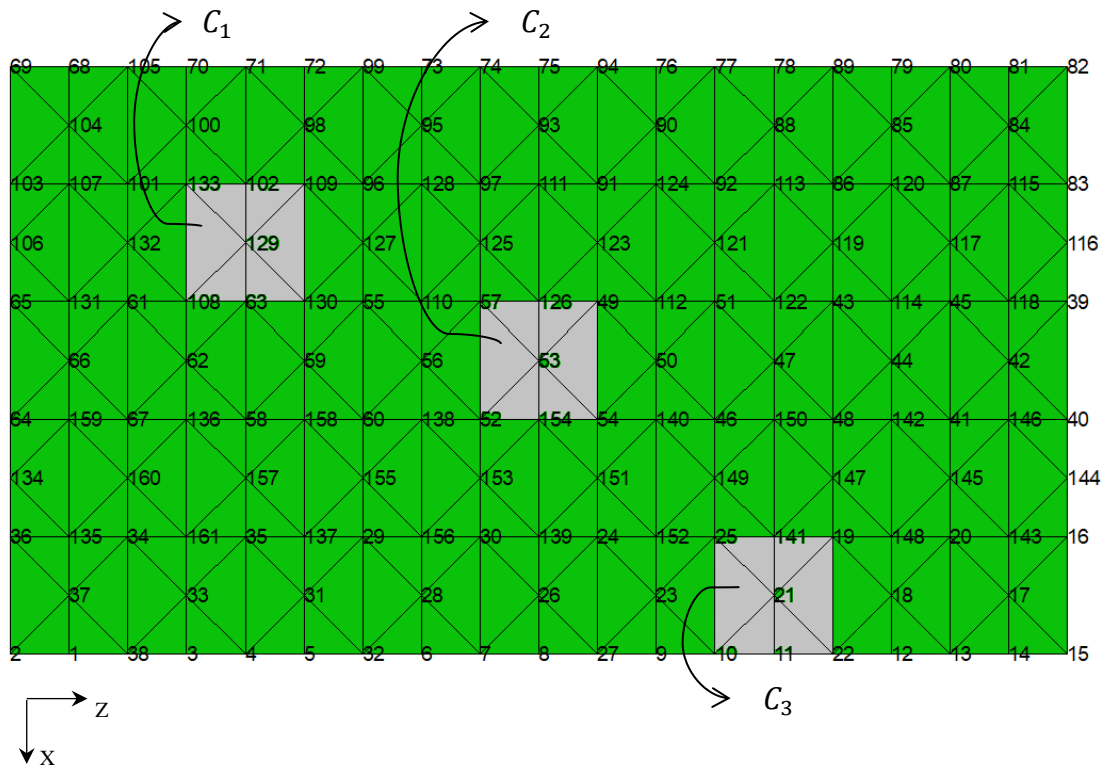


Figure 5-6: 5×9 waterbomb tessellation generated from a squared waterbomb unit cell. The cells C_1 , C_2 and C_3 are highlighted.

The folding process ability inherent of origami tessellations conceives an interesting property of undergoing relatively large deformations. We put it here as “relative” because, when analyzed locally, the deformation happening on the creases are not expressive even for large angle variations. If instead of looking to the creases we analyze the structure as a single body and consider its deformation according to the classical description, it has the capability to present an expressive deformation, since a chosen dimension of the origami (transversal section, for example) could have a measure of 1 cm in a completely folded (or simply folded) state (Figure 5-7-a), while it can increase more than 20 times this dimension, measuring 22,5 cm in a completely unfolded (or simply unfolded) condition. Figure 5-7-b shows the tessellation for a half-folded configuration, where the origami is stable without constraints or external efforts.

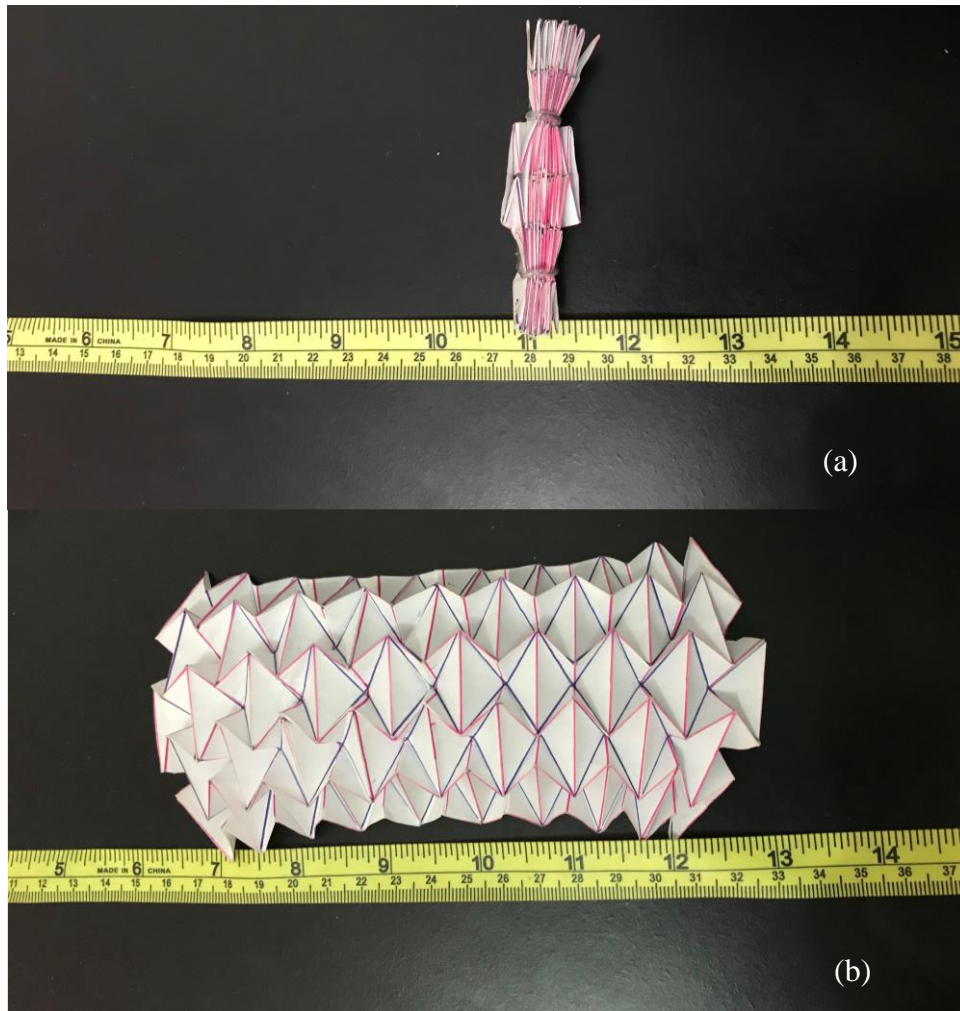


Figure 5-7: Waterbomb tessellation in a fully closed (a) and in an opened (b) configuration

Even though it is fairly uncommon, some materials and material constructions exhibit negative Poisson's ratios, including tessellation origami. Lakes (1987) identified a foam structure with a negative Poisson's ratio expanding laterally when stretched. The foam is composed by a plurality of 24-sided polyhedron that, ideally, collapses symmetrically when mechanically solicited. Similar study is developed by Prall & Lakes (1997), where a 2D analysis on a honeycomb with re-entrant cells provides a structure with a -1 Poisson's ratio. It is interesting to point out that the re-entrant 2D pattern studied by Prall & Lakes (1997) resembles a top view of the waterbomb unitary cell in a half-folded configuration. A similar structure is evaluated by Grima *et al.* (2005), exploiting the hinge rotation of a plurality of units (Grima *et al.*, 2005a) and the re-entrant

cells in a polyurethane foam (Grim *et al.*, 2005b), that presents an auxetic behavior (expand instead of contract when stretched in a transverse direction).

In section 5.1 we verified that the waterbomb unit has a negative Poisson's ratio. In addition to its natural spherical behavior, it is expected that the waterbomb tessellation behaves in a synclastic way under bending effort, presenting a spherical shape. Therefore, the 6-creased waterbomb tessellation is submitted initially to a sequence of numerical bending tests, where the boundary conditions are defined as simply supported (translations are restricted, rotations are allowed) and a punctual load is applied to vertex 53 (see Figure 5-6). A total of six conditions are tested, being a combination between a downwards (Case A) or an upwards (Case B) punctual load, and a two-points (Case I), three-points (Case II) or four-points (Case III) support for bending test. The numerical simulations are performed as shown in Table 5-2.

Table 5-2: Nodes for applied boundary conditions for each bending test, considering the number of the supports and the direction of the punctual load.

		Boundary			
		B_{E_1}	B_{E_2}	B_{D_1}	B_{D_2}
2-points	Case I-A	66	-	42	-
	Case I-B	66	-	42	-
3-points	Case II-A	37	104	42	-
	Case II-B	37	104	42	-
4-points	Case III-A	37	104	17	84
	Case III-B	37	104	17	84

The simulations for A-type cases are shown in Figure 5-8 (a) to (c), and simulations for B-type cases are shown in Figure 5-8 (d) to (f). It is expected that, for all bending cases, the tessellation behaves as a stiffer structure for B-type cases when compared to A-type cases, since the opening process of the tessellation occurs naturally according to the A-type condition. This behavior is observed when comparing the results of A-type and B-type for the same boundary condition.

It is interesting to notice that the tessellation behavior differs substantially from A-type to B-type, even when looking into the same case. A-type cases present an increasing on the load factor until a maximum value is reached and, after that, the load factor decreases. The increasing is associated to the folding process of the cells on the border of the tessellation (columns 1 and 3) and, when the maximum point is reached, these cells start to unfold, which decreases the load factor. This folding/ unfolding process can be seen in more details in Figure 5-9. The number of supporting points influences on the maximum value. More specifically, it is possible to notice from Figure 5-8 (a) to Figure 5-8 (c) that the increasing on the supporting points dislocates the maximum value to the left, meaning that the unfolding of the cells on the columns 1 and 3 starts earlier. For the 3-points case (Case II-A, shown in Figure 5-8 (b)), the unfolding process is so expressive that even though cell 53 is being pushed, upwards, it results in a dislocation downwards.

Another interesting observation is that in the B-type cases it is noticeable a saturation-like or plateau after a percentage of folding. It can be understood as a resistance of the material to undergo large local deformations, since the folding limit is achieved for a few cells prior than to others, and it is not possible to continue the material accommodation. Also, B-type cases (Figure 5-8 (d) to (f)) does not present a maximum load factor value. In fact, some cases such as the 3-points (Case II-B) and 4-points (Case III-B) cases might present multiple inversions on the load factor temporal evolution. Each one of these inversions is associated to a new cycle of folding/unfolding process. Similar to the A-type cases, the increasing on the number of supporting points results in an earlier event of said inversion. This behavior can be seen in more details in Figure 5-10 for all three cases.

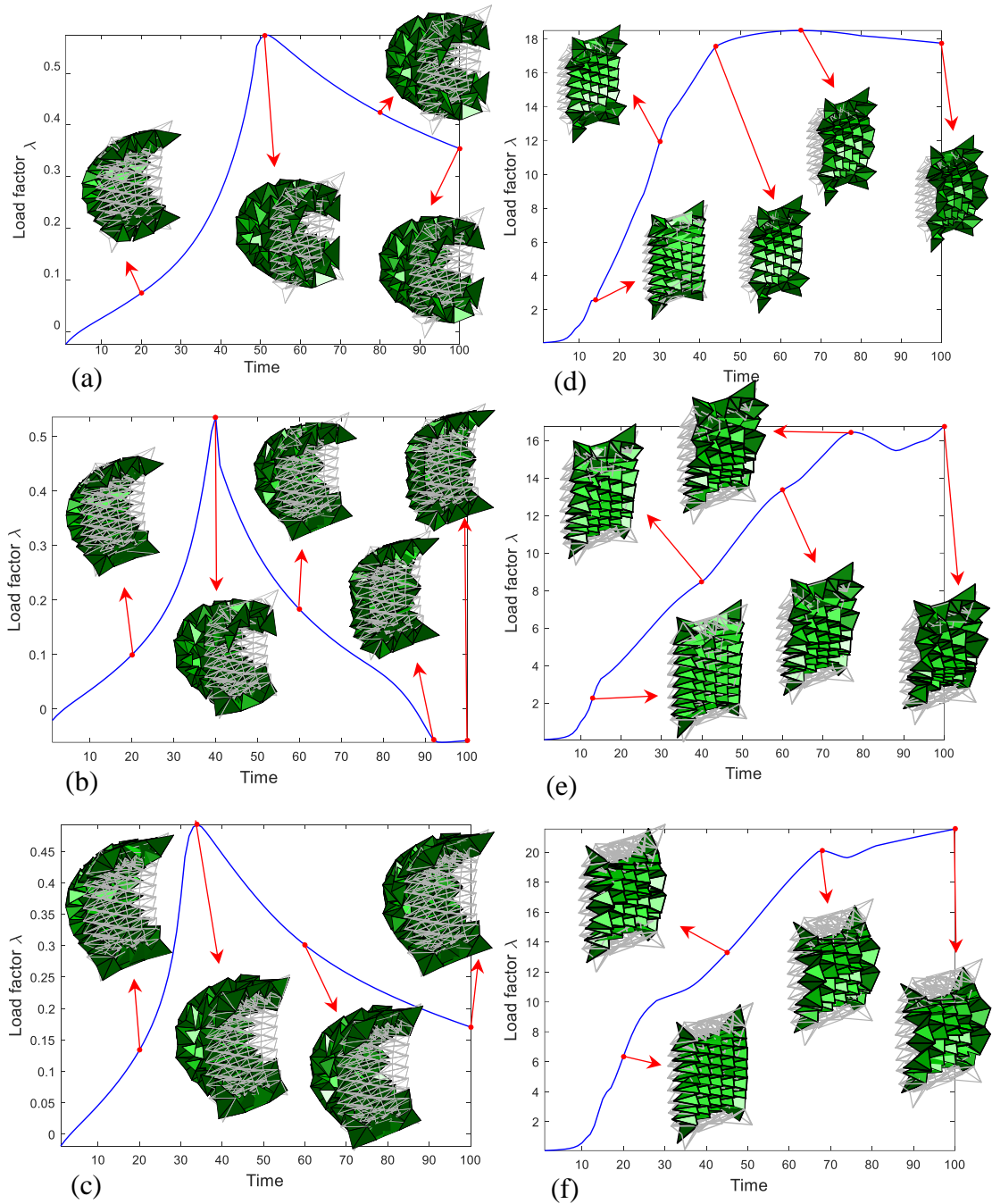


Figure 5-8: Waterbomb tessellation under bending. (a) Case I-A: 2-points boundary condition; (b) Case II-A: 3-points boundary condition; (c): Case III-A: 4-points boundary condition; (d) Case I-B: 2-points boundary condition; (e) Case II-B: 3-points boundary condition; (f): Case III-B: 4-points boundary condition.

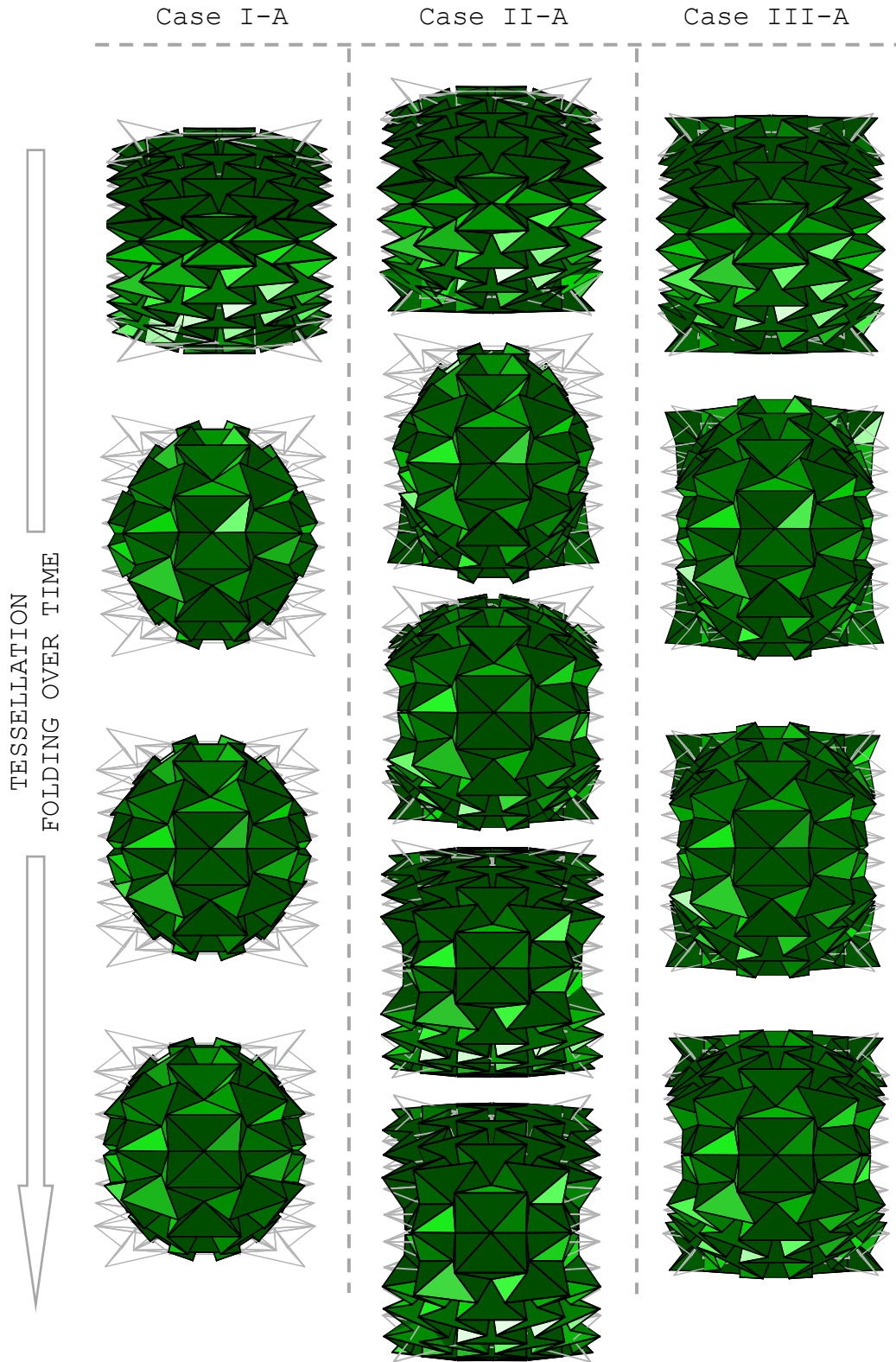


Figure 5-9: Top view of the waterbomb tessellation's folding process over time for an A-type bending actuation, for Cases I, II and III.

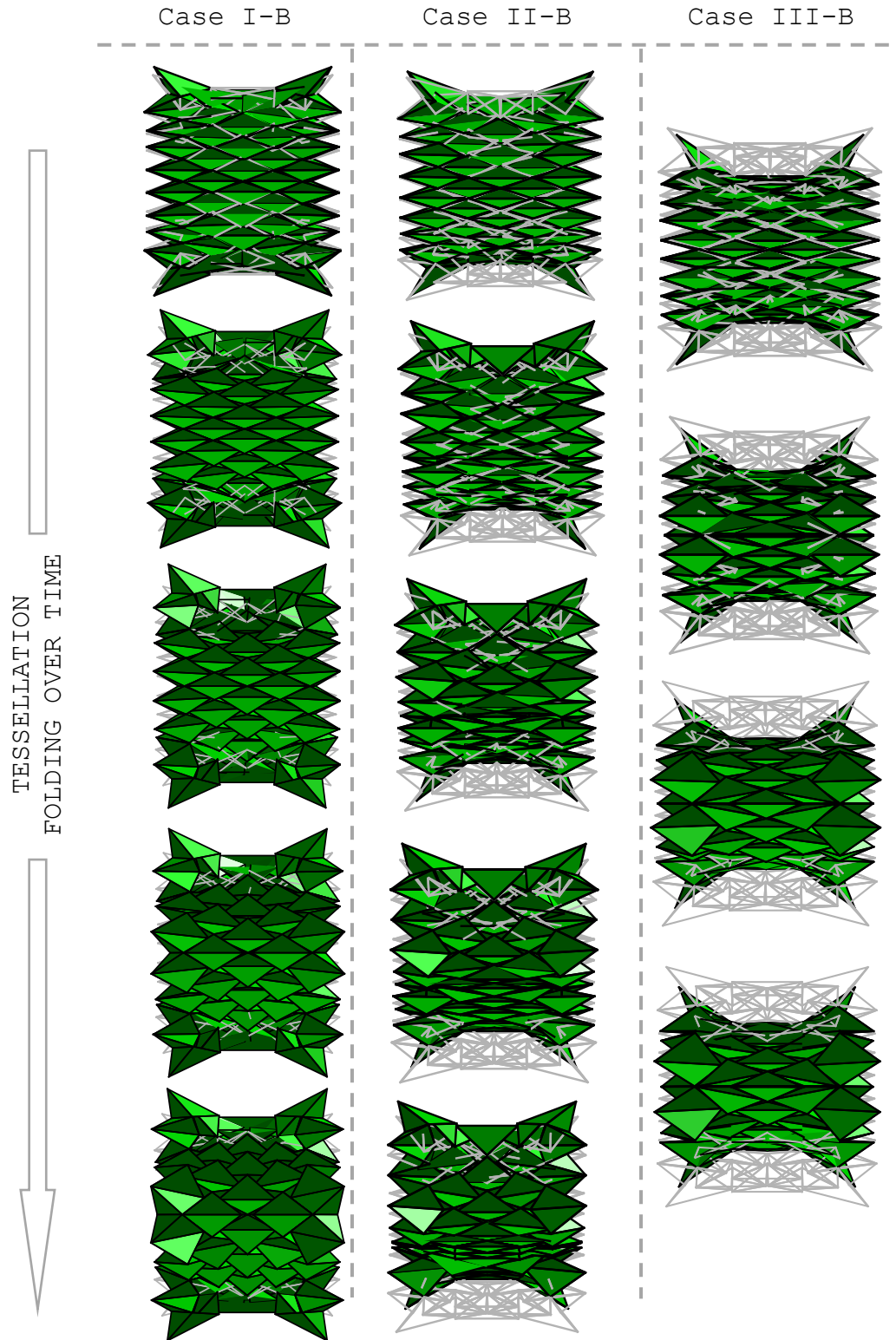


Figure 5-10: Top view of the waterbomb tessellation's folding process over time for a B-type bending actuation, for Cases I, II and III.

We can also evaluate the behavior of the tessellation by looking into its inner cells. More specifically, the folding/unfolding process of each cell can be described by its inner angles' variation. Keeping that in mind, we observe the inner angles of unit cells C_1 , C_2 and C_3 highlighted in Figure 5-6. Without loss of generality, we can observe the inner angle D of all three cells for each one of the cases presented in Table 5-2, and this plot is shown in Figure 5-11. The vertical lines point to each inversion, maximum or minimum for each case. It is interesting to notice that for all A-type cases the maximum points found in Figure 5-8 (a) to (c) are directly related to unfolding or saturation (plateau) of cells contained within the middle column (column 2), while for all B-type cases the inversions found in Figure 5-8 (d) to (f) are directly related to unfolding or saturation (plateau) of cells contained within the borders (columns 1 and 3).

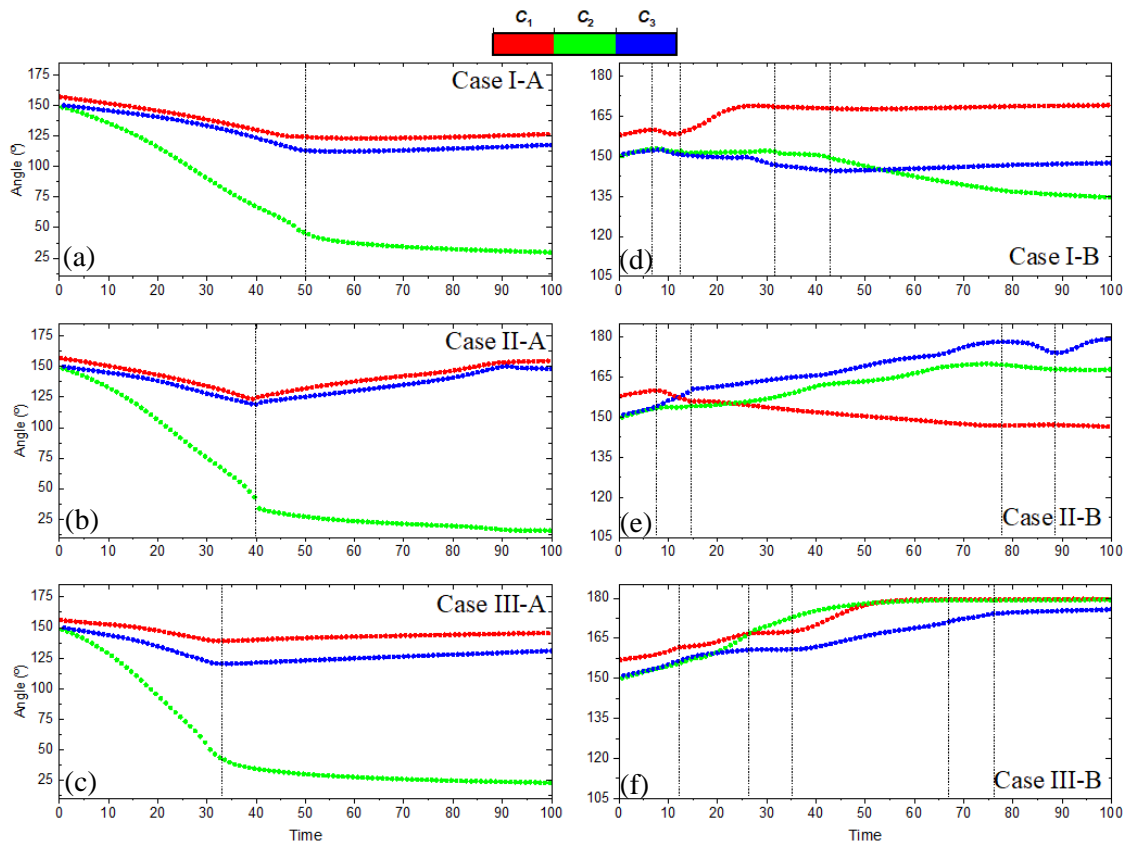


Figure 5-11: Time evolution of inner angle D of unitary cells C_1 , C_2 and C_3 for folding A-type cases I (a), II (b) and III (c); and for B-type cases I (d), II (e) and III (f).

It is also important to highlight the fact that when bended on the B-type condition, the waterbomb presents a saddle-like shape, that is characteristic of structures with a

globally negative Gaussian curvature. Also, even though the waterbomb tessellation has a negative Poisson's ratio, it is intriguing that it can be bended in a saddle-like shape, since it is a typical behavior of materials with a positive Poisson's ratio. The saddle-like shape can be seen in detail in the front and side views in Figure 5-12.

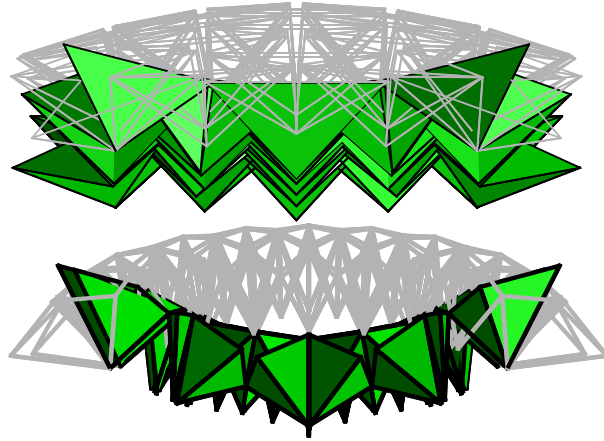


Figure 5-12: Front view (top) and side view (bottom) of the final configuration of the waterbomb tessellation for Case III-B (green), compared to the initial configuration (gray).

Aiming to evaluate the behavior of the tessellation when subjected to a uniaxial force, Node 66 is simply supported ($[x_{66}, y_{66}, z_{66}] = [0,0,0]$) and an external load is applied to Node 42 along Z direction (see Figure 5-6). The natural spherical motion of the waterbomb unit cell is dominant on the folding/unfolding process. Notice that even though the external load is applied along Z direction, the tessellation presents an expressive motion on Y direction, maintaining a spherical-like shape. The tessellation behavior under traction/ compression effort resembles an hyperelastic material. Besides, the unfolding process (Figure 5-13 (a)) presents a larger load factor than the folding process (Figure 5-13 (b)).

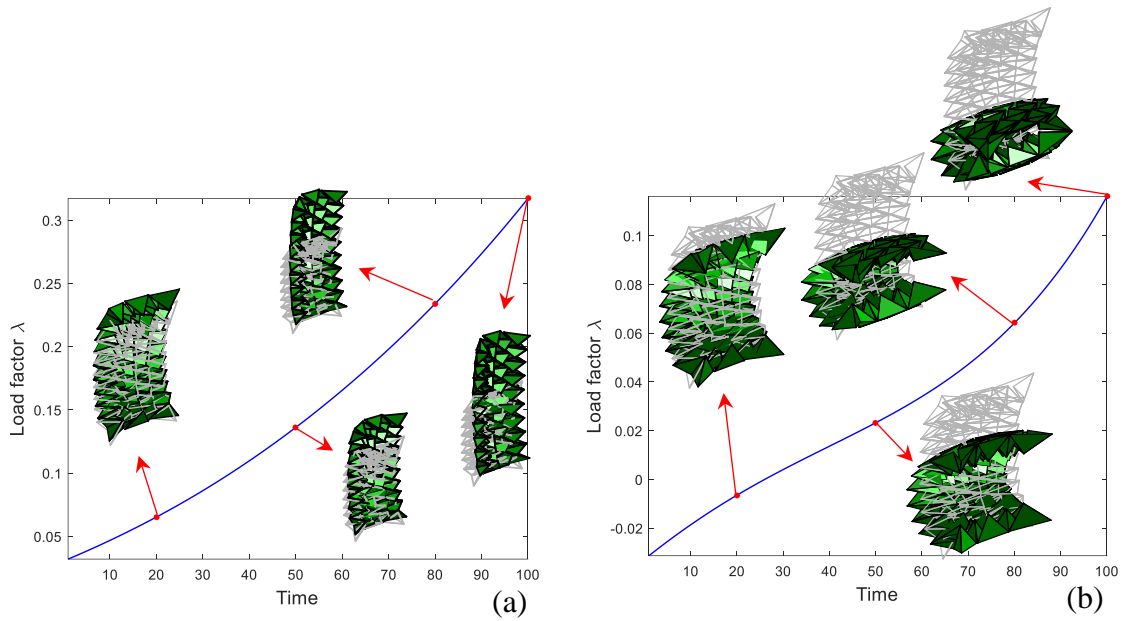


Figure 5-13: Waterbomb tessellation under uniaxial loading. (a) Uniaxial load inducing the unfolding of the waterbomb tessellation (traction); (b) uniaxial load inducing the folding of the waterbomb tessellation (compression).

The spherical-like shape assumed during folding/unfolding process can be seen in detail in Figure 5-14, where Case I refers to the unfolding (traction) and Case II refers to the folding (compression) process. It is important to note that in the uniaxial loading Cases I and II, the structure does not present a saddle-like shape. Instead, it preserves the spherical-like shape.

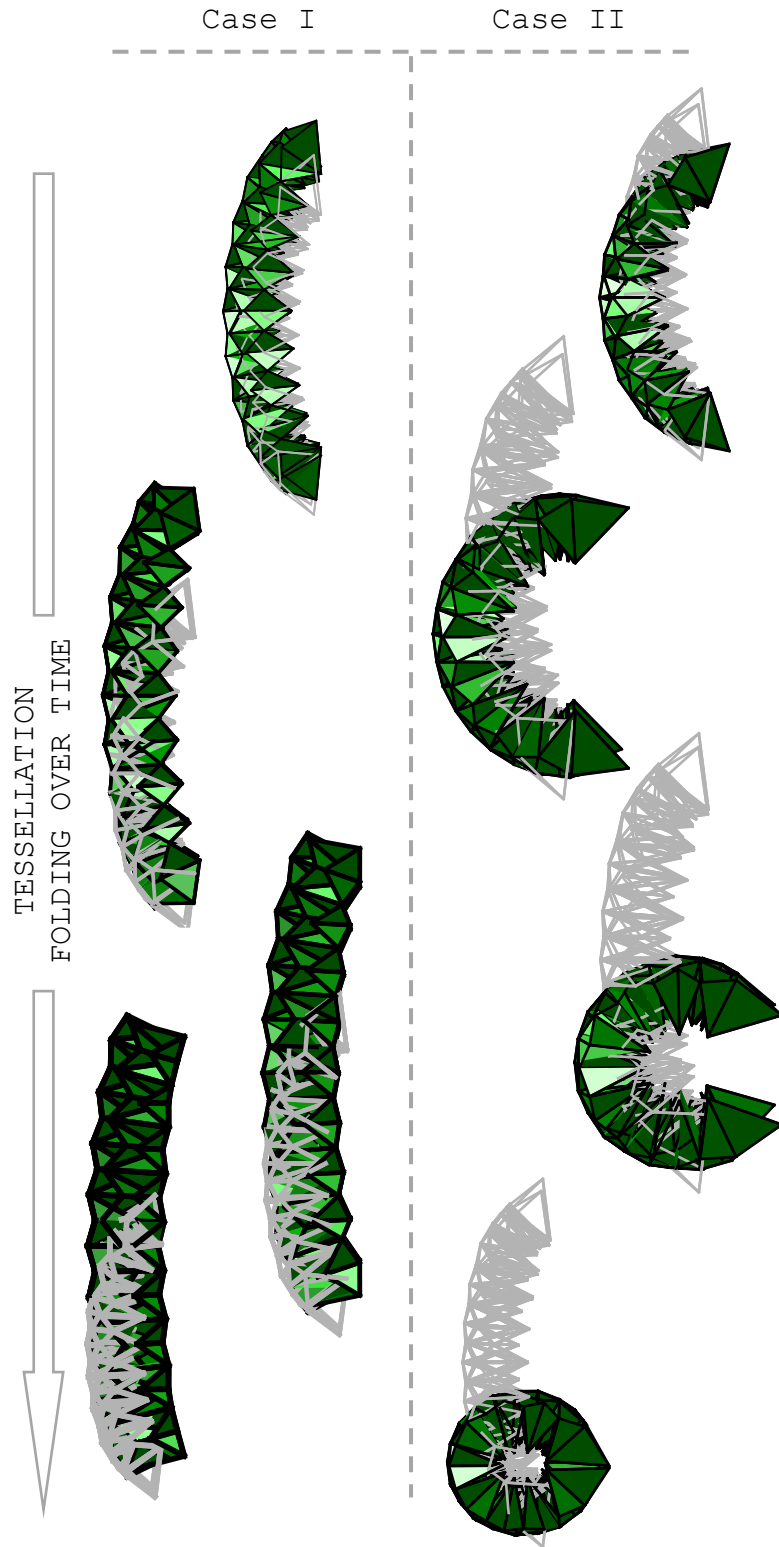


Figure 5-14: Side view of the waterbomb tessellation's folding process over time for a uniaxial actuation, for Cases I and II.

It is important to highlight here that synclastic structures are non-developable, by definition, since it is not possible to take the structure from a flat geometry to a double curvature geometry without introducing gaps. The foldability of origami-like structures allows the design of synclastic surfaces from a flat hole-less surface through the replacement of the gaps by foldable unitary cells. This foldability also results in a fluid surface that interchanges between singly curved (cylindrical and conic geometries) and doubly curved (saddle-like and domes).

This fluidity can be seen in Figure 5-15 for an asymmetric actuation of the waterbomb tessellation taken according to Table 5-3, where $f = 9.216$ N.

Table 5-3: Boundary conditions and Inputs given by (x, y, z) and the respective numeric reference for the Node

		x	y	z
Boundary Conditions	53	1	1	1
	52	0	1	0
	49	0	1	0
	66	1	1	0
	42	0	1	0
Inputs	82	$-f$	0	0
	15	f	f	0
	2	$-f$	$-2f$	0
	69	f	$3f$	0

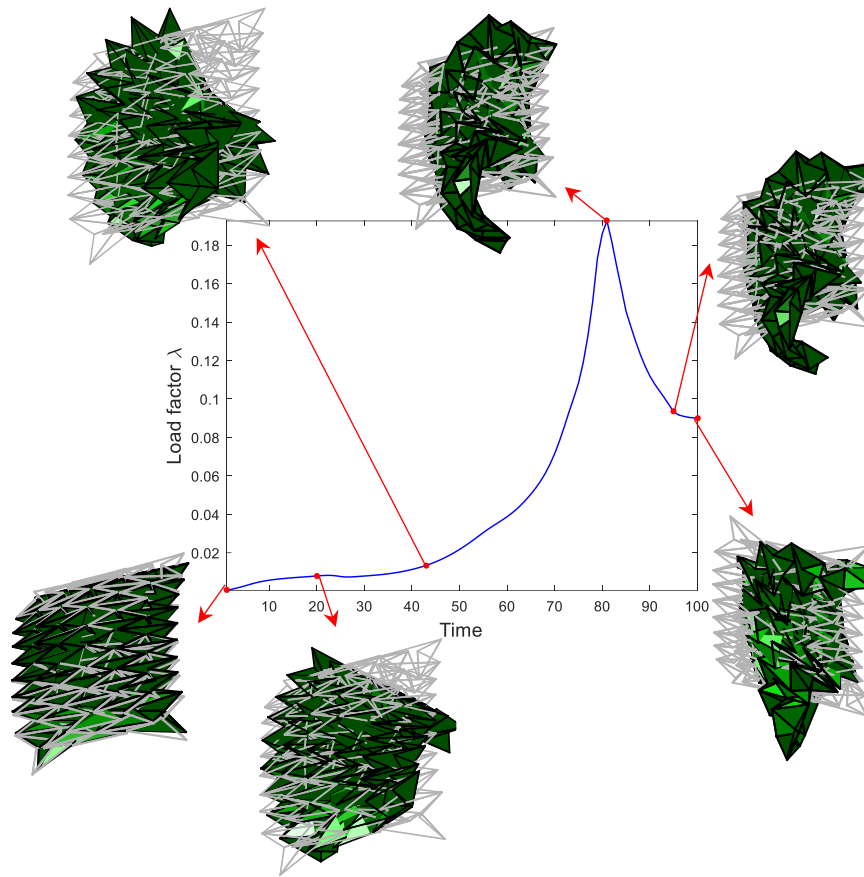


Figure 5-15: Time evolution of the Load factor for an asymmetric folding process of the waterbomb tessellation.

The tessellation starts as a singly curved surface in a cylindrical-like shape and, as time evolves, the tessellation goes from singly to doubly curved surface presenting a saddle-like shape, that is associated with an asymmetric opening of each waterbomb unit cell. This asymmetry can be better analyzed by looking to the inner angles of cells C_1 , C_2 and C_3 (Figure 5-16). Note that until approximately the time 20 (line I in Figure 5-16) all three cells C_1 , C_2 and C_3 behave near the Π_2 plane-symmetric case, i.e., angles $A \approx D$ and $C \approx F$, with a larger deviance observed in cell C_3 . From this time on, the tessellation changes its general curvature from singly to doubly curved, presenting a saddle-like shape and imputing a significative deviation from a plane-symmetric condition on inner cells C_1 , C_2 and C_3 .

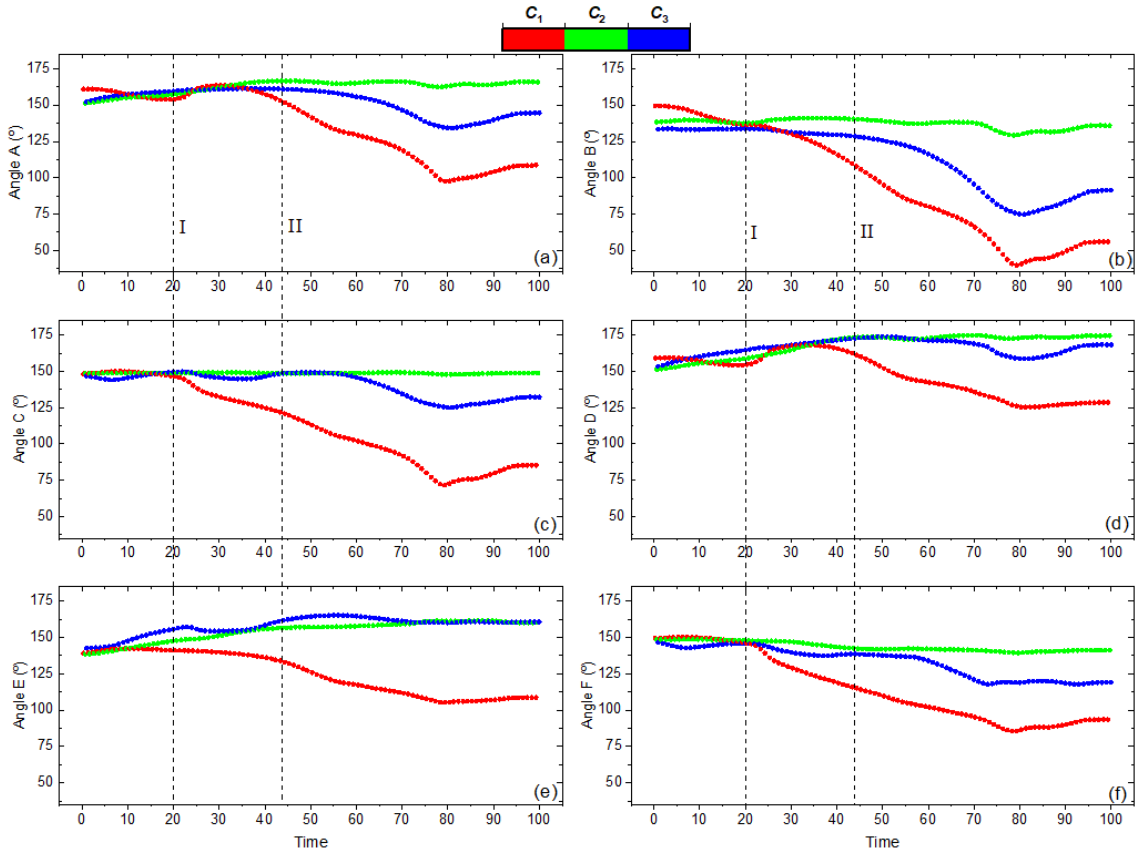


Figure 5-16: Time evolution of inner angles A to F of unit cells C_1 , C_2 and C_3 .

5.3. Closed tessellation

Closed tessellations have a reduced number of DoF when compared to the opened ones. Besides, the coupling due to the closure of the tessellation promotes some periodicity along the structure, which can be described considering different kinds of symmetries (Fonseca & Savi, 2021). Initially, it is important to consider the differentiation presented here between local and global symmetries. A global symmetry is related to the structure, and it is noticeable on a repetition of a line or a group of lines periodically, and this group is named *representative volume element* (RVE). Global symmetries are usually considered when the outer surface of the origami is of interest, and local asymmetries can be neglected. On the other hand, a local symmetry is related to a unit cell, and the behavior of each cell individually is of importance or needs to be controlled somehow. In this regard, it is possible to imagine a total symmetry where the fundamental substructure is the unit cell, or other situations where the fundamental

structure is built by a set of unit cells, RVE. Besides, symmetry conditions might need to be associated with both geometrical and mechanical aspects. The complexity of the origami description increases as the asymmetry of the fundamental representative element accentuates. Therefore, the complexity of the closed tessellation representation relies mostly on the unit cell configuration, regarding its degree of asymmetry. Figure 5-17 illustrates different kinds of symmetry related to a closed waterbomb tessellation with 18 unit cells disposed in 3 lines with 6 cells each.

Figure 5-17 (a) explores the local symmetry through a unit cell with a symmetric configuration (equivalent mobility 1). The repetition of this element through a line generates a symmetric RVE, and the result of this element repetition through a column generates a totally symmetric tessellation. In this case, the behavior of the whole structure can be extrapolated from the analysis of a single unit cell.

Figure 5-17 (b) presents a unit cell with a plane-symmetric configuration (equivalent mobility 2). Note that the repetition of this unit cell through a line generates a structure with no mirror symmetry, but which configuration can be extrapolated from the analysis of a single unit cell. The repetition of this RVE through a column, however, generates two different structures: the first one (Figure 5-17 (b)-i) is obtained by piling the RVE, while the second one (Figure 5-17 (b)-ii) is obtained by mirroring every other RVE while piling them. On both cases, the structure has longitudinal and circumferential symmetry and, therefore, global symmetry, but with a local asymmetry (or plane-symmetry). Although the tessellation Figure 5-17 (b)-i can be fully described through the extrapolation of the analysis of one line (RVE), the tessellation Figure 5-17 (b)-ii requires the knowledge of two consecutive lines or minimally the coupling between a cell from line k to a cell on line $k+1$.

Figure 5-17 (c) highlights two asymmetric unit cells that belong to a line composed exclusively by asymmetric cells. Depending on the final configuration achieved by the line, it might be possible to generate a tessellation with some identifiable periodicity along the lines, where the RVE is a line or a set of lines. For a general case, the tessellation has neither local nor global symmetry.

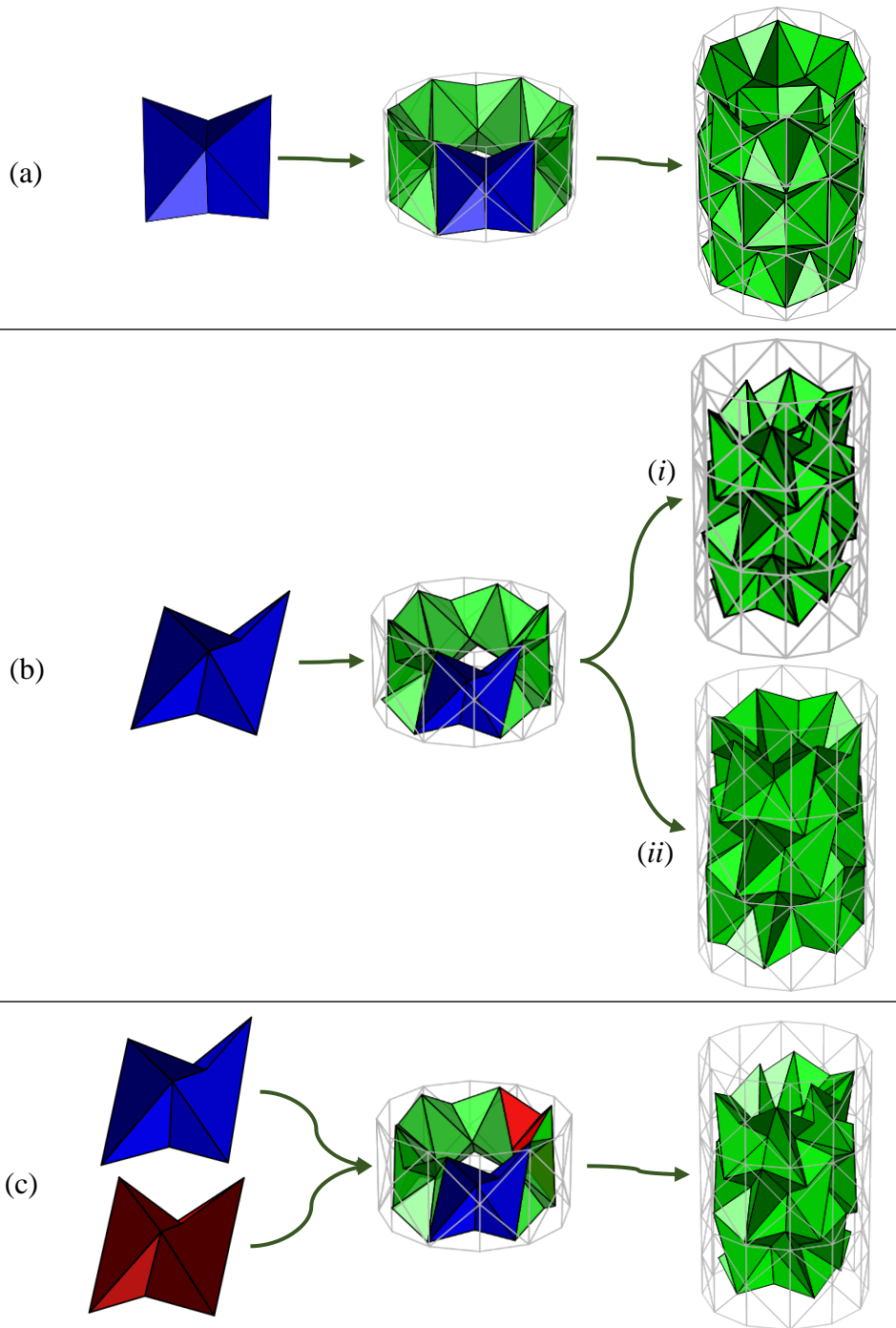


Figure 5-17: Three different configurations assumed by a closed waterbomb tessellation. (a) The RVE is the symmetric unit cell, and, in this case, the structure has both local and global symmetries; (b) The RVE is a set of cells, where the set is composed by two cells from consecutive lines for (i) case and by a single plane-symmetric unit cell for (ii) case. The (ii) case has global symmetry; (c) A RVE is not identified, resulting in a structure with neither local nor global symmetry.

The closed tessellation generated with the 6-creased waterbomb pattern (Figure 5-18a) results in a cylindrical-like structure. The natural force (Kresling, 2008; Ma *et al.*, 2020) associated with the folding process of the closed tessellation tends to generate a conic-like structure (Figure 5-18b), which results in local asymmetries even for a symmetric actuation. This conic-like natural force can generate several 3D structures, including a double-curved surface or ball-shaped origami (Figure 5-18c) and a singly curved surface or cylindrical origami (Figure 5-18d).

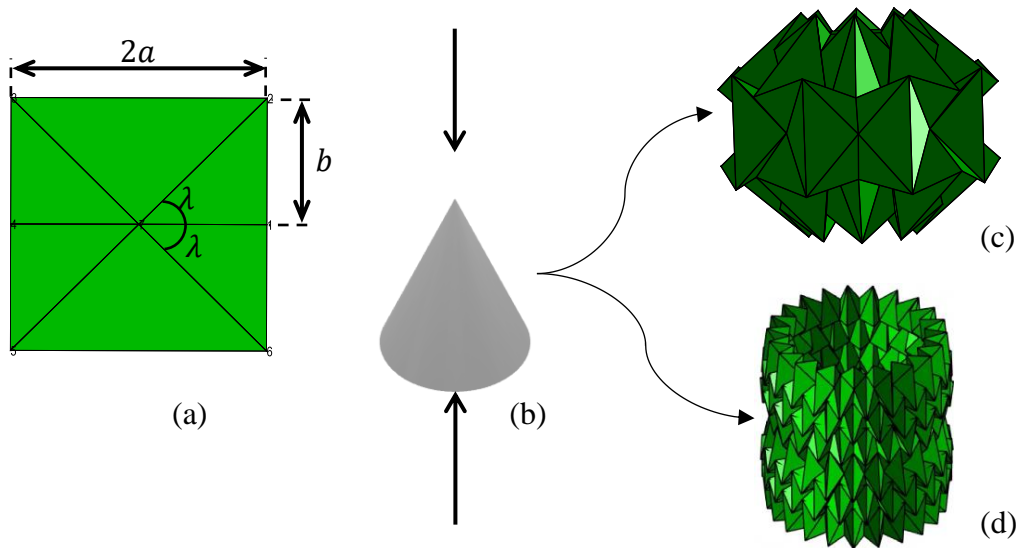


Figure 5-18: Waterbomb pattern and natural way of folding. (a) 6-creased waterbomb unitary cell; (b) Illustration of the geometric relationship between natural force and waterbomb fold pattern; (c) Illustration of a closed waterbomb tessellation with a double-curved surface; (d) Illustration of a closed waterbomb tessellation with a single-curved surface.

From this point on, the closed tessellation is defined by a $m \times n$ configuration, where m is the number of lines and n is the number of cells on each line (Figure 5-19). It is clear from the previous analysis that the waterbomb tessellation has a considerably large number of Degrees of Freedom (DoFs), even if reduced on a closed tessellation. Aiming to reduce the number of DoFs and still be able to capture local asymmetric behaviors, the analyses are performed considering a symmetric distribution on external loadings. Therefore, a longitudinal symmetry is placed on the unitary cells' vertex, such

that the radius of each line measured from the tessellation axis to each cell vertex (point O) is the same between lines and within the same line.

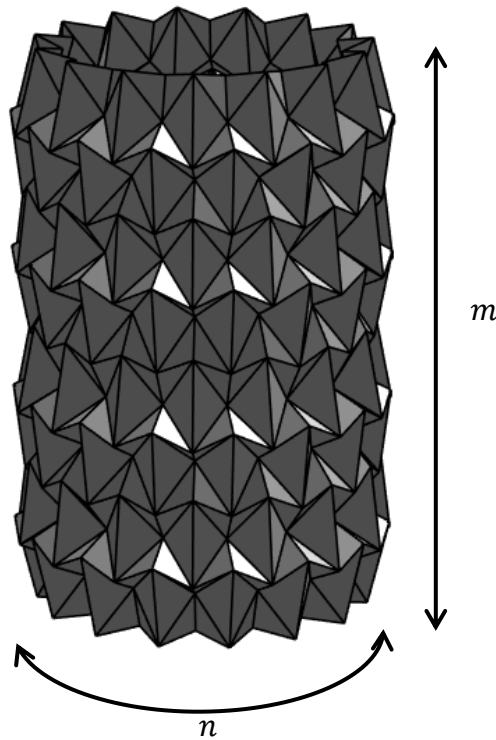


Figure 5-19: Closed waterbomb tessellation generated with the 6 creased waterbomb unit cell. The tessellation is defined by the number of lines (m) and the number of cells on each line (n).

Initially, the general motion of the closed tessellation is evaluated. A 3×6 closed tessellation starts in an unfolded configuration and its folding process is represented in Figure 5-20, with panels highlighted in the time evolution of the load factor λ . The first thing that is noticeable is a strangulation effect due to the natural force or natural way of folding of this closed tessellation (Figure 5-18-b). The middle line starts the folding process, increasing λ substantially between time 10 and 26. It reaches a peak and drops when the middle line stops folding and the remaining lines start the folding process, reaching its bottom around time 52. With all creases activated, the remaining lines continue their folding process until the middle line starts to fold again. At this point, the load factor reaches a near zero value and the whole tessellation folds homogeneously, with barely any resistance. It is interesting to notice that in this case the larger radius of

the folded structure is the same of the unfolded one, as can be seen in Figure 5-21, and the structure presents only a reduction on its height.

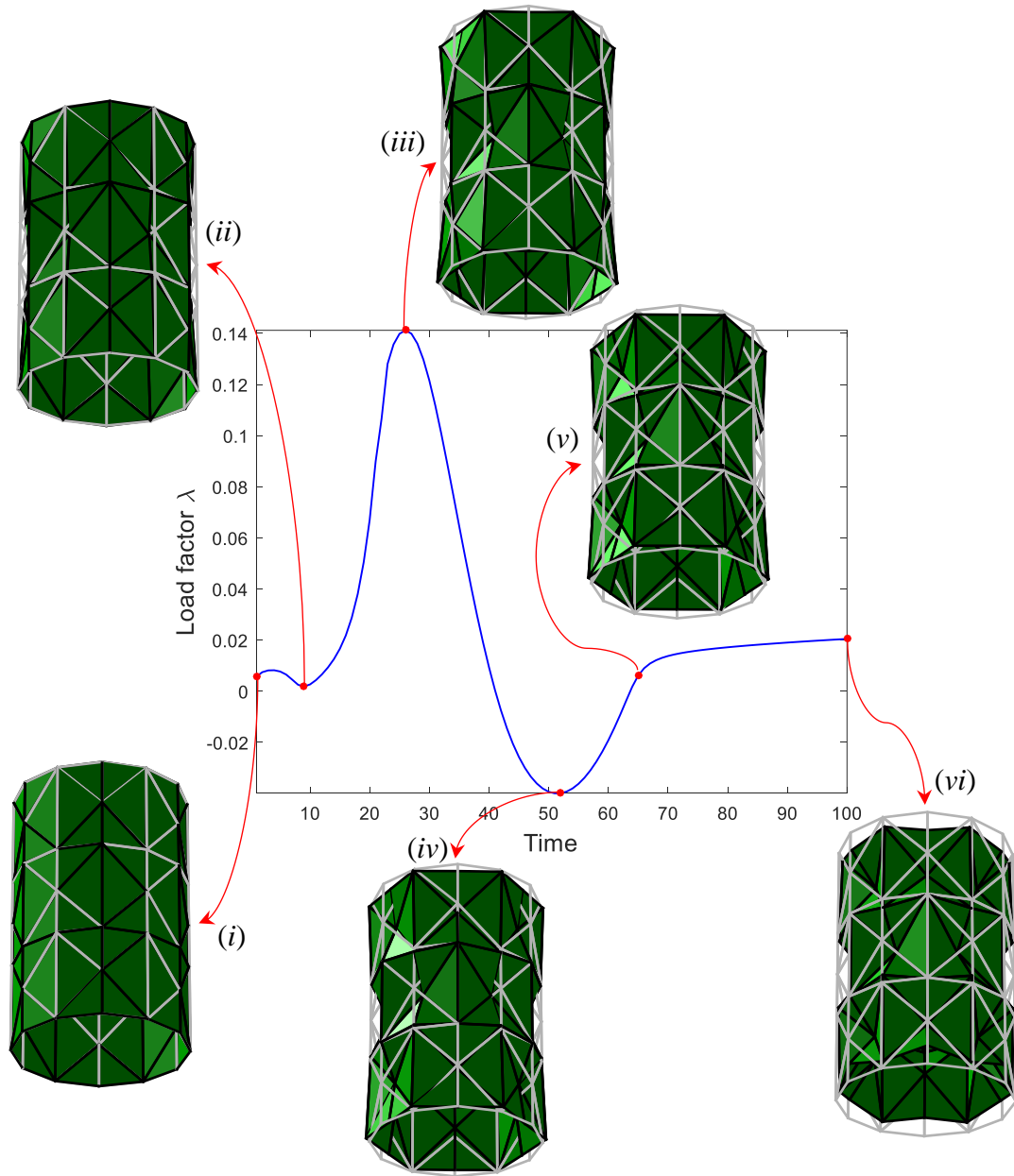


Figure 5-20: Load factor λ evolution during the symmetric folding process of a closed 3×6 waterbomb tessellation. The panels (i) to (vi) show, sequentially, a closer look into the origami configuration for each remarkable variation in the load factor evolution.

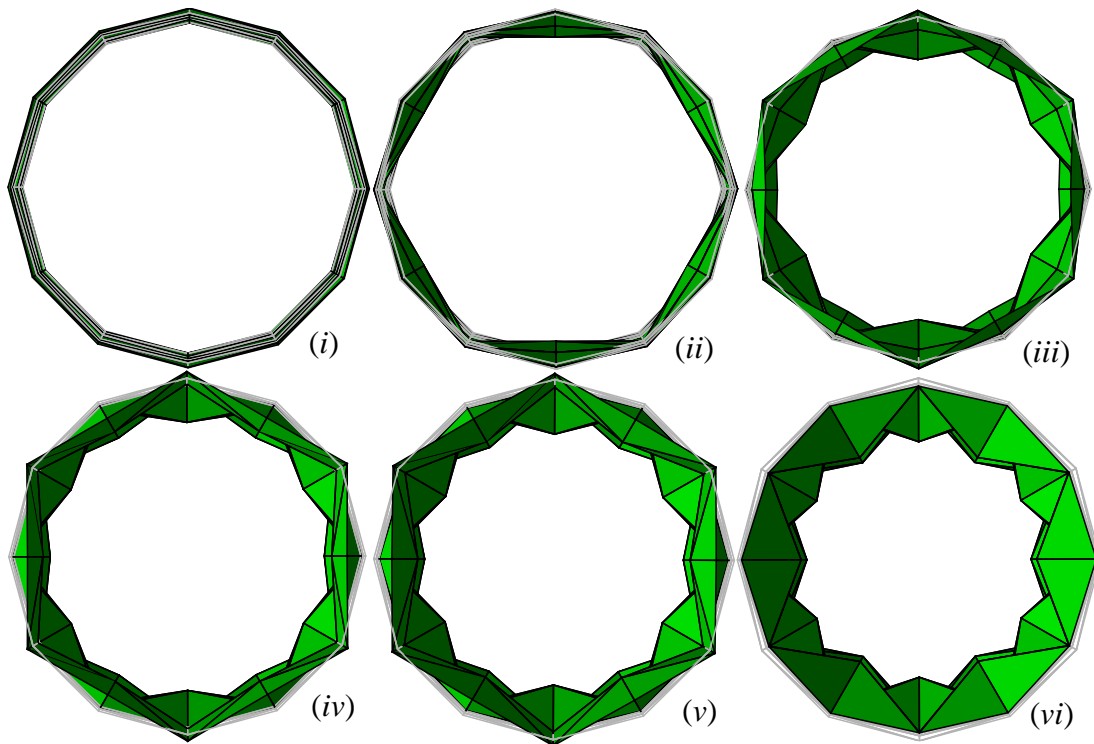


Figure 5-21: Top view of the closed waterbomb tessellation during the folding process. On each view from (i) to (vi), the gray line represents the initial configuration, and the green panels are the tessellation.

In sequence, some analyses are performed on the $m \times n$ tessellation, aiming to evaluate both behaviors seen in Figure 5-18. All analyses are performed according to a symmetric actuation, where each cell is pulled radially through its middle vertex.

Initially, an analysis is performed on the tessellation according to Figure 5-18-d behavior. The first study evaluates the influence of the number of lines (m) and, for this case, it is considered a tessellation with $n = 6$ cells on each line. The second study evaluates the influence of the number of cells on each line (n) and, for this case, two tessellations are considered: one with $m = 5$ lines and one with $m = 6$ lines.

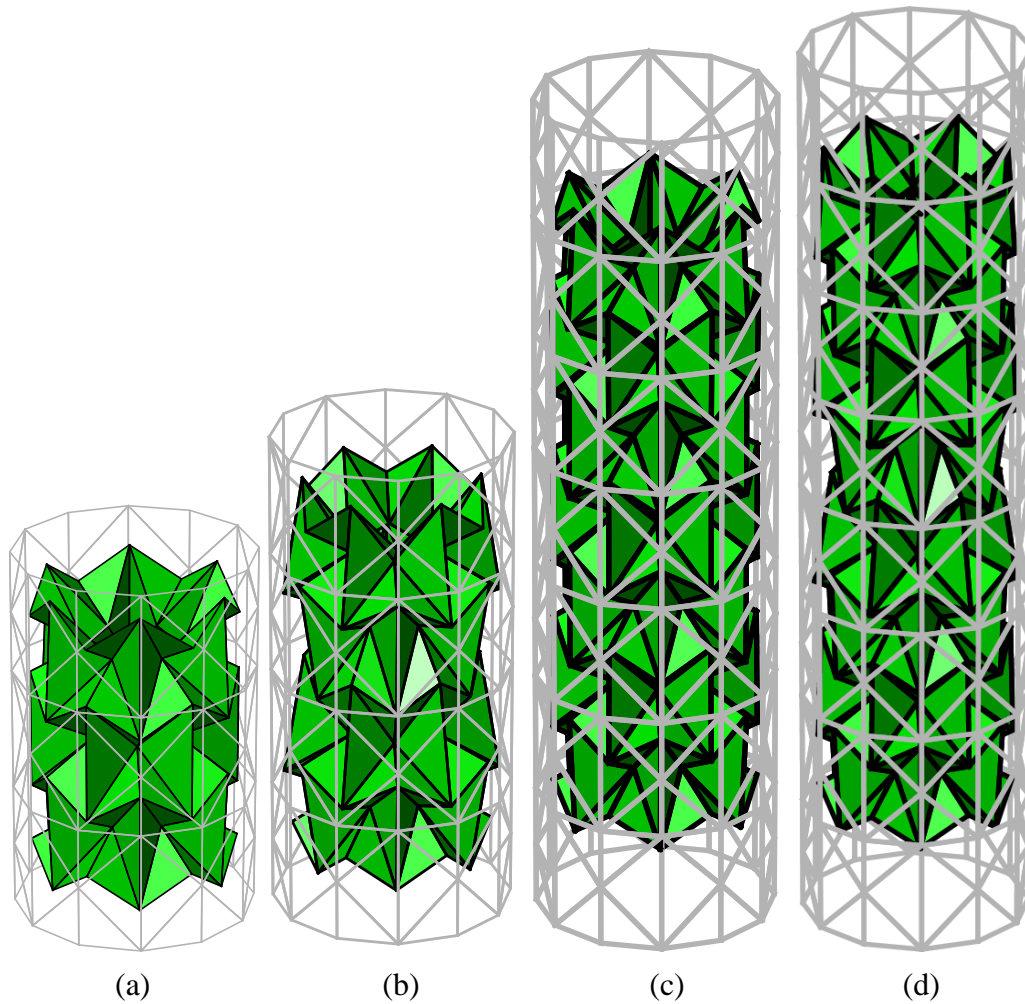


Figure 5-22: Closed waterbomb tessellation formed by m lines, with each line composed by $n=6$ squared cells. (a) $m=3$; (b) $m=4$; (c) $m=7$; (d) $m=8$.

In order to evaluate the influence of the number of lines (m), four tessellations formed by waterbomb unit cells on each line are of concern, varying the numbers of lines (Figure 5-22): $m = 3$ lines (Figure 5-22-a); $m = 4$ lines (Figure 5-22-b); $m = 7$ lines (Figure 5-22-c) and $m = 8$ lines (Figure 5-22-d). For all tessellations, the initial configuration is the opened one (gray color) and each line is formed by $n = 6$ waterbomb unit cells. The purpose of these simulations is to evaluate the behavior of each individual waterbomb when the structure is folded in a symmetric way, looking for similarities between the behavior of the waterbomb cells. To visualize any local asymmetry, the inner angles are represented according to at least one of the previous cases: Π_1 , Π_2 and Π_3 .

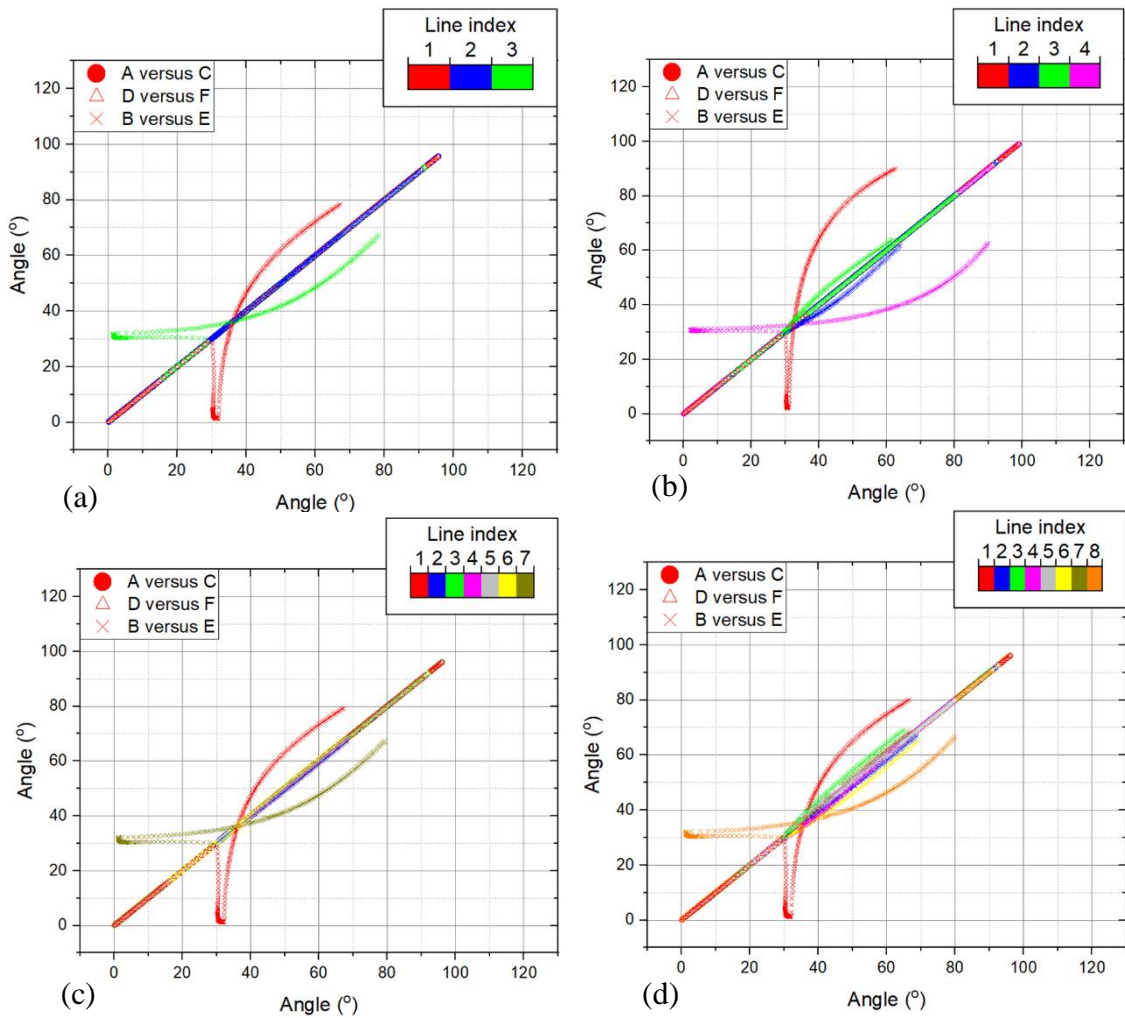


Figure 5-23: Relation between the inner angles of each one of the $6m$ cells of the tessellation, where m is the number of lines of that tessellation. (a) Relation for the case $m = 3$; (b) Relation for the case $m = 4$; (c) Relation for the case $m = 7$; and (d) Relation for the case $m = 8$. For all four cases, the bisector line represents the symmetric behavior (case Π_3).

This first set of simulations is represented in Figure 5-23, by a relation between the inner angles of each one of the cells. The inner angles are represented according to the relation of Π_2 . Therefore, they are plotted as: A versus C , D versus F and B versus E , where the bisector line represents the symmetric case (Π_3). Figure 5-24 shows, respectively, the inner angle relation for the tessellation with $m = 3$ lines (Figure 5-24-a), $m = 4$ lines (Figure 5-24-b), $m = 7$ lines (Figure 5-24-c) and $m = 8$ lines (Figure 5-24-d).

Two major observations can be made about these cases. The first one is related to the influence of the tips or endings in this tessellation. Note that the tessellation studied here has free ends, where at least 6 vertexes on the top (related to vertex E) and at least 6 vertexes on the bottom (related to vertex B) are not restrained in any way, and an inversion of crease type (from mountain to valley fold) might occur freely. Besides, these free endings result in additional degrees of freedom for the structure, even when a controlled symmetric folding process is performed. The ending influence can be seen on all four graphs by the deviance of both vertexes B and E from the symmetric condition (case Π_3). Note that for all four cases, the first and the last lines, associated to the bottom and the top of the tessellation, behave according to case Π_2 , while the lines contained within the first and the last one tends to behave according to Π_3 . This analysis comes from the observation of the points outside the bisector line.

The second observation is related to the influence of the number of lines in the structure behavior. Specifically, the waterbomb cell in the tessellation with an odd number of lines (Figure 5-22-a and Figure 5-22-c) presents a plane-symmetric behavior (according to case Π_2) for all cells on the first and last lines (Figure 5-23-a and Figure 5-23-c), while it presents a symmetric behavior (case Π_3) for the remaining lines. In the other hand, the waterbomb in the tessellation with an even number of lines (Figure 5-22-b and Figure 5-22-d) tends to behave in a plane-symmetric condition (according to case Π_2), with a more prominent plane-symmetry occurring on the external lines (first and last one) and a more prominent symmetry occurring on the other lines (Figure 5-23-b and Figure 5-23-d).

The second study evaluates the influence of the number of cells on each line on the structure behavior during the folding process. For this study, a series of tessellations are considered, going from 6 cells per line until 22 cells per line. As observed in Figure 5-23-a to Figure 5-23-d, the major deviance occurs on the first and last lines, due to the effect of the endings. However, we are not focused on this point in the effect of the endings, but on the influence of the number of cells on the symmetric behavior of the inner lines. Therefore, we will focus on the line that presents the major deviance from the symmetric behavior (case Π_3) for each simulation, disregarding the first and the last lines (ending effect). In addition, it should be pointed out that there is a point for each simulation where this deviance reaches its maximum value, as can be seen in Figure 5-23-a to Figure 5-23-d. Figure 5-24 brings the maximum deviance observed for each case,

going from $n = 6$ to $n = 22$. Figure 5-24-a shows this evaluation for a tessellation with an odd number of lines ($m = 5$ lines), while Figure 5-24-b shows the deviance for a tessellation with an even number of lines ($m = 6$ lines). The deviance is evaluated as the absolute difference between the angles of a cell on the line j and a cell on the line $m/2$, for the tessellation with an even number of lines, and on the line $(m + 1)/2$, for the tessellation with an odd number of lines.

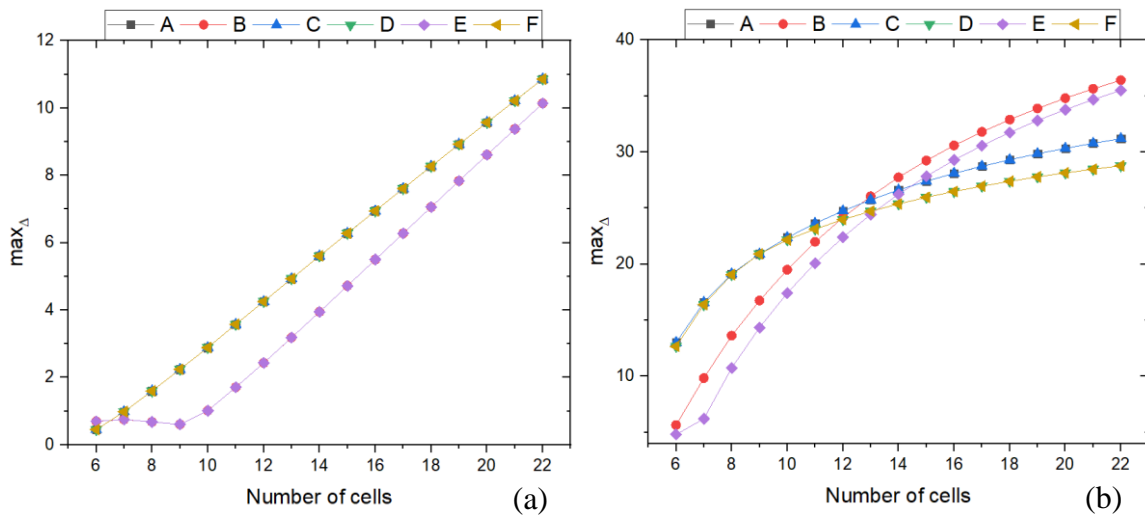


Figure 5-24: Maximum deviation of each inner angle with the increasing of the number of cells per line, considering a tessellation with m lines. (a) Maximum deviation for a tessellation with an odd number of lines, with $m = 5$; (b) Maximum deviation for a tessellation with an even number of lines, with $m = 6$.

It is noticeable that the tessellation with an odd number of cells (Figure 5-24-a) presents a maximum absolute deviance that tends to grow linearly with the increasing of the number of cells per line (increase of n). Besides, all cells outside the central line $(m + 1)/2$ behave according to the Π_2 plan-symmetric case. It is also noticeable that for a tessellation with up to 10 cells per line, the maximum deviance observed is around 1° . The combined result from simulation presented at Figure 5-23-a and Figure 5-23-c and the simulation presented at Figure 5-24-a indicates that, for a tessellation with an odd number of lines and a maximum of 10 cells per line, a simplified model describing the unitary cell behavior, such as the trigonometric formulation, can be extrapolated as a

representative of the structure behavior, and the influence of the endings is contained within the cells from the first and the last line. In addition, a tessellation with an even number of cells per line (Figure 5-24-b) presents a significant deviance from the symmetric behavior (case Π_3). In opposition to the result presented at Figure 5-24-a, Figure 5-24-b indicates a smoother increasing on the maximum deviance. Besides, the increase of the number of cells causes the loss of the circumferential symmetry.

The natural force (Figure 5-18-b) associated with the folding process of the closed tessellation evaluated in Figure 5-24 tends to generate a ball-shaped origami, where the middle lines tend to present a symmetric behavior, and the endings tend to be asymmetric. On the other hand, if this natural force (Figure 5-18-b) tends to generate a cylindrical-like origami, a different behavior is observed, where the middle lines tend to present an asymmetric behavior and the endings tend to have a symmetric behavior.

The folding process of a cylindrical-like origami is shown in Figure 5-25. The structure presents a motion that can be translated as a circumferential reduction, followed by an axial compression, a strangulation, and an axial relaxation. This motion sequence is presented at Figure 5-25-a, for a tessellation with $m = 5$ lines, and at Figure 5-25-b, for a tessellation with $m = 6$ lines. Note that the strangulation is more prominent on the tessellation with an even number of lines (Figure 5-25-b).

The strangulation effect is further explored by considering an index, Δ , expressed by the difference between the tessellation radius measured from the middle axis to the vertex B of a cell in the middle line, and the tessellation radius measured from the tessellation axis to the vertex B of a cell in the first line. Thus, $\Delta=1$ means that the tessellation does not present a strangulation, having a cylindrical surface (zero Gaussian curvature). On the other hand, $\Delta \neq 1$ means that the tessellation presents a strangulation that can be a positive Gaussian curvature ($\Delta > 1$) or a negative Gaussian curvature ($\Delta < 1$). It is important to notice that closed waterbomb tessellations with an even number of lines always presents a negative Gaussian curvature under symmetrical actuation, which is an important consideration when designing closed waterbomb tessellations.

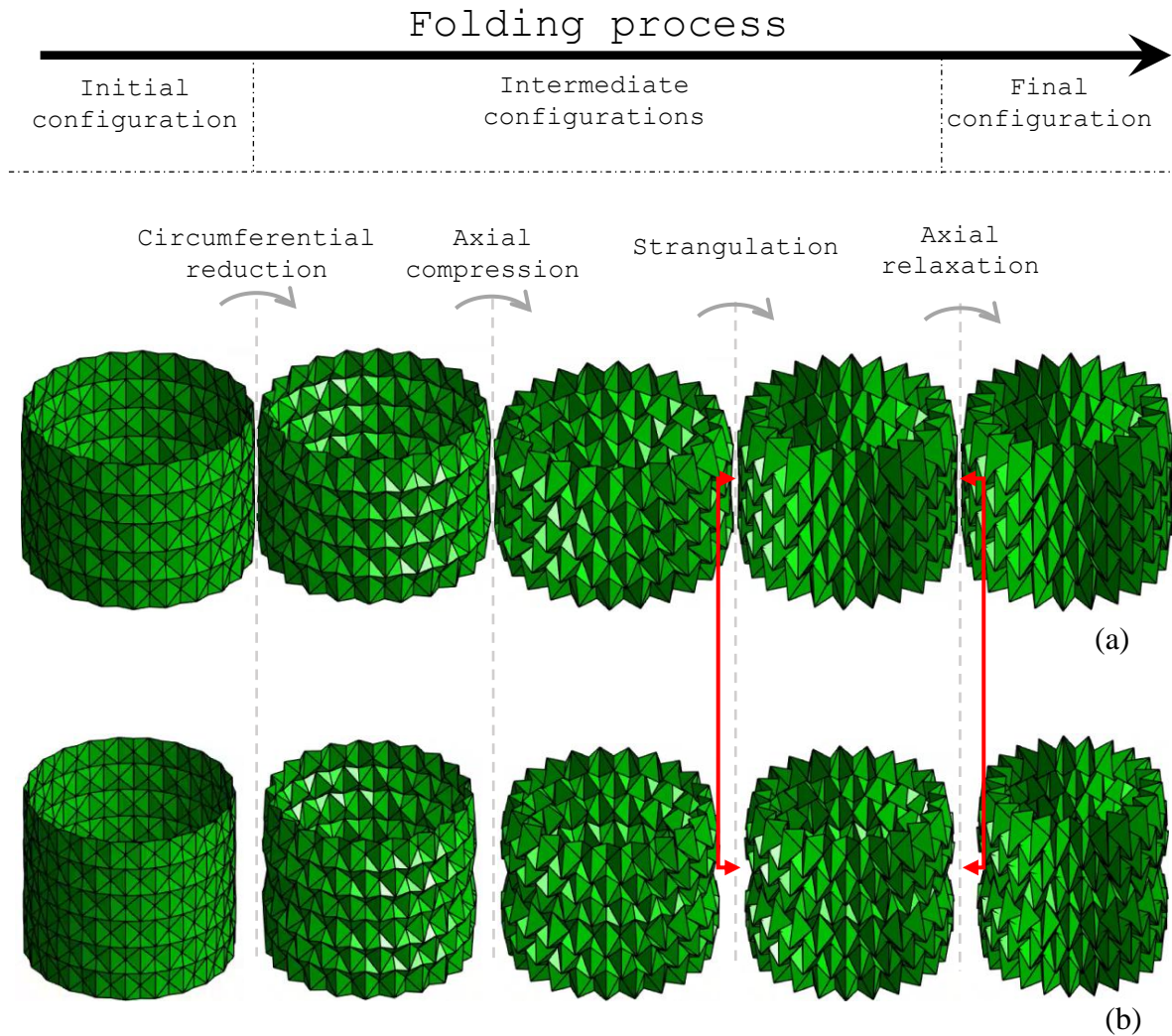


Figure 5-25: Folding process of a tessellation with $m = 5$ lines (a) and $m = 6$ lines (b), with each remarkable phase highlighted. The strangulation that happens in the middle of the tessellation is highlighted by red arrows.

Figure 5-26 presents the relation between the number of origami lines (m) and its even/odd parity with the prominence of the strangulation effect. Origamis with an odd parity present a small strangulation, with a variation of ± 0.025 ($0.975 < \Delta < 1.025$). On the other hand, origamis with an even parity present a significant strangulation, with variations almost 10 times higher than origamis with odd parity ($0.80 < \Delta < 0.975$).

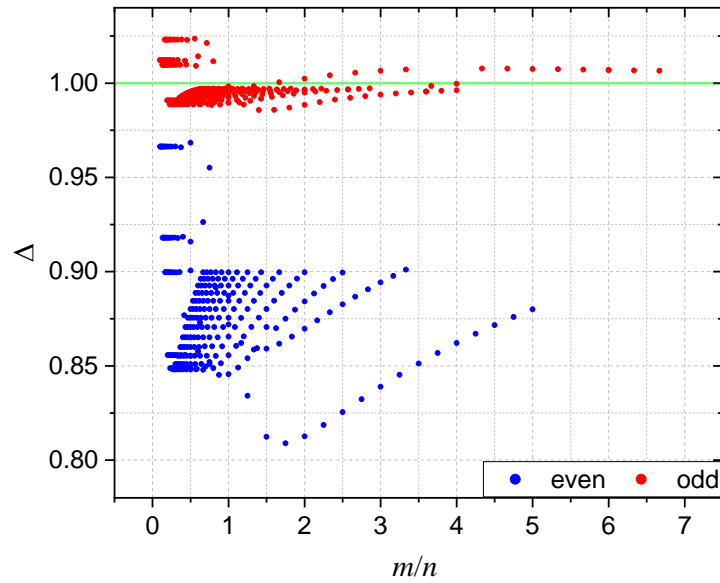


Figure 5-26: Strangulation (Δ) evaluation for an even and an odd tessellation, as a function of the ratio between the number of cells on each line (n) and the number of lines (m).

Figure 5-27 presents the influence of the number of cells on each line (n) on the strangulation (Δ), for both even and odd closed waterbomb tessellations. Figure 5-27 also brings the information regarding the influence of the number of lines (m). The first important thing to notice is that the parity of lines (m odd or even) of the tessellation seems to be more expressive in the strangulation than the number of lines itself (m). For a fixed number of cells on each line (n), the tessellation with an even number of lines (m) always presents a negative Gaussian curvature. Besides, the increase of the number of lines (m) does not have an expressive influence on the strangulation effect (Δ), apart from the increasing from $m=3$ to $m=5$ that stands out. A similar analysis is made on the tessellation with an odd number of lines, where the increase of the number of lines slightly changes the curvature of the outer surface of the closed waterbomb tessellation, varying between positive ($\Delta > 1$) and negative ($\Delta < 1$) Gaussian curvature. The increase of the number of lines in cases where $m < 6$ can be an improvement for applications such as stents, since a positive Gaussian curvature surface does not present a gap. Cases where $m \geq 6$, however, tends to generate an unfolded closed waterbomb tessellation with a negative Gaussian curvature, which generates the gap on the middle line. The increase of the number of cells on each line (n) does not present a significant influence on the tessellation with an odd number of lines for cases where $n > 5$. Nevertheless, the number

of cells on each line (n) significantly influences the strangulation effect (Δ), reducing its expressivity with the increasing on the number of lines (m).

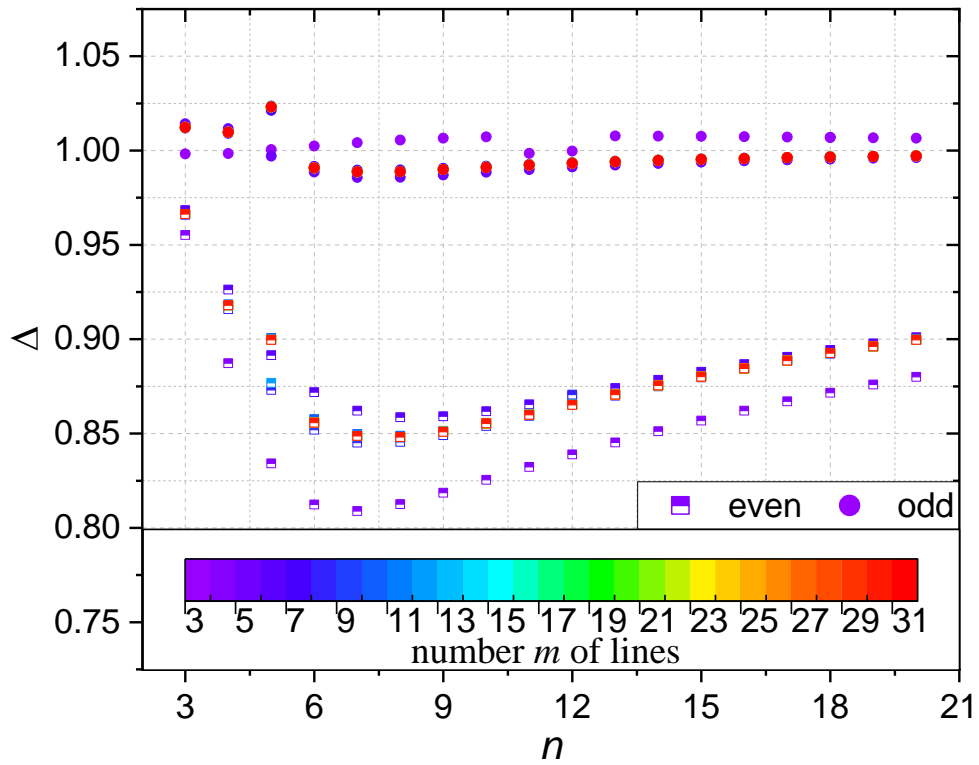


Figure 5-27: Strangulation (Δ) evaluation for both even and odd tessellations as a function of the number cells on each line (n), with a color map on the number of lines (m).

6 Origami-Wheel

This chapter presents a study of the modified waterbomb closed tessellation, evaluating the general behavior and the influence of the modification on the structure's folding process. The chapter starts with an evaluation of the modified closed tessellation compared to the closed tessellation explored in Section 5.3; it is followed by an analysis on the folding process of the origami-wheel and explore symmetric behaviors. At the end, a reduced-order model is presented for the symmetric case.

6.1. Mechanical evaluation of the origami-wheel

It is known that the natural force (Figure 5-18-b) associated with the folding process of the waterbomb closed tessellation can produce a strangulation on the structure, changing its original outer surface Gaussian curvature. When a strangulation effect is present, the tessellation outer surface changes from cylindrical (zero Gaussian curvature, $\Delta=1$) to either double-curved (negative Gaussian curvature, $\Delta<1$) or single-curved (positive Gaussian curvature, $\Delta>1$). Besides, tessellations with an odd parity tend to present a small local asymmetry or strangulation on both double-curved and single-curved surfaces, as seen on Figure 5-24 and Figure 5-26. Therefore, a tessellation with an odd parity is of interest.

The application of a closed waterbomb tessellation as a deformable wheel, as studied here, requires the shape changing from a cylindrical-like structure ($\Delta=1$) to a single-curved structure surface ($\Delta>1$). One way to ensure that the folding/unfolding process will lead exclusively to a positive Gaussian curvature surface is to constrain the endings, removing the additional Degrees of Freedom (DoFs). One interesting modification that produces the desired effect was introduced by Lee *et al.* (2013), by

creating an origami-based ending that couples the additional Degrees of Freedom by removing their radial variation. Such variation corresponds to including a set of folds on the structure shown in Figure 5-6 such that, once folded, the added tips are glued together. Figure 6-1 shows the 3×8 waterbomb tessellation with the added tips.

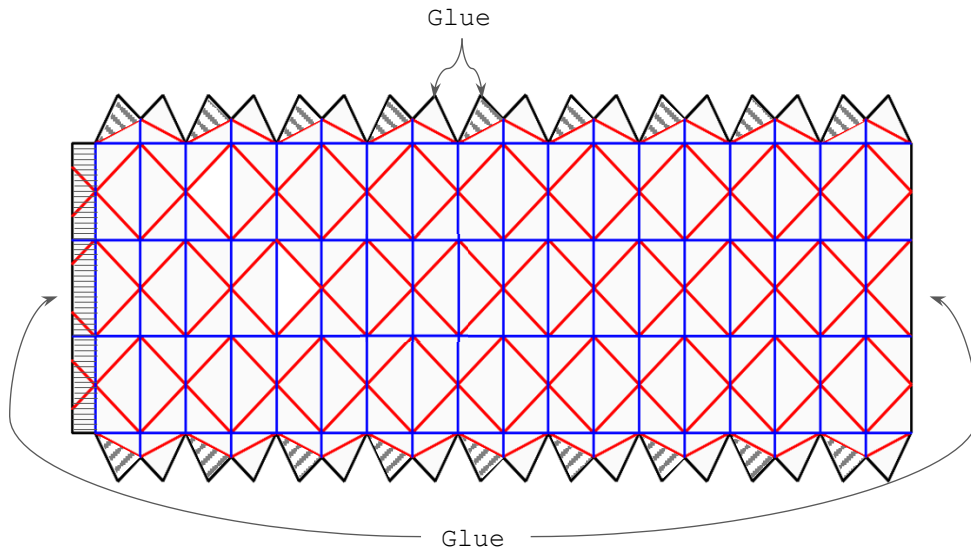


Figure 6-1: Representation of an opened waterbomb tessellation in an opened configuration, showing the colored-defined folds (mountain in blue and valley in red). The inserted tips are also present, with a dashed mark for regions that will be glued.

This modification produces a significant influence on the structure behavior regarding the shape changing and the controllability of the process. The major contribution relies on the constraint of the additional Degrees of Freedom (DoFs) associated to the first and last rows. Even more than that, the modification restricts the motion of the cells on first and last rows to a behavior according to Π_2 plane-symmetry case. Aiming to evaluate and better visualize the influence of this modification, a 3×8 closed waterbomb tessellation is subjected to a folding process with and without the modification.

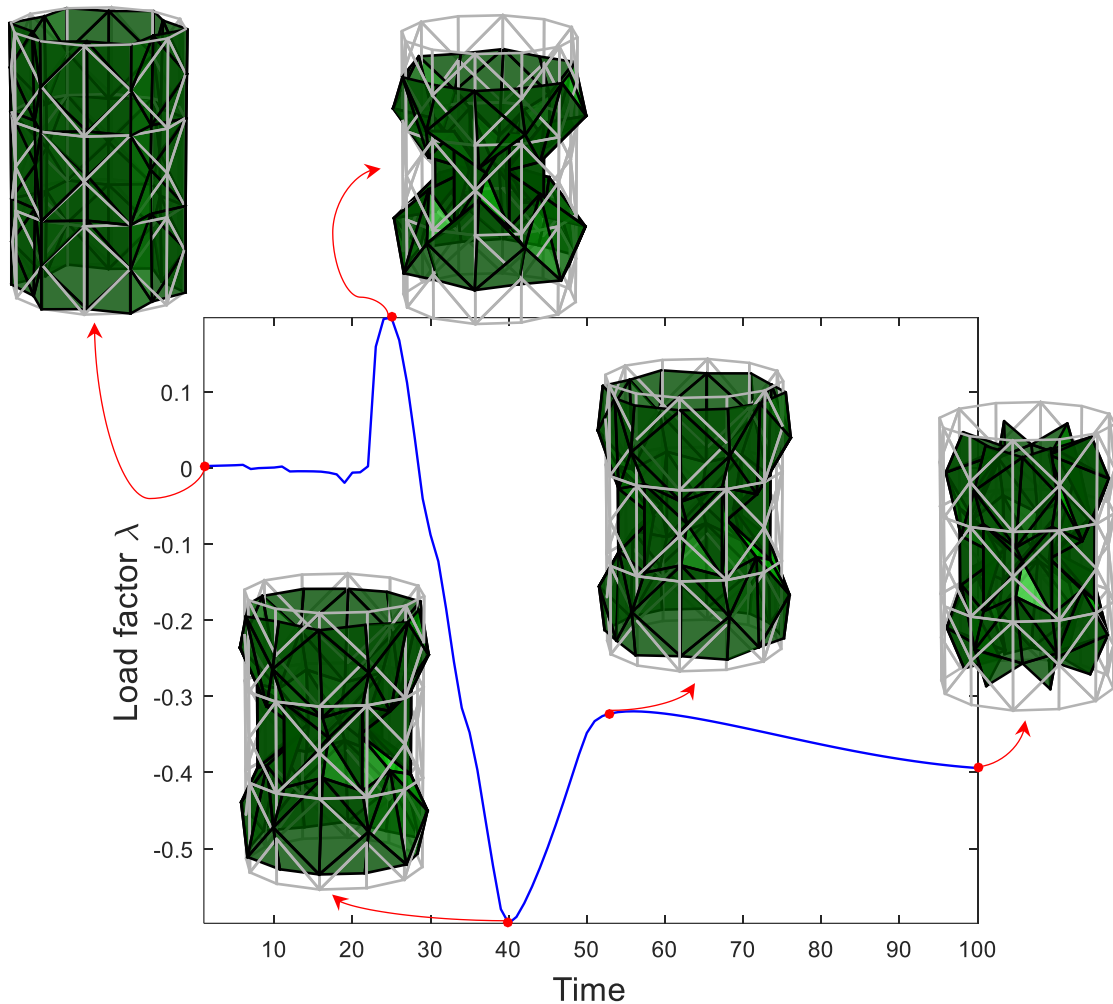


Figure 6-2: Folding process of a 3×8 closed waterbomb tessellation starting in an unfolded configuration and reaching a half-folded configuration.

Since the inclusion of said modification allows a reduced number of Degrees of Freedom (DoFs), the simulations presented here have a smaller number of inputs. Looking for a symmetric or quasi-symmetric behavior, the external load is applied to the middle row by pulling the vertex (point O) on each unit cell. Firstly, the tessellation without the modification is subjected to a closing process, starting from an opened cylindrical-like configuration (Figure 6-2). It is possible to see the strangulation happening along the entire folding process with a substantial variation on the load factor. There is a peak near time 25 that corresponds to the folding of the middle row, along with an axial contraction. Then, there is an axial expansion followed by the folding process of the first and last rows. The final configuration corresponds to a double-curved surface

structure. The modification forces the tessellation to fold presenting a single-curved surface during the entire process, without the presence of a strangulation (Figure 6-3).

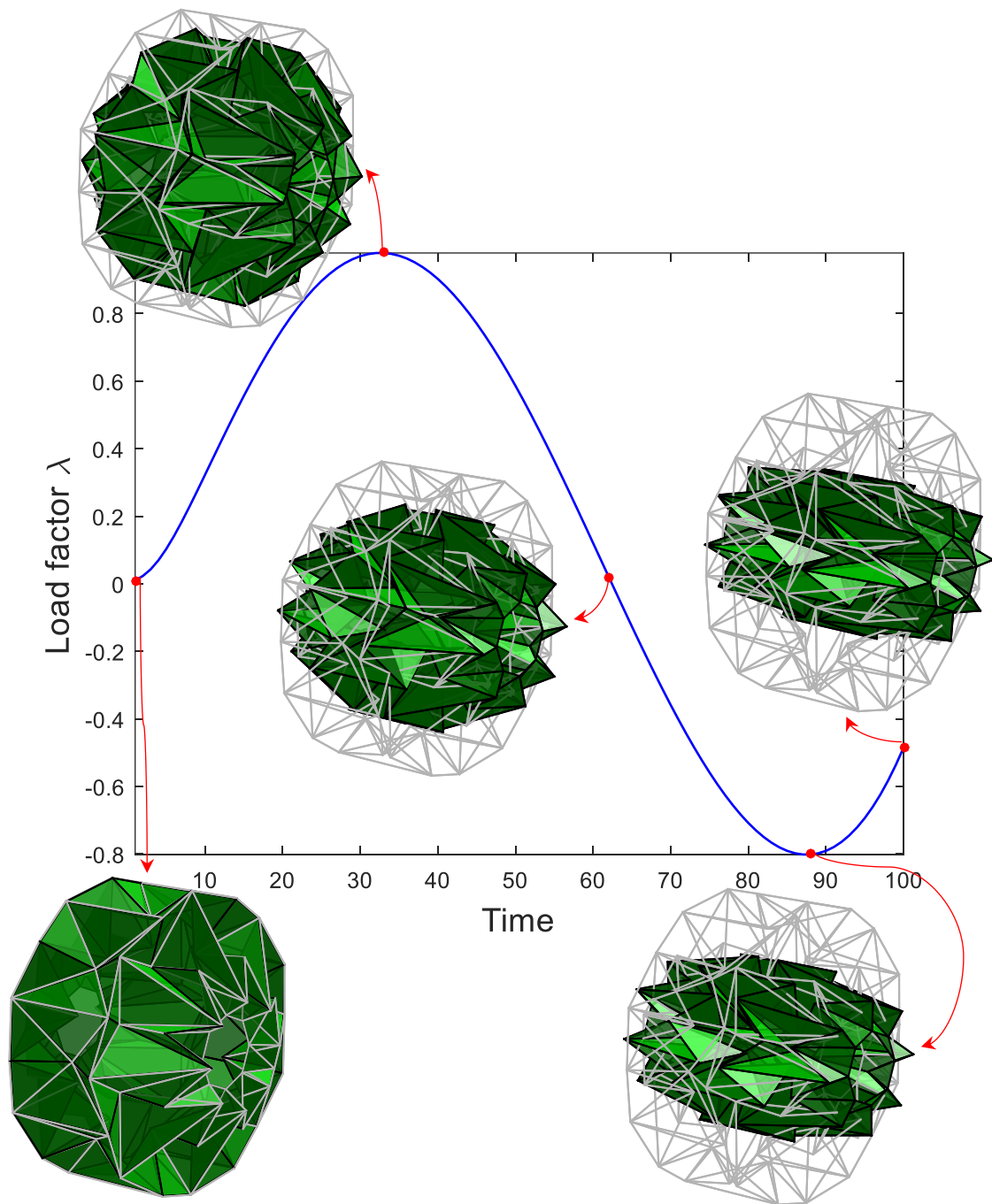


Figure 6-3: Folding process of a 3×8 modified closed waterbomb tessellation starting in an unfolded configuration and reaching a half-folded configuration.

This single-curved surface is also present during the unfolding process of the closed waterbomb tessellation with the modified endings (Figure 6-4).

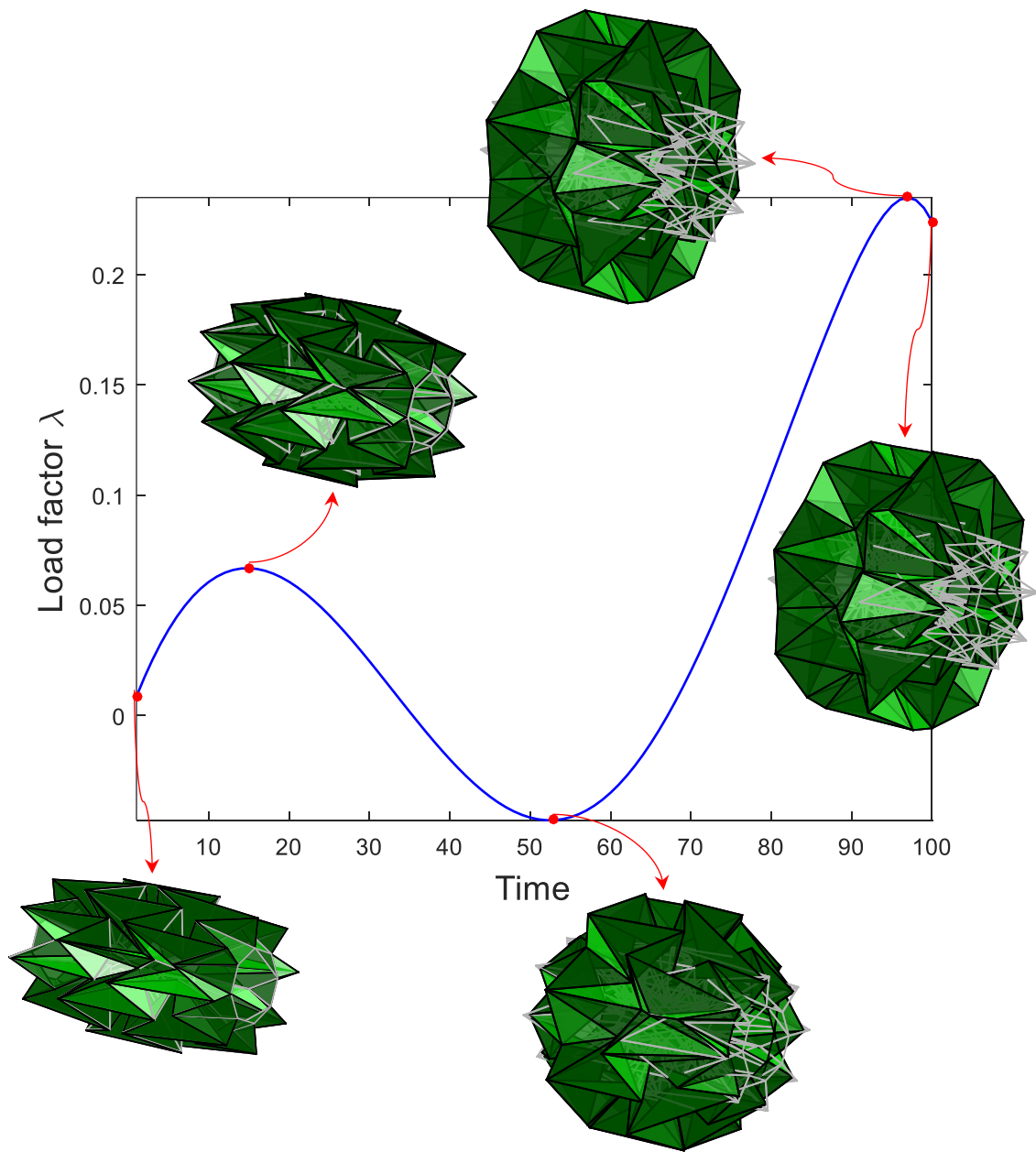


Figure 6-4: Unfolding process of a 3×8 modified closed waterbomb tessellation starting as a half-folded configuration and reaching an unfolded configuration.

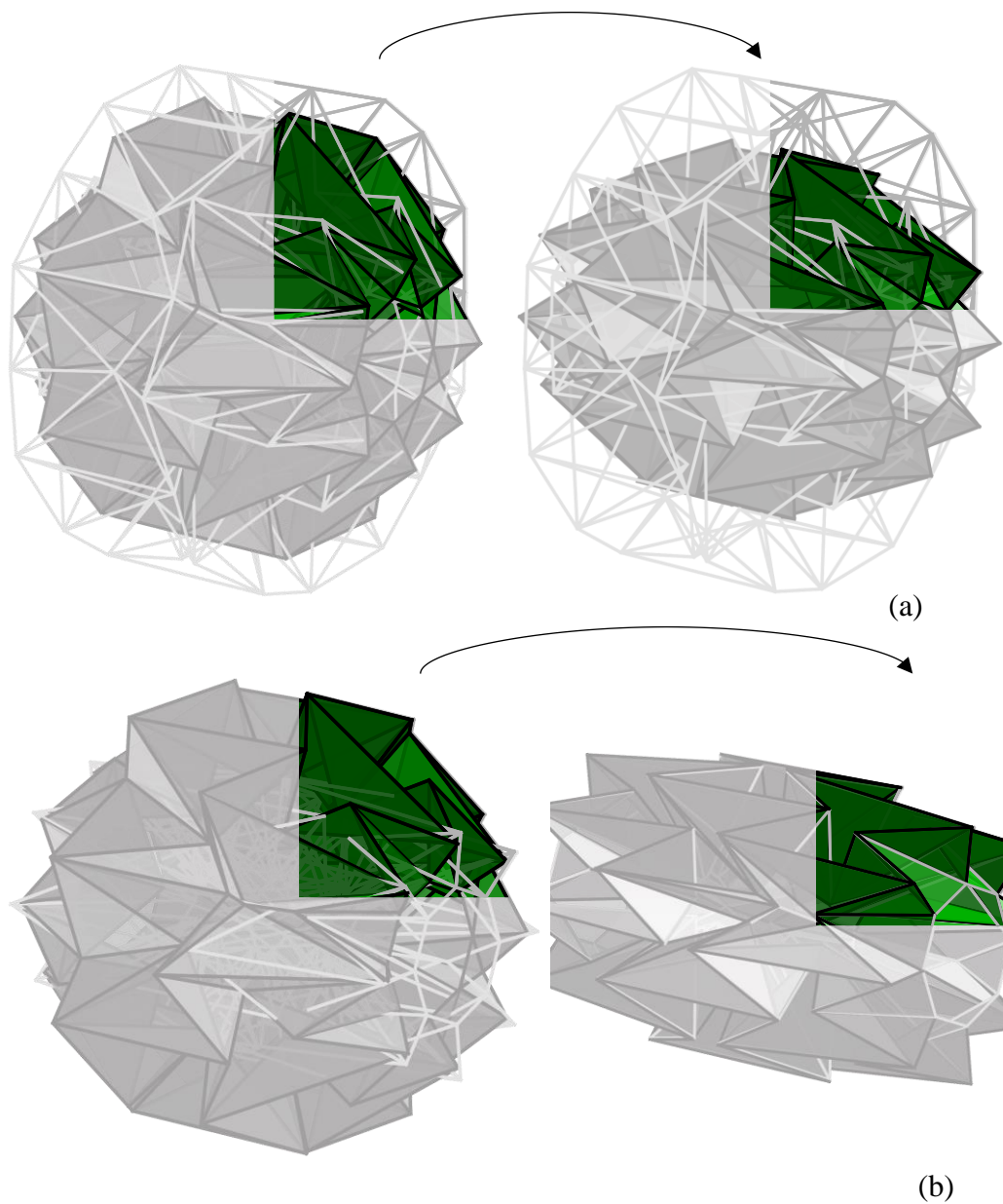


Figure 6-5: Highlight of one cell of an odd parity line for the modified closed waterbomb tessellation. (a) Pop-in behavior happening during the folding process; (b) Pop-out behavior happening during the unfolding process.

It is possible to notice that, during the folding process, the load factor decreases considerably once the unit cells on both endings of the waterbomb tessellation (lines with an odd parity) ‘pop in’. This situation happens around time 32 (Figure 6-3). Similarly, the load factor for the unfolding process increases considerably while both endings of the waterbomb tessellation (lines with an odd parity) ‘pop out’, which happens around time 53 (Figure 6-4). This behavior differs from the previous one observed for the closed

tessellation without the ending modification (Figure 6-2), where the peak on the load factor is due to the folding of the middle line (even parity line).

Another interesting observation is that the tessellation requires a larger force for the folding motion (closing it) than it requires for the unfolding motion (opening it), as can be seen by the difference in the maximum load factor, which influences the proper design of the actuators, avoiding under or oversizing.

The chosen actuation evaluated in this work is a BIAS system, composed at least by one Shape Memory Alloy (SMA) as an active actuator. The second component of the BIAS system can be, for example, another SMA with a different transformation critical temperature and stress. Another possibility for the second component of the BIAS system is a passive component, such as an elastic or super elastic spring. The consideration of the actuation is important at this point because it will influence the origami design, which might result in slight changes to the system behavior.

The case studied further in this work considers an actuation as initially presented by Lee *et al.* (2013), that assumes an elastic passive spring as the second element of the BIAS system. The elastic spring is attached to acrylic plates located at both ends of the closed waterbomb tessellation, and the presence of this additional structure results in interesting modifications to the folding/ unfolding process.

The presence of rigid plates on both endings results in a restriction of motion of the vertices positioned along said endings, keeping the initial distance between them unchanged during the entire folding process. The referred distance is described through a geometric parameter associated with the plate apothem (a_{pth}) and/or its side (l_{pth}). As a reference, assume that each rigid plate is a regular octagon with polar axis of inertia Y and planar axes of inertia X and Z, and Y axis is aligned with the tessellation longitudinal axis (Figure 6-6).

Figure 6-7 shows a first study of the folding process of the closed waterbomb tessellation with rigid endings. In this first study, it is assumed that both rigid plates are stiffer on Z axis than on X axis, which results in an asymmetric distribution of loads. Four cases are evaluated in this first study, being the first one a simulation with the same external load applied on the case of Figure 6-3 and the remaining three cases increases of 10%, 20% and 30% on the external load. The final configuration of each simulation is shown in Figure 6-7-b to Figure 6-7-e for each one of the previously mentioned cases, respectively.

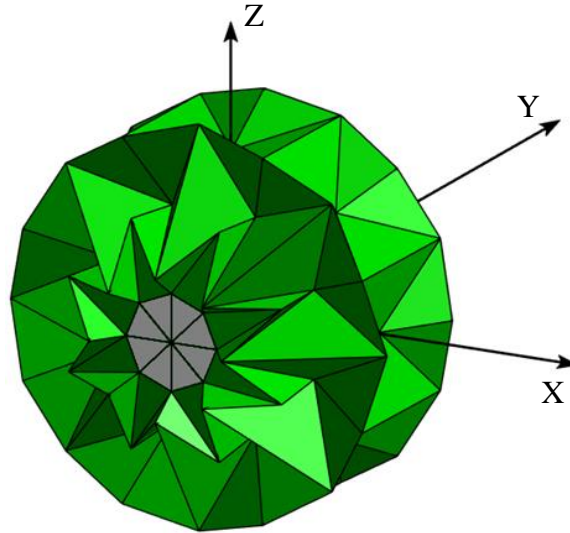


Figure 6-6: Axis definition for the closed waterbomb tessellation, where the longitudinal direction is defined as Y axis. The rigid plate is highlighted in gray.

Note that for all cases there are two slight discontinuances on the load factor curve (indicated on Figure 6-7-a). These discontinuances mark important steps during the folding process of the closed waterbomb tessellation, where a bifurcation on the angle evolution occurs. Until the first bifurcation, the cells contained within the same line behave equally and the origami presents a global symmetry. Cells contained within odd parity lines (lines 1 and 3) behave according to Π_2 plane-symmetry type, and cells contained within even parity lines (line 2) behave symmetrically (Π_3). An asymmetric behavior within each line is observed between the first and the second discontinuances, and this asymmetry is due to the asymmetric stiffness of the rigid endings.

In order to evaluate the plane-symmetry case for each cell, Figure 6-8 shows the relation between angles instead of the angles themselves. As evaluated in section 4.3, Π_2 type cases present the relations $A = C$ and $D = F$, Π_1 type cases present the relations $A = D$ and $C = F$, and Π_3 type cases have the relations $A = C = D = F$ and $B = E$. Figure 6-8 brings the time evolution of the difference between angles A and C (a), between angles A and D (b), between angles C and D (c) and between angles B and E (d), for each cell.

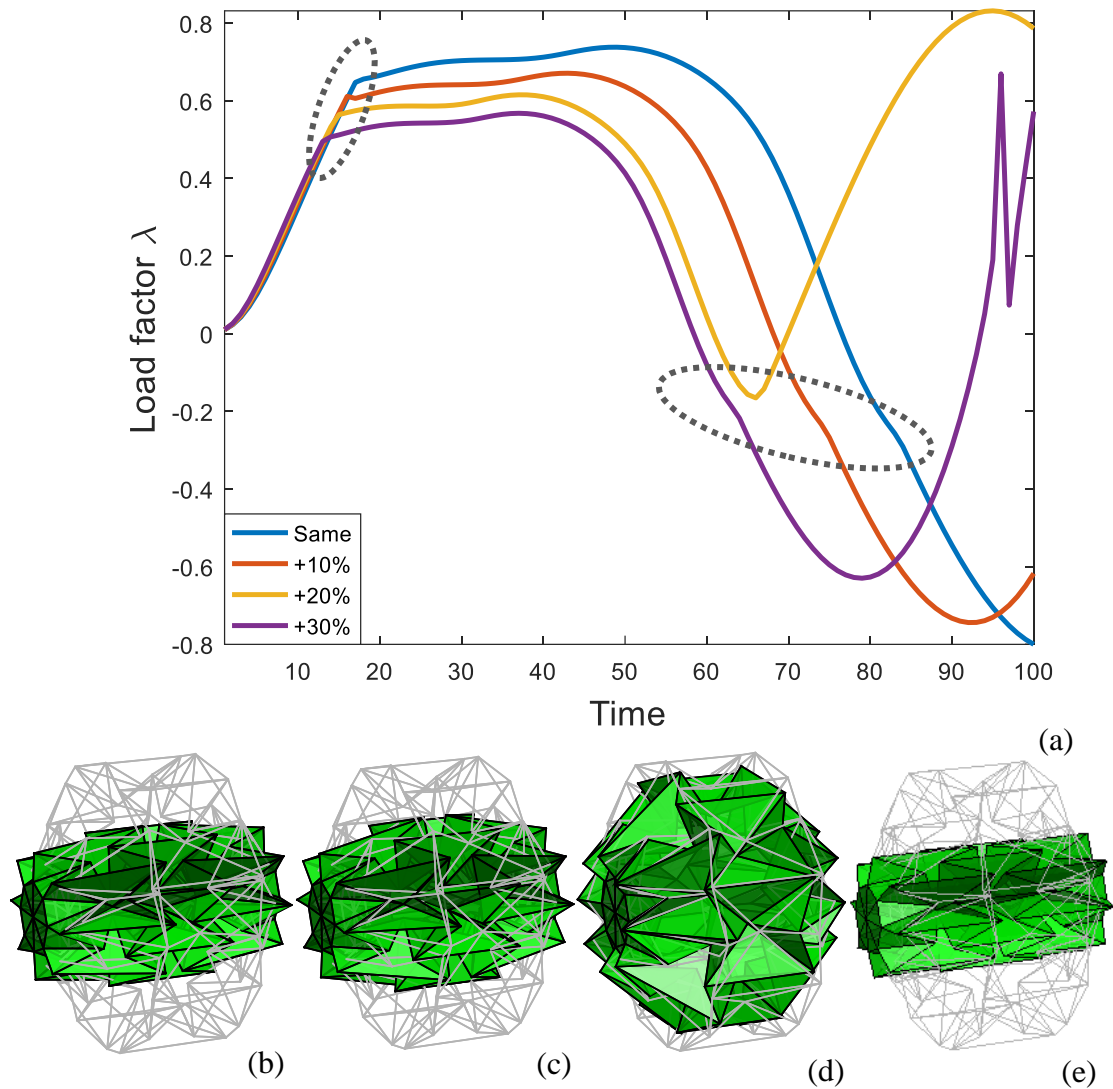


Figure 6-7: Load factor over time for the folding process of the closed waterbomb tessellation with rigid elements on both endings, and final configurations. (a) Time evolution of the Load factor, with a highlight for the bifurcation region; (b) to (e) Final configuration (at time 100) achieved for each case.

It is possible to notice in Figure 6-8 that line 2 behaves symmetrically (according to Π_3 type) for the entire folding process, even with the asymmetry. Outside the bifurcation region, i.e., before the first bifurcation and after the second one, lines 1 and 3 behave according to Π_2 . Inside the bifurcation region, it is possible to observe four curves for each line. Even though there is an asymmetry on the force distribution, there is still a mirrored behavior on the tessellation such that diagonally opposed cells within the same line behave equally. Therefore, each curve in Figure 6-8-a to Figure 6-8-c is

representative of two superposed curves, and each curve in Figure 6-8-d is representative of four superposed curves. Additionally, it is possible to observe a symmetric behavior on each graph in Figure 6-8, either between lines or within the same line.

Note that the existent bifurcation changes the local symmetry but not the global symmetry, which means that outside the bifurcation region, the plane-symmetric behavior of lines 1 and 3 will always be according to Π_3 . The change observed for the case with an increasing of 20% on the external load in Figure 6-7 is not due to a change on the local plane-symmetry, but to a reversal on the folding process, where even though an external load is applied to fold the structure, it unfolds. This change on behavior can be seen in Figure 6-9, where the difference between angles A and D and between angles C and D decreases instead of increasing, and the difference between angles B and E increases, instead of decreasing. Therefore, asymmetric conditions of the folding process might trigger a bi-stability condition.

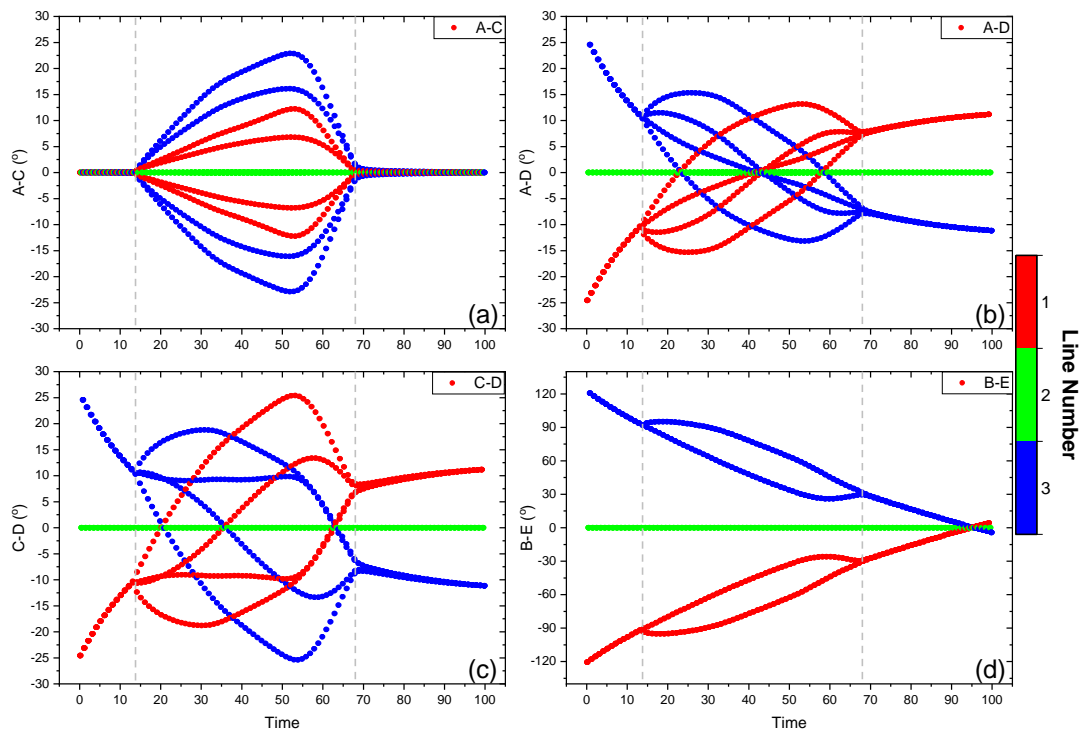


Figure 6-8: Time evolution of inner angles relation for each cell for the case with an increasing of 24% on the external load. From (a) to (d), respectively, the difference between angles A and C, A and D, C and D, and B and E.

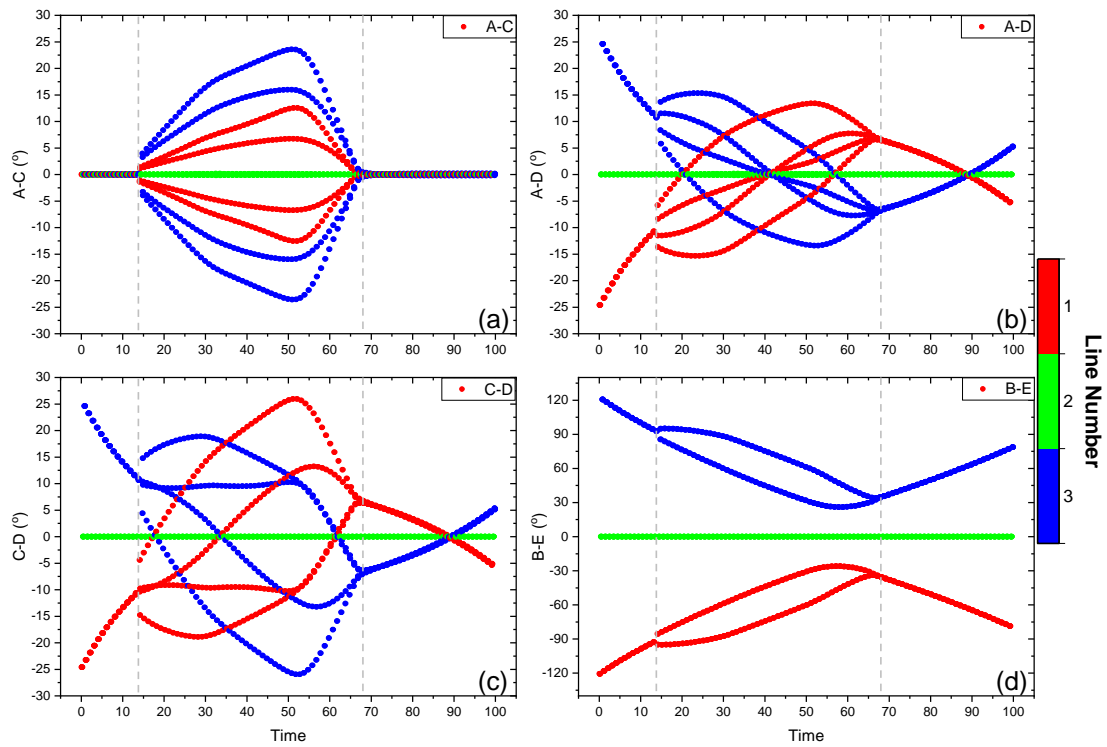


Figure 6-9: Time evolution of inner angles relation for each cell for the case with an increasing of 20% on the external load. From (a) to (d), respectively, the difference between angles A and C, A and D, C and D, and B and E.

Another bi-stability that is observed on the tessellation is the well-known behavior of the waterbomb unit cell of inverting the mountain folds into valley folds, which inactivates the other four existent creases. This behavior is observed in Figure 6-10 under an asymmetric actuation of the closed waterbomb tessellation. For this case, a rigid plate is placed in just one end, that is fixed, while the other end is free. A single cell on the middle row (line 2) is pinched and the load factor evolution is shown in Figure 6-10, with panels representing the structure shape at some instants during the folding process. It is noticeable the natural bi-stable behavior of the waterbomb unit cell at time 30, when one cell ‘pops out’, creating a jump on the load factor curve. This is a rather critical situation for applied origami structures, particularly on dynamical systems, because this snap-through condition or ‘popped out’ configuration is not easily reversible and can be understood as a collapse or failure of the origami structure, since the function for which it was designed is no longer feasible.

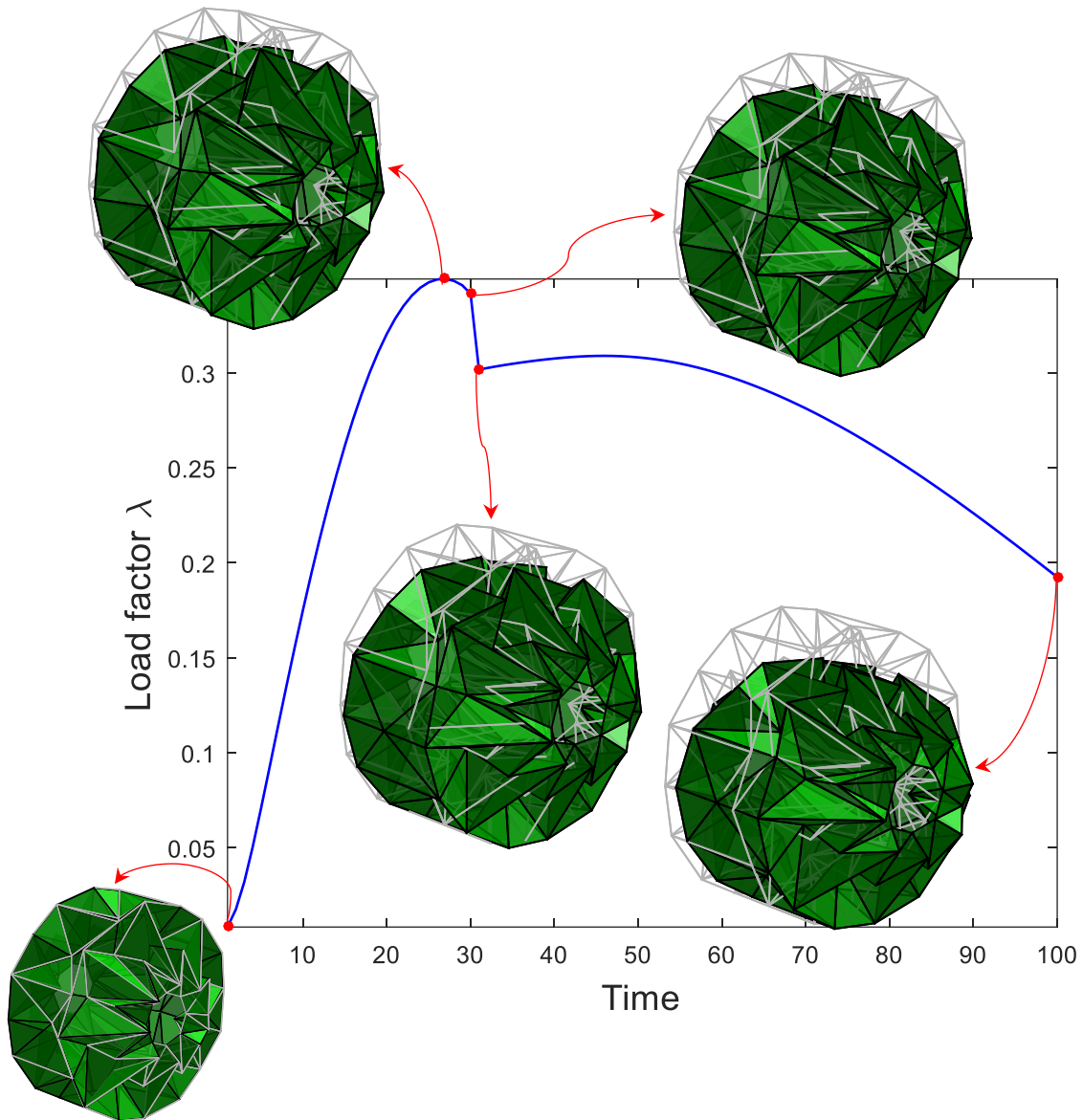


Figure 6-10: Load factor over time for the folding process of the closed waterbomb tessellation with a rigid element on one end.

Once the cell ‘pops out’, it tends to keep the entire folding/ unfolding process on the ‘popped out’ configuration. Thus, only angles B and E , that correspond to the reversed creases, will change over time and the other inner angles (A , C , D and F) will be nearly zero (Figure 6-11). If the tessellation is built and modeled such that it can be described as a rigid origami, i.e., there is only deformation on the creases, A , C , D and F are identically zero.

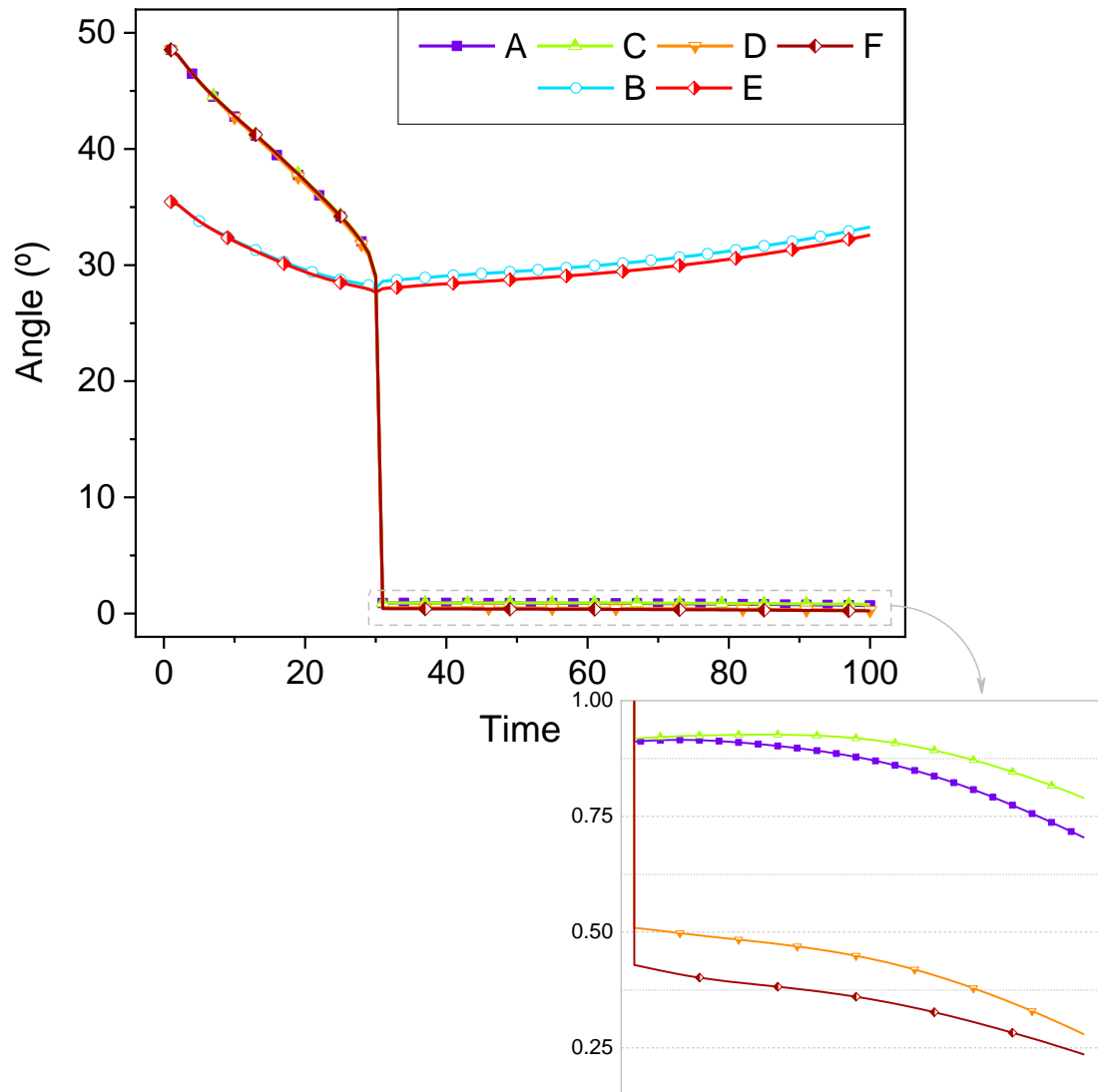


Figure 6-11: Time evolution of inner angles for the ‘popped out’ unit cell, with a zoom for inner angles A, C, D and F after the inversion of crease.

The presence of rigid plates on both endings avoids in some cases the failure of the origami that happens due to an inversion of crease. Nevertheless, it reduces considerably the asymmetries associated to uneven external load distribution or uneven distribution of material properties along the structure.

Finally, a folding process of the closed waterbomb structure with rigid plates on both endings is evaluated. As can be seen in Figure 6-12-a to Figure 6-12-d, all curves are superposed and cells on odd parity lines behave according to Π_2 during the entire folding process. It is worth noticing that a bifurcation occurs around time 96 and is associated to an overloading of the structure. From this point on, the folding process is

finished, and the structure presents a torsion or an increasing deformation on panels, depending on the overload.

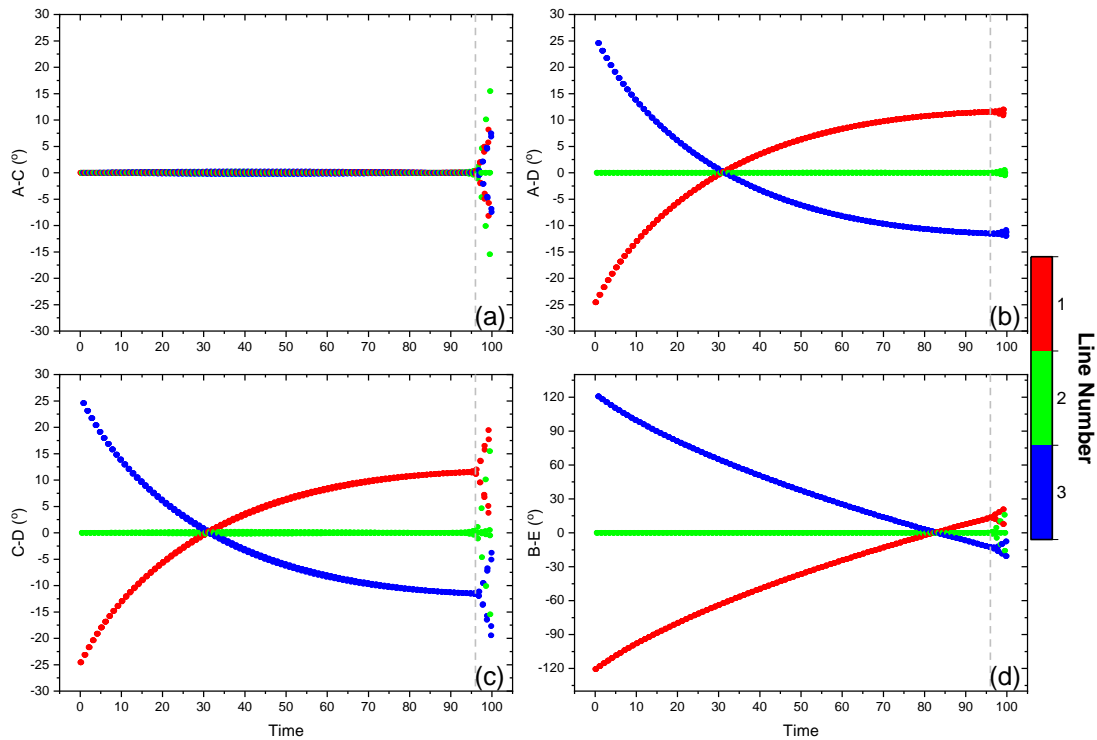


Figure 6-12: Time evolution of inner angles relation for each cell for the case with an increasing of 24% on the external load. From (a) to (d), respectively, the difference between angles A and C, A and D, C and D, and B and E.

6.2. Reduced-order model

The reduced-order model is developed considering symmetry planes, reducing the structure description to two planes only, as can be seen at Figure 6-13. This reduced-order formulation is proposed for situations where the load distribution is symmetrical, or the application requires a global symmetry. The XZ plane contains the radial symmetry, and it is assumed that the cells in the middle column expand/ contract equally. On the other hand, the YZ plane contains the longitudinal symmetry, and it is assumed that the origami-wheel has a mirrored symmetric behavior where the 2 columns on the tips are mirrored images from each other.

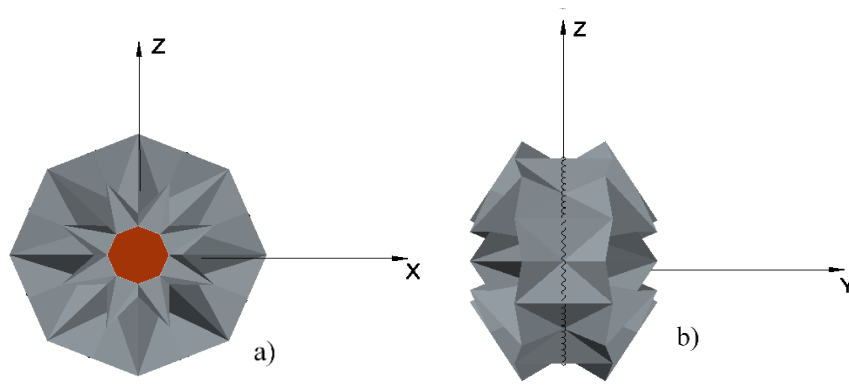


Figure 6-13: Plane views of the origami-wheel.

Beside angles α and θ , that describe the opening/closure process of the unit cell, the angles β and γ are associated to the opening/closure process of the entire structure. These angles are related to each other, and this relation is a function exclusively of the number of cells (N) that compound the origami-wheel column, and can be obtained by observing the cells on the tips (near the acrylic plate) (Figure 6-14a).

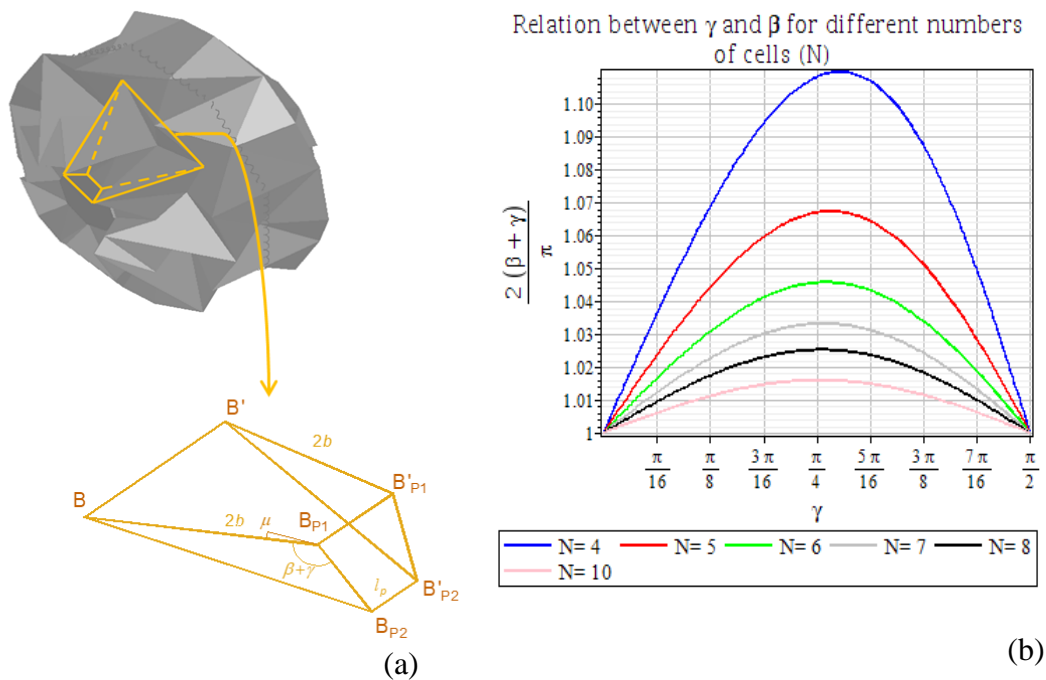


Figure 6-14: Trapezoidal pyramid (a) used to obtain the relation between β and γ (b).

The acrylic plate length is given by $l_p = 2r \sin(\pi/N)$, and the bases of the trapeze $BB'B_{P_1}B'_{P_1}$ are functions of R_2 , the cell size and the number of cells, given by $\overline{BB'} = R_2 \sin(\pi/N)$ and $\overline{B_{P_1}B'_{P_1}} = (R_2 - 2b \sin \beta) \sin(\pi/N)$. Besides, once that the symmetrical behavior is established, one can see that $\overline{BB'} \parallel \overline{B_{P_1}B'_{P_1}} \parallel \overline{B_{P_2}B'_{P_2}}$.

Thus, the final relation between β and γ is established as $\sin \gamma = \frac{\cos \beta}{\sqrt{1 - \sin^2 \beta \sin^2(\pi/N)}}$, and it is represented in Figure 6-14b. Note that, by

increasing N , the angles β and γ tend to be complementary. By using $N=8$, the maximum error considering the complementary assumption is around 2.5%, ensuring that $\beta + \gamma \approx \pi/2$, a value assumed by Lee *et al.*, 2013.

If the origami-wheel behaves with a global symmetry, the plane views from Figure 6-13 can be modeled by equivalent mechanisms, as shown in Figure 6-15.

Plan view XZ (Figure 6-15-a) is modeled according to Figure 6-15-b and is associated to the folding/ unfolding process of the unit cells from the middle row (line 2). Said folding/ unfolding process is described through the opening length (L_1) and opening angle (θ), and each cell single vertex can be located on a circumference of radius R_1 . Additionally, vertices A, C, D and F of each cell from the middle row (line 2) can be located on a circumference of radius R .

Plan view YZ (Figure 6-15-c) is modeled according to Figure 6-15-d and is associated to the relative motion between the acrylic plates ($2L_2$). The second angle (α) associated to the opening of the unit cell placed on the middle row (line 2) is evaluated in relation to the Z axis. The relative motion of the acrylic plates promotes a folding/ unfolding process of the cells located on both endings of the origami-wheel (lines 1 and 3), and this folding/ unfolding process is described by the angles β and γ . The vertices B and E of each unit cell from the middle row (line 2) can be located over the surface of a cylinder with radius R_2 .

Each unit cell is conceived as a rectangle of sides $2a$ and $2b$ with $a = b \tan(\lambda)$, and each acrylic plate is conceived as a regular octagon with apothem r . The variable c is arbitrary and it is only constrained by the geometric restrictions of the structure.

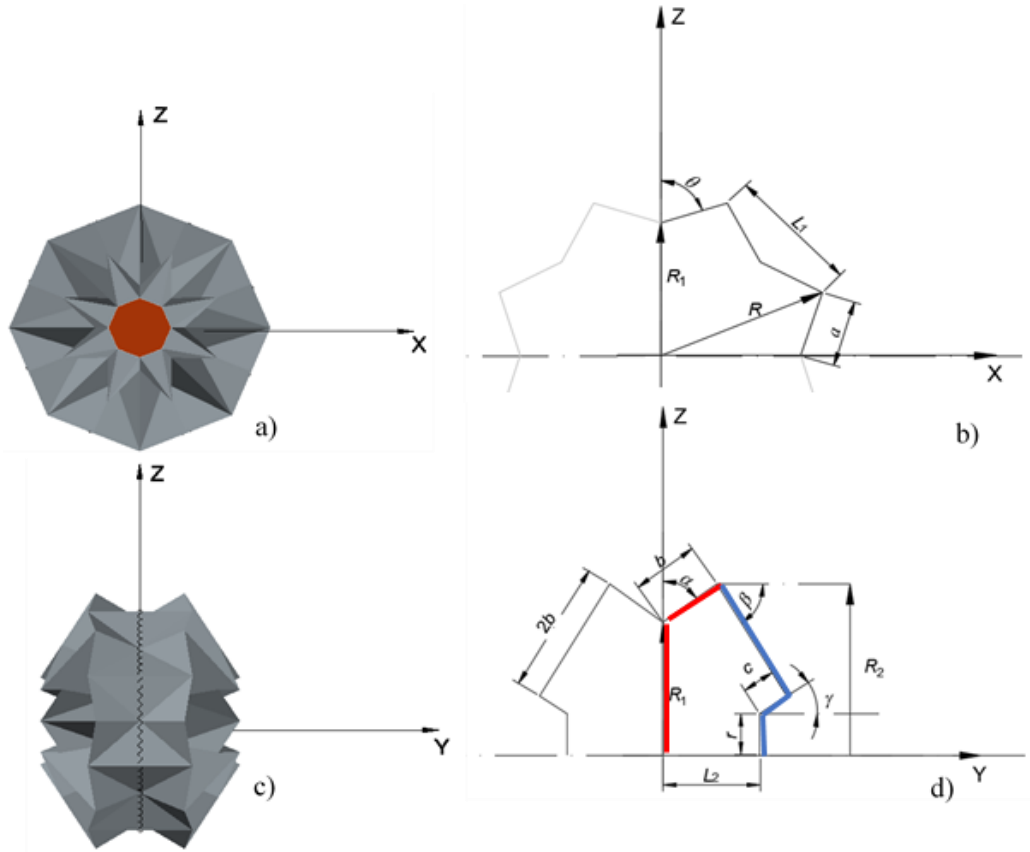


Figure 6-15: Origami-wheel and symmetric plane views. (a) Radial symmetry $-XZ$ plan; (b) Simplified view; (c) Longitudinal symmetry $-YZ$ plan; (d) Simplified view.

By considering the complementary condition described above, and assuming that $c=b/2$, it is possible to obtain the following relations for the origami, projecting the lengths on axis X , Y and Z in Figure 6-15:

$$L_2 = b \sin \alpha + 2b \cos \beta - \frac{b}{2} \sin \beta \quad (6.1)$$

$$R_2 = r + 2b \sin \beta + \frac{b}{2} \cos \beta \quad (6.2)$$

$$R_2 = R_1 + b \cos \alpha \quad (6.3)$$

$$L_1 = 2a \sin \theta \quad (6.4)$$

$$R_1 = a \left(\frac{\sin \theta}{\tan \frac{\pi}{8}} - \cos \theta \right) \quad (6.5)$$

$$R = \frac{L_1}{2 \sin \frac{\pi}{8}} \quad (6.6)$$

Note that there are two expressions for R_2 . These two forms can be obtained considering either the decomposition of the red edges on Figure 6-15-d, leading to (6.2), or the decomposition of the blue edges on Figure 6-15-d, leading to (6.3), being both decompositions made on axis Z .

Based on geometric relations, an explicit relation between L_2 and L_1 is established by solving the system of equations (4.4 and 6.1 – 6.6), leading to a function $L_2 = g(L_1)$. It is also possible to explicit R_1 and R_2 as functions of L_1 . Figure 6-16 shows graphical representations of these relations considering $r = 0.04\text{m}$, $b = 0.065\text{m}$ and $\lambda = \pi/4$ (a squared cell). Figure 6-16a shows the curve $L_2 = g(L_1)$ and Figure 6-16b shows the curves of the external radius, R_2 , and internal radius, R_1 , as a function of L_1 .

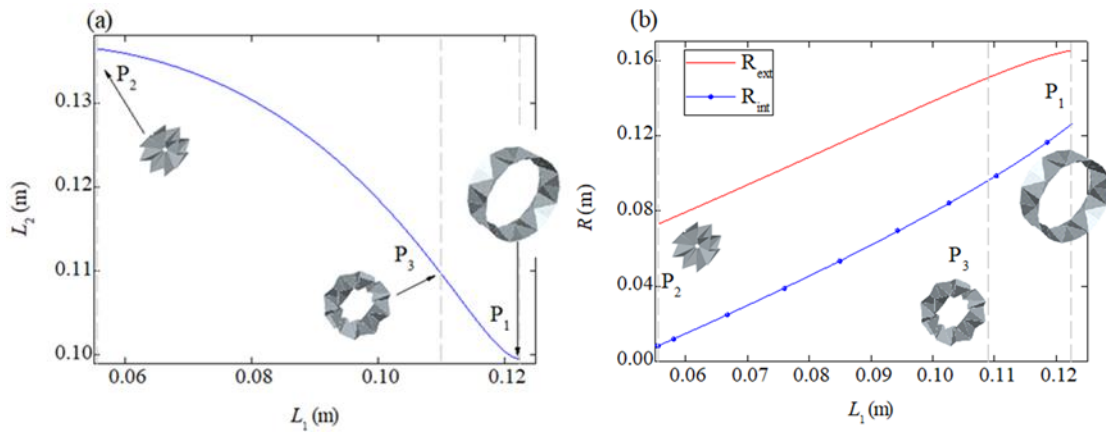


Figure 6-16: Origami-wheel geometric relations. (a) Curve of the distance between the acrylic plates (L_2) as a function of the middle row opening (L_1); (b) Curve of the inner (R_1) and outer (R_2) radii of the origami-wheel as a function of the middle row opening (L_1).

The next chapter deals with the dynamical analysis of the origami-wheel actuated by a BIAS system composed by SMAs, placed on the middle row along L_1 , and an elastic passive spring connecting the acrylic plates, along $2L_2$.

7 Origami-Wheel Dynamics

This chapter presents the dynamical analysis of the origami-wheel described by the reduced-order formulation shown in Section 6.2. This chapter starts with the dynamical formulation, followed by a quasi-static analysis that covers the origami stability and shape changing. Finally, a dynamical study is developed, including bifurcation analysis and dynamical jumps.

In the closed-form tessellation analysis, it is verified that, under symmetric or quasi-symmetric actuation, the origami-wheel structure behaves as a single DoF system, and thus its shape changing can be described by a simplified model.

Figure 7-1 shows the SMA actuators, that act by closing the wheel (reducing its radius), and the passive elastic spring, that restores the wheel configuration. The elastic spring is connected to two octagonal acrylic plates. The SMAs are designed with a residual deformation, such that, in the opened configuration, all springs are free of stress and the SMA has a tractive detwinned martensite (M^+) crystallographic phase. Thus, the shape changing is promoted by inducing the phase transformation $M^+ \rightarrow A$, increasing the SMA stiffness and reducing the SMA length. During this process, the elastic passive spring is extended, reducing the wheel's radius. The cooling down process of the SMA induces the reverse transformation, releasing the stress on the SMA. The elastic spring acts as a restitutive force in the BIAS system, restoring the initial configuration of the wheel.

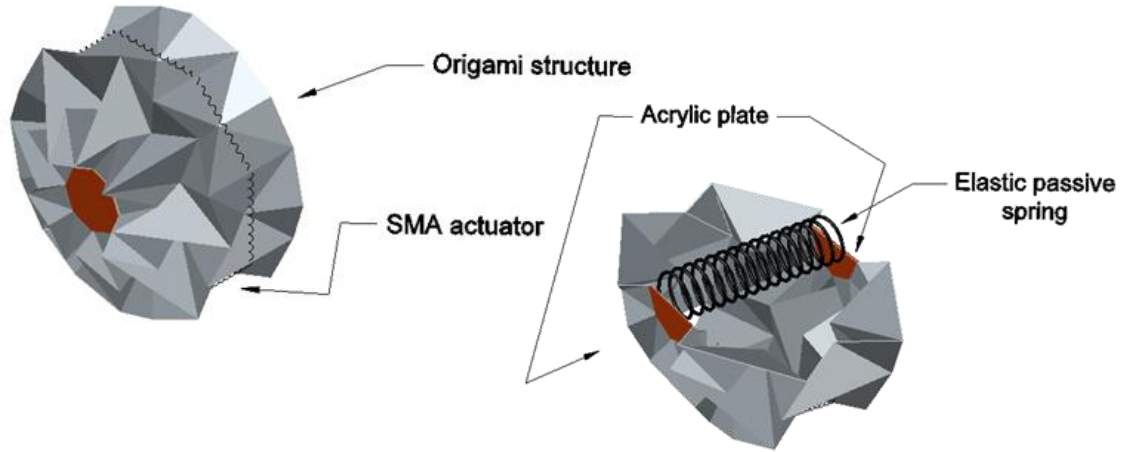


Figure 7-1: Origami-wheel with SMAs placed along the middle row to promote the folding process (left) and a cut exposing the elastic passive spring, connecting the acrylic plates, to promote the BIAS effect (right).

Concerning the origami construction, it is assumed that, when elastic springs are free of tension, the SMA actuator is pre-deformed at the martensitic phase ($T=288\text{K}$) and the origami-wheel is not totally opened. This means that the SMA actuator has a residual strain that can be recovered by heating, and the relaxed spring size is given by $L_1=0.089$. It should be highlighted that, for the considered values of b and r , the range of feasible values for constructive reasons is $L_1 \in [0.0555, 0.1225]$ m. In this regard, point P_1 represents the construction configuration; point P_2 represents the minimum configuration, where the origami-wheel is completely closed (minimum radius); and point P_3 is the built configuration, where the origami-wheel is half-opened. Table 7-1 presents origami-wheel configuration characteristics.

Table 7-1: Configurations of the origami-wheel for $b = 0.04$ m and $r = 0.065$ m.

P	($^\circ$)			(m)			
	α	β	θ	L_1	L_2	R_2	R_1
1	52.98	55.14	70.44	0.1225	0.0995	0.1652	0.1261
2	5.75	0.17	25.27	0.0555	0.1364	0.0729	0.0082
3	32.82	41.72	56.98	0.1090	0.1106	0.1508	0.0962
Maximum variation				0.0670	0.0369	0.0923	0.1179

Another interesting definition for geometrical modeling is the use of spring displacement instead of its length. Hence, assuming that the reference configuration is

that at which the SMA spring is free of both stress and strain, $L_1^0 = 0.089\text{m}$, the SMA length can be written as $L_1 = L_1^0 + u$, where u is the SMA displacement. The same assumption can be made for the elastic passive spring: $L_2 = L_2^0 + u_E$, where u_E is the elastic spring displacement and $L_2^0 = g(L_1^0 + u_0)$. Note that the reference configuration for the elastic spring is the built structure. It is important to highlight that the free stress and strain condition of the elastic spring depends on the structure initial configuration, being assumed at point P_3 , which means that $u_0 = 0.02\text{m}$.

7.1. Dynamical formulation

Kinematics analysis established that symmetry assumptions define a 1 DoF system to describe origami movements. Therefore, a one degree of freedom reduced order model is able to describe the system dynamics. Initially, it is necessary to describe the thermomechanical behavior of SMA by considering a constitutive model. This work uses the polynomial constitutive model (see Appendix) to describe the constitutive behavior of the SMA.

Aguiar *et al.* (2010) and Enemark *et al.* (2016) showed that force-displacement-temperature relation of SMA springs is similar to one-dimensional stress-strain-temperature relations when homogeneous behavior is assumed through the wire cross-section. Therefore, considering a helical spring with N_s coils with diameter D and wire diameter d , the SMA actuator restitution force, F_{SMA} , is given by:

$$F_{SMA} = \frac{\partial E_{SMA}}{\partial u} = \bar{c}_1(T - T_M)u - \bar{c}_2u^3 + \bar{c}_3u^5 \quad (7.1)$$

where E_{SMA} is the SMA potential energy (A.3); $\bar{c}_i, i = 1,2,3$ are model parameters and T_M represents the temperature below which the martensite phase is stable.

Concerning the passive elastic spring, a linear relation describes the restitution force, F_E ,

$$F_E = \frac{\partial E_E}{\partial u} = \frac{\partial u_E}{\partial u} \eta u_E \quad (7.2)$$

where E_E is the elastic potential energy; $\eta = \frac{Gd_{EL}^4}{6D_{EL}^3N_{EL}}$ and G is the shear modulus.

The dynamical model assumes that the origami has a mass $8m$, located as punctual masses around the middle row such that each SMA actuator is related to a mass m . Besides, each acrylic plate associated with the passive elastic spring half-length has a mass M . Based on that, it is possible to write the system energy, where E_C is the kinetic energy and E_P is the potential energy, defined as follows:

$$\begin{aligned} E_C &= \frac{8mr_{SMA}^2}{2} + \frac{2M\dot{u}_{EL}^2}{2} \\ E_P &= 8E_{SMA} + 2E_{EL} \end{aligned} \quad (7.3)$$

r_{SMA} is the variation of the radii presented at equation (7.4), and it is related to the radial displacement of the mass associated with the SMA actuator (Figure 6-15):

$$r_{SMA} = R - R^0 = \frac{L_1}{2 \sin \frac{\pi}{8}} - \frac{L_1^0}{2 \sin \frac{\pi}{8}} = \frac{u}{2 \sin \frac{\pi}{8}} \quad (7.4)$$

Note that the expression of u_E can be obtained by rewriting the solution $L_2 = g(L_1)$ as a function of the initial configuration and the SMA spring displacement. Since $u_E = L_2 - L_2^0$ and $u = L_1 - L_1^0$, it is possible to write $u_E = g(L_1) - L_2^0 = g(L_1^0 + u) - L_2^0 = f(u)$.

Using the chain rule on $f(u)$ derivation:

$$\ddot{u}_E = \frac{d}{dt} \left(\frac{df}{du} \frac{du}{dt} \right) = f' \ddot{u} + f'' \dot{u}^2 \quad (7.5)$$

A linear viscous dissipation is included on the formulation, with coefficient ξ . External stimuli are also incorporated by considering an external force $F(t)$ that is assumed to be symmetrically applied through the middle column of the origami-wheel, respecting the rotational symmetry. Under these assumptions, equations of motion are written as follows:

$$\begin{cases} \dot{u} = v \\ \dot{v} = \frac{F(t) - 4F_{SMA} - Mf'f''v^2 - \eta f f' - \xi v}{\frac{m}{\sin^2 \frac{\pi}{8}} + Mf'^2} \end{cases} \quad (7.6)$$

Table 7-2 shows mechanical and geometric properties of origami-wheel used on the numerical simulations. All simulations consider a dissipative system with a viscous damping constant $\xi = 1\text{N s/m}$.

Table 7-2: Material and system parameters.

Inertial terms	m (kg)	M (kg)			
	0.008	0.012			
Polynomial constitutive model	c_1 (MPa/K)	c_2 (MPa)	c_3 (MPa)		
	5	7.0×10^4	7.0×10^6		
Elastic spring	d_E (m)	N_E	D_E (m)	G_E (GPa)	
	2.0×10^{-3}	40	30.0×10^{-3}	30.0	
SMA spring	d_{SMA} (m)	N_{SMA}	D_{SMA} (m)	T_M (K)	T_A (K)
	1.0×10^{-3}	10	2.5×10^{-3}	291.4	326.4

7.2. Quasi-static analysis

In order to evaluate the model capability to describe the origami behavior, a quasi-static analysis is performed neglecting inertia and dissipation terms. This analysis is shown in Figure 7-2, that contains the origami resultant force.

The SMA-origami system is temperature dependent, meaning that it is possible to change the origami-wheel radius with temperature variations. Different equilibrium configurations can be observed depending on the temperature: three configurations for low temperature ($T < T_M$); five configurations for intermediate temperatures ($T_M < T < T_A$); and one configuration for higher temperatures ($T > T_A$). Note that the increase of SMA temperature by 7 K induces the reduction of the larger origami radius (R_2) from 0.147 m to 0.122 m ($A \rightarrow B$ indicated in Figure 7-2). The maximum radius reduction observed ($C \rightarrow D$ indicated in Figure 7-2) is around 0.058 m, representing a reduction of almost 39%. The total reduction between limit configurations (points $P_1 \rightarrow P_2$ in Figure 6-16) implies a reduction of about 56%, and these values matches with the experimental ones developed by Fang *et al.* (2017).

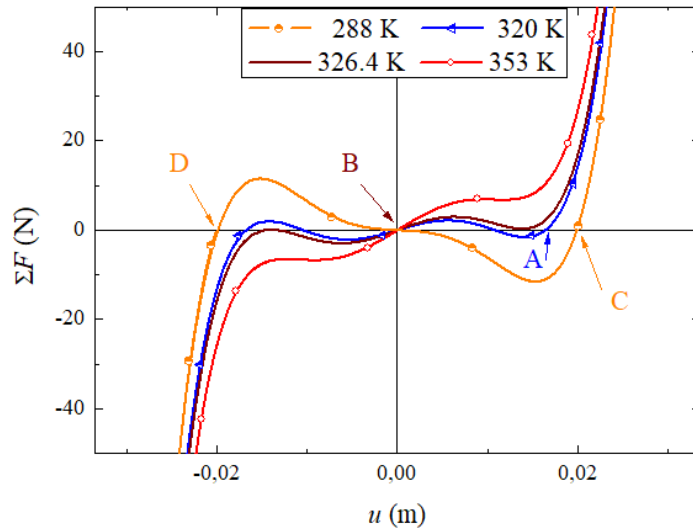


Figure 7-2: Quasi-static analysis of the origami wheel, considering the sum of the efforts of the SMA and elastic springs.

Figure 7-3 shows changes in the configuration due to temperature variations. Basically, it is presented the time history for the temperature and the origami response, path $C \rightarrow B \rightarrow C$, indicated in Figure 7-2. At initial configuration, $T_0=288\text{K}$, SMA actuators have an initial displacement $u=0.02$ m, meaning that the origami-wheel is half-opened. A thermal load from $T=288\text{K}$ to $T=373\text{K}$ on SMA (Figure 7-3a) recovers the SMA residual strain folding (closing) the origami, as can be noticed by the radius reduction (Figure 7-3b). Figure 7-3c shows the SMA and elastic spring displacements during the application of the thermal load. The first vertical dashed line indicates the beginning of the shape changing during the heating process. At this point ($T=T_M$), the SMAs start the phase transformation from martensite to austenite, recovering the residual strain and closing the origami-wheel. This process takes around 4 seconds.

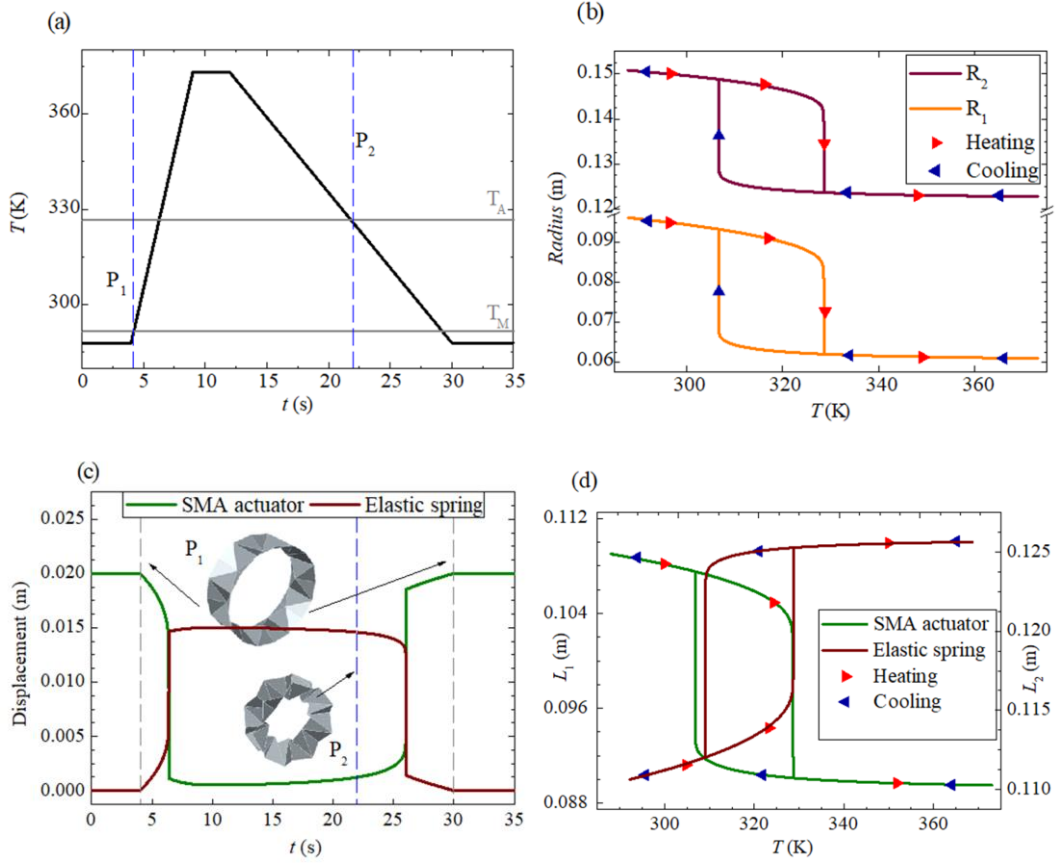


Figure 7-3: Origami structure quasi-static behavior due to temperature changes. (a) Thermal load; (b) External and internal radii evolution during heating/cooling process; (c) Displacements on elastic spring and on each SMA actuator; (d) Actuators' length.

The second and third vertical dashed lines define the beginning and the end of the origami reopening (unfolding) process that occurs when cooling the SMAs. This process takes around 15 seconds, and these results are in agreement with experimental data from the references Fang *et al.* (2017) and Lee *et al.* (2013).

7.3. Dynamical analysis

The origami-wheel, in an operational condition, is subject to thermal and mechanical loads, which modify the shape of the structure and its dynamic behavior. This section analyzes the origami behavior when subjected to external loads and environmental variations, such as thermal disturbances and oscillations. The numerical simulations performed consider a 4th-order Runge-Kutta to solve the dynamic system.

For the sake of simplicity, it is adopted an external mechanical stimulus represented by two terms: $F(t) = F_1(t) + F_2(t)$, where $F_1(t) = \delta_1 \sin(\omega_1 t)$ and $F_2(t) = \delta_2 \sin(\omega_2 t)$. The term $\delta_1 \sin(\omega_1 t)$ represents different forms of the soil (sinusoid, for instance – Figure 7-4a). On the other hand, the second term, $\delta_2 \sin(\omega_2 t)$, represents a perturbation over the original stimulus (Figure 7-4b), that could be related to floor irregularities.

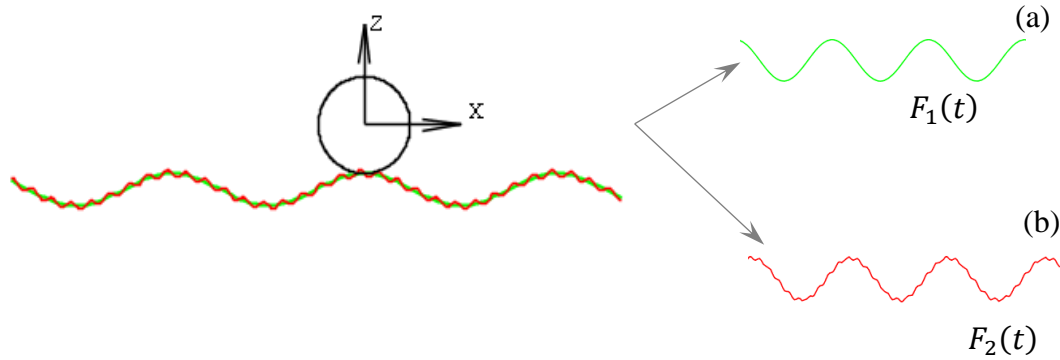


Figure 7-4: Representation of the external excitation represented by the force $F(t) = F_1(t) + F_2(t)$, where the contribution of each $F_i(t)$ is highlighted on the right, being (a) for $F_1(t)$ and (b) for $F_2(t)$.

$$F(t) = \delta_1 \sin(\omega_1 t) + \delta_2 \sin(\omega_2 t) \quad (7.7)$$

The thermal load perturbation is related to environmental temperature oscillation, and its influence on the structure response is investigated. This perturbation is represented by a sine fluctuation of amplitude δ_T , and frequency ω_T , around the nominal temperature, T_N , defined by the following equation,

$$T(t) = T_N + \delta_T \sin(\omega_T t) \quad (7.8)$$

The structure of equilibrium points is analyzed from basins of attraction presented in Figure 7-5, built from free vibration analysis of the dissipative system with different initial conditions. Each equilibrium point structure is associated with forces acting on the origami, presented in Figure 7-2, representing distinct origami-wheel configurations, showed in Figure 7-5a.

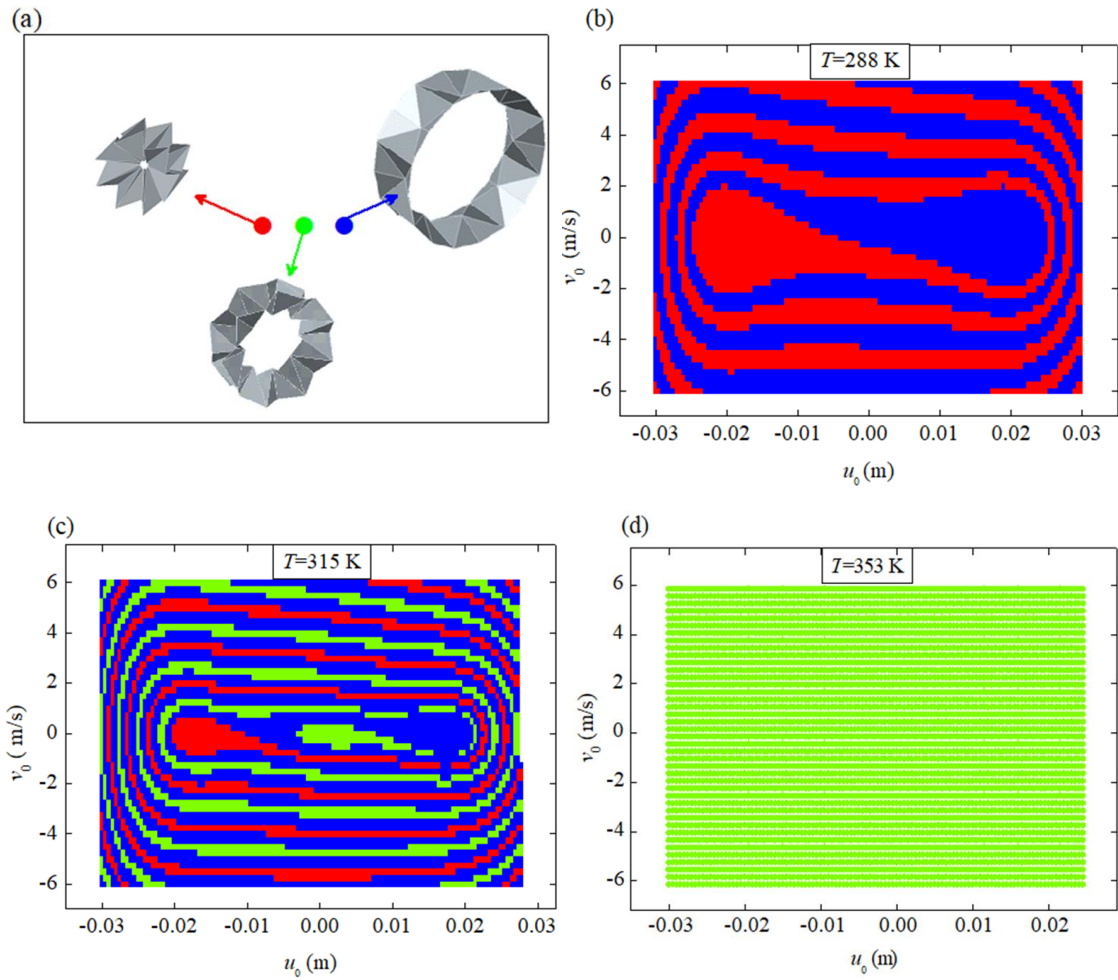


Figure 7-5: Origami-wheel basins of attraction. (a) Shape configuration for the three stable positions and its color representation; (b) Basin of attraction for $T < T_M$; (c) Basin of attraction for $T_M < T < T_A$; (d) Basin of attraction for $T > T_A$.

Figure 7-5b shows a situation where $T < T_M$, with three equilibrium points (two stable and one unstable) that can be reached changing initial conditions. By increasing the temperature for intermediate values ($T_M < T < T_A$), the system changes from three to five equilibrium points (three stable and two unstable), as can be seen at Figure 7-5c. By increasing the temperature above T_A , the stable points get closer until they coalesce to each other. This causes a change from five equilibrium points to one stable equilibrium point (Figure 7-5d). Depending on the initial conditions, it is possible to reach different configurations, changing the origami-wheel radius.

The origami slender characteristic is associated to a rich dynamic with strong sensitivity to either parameter changes or initial conditions. In this regard, it is important

to have a deep comprehension of the origami-wheel nonlinear dynamics, evaluating high periodic, quasi-periodic and chaotic behaviors.

In order to perform a global analysis of the origami response, bifurcation diagrams are built varying the amplitude of the load perturbation δ_2 , keeping a constant frequency $\omega_2 = 300\text{rad/s}$, for $\delta_1 = 10\text{N}$ and $\omega_1 = 200\text{rad/s}$. The objective of this analysis is to evaluate the system response under perturbations that represent soil roughness. Different temperature ranges are analyzed: $T = 288\text{K}$ ($T < T_M$), $T = 315\text{K}$ ($T_M < T < T_A$), and $T = 320\text{K}$ ($T > T_A$).

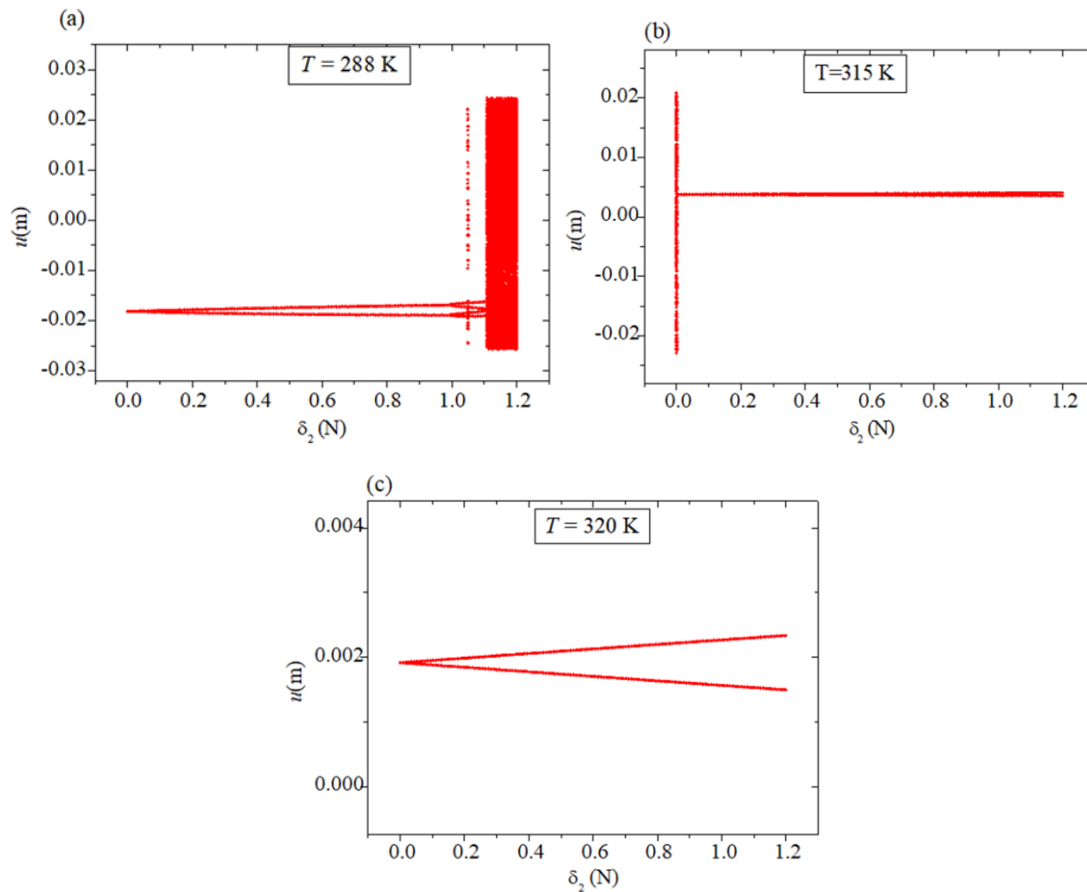


Figure 7-6: Origami bifurcation diagrams varying perturbation forcing amplitudes: (a) $T = 288\text{ K}$ ($T < T_M$); (b) $T = 315\text{ K}$ ($T_M < T < T_A$); (c) $T = 327\text{ K}$ ($T > T_A$).

Figure 7-6 shows bifurcation diagrams varying the load perturbation amplitude from zero ($\delta_2=0$, unperturbed excitation forcing) to $\delta_2=1.2\text{N}$. Note that for the intermediate temperatures ($T = 315\text{ K}$) the chaotic response disappears with the increasing of the perturbation, changing to a periodic response of period-2 (Figure 7-6b).

A different behavior is observed for the low temperature case ($T=288K$), wherein the perturbation increasing tends to increase the response complexity, resulting in a chaotic response (Figure 7-6a). Under this condition, the bifurcation diagram shows bifurcations and crisis. For δ_2 smaller than 1.1 N, the system presents a period doubling, from period-1 to period-4. For $\delta_2 > 1.1N$, a crisis phenomenon is observed, presenting sudden changes from a periodic response to a chaotic-like behavior. For high temperatures (Figure 7-6c), when austenite is stable ($T = 320K > T_A$), the system has a period-2 behavior for the perturbed case ($\delta_2 \neq 0$) and a period-1 response for the unperturbed case ($\delta_2 = 0$). It is possible to notice that the increase in temperature tends to simplify the behavior of the structure, reducing its periodicity and complexity.

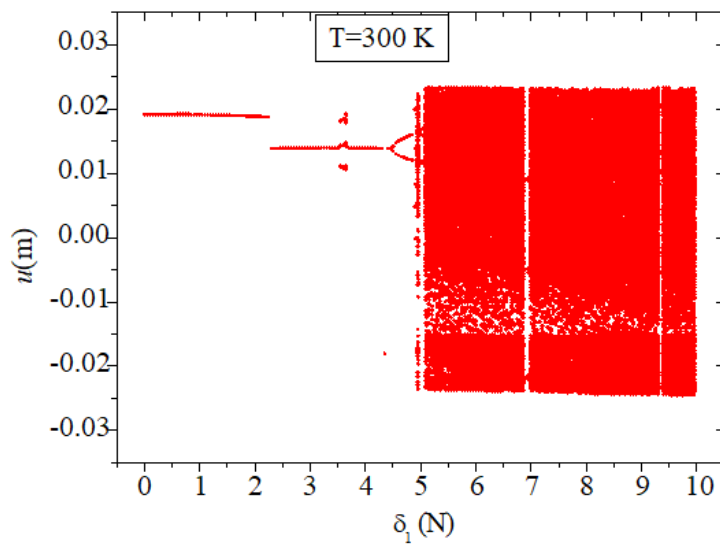


Figure 7-7: Bifurcation diagram for an intermediate temperature ($T_M < T = 300\text{ K} < T_A$).

Note that the system response to an external force without disturbance is periodic of period 1 for $T = 288\text{ K}$ and chaotic for $T = 315\text{ K}$ (intermediate temperature). Due to the observed change in the behavior, a study on the system at intermediate temperature is carried out, aiming to evaluate the impact of the base of the external load function ($F_1(t)$) on the system's behavior. A complex bifurcation diagram is noted for $T = 300\text{ K}$. Figure 7-7 shows the bifurcation diagram for the system subjected to an external load without disturbance ($\delta_2 = \omega_2 = 0$), with excitation frequency $\omega_1 = 200\text{ rad/s}$, varying the forcing amplitude δ_1 from 0 N to 10 N. Again, the typically nonlinear phenomena cascade of

bifurcation and crisis are observed. The diagram starts with a periodic response of period 1, with a bifurcation cascade around 3.5 N, later returning to a period 1 response. At 4.5 N another bifurcation is observed, and the system suddenly shows a chaotic response (crisis phenomenon). It is possible to notice that for $\delta_1 > 5$ N the system response is basically chaotic for the intermediate temperature $T = 300K$, even without disturbance in the external forcing, with some periodic windows in 7 N and 9.4 N.

The influence of the soil roughness (or the external force perturbation) can be better understood in the sequence. Initially, it is considered a forcing amplitude $\delta_1 = 10N$ and $\omega_1 = 200\text{rad/s}$ with a constant low temperature $T = 288K$ (Figure 7-8a), without perturbation. Under this condition, the origami presents a period-1 behavior, oscillating around the closed configuration with small oscillation amplitude, as shown in the phase space and the Poincaré section contained within Figure 7-8b.

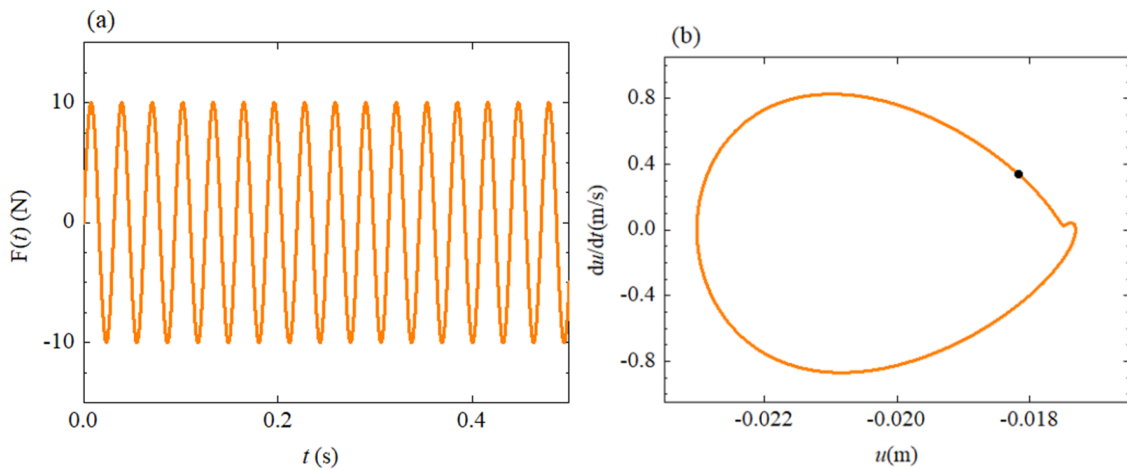


Figure 7-8: Origami response subjected to mechanical forcing ($\delta_1 = 10$ N, $\omega_1 = 200$ rad/s) at $T = 288$ K. (a) Mechanical load $F(t)$; (b) phase space and Poincaré section.

A perturbation is now introduced into the system, considering $\delta_2 = 1.5N$ and $\omega_2 = 300\text{rad/s}$ (Figure 7-4). Figure 7-9a shows the original and the perturbed excitations. Under this new condition, the origami presents a chaotic motion, which is dramatically different when compared with the previous one. Figure 7-9b presents phase space together with Poincaré section that shows a strange attractor. The chaotic behavior is confirmed by the Lyapunov exponents estimated using Wolf *et al.* (1985) algorithm: $\{60, -80\}$. The use of Kaplan-Yorke conjecture points to a fractal dimension of 1.737. Figure 7-9c shows a phase space identifying some regions associated with stable

equilibrium point configurations. Note that the origami presents oscillations around several configurations, resulting in large radius variations. This kind of behavior represents an important issue to be considered during the design stage, since it can be related to unexpected oscillations or related to the structure integrity once high rate of folding process can induce damage on the creases.

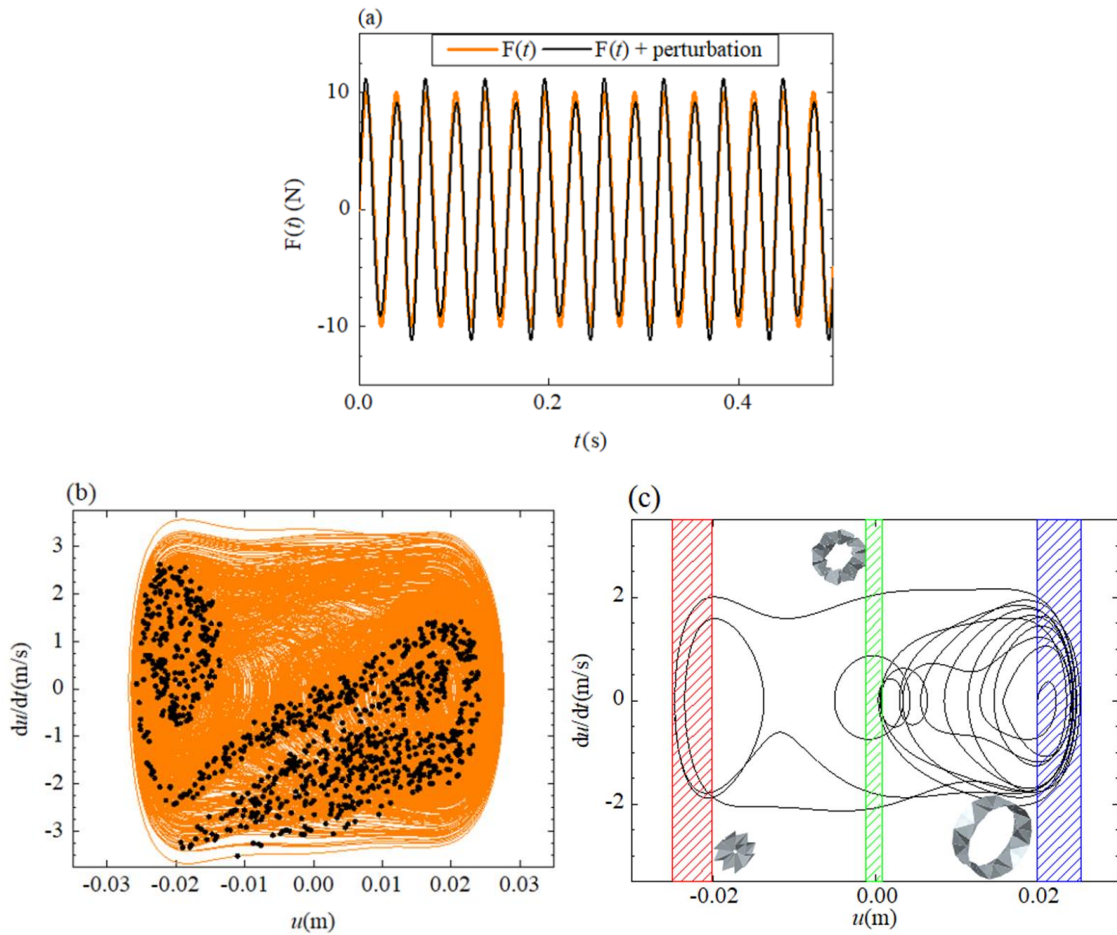


Figure 7-9: Origami response to a perturbed mechanical load at $T=288$ K. (a) Mechanical loading process (without and with a small perturbation); (b) Phase space and strange attractor; (c) Origami configurations.

Origami sensitivity is important even when the system presents periodic behavior. Figure 7-10 shows three kinds of periodic response, obtained at $T=288$ K: in the first case, $F(t)$ is such that $\delta_1=10$ N and $\omega_1=180$ rad/s ($F_1(t)$); in the second case, $\delta_1=10$ N and $\omega_1=280$ rad/s ($F_2(t)$); in the third case, $\delta_1=14$ N and $\omega_1=200$ rad/s ($F_3(t)$). When the system is subjected to $F_1(t)$, the origami presents a period-1 response, oscillating around

a closed configuration, with small amplitudes. When the system is subjected to $F_2(t)$, an external force with the same amplitude as the previous one but with a higher frequency, the origami opens and oscillates around an opened configuration, with a period-3 response. Although the SMA displacement, u , is bigger in the second case, the external radius has a small variation, which means that the creases fold with smaller amplitudes when compared to the first case. By considering the forcing to $F_3(t)$, the origami has a period-1 response, oscillating in the entire space, meaning that it opens and closes completely, repeatedly. Therefore, the external radius has large variations, and the creases are subjected to large oscillations. Thus, not only the frequency of the folding process can result in a rupture of the joints, but also its amplitude.

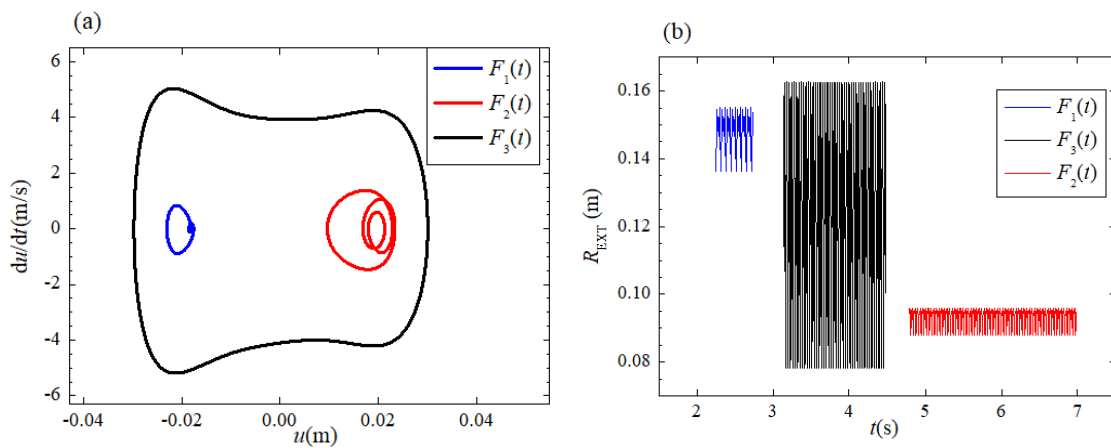


Figure 7-10: Different periodic orbits for different external mechanical forces at $T=288$ K. (a) Phase portraits; (b) External radius variation.

The objective now is to study the base forcing, evaluating the system's response to a run-up and run-down test (frequency diagram). To this end, a study is made of the frequency of mechanical forcing for three different temperatures: $T = 288 K < T_M$; $T_M < T = 315K < T_A$ and $T = 320K > T_A$. The frequency varies in the range of $\omega_1 = (200, 2000) rad/s$, without disturbance ($\delta_2 = 0N$ and $\omega_2 = 0 rad/s$). Figure 7-11 shows the frequency curve for the low temperature. The presence of dynamic jumps is noted, which usually defines regions of critical behavior (Oliveira *et al.*, 2014; Bernardini & Rega, 2005). Thus, aiming at an operational condition, this behavior must be evaluated to avoid unwanted responses and possible damage to the integrity of the structure (Scheffer *et al.*, 2001; Scheffer & Carpenter, 2003).

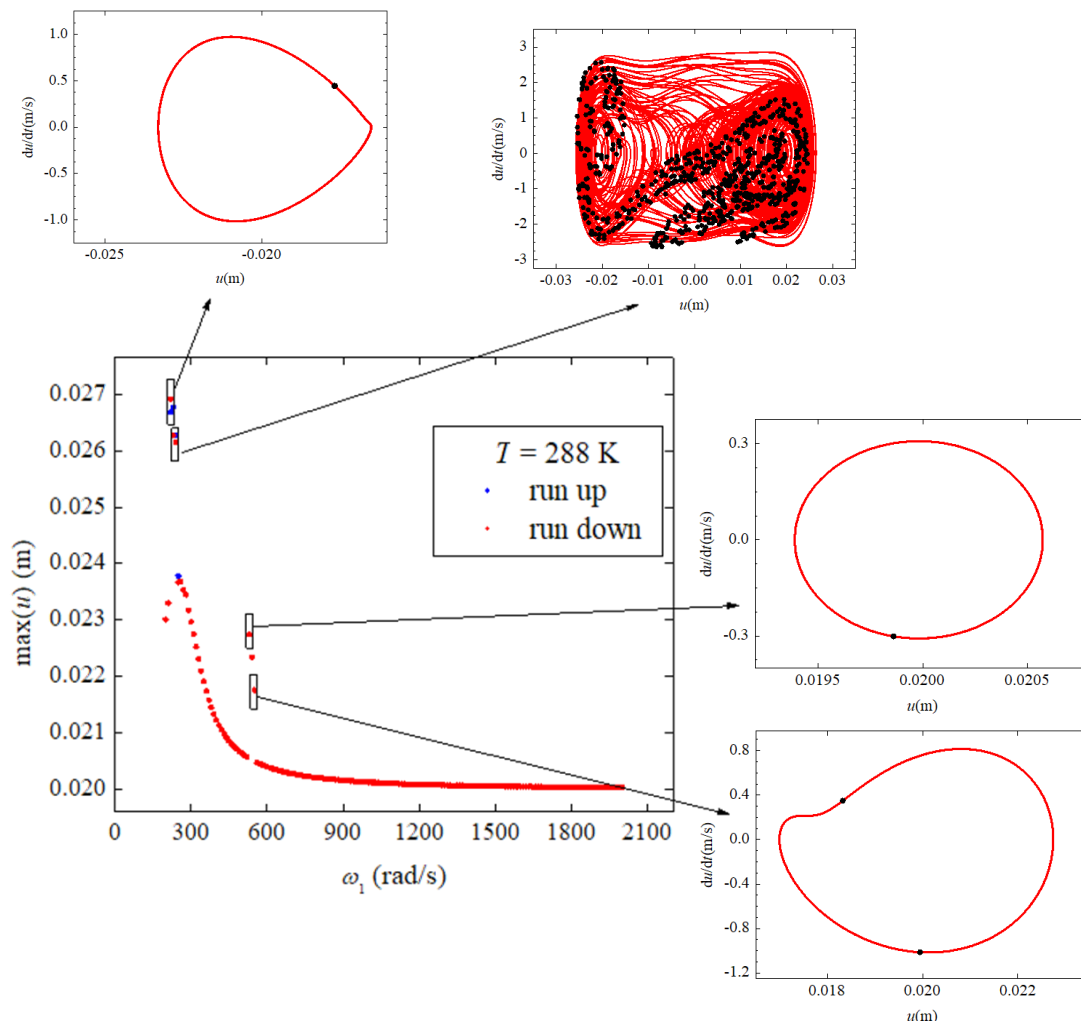


Figure 7-11: Frequency response of the origami for $T = 288 \text{ K}$ ($T < T_M$) in a run-up and run-down simulation. Some phase spaces positioned in high dynamic regions are highlighted.

The low temperature response has two dynamic jumps: the first jump is related to a chaotic behavior, while the second jump is related to a period multiplicity, as can be seen from the period 2 phase space shown in Figure 7-8. When raising the temperature for the same external force, the system does not present a chaotic response, but a change in periodicity (Figure 7-12). Note that the high temperature response does not show dynamic jumps, as the system response remains periodic for period 1 over the entire frequency range. These results show that the forcing frequency has a substantial influence on the shape of the origami, which can range from the closed configuration ($u = 0 \text{ m}$) to the opened configuration ($u = 0.027 \text{ m}$).

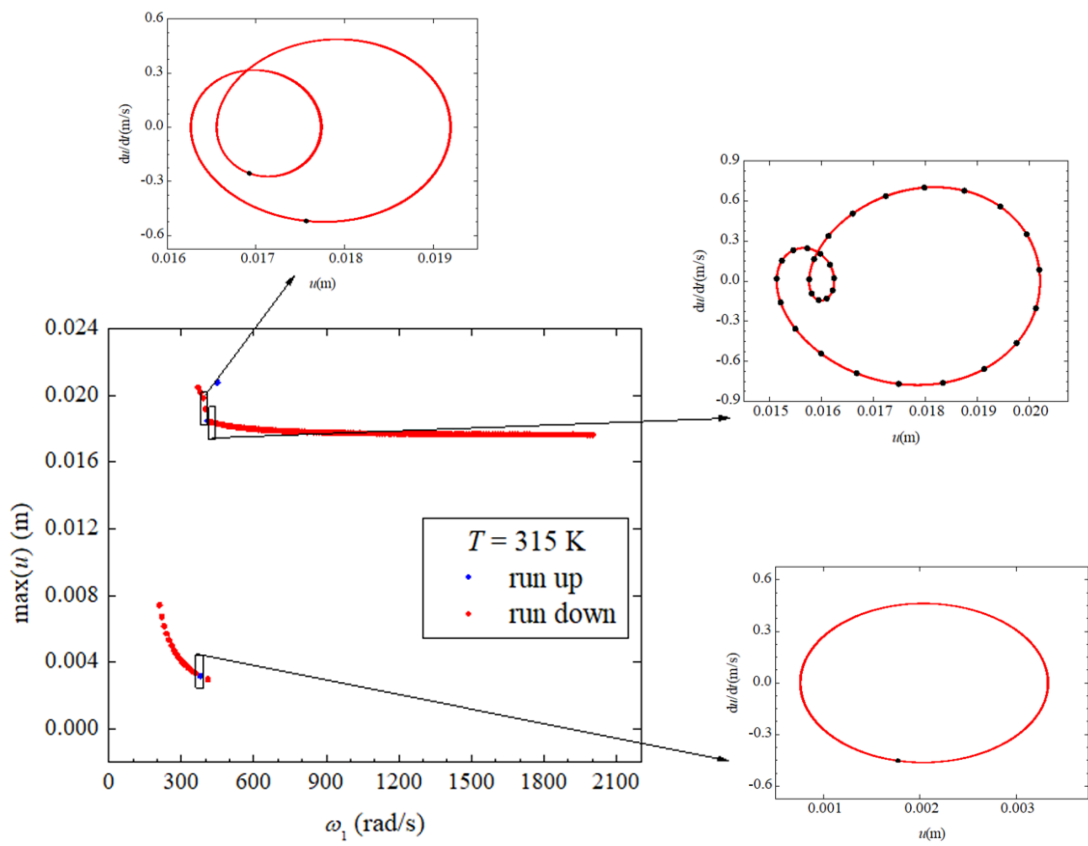


Figure 7-12: Frequency response of the origami for $T = 315$ K ($T_M < T < T_A$) in a run-up and run-down simulation. Some phase spaces positioned in high dynamic regions are highlighted.

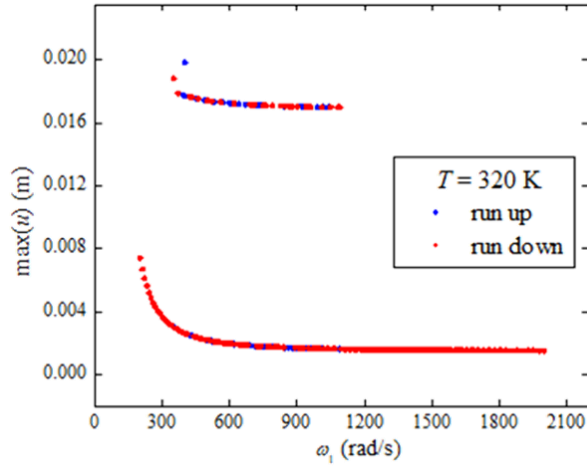


Figure 7-13: Origami frequency response for $T = 320\text{K}$ ($T_A < T$) in a run-up and run-down simulation.

Besides mechanical fluctuations, thermal fluctuations also present some influence on the origami response. In order to show this kind of behavior, consider a case where the origami is subjected to an external force ($\delta_1=10\text{ N}$, $\omega_1=200\text{ rad/s}$) at $T=288\text{K}$, as the case discussed in Figure 7-8. Thermal perturbations are now introduced, being represented by a thermal oscillation: $\delta_T = 2\text{K}$ and $\omega_T = 100\text{ rad/s}$. Under this new condition, the thermal oscillation induces a transient chaos that stabilizes in a periodic steady state (Figure 7-14). Figure 7-14a shows the time response evolution of the SMA displacement, where the origami starts with a transient chaos and stabilizes in a period-2 response approximately after 22 seconds (blue line). During the chaotic response, the structure presents large oscillations, changing between all possible shapes (from completely opened to completely closed). Figure 7-14b presents phase spaces for the whole period, showing the same behavior. Figure 7-14c presents the chaotic saddle during transient period, while Figure 7-14d shows the periodic steady state stabilized response where the origami oscillates around the closed configuration.

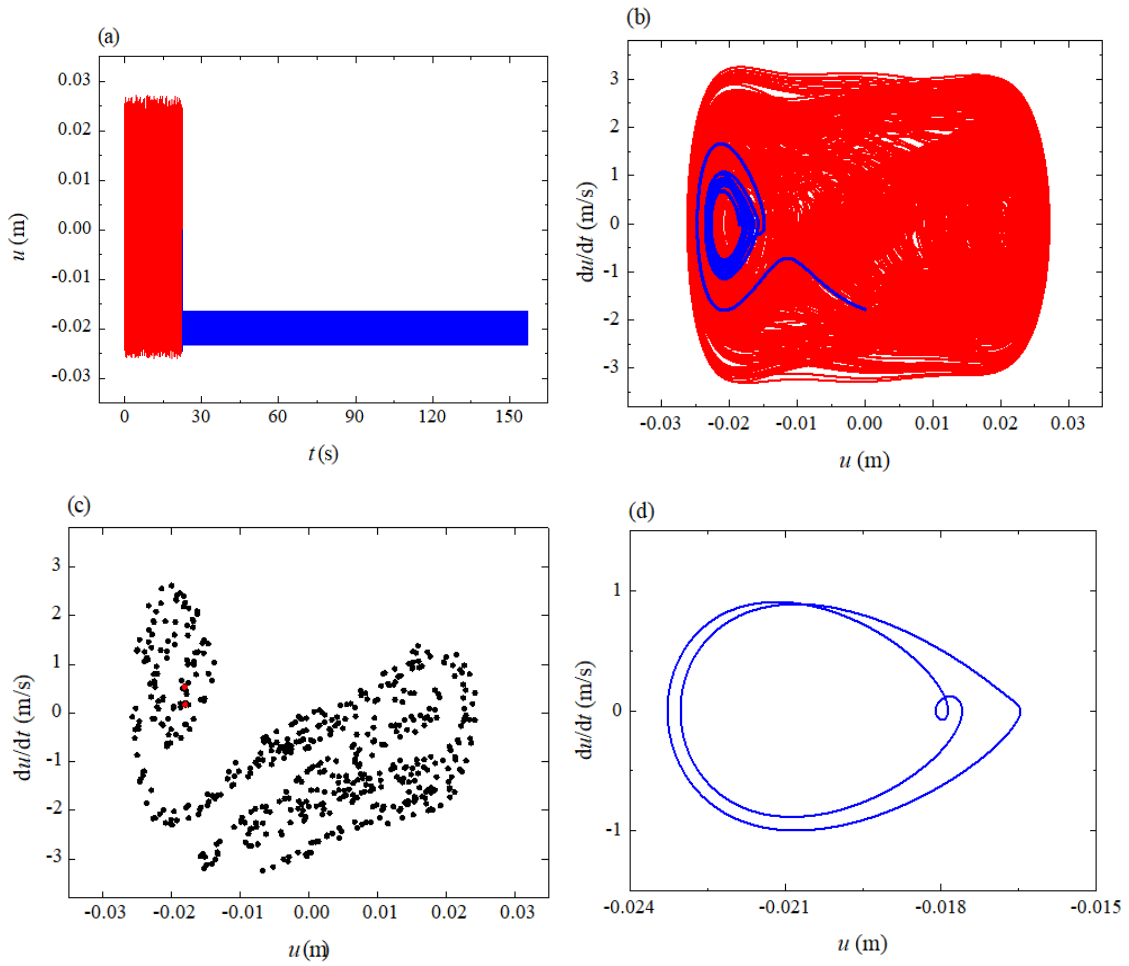


Figure 7-14: Origami response subjected to thermal fluctuation. Transient response is represented by a red line, while stabilized response is represented by a blue line. (a) SMA displacement time history; (b) phase space; (c) Poincaré section associated with transient chaos (chaotic saddle); (d) steady state periodic phase space.

8 Origami-Wheel Robot

Autonomous mobile robots have several applications in the field of industry, military, and security environment. An interesting problem in the design of these robots lies in the control and autonomous movement, promoting an increasing study in the field of robotics. One way to produce these mobile robots is to use two-wheel drive with differential steering and a free balancing wheel (caster). Controlling the two engines independently makes these robots maneuverable and work well indoors (Malu *et al.*, 2014).

The replacement of conventional wheels with deformable wheels allows the car to overcome obstacles more easily, from small cracks to the elevation in steps (Lee *et al.*, 2013). In addition, the trajectory control is done by acting directly on the wheels, using a small number of actuators, significantly reducing the weight of the structure. The response of the car submitted to specific fields can be predicted by a geometric description.

This chapter proposes a mathematical model that describes the trajectory of the origami-wheel robot. The model is based on a dynamic analysis of the GC positioning of the car and each of the wheels. Each origami wheel is attached by the geometric center and has a symmetrical behavior in relation to the attachment point. In addition, all the origami symmetry hypotheses presented in Chapter 6 remain valid. The chapter begins with the proposal of a kinematic model and evolves to dynamic analysis. The model is developed independently of the geometric description of the origami and the constitutive models that describe the phase transformation of SMA springs.

8.1. Kinematics

The robot is composed by a chassis with mass center, G , rigidly attached to weightless axes that are connected to two independent deformable origami wheels with mass centers G_A and G_B (Figure 8-1a). Additionally, the chassis touch the ground at the point H , where a roller is placed. The roller is touching the ground throughout the entire motion of the robot, avoiding a pendular motion of the chassis.

There are basically two ways to attach the origami wheel to the axle: you can attach the axle to one of the acrylic plates, so that the GC of the origami wheel slides over the axle; or the origami can be attached by a support on the shaft, attached to the elastic spring. The analysis made here considers this second form of assembly.

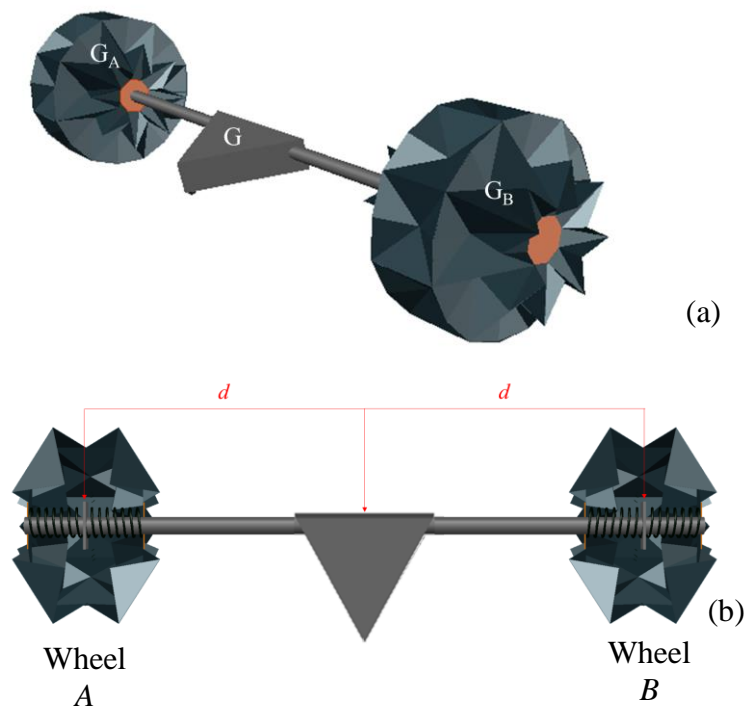


Figure 8-1: Origami-wheel robot of two deformable wheels. (a) Isometric view with indications of the mass centers for the wheels, G_A and G_B , and mass center of the chassis, G ; (b) Superior view, with cuttings on the wheels, for details of the attachment of the wheels to the axes.

The chassis is built such that the mass centers G_A , G_B and G are always aligned and along the axle connecting the wheels. Besides, each wheel is attached to the axle in such a way that its mass center does not slide through the axle, *i.e.*, the mass centers of G_A and G_B are symmetrically positioned with respect to G , kept at a constant distance d (Figure 8-1b).

The yaw movement of the car is promoted by reducing the radius of one of the wheels, keeping the radius of the other wheel fixed. In this way, it is possible to perform a route control or a change of trajectory acting locally on one of the wheels, through the application of a thermal, electric, or magnetic field, depending on the actuator element used.

The position of the car at any time, in relation to an observer fixed in space, is fully described by the positioning of the CG of the car body (x, y, z) and by the inclination of the axle (Φ) . Some of these variables, however, can be rewritten as a function of (or replaced by) R_A and R_B , the spokes of the origami wheels. Figure 8-2 brings the referential frames (RFs) and the variables used to obtain the kinematic model. The robot movement is described with respect to a fixed observer, F , by the positioning of the G point (X, Y, Z) and the yaw angle (Φ) . These variables can be written as a function of R_A and R_B , the A and B wheels radii, respectively. The reduction of the radius of one wheel promotes the yaw motion of the car, allowing maneuverability. The yaw motion is described by the reference frame C (x_1, y_1, z_1) attached to the G point (Figure 8-2-a). The roll movement of the car is characterized by a rotation θ (Figure 8-2-b), related to the wheel radius' reduction, being described by the reference frame P (x_2, y_2, z_2) . The kinematics description of the origami-wheel robot considers a reference frame attached to each wheel: reference frame A (x_3^A, y_3^A, z_3^A) , which describes the rotation of the wheel A , and B (x_3^B, y_3^B, z_3^B) , which describes the rotation of the wheel B (Figure 8-2-c and Figure 8-2-d, respectively). The reference frame A rotates following the point N_A . Similarly, the reference frame B rotates following the point N_B . Under these assumptions, the system kinematics can be described by eight variables: position of the chassis (G point) on plane (x, y) , yaw angle (Φ) , roll angle (θ) , wheel radius (R_A, R_B) and wheel rotation (ϕ_A, ϕ_B) .

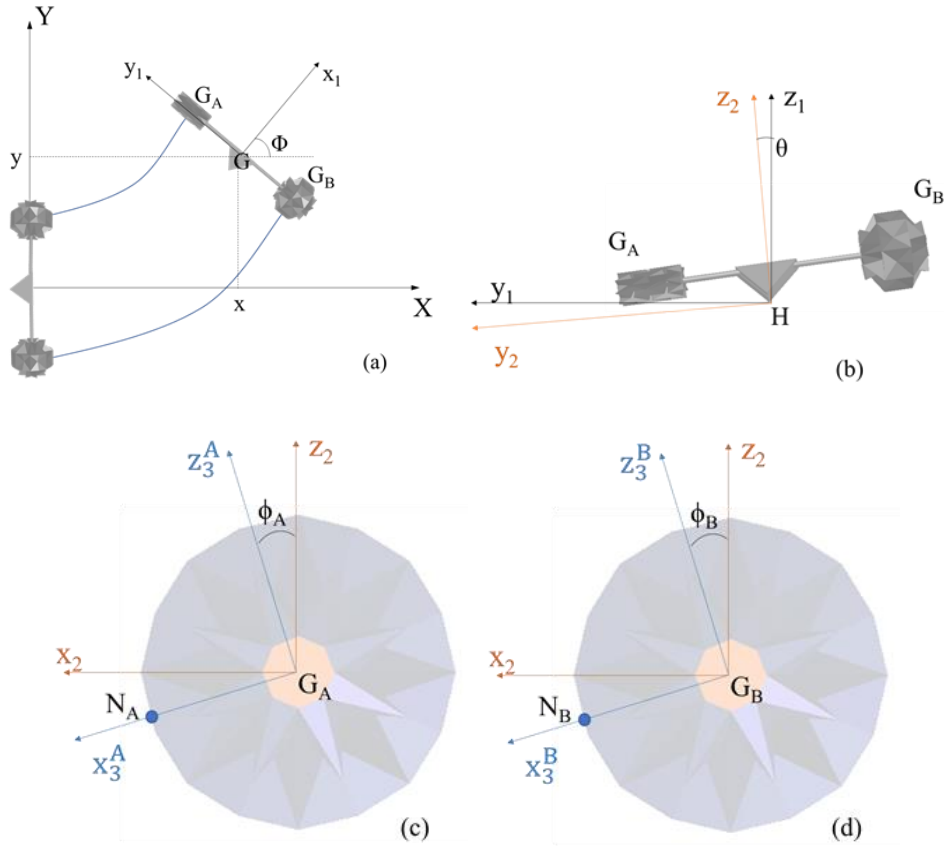


Figure 8-2: Representation of the referential frames to describe the origami-wheel trajectory. (a) indication of the yaw motion (Φ); (b) indication of the roll movement (θ); (c) and (d) indication of the referential frame attached to each wheel for spinning (Φ_A, Φ_B).

The rolling motion of the carriage (θ) occurs due to a difference between the spokes of the two origami wheels. Considering that there is no detachment of the wheels from the ground (the wheels remain in contact with the ground during the entire course), it is possible to extract the relation $\tan(\theta) = (R_B - R_A)/2d$.

The transformation matrices among these frames are presented in the sequence considering a general notation ${}^{S_1}T^{S_2}(\zeta)$ that maps the transformation from reference frame S_1 to S_2 , according to a rotation ζ .

$${}^F T^C = \begin{bmatrix} \cos(\Phi) & -\sin(\Phi) & 0 \\ \sin(\Phi) & \cos(\Phi) & 0 \\ 0 & 0 & 1 \end{bmatrix} \quad (8.1)$$

$${}^C\mathbf{T}^P = \begin{bmatrix} 1 & 0 & 0 \\ 0 & \cos(\theta) & \sin(\theta) \\ 0 & -\sin(\theta) & \cos(\theta) \end{bmatrix} \quad (8.2)$$

$${}^P\mathbf{T}^A = \begin{bmatrix} \cos(\phi_A) & 0 & \sin(\phi_A) \\ 0 & 1 & 0 \\ -\sin(\phi_A) & 0 & \cos(\phi_A) \end{bmatrix} \quad (8.3)$$

$${}^P\mathbf{T}^B = \begin{bmatrix} \cos(\phi_B) & 0 & \sin(\phi_B) \\ 0 & 1 & 0 \\ -\sin(\phi_B) & 0 & \cos(\phi_B) \end{bmatrix} \quad (8.4)$$

Inertial reference frame is denoted by F and therefore quantities described with respect to it are called absolute. Four other mobile referential frames are considered: C , P , A and B . The velocity and position of each mass of the car (wheels and chassis) are described on the referential frame that follows its entity, meaning that is preferable to use the least number of transformations. Based on that, the chassis is represented on the referential frame P and each wheel is represented at its own referential frame, A or B .

The absolute linear velocity of the chassis, ${}^P\mathbf{v}_G$, and the absolute angular velocity of the chassis, ${}^P\boldsymbol{\omega}_P$, are given by

$${}^P\mathbf{v}_G = \begin{bmatrix} -\dot{\Phi}R \sin(\theta) + \dot{x} \cos(\Phi) + \dot{y} \sin(\Phi) \\ \dot{\theta}R + \cos(\theta) (\dot{y} \cos(\Phi) - \dot{x} \sin(\Phi)) \\ \dot{R} + \cos(\theta) (\dot{y} \cos(\Phi) - \dot{x} \sin(\Phi)) \end{bmatrix} \quad (8.5)$$

$${}^P\boldsymbol{\omega}_P = \begin{bmatrix} -\dot{\theta} \\ -\dot{\Phi} \sin(\theta) \\ \dot{\Phi} \cos(\theta) \end{bmatrix} \quad (8.6)$$

where $R = (R_A + R_B)/2$. Besides, the absolute linear velocity of the center of mass of the wheel, ${}^P\mathbf{v}_i$, and the absolute angular velocity of the wheel, ${}^i\boldsymbol{\omega}_i$, are given by

$${}^P\mathbf{v}_i = \begin{bmatrix} -\dot{\Phi}(R \sin(\theta) + \rho \cos(\theta)) + \dot{x} \cos(\Phi) + \dot{y} \sin(\Phi) \\ \dot{\theta}R + \cos(\theta) (\dot{y} \cos(\Phi) - \dot{x} \sin(\Phi)) \\ \dot{R} - \rho\dot{\theta} + \sin(\theta) (\dot{y} \cos(\Phi) - \dot{x} \sin(\Phi)) \end{bmatrix} \quad (8.7)$$

$${}^i\boldsymbol{\omega}_i = \begin{bmatrix} -\dot{\theta} \cos(\phi_i) - \dot{\Phi} \cos(\theta) \sin(\phi_i) \\ \dot{\phi}_i - \dot{\Phi} \sin(\theta) \\ -\dot{\theta} \sin(\phi_i) + \dot{\Phi} \cos(\theta) \cos(\phi_i) \end{bmatrix} \quad (8.8)$$

where it is assumed, for wheel A , $i = A$, $\phi_i = \phi_A$ and $\rho = d$, and, for wheel B , $i = B$, $\phi_i = \phi_B$ and $\rho = -d$.

The robot performs a roll movement around the axis x_1 , defining the yaw motion, being H the contact point between the chassis and the floor (Figure 8-2b). The absolute linear velocity ${}^c\mathbf{v}_H$ is given by,

$${}^c\mathbf{v}_H = \begin{bmatrix} \dot{x} \cos(\Phi) + \dot{y} \sin(\Phi) \\ \dot{y} \cos(\Phi) - \dot{x} \sin(\Phi) \\ 0 \end{bmatrix} \quad (8.9)$$

The velocity of point N_i $i = (A, B)$ is described on the referential frame that follows the wheel rotation. Hence, the velocity of N_i of the wheel i , $i = A, B$, is given by ${}^i\mathbf{v}_{N_i} = [v_{x_3} \quad v_{y_3} \quad v_{z_3}]^T$, where each component is presented in the sequence

$$\begin{aligned} v_{x_3} = & [\dot{x} \cos(\Phi) + \dot{y} \sin(\Phi)] \cos(\phi_i) - [-\dot{x} \sin(\Phi) + \\ & \dot{y} \cos(\Phi)] \sin(\theta) \sin(\phi_i) + \dot{R}_i - \dot{R} \sin(\phi_i) + \dot{\theta} \rho \sin(\phi_i) - \dot{\Phi} [\rho \cos(\theta) \cos(\phi_i) + \\ & R \cos(\phi_i) \sin(\theta)] \end{aligned} \quad (8.10a)$$

$$v_{y_3} = \cos(\theta) [-\dot{x} \sin(\Phi) + \dot{y} \cos(\Phi) + \dot{\Phi} R_i \cos(\phi_i)] + \dot{\theta} [R - R_i \sin(\phi_i)] \quad (8.10b)$$

$$\begin{aligned} v_{z_3} = & [\dot{x} \cos(\Phi) + \dot{y} \sin(\Phi)] \sin(\phi_i) + [-\dot{x} \sin(\Phi) + \dot{y} \cos(\Phi)] \sin(\theta) \cos(\phi_i) + \\ & \dot{R} \cos(\phi_i) - \dot{\Phi} R_i - \dot{\theta} \rho \cos(\phi_i) - \dot{\Phi} [\rho \cos(\theta) \sin(\phi_i) + (R \sin(\phi_i) - R_i) \sin(\theta)] \end{aligned} \quad (8.10c)$$

where $\rho = d$ and $i = A$, for wheel A , and $\rho = -d$ and $i = B$, for wheel B .

8.1.1. Constraints

The robot movement needs to be associated with constraints in order to be properly described. Five nonslip conditions are described in this formulation: each wheel roll without slipping in the direction of the motion; both wheels maintain contact with the floor during the entire motion, without penetration or jumping; and there is no slide on

the contact between the chassis and the soil, represented by the contact point H . The description of these constraints considers that, $\phi_A = \pi/2$ and $\phi_B = \pi/2$; \mathbf{e}_{z_3} is the unitary vector on the motion direction z_3^i ($i = A, B$), and \mathbf{e}_{z_1} is the unitary vector on the direction perpendicular to the motion z_1^C .

Considering the first nonslip condition, the velocity of the wheel vanishes at the point of contact of each wheel on the direction of the motion, z_3^i . Therefore, the first nonslip condition is given by $v_{z_3}^i = 0$ at $\phi_i = \pi/2$. Therefore, the constraints are expressed by,

$$\begin{aligned} v_{z_3}^A &= {}^A\mathbf{v}_{N_A}(\phi_A = \pi/2) \cdot \mathbf{e}_{z_3} = 0 \\ v_{z_3}^B &= {}^B\mathbf{v}_{N_B}(\phi_B = \pi/2) \cdot \mathbf{e}_{z_3} = 0 \end{aligned} \quad (8.11)$$

Based on these equations, the following constraints are defined,

$$\dot{x} \cos(\Phi) + \dot{y} \sin(\Phi) - \dot{\Phi}[d \cos(\theta) - D \sin(\theta)] = \dot{\phi}_A R_A \quad (8.12)$$

$$\dot{x} \cos(\Phi) + \dot{y} \sin(\Phi) + \dot{\Phi}[d \cos(\theta) - D \sin(\theta)] = \dot{\phi}_B R_B \quad (8.13)$$

where $D = R_A - R_B/2$.

Next step is to analyze the vertical component of each wheel velocity described on either C or P referential frame. In the contact point of each wheel with the soil, the vertical component of the velocity (v_{z_1}) vanishes. Therefore,

$$\begin{aligned} v_{z_1}^A &= {}^C\mathbf{v}_{N_A}(\phi_A = \pi/2) \cdot \mathbf{e}_{z_1} = 0 \\ v_{z_1}^B &= {}^C\mathbf{v}_{N_B}(\phi_B = \pi/2) \cdot \mathbf{e}_{z_1} = 0 \end{aligned} \quad (8.14)$$

Considering the components described by equations (8.10a) to (8.10c) and the transformation matrixes (8.1 to 8.4), the vertical component of the velocity in the contact point ($\phi_i = \pi/2$), $i = A, B$, is given by

$$v_{z_1} = -\dot{\theta}[(R - R_i) \sin(\theta) + \rho \cos(\theta)] + (\dot{R} - \dot{R}_i) \cos(\theta) \quad (8.15)$$

where $\rho = d$ and $i = A$, for wheel A , and $\rho = -d$ and $i = B$, for wheel B . Since $R = R_A + R_B/2$ and $D = R_A - R_B/2$, and imposing the nonslip condition ($v_{z_1} = 0$), the third constraint is reduced for a single equation given by

$$-\dot{\theta}[-D \sin(\theta) + d \cos(\theta)] - \dot{D} \cos(\theta) = 0 \quad (8.16)$$

Finally, the nonslip condition considers the contact between the chassis and the soil. Since there is no sliding motion in the direction perpendicular to the motion, the constraint is obtained by imposing that the lateral absolute velocity vanishes,

$$v_{y_1}^H = {}^c \mathbf{v}_H \cdot \mathbf{e}_{z_1} = 0 \quad (8.17)$$

Therefore, based on the previous definitions, (8.17) is represented by the following equation

$$\dot{x} \sin(\Phi) - \dot{y} \cos(\Phi) = 0 \quad (8.18)$$

Therefore, the kinematics is described with 8 variables ($x, y, \Phi, \theta, R_A, R_B, \phi_A, \phi_B$) and 4 constraints (Equations 8.12, 8.13, 8.16, 8.18), resulting in a 4-DOF model.

8.2. Dynamical formulation

The dynamical model is obtained by energetic approach, considering Lagrange multipliers on the constraints. By considering the Lagrangian as the difference between the kinetic, E_k , and potential, E_p , energies ($\mathcal{L} = E_k - E_p$), described as a function of generalized coordinates, $q_i^* = [x, y, \Phi, \theta, R_A, R_B, \phi_A, \phi_B]^T$, the Lagrange formulation is given by

$$\frac{d}{dt} \left(\frac{\partial \mathcal{L}}{\partial \dot{q}_i^*} \right) - \frac{\partial \mathcal{L}}{\partial q_i^*} = Q_i + \sum_{j=1}^{N_{var} - N_0} \lambda_j f_{ij} \quad (i = 1, \dots, N) \quad (8.19)$$

where Q_i are the generalized forces, N_{var} is the number of variables that describe the system, N_0 is the number of degrees of freedom, λ_j are the Lagrange multipliers and f_{ij} are the multiplier factors for the constraint equation.

Nonslip conditions are defined as non-holonomic restrictions, being expressed by the following equation.

$$\sum_{j=1}^N f_{ij} \delta q_i^* = 0 \quad (i = 1, \dots, N - N_0) \quad (8.20)$$

The multiplier factors for the Lagrange equation are obtained by comparing Equation (8.20) with each one of the four restrictions (Equations 8.12, 8.13, 8.16, 8.18), and they are expressed in Table 8-1.

Table 8-1: Multiplier factors for the constraint equations associated with each Lagrange multiplier.

f_{ij}	$j = 1$	$j = 2$	$j = 3$	$j = 4$
$i = 1$	$\cos(\Phi)$	$\cos(\Phi)$	0	$\sin(\Phi)$
$i = 2$	$\sin(\Phi)$	$\sin(\Phi)$	0	$-\cos(\Phi)$
$i = 3$	$D \sin(\theta)$ $-d \cos(\theta)$	$d \cos(\theta)$ $-D \sin(\theta)$	0	0
$i = 4$	0	0	$d \cos(\theta)$ $-D \sin(\theta)$	0
$i = 5$	0	0	$\cos(\theta)/2$	0
$i = 6$	0	0	$-\cos(\theta)/2$	0
$i = 7$	$-R_A$	0	0	0
$i = 8$	0	$-R_B$	0	0

The Lagrange method requires the explicit definition of system energy (Lanczos, 1966). The kinetic energy can be divided into translational, E_k^T , and rotational E_k^R energies, presented in the sequence,

$$\begin{aligned}
E_k^T = & \frac{m_t}{2} \{ \dot{x}^2 + \dot{y}^2 + \dot{R}^2 + [\dot{\Phi}^2 \sin^2(\theta) + \dot{\theta}^2] R^2 - 2\dot{\Phi}R \sin(\theta) [\dot{x} \cos(\Phi) + \\
& \dot{y} \sin(\Phi)] + 2[\dot{\theta}R \cos(\theta) + \dot{R} \sin(\theta)] [\dot{y} \cos(\Phi) - \dot{x} \sin(\Phi)] \} + \left[\frac{(m_t - m_G)}{2} d^2 + \right. \\
& \left. M(f_A^2 + f_B^2) \right] [\dot{\Phi}^2 \cos^2(\theta) + \dot{\theta}^2] + M(\dot{f}_A^2 + \dot{f}_B^2)
\end{aligned} \tag{8.21}$$

$$\begin{aligned}
E_k^R = & \frac{\dot{\theta}^2}{2} (I_{A1} + I_{B1} + J_1) + \frac{\dot{\Phi}^2}{2} [(I_{A1} + I_{B1} + J_3) \cos^2(\theta) + (I_{A2} + I_{B2} + \\
& J_2) \cos^2(\theta)] - \dot{\Phi} \sin(\theta) \left(\frac{\dot{\Phi}_A I_{A2}}{2} + \frac{\dot{\Phi}_B I_{B2}}{2} \right)
\end{aligned} \tag{8.22}$$

where m_G is the mass of the chassis, M is the mass of each acrylic plate and m_t is the total mass of the robot, including chassis and wheels; I_1^i , I_2^i and I_3^i are the principal inertia moments of the origami wheel ($i = A$ or B) related to the axis x_3^i , y_3^i and z_3^i , correspondingly; and J_1 , J_2 and J_3 are the principal inertia moments of the chassis related to the axis x_2 , y_2 and z_2 , correspondingly.

The potential energy of the system is a function of the actuators potential energy (SMAs and elastic passive spring) and the gravitational energy, being expressed as,

$$E_P = E_{SMA_A} + E_{SMA_B} + E_{E_A} + E_{E_B} + m_t g R \cos(\theta) \tag{8.23}$$

where the potential energy of each shape memory alloy spring (E_{SMA}) and the elastic passive spring (E_E) depends on the constitutive model chosen to describe their behavior, and g is the gravitational constant. Thus, $\mathcal{L} = E_k^T + E_k^R - E_P$.

The SMA has its behavior described by the polynomial constitutive model presented at subsection A.2, and the elastic passive spring has its behavior described by the elastic model presented at section A.4.

By employing the Lagrange equation (8.19), considering the constraints expressed in Table 8-1, and the non-conservative forces acting on the system, it is possible to obtain the following equations. Note that external forces applied to the wheels are represented by $F_A(t)$ and $F_B(t)$, ξ is the damping coefficient that represents the general dissipation of the systems, ξ_w is the viscous damping coefficient from the wheel rotation on the massless axes and τ_A and τ_B are the torques acting on each wheel.

$$\begin{aligned}
\frac{d}{dt} \left(\frac{\partial \mathcal{L}}{\partial \dot{q}_1^*} \right) - \frac{\partial \mathcal{L}}{\partial q_1^*} &= \lambda_1 \cos(\Phi) + \lambda_2 \cos(\Phi) + \lambda_4 \sin(\Phi) \\
\frac{d}{dt} \left(\frac{\partial \mathcal{L}}{\partial \dot{q}_2^*} \right) - \frac{\partial \mathcal{L}}{\partial q_2^*} &= \lambda_1 \sin(\Phi) + \lambda_2 \sin(\Phi) - \lambda_4 \cos(\Phi) \\
\frac{d}{dt} \left(\frac{\partial \mathcal{L}}{\partial \dot{q}_3^*} \right) - \frac{\partial \mathcal{L}}{\partial q_3^*} &= (\lambda_1 - \lambda_2)[D \sin(\theta) - d \cos(\theta)] \\
\frac{d}{dt} \left(\frac{\partial \mathcal{L}}{\partial \dot{q}_4^*} \right) - \frac{\partial \mathcal{L}}{\partial q_4^*} &= -\lambda_3[D \sin(\theta) - d \cos(\theta)] \\
\frac{d}{dt} \left(\frac{\partial \mathcal{L}}{\partial \dot{q}_5^*} \right) - \frac{\partial \mathcal{L}}{\partial q_5^*} &= F_A(t) - \xi \dot{R}_A + \lambda_3 \cos(\theta)/2 \\
\frac{d}{dt} \left(\frac{\partial \mathcal{L}}{\partial \dot{q}_6^*} \right) - \frac{\partial \mathcal{L}}{\partial q_6^*} &= F_B(t) - \xi \dot{R}_B - \lambda_3 \cos(\theta)/2 \\
\frac{d}{dt} \left(\frac{\partial \mathcal{L}}{\partial \dot{q}_7^*} \right) - \frac{\partial \mathcal{L}}{\partial q_7^*} &= \tau_A - \xi_w \dot{\phi}_A - R_A \lambda_1 \\
\frac{d}{dt} \left(\frac{\partial \mathcal{L}}{\partial \dot{q}_8^*} \right) - \frac{\partial \mathcal{L}}{\partial q_8^*} &= \tau_B - \xi_w \dot{\phi}_B - R_B \lambda_2
\end{aligned} \tag{8.24}$$

Eliminating the Lagrange multipliers of the set of equations (8.24), four equations of motion describe the origami robot movement

$$\begin{aligned}
\left(\frac{d}{dt} \left(\frac{\partial \mathcal{L}}{\partial \dot{q}_1^*} \right) - \frac{\partial \mathcal{L}}{\partial q_1^*} \right) \cos(\Phi) + \left(\frac{d}{dt} \left(\frac{\partial \mathcal{L}}{\partial \dot{q}_2^*} \right) - \frac{\partial \mathcal{L}}{\partial q_2^*} \right) \sin(\Phi) &= \frac{\tau_A - \xi_w \dot{\phi}_A - \left(\frac{d}{dt} \left(\frac{\partial \mathcal{L}}{\partial \dot{q}_7^*} \right) - \frac{\partial \mathcal{L}}{\partial q_7^*} \right)}{R_A} + \\
\frac{\tau_B - \xi_w \dot{\phi}_B - \left(\frac{d}{dt} \left(\frac{\partial \mathcal{L}}{\partial \dot{q}_8^*} \right) - \frac{\partial \mathcal{L}}{\partial q_8^*} \right)}{R_B} &
\end{aligned} \tag{8.25a}$$

$$\begin{aligned}
\frac{d}{dt} \left(\frac{\partial \mathcal{L}}{\partial \dot{q}_3^*} \right) - \frac{\partial \mathcal{L}}{\partial q_3^*} &= \left(\frac{\tau_A - \xi_w \dot{\phi}_A - \left(\frac{d}{dt} \left(\frac{\partial \mathcal{L}}{\partial \dot{q}_7^*} \right) - \frac{\partial \mathcal{L}}{\partial q_7^*} \right)}{R_A} - \frac{\tau_B - \xi_w \dot{\phi}_B - \left(\frac{d}{dt} \left(\frac{\partial \mathcal{L}}{\partial \dot{q}_8^*} \right) - \frac{\partial \mathcal{L}}{\partial q_8^*} \right)}{R_B} \right) [D \sin(\theta) - \\
d \cos(\theta)] &
\end{aligned} \tag{8.25b}$$

$$\frac{d}{dt} \left(\frac{\partial \mathcal{L}}{\partial \dot{q}_5^*} \right) - \frac{\partial \mathcal{L}}{\partial q_5^*} = F_A(t) - \xi \dot{R}_A - \frac{\frac{d}{dt} \left(\frac{\partial \mathcal{L}}{\partial \dot{q}_4^*} \right) - \frac{\partial \mathcal{L}}{\partial q_4^*}}{D \sin(\theta) - d \cos(\theta)} \cos(\theta)/2 \tag{8.25c}$$

$$\frac{d}{dt} \left(\frac{\partial \mathcal{L}}{\partial \dot{q}_6^*} \right) - \frac{\partial \mathcal{L}}{\partial q_6^*} = F_B(t) - \xi \dot{R}_B + \frac{\frac{d}{dt} \left(\frac{\partial \mathcal{L}}{\partial \dot{q}_4^*} \right) - \frac{\partial \mathcal{L}}{\partial q_4^*}}{D \sin(\theta) - d \cos(\theta)} \cos(\theta)/2 \tag{8.25d}$$

Equations of motion (8.25a) to (8.25d) can be rewritten in a matrix form as follows,

$$\mathbf{M}(\mathbf{q})\ddot{\mathbf{q}} + \mathbf{C}(\dot{\mathbf{q}}, \mathbf{q})\dot{\mathbf{q}} + \mathbf{D}(\mathbf{q})\dot{\mathbf{q}} + \mathbf{g}(\mathbf{q}) = \mathbf{f}_{ext} \tag{8.26}$$

where $\mathbf{q} = [x, \Phi, R_A, R_B]^T$ is the independent generalized coordinate vector, $\mathbf{M}(\mathbf{q})$ is the inertia matrix, $\mathbf{C}(\dot{\mathbf{q}}, \mathbf{q})$ is the matrix containing the higher-order terms on $\dot{\mathbf{q}}$,

$\mathbf{D}(\mathbf{q})$ is the damping matrix, $\mathbf{g}(\mathbf{q})$ is the stiffness and gravitational vector and \mathbf{f}_{ext} is the vector with the external forces. The inertia matrix is composed by terms that evolve on time with the form.

$$\mathbf{M}(\mathbf{q}) = \begin{bmatrix} m_{11} & m_{12} & 0 & 0 \\ m_{21} & m_{22} & 0 & 0 \\ 0 & 0 & m_{33} & m_{34} \\ 0 & 0 & m_{34} & m_{44} \end{bmatrix} \quad (8.27)$$

with determinant $\det(\mathbf{M}(\mathbf{q})) = (m_{11}m_{22} - m_{12}m_{21})(m_{33}m_{44} - m_{34}^2)$.

Since its determinant is always non-zero, it is possible to invert the inertia matrix, resulting in the following equation.

$$\ddot{\mathbf{q}} = \mathbf{M}^{-1}(\mathbf{q})[\mathbf{f}_{ext} - \mathbf{C}(\dot{\mathbf{q}}, \mathbf{q})\dot{\mathbf{q}} - \mathbf{D}(\mathbf{q})\dot{\mathbf{q}} - \mathbf{g}(\mathbf{q})] \quad (8.28)$$

This equation of motion is solved using a fourth order Runge-Kutta method with fixed steps using the equation in its canonical form.

$$\begin{aligned} \dot{z}_i &= z_{i+1} & i &= 0,2,4,6 \\ \dot{z}_{i+1} &= \mathbf{M}_{ip}^{-1}[F_p - [\mathbf{C} + \mathbf{D}]_{pj}z_{2j+1} - G_p] & 'j &= 0,1,2,3 \end{aligned} \quad (8.29)$$

The terms of inertia presented in (8.27) are functions of the geometry of the constituent elements of the system, and some simplifications are considered. The moments of inertia of origami wheels are a function of origami and acrylic plates. The acrylic plates are regular octagons, by construction, making the rotation inertia in the z_3 and x_3 directions equal. Thus, for an apothem octagon l_p , we have $I_1 = I_3 = \frac{4}{3}(4\sqrt{2} - 5)l_p^4$ and $I_2 = 2I_1$. The inertia of the origami is calculated as eight masses, distant from R_i from the center of the wheel, with $i = A, B$. The body of the car is considered to be a parallelepiped in width, length and thickness l , c and e , respectively. Thus, $J_1 = \frac{m_G}{12}(c^2 + l^2)$, $J_2 = \frac{m_G}{12}(l^2 + e^2)$ and $J_3 = \frac{m_G}{12}(c^2 + e^2)$.

8.3. Dynamical analysis

This section presents the study of the dynamics of the car with origami wheels and the behavior of the system is evaluated for usual operating conditions, regarding the soil conditions (flat or irregular) and temperature (without and with disturbances). The purpose of the analysis is to verify the influence of dynamics on the car's behavior, especially on the car's trajectory.

8.3.1. Different driven cases

The movement of the robot is driven by the motors attached to each one of the wheels, described by a torque τ_i ($i = A, B$). Alternatively, the motion can be driven by the robot linear velocity, instead of prescribing the torques. The two driving possibilities are represented in Figure 8-3.

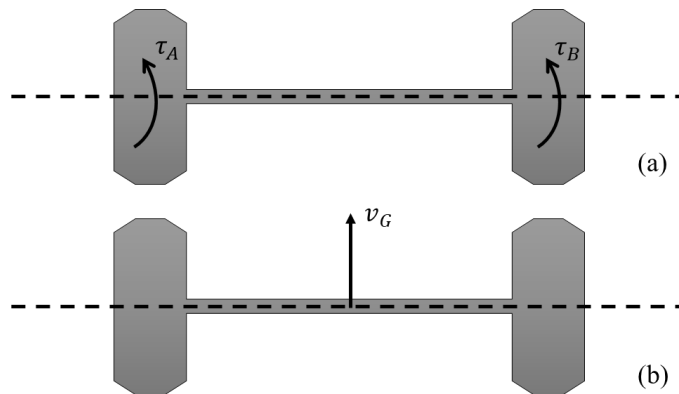


Figure 8-3: Driven situations of the robot: (a) driven torques at each wheel; (b) robot linear velocity.

Based on that, consider a situation where the torques are prescribed. The resistance to rotation is assumed to be the same for both wheels, being represented by $\xi_w \dot{\phi}_i$. In this regard, the torque driven motion of the robot has the following velocity,

$$v_G = \frac{v_A + v_B}{2} = \frac{\tau_A R_A}{2\xi_w} + \frac{\tau_B R_B}{2\xi_w} \quad (8.30)$$

Alternatively, by considering a motion driven by the robot linear velocity, since the wheels radius change, the linear velocity is a function of the angular velocity of the wheel and the radius rate variation, given by

$$v_i = \dot{\phi}_i R_i + \phi_i \dot{R}_i \quad (i = A \text{ or } B) \quad (8.31)$$

By considering the dynamic equilibrium of a single wheel under rotation, the torques τ_A and τ_B are obtained as follows: $\tau_i - \xi_w \dot{\phi}_i = I_i \ddot{\phi}_i$ ($i = A$ or B). By calculating $\dot{\phi}_i$ and $\ddot{\phi}_i$ from kinematics argues, the following equation is obtained,

$$\tau_i = -\frac{I_i}{R_i} \phi_i \ddot{R}_i - 2 \frac{I_i}{R_i} \dot{\phi}_i \dot{R}_i - \frac{\phi_i \xi_w}{R_i} \dot{R}_i + \xi_w \frac{v_G}{R_i} \quad (i = A \text{ or } B) \quad (8.32)$$

Figure 8-4 presents a comparison between the velocity driven and torque driven cases, considering the temperature cycles presented in Figure 8-4-a. Figure 8-4-b presents both paths followed by the origami robot, showing dramatic differences. During the heating/cooling process, each wheel individually reduces/increases its radius, promoting a change on the origami robot velocity. Note that the velocity driven case is associated with torques that change their values during the heating/cooling process. The torque of the wheel under the temperature variation increases its value to compensate the radius reduction, keeping the velocity constant at 2 m/s. Once the SMA is cooled down and the initial shape is restored, the torque goes back to the initial value of 0.0141 Nm, as can be seen at Figure 8-4-c. On the other hand, for the torque driven case, a reduction on the wheel radius results on a reduction of the wheel velocity to compensate it and keep the torque constant (Figure 8-4-d).

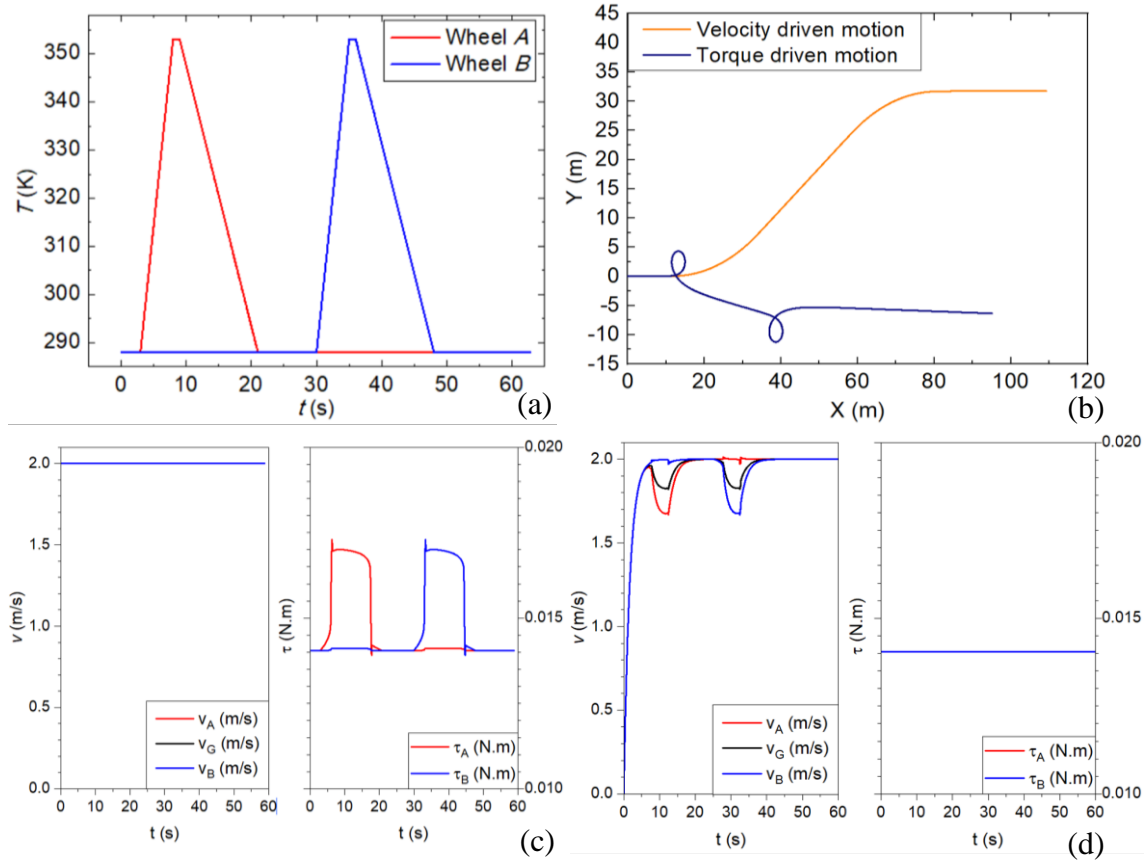


Figure 8-4: Origami wheel robot movement for different driven conditions. (a) Thermal load; (b) Path; (c) velocity driven motion: time evolution of the velocities of the chassis and wheels and time evolution of the torques; (d) torque driven motion: time evolution of the linear velocities of the chassis and wheels and time evolution of the torques.

From now on, all simulations are performed considering the velocity driven case with $|\mathbf{v}_G| = 2$ m/s.

8.3.2. Free vibration system – definition of a preferred path

The free vibration analysis aims to study the route taken by the car after applying a thermal load to the SMA actuators. Initially consider that the origami robot moves with a known initial speed of $|\mathbf{v}_G| = 2$ m/s, with the wheels half-opened ($u_0 = 0.02$ m) at low temperature ($T = 288$ K).

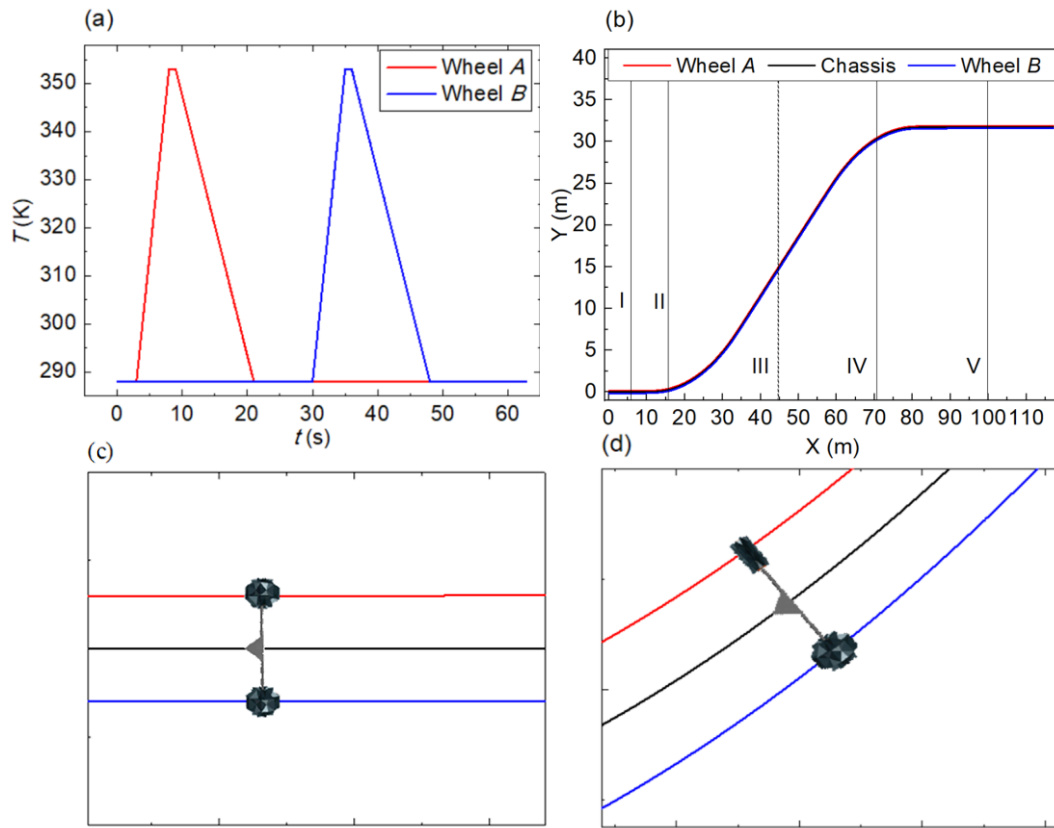


Figure 8-5: Representation for an arbitrary desired path of the origami wheel robot. (a) Thermal load applied to each wheel individually, promoting a turn counterclockwise and then clockwise; (b) desired arbitrary path, starting with a straight line and ending on a straight line, shifted vertically from the original one; (c) zoom on the region I pointed at (b), where the car follows a straight line; (d) zoom on the region II, where the car turns left (counterclockwise turn from wheel B to wheel A).

Figure 8-5 shows the behavior of the origami car when subjected to a history of thermal loading considering a viscous dissipation of 5 Ns/m. The car's trajectory is controlled by heating the SMA actuators on each wheel. Figure 8-5a presents the thermal cycles applied to the wheels and Figure 8-5b shows the path followed by the origami robot. The origami robot starts moving forward, in a straight path (excerpt I in Figure 8-5b, zoom at Figure 8-5c). A heating/cooling cycle is then applied to the wheel A . During the heating process, the SMA recovers its residual displacement, reducing the wheel radius, promoting a path change of the robot to the left (counterclockwise rotation – excerpt II in Figure 8-5b, zoom in Figure 8-5d). When it is cooled, the elastic spring

induces a displacement like the initial one, recovering the original origami shape. Since both radii are the same, the car returns to a straight path (excerpt III). The same process is then applied to the wheel *B*, turning the origami car to the right (clockwise rotation – excerpt IV), and putting it back to a straight path (excerpt V) on a subsequent cooling process. Note that both heating/cooling cycles have the same rate, and the phase transformation martensite-austenite is completed during the heating process and the reverse austenite-martensite is completed during the cooling process, which makes the final excerpt (V) and the first one (I) parallel to each other. This route will be defined as a preferred or desired route, and the subsequent analysis assess disturbances in this trajectory promoted by different thermal loading cycles and by mechanical efforts.

Different thermal loads are investigated, considering that the origami wheel robot path is described by the projection of the *G* point (path followed by the mass center of the robot). Basically, four cases are treated: a desired reference path, Case I (Figure 8-6a); both wheels are heated in the same way inducing a partial phase transformation, Case II (Figure 8-6b); heating induce incomplete phase transformation on wheel *A* and complete on wheel *B*, Case III (Figure 8-6c); and heating induce the opposite case of the previous one, complete phase transformation on wheel *A* and incomplete on wheel *B*, Case IV (Figure 8-6d).

When the thermal cycle is applied symmetrically, with the same rate and limits on both wheels, the origami robot follows a similar path (final straight line is parallel to the excerpt V in Figure 8-5b), despite of the path curvature, returning to the initial orientation (*X* axis). The partial phase transformation promotes a smaller radius curvature that makes the origami robot to follow a straight path either towards south-east (Case III) or towards north-east (Case IV) with the same inclination related to *X* axis. After the heating cycle is finished, a plateau of constant temperature is reached where $T > T_A$. Under this condition, it is possible to find a linear relation between the length of the plateau (time that the high temperature is kept constant) and the path curvature described by origami robot.

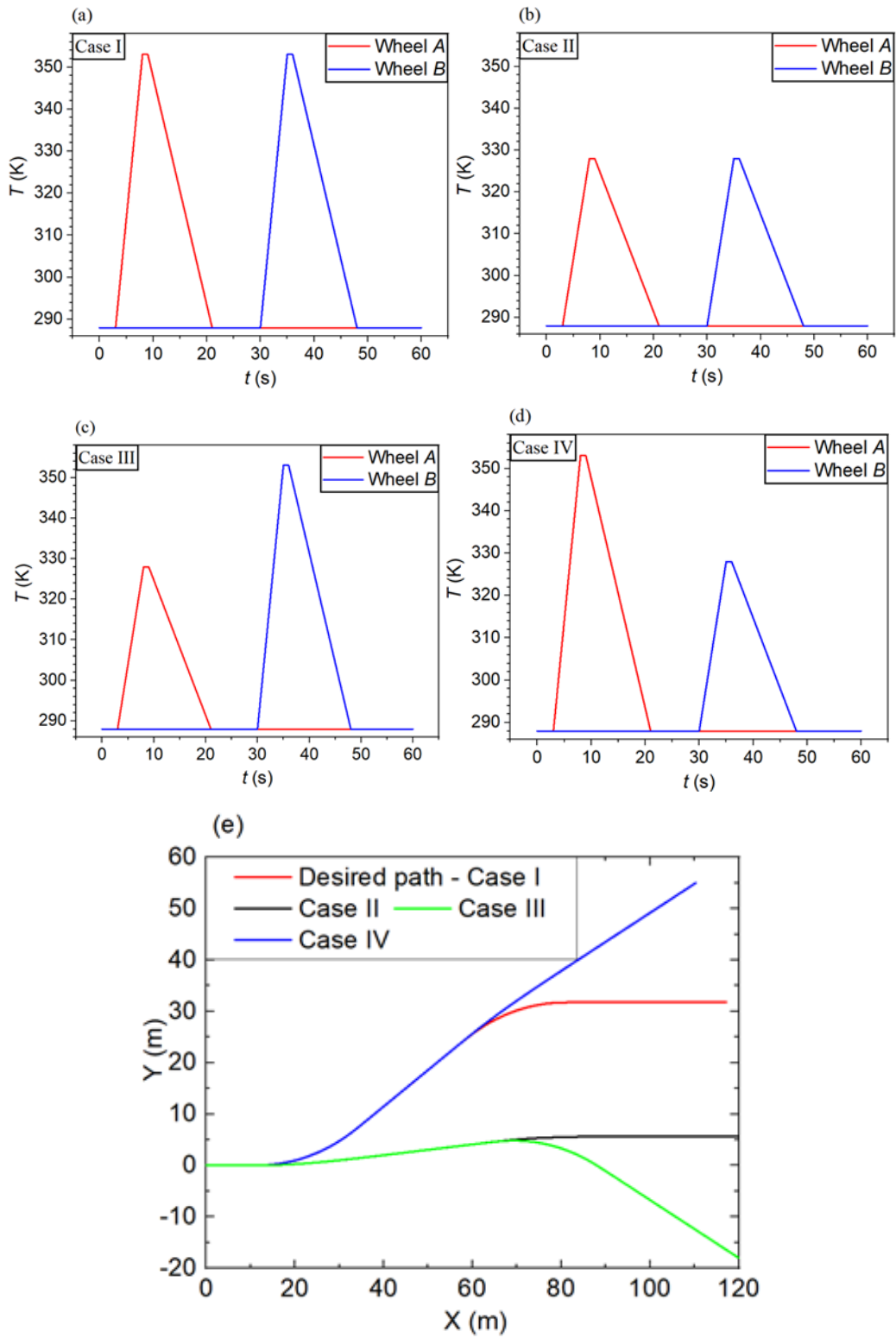


Figure 8-6: Thermal cycles (a) to (d) and path (e) described by the projection of G point on the fixed frame (X, Y, Z) .

8.3.3. Forced vibration system – origami-soil interaction and temperature variation

This sub-section discusses the origami robot subjected to forced vibrations applied to the origami wheels, simulating soil disturbances. This forcing causes changes to the wheels' radii, as seen in Section 7.3. The radius change is reflected in changes in the robot's trajectory since the difference in wheel radius promotes rotations θ and Φ . If radius R_A is smaller than radius R_B , there is a yaw motion to the left (counterclockwise). On the other hand, if $R_B < R_A$, there is a yaw motion to the right (clockwise). Initially, the change in the origami robot's trajectory is evaluated considering that it is only subjected to mechanical loading, at constant temperature, but with the wheels placed on different soils.

The origami-soil interaction is a difficult problem to be described. The essence of the interaction is the nonlinearity in contact mechanics, where the contact reaction and contact surface can only be specified after contact (Nishiyama *et al.*, 2016). Usually, the wheel-soil interaction takes into account the contact area between the wheel and the soil, the wheel flexibility, soil malleability and wheel sinkage (Chen *et al.*, 2020). Flexible wheels, however, require a modified study of the pressure-sinkage models, once that the wheel flexibility might lead to larger sinkage areas when comparing a rigid and a flexible wheel with same radius (Favaedi *et al.*, 2011; Nishiyama *et al.*, 2016; Sharma *et al.*, 2018). A simplified description of origami wheel-soil interaction can be represented by an external mechanical stimulus shaped as an external force. In this regard, soil interaction can be described by different harmonic excitations, representing the main excitation and the soil roughness, for instance.

Dissipative aspects are represented by the general term presented in Chapter 7 . This approach allows one to exploit deviations of the robot desired path. Hence, for the sake of simplicity, it is adopted an external stimulus represented by two terms: $F(t) = F_1(t) + F_2(t)$, where $F_1(t) = \delta_1 \sin(\omega_1 t)$ and $F_2(t) = \delta_2 \sin(\omega_2 t)$. The term $\delta_1 \sin(\omega_1 t)$ represents different forms of the soil (sinusoid, for instance – Figure 8-7a). On the other hand, the second term, $\delta_2 \sin(\omega_2 t)$, represents a perturbation over the original soil (Figure 8-7b).

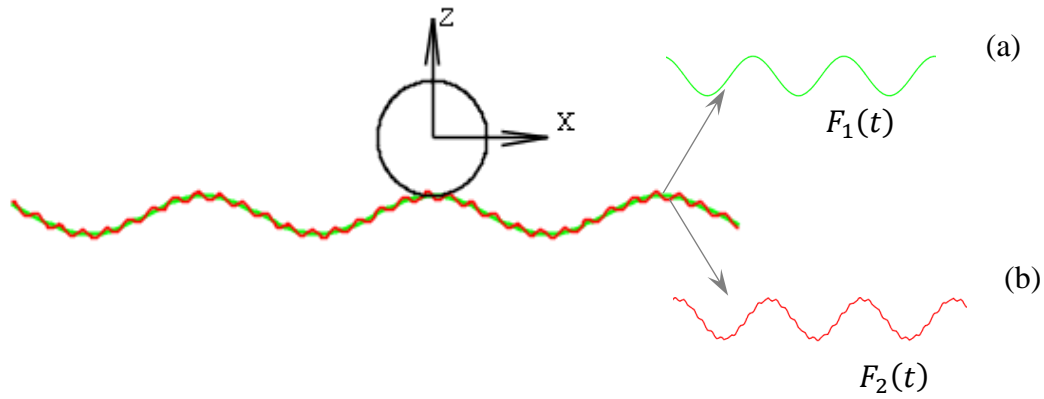


Figure 8-7: Representation of the external mechanical excitation shaped as a force $F(t) = F_1(t) + F_2(t)$, where the contribution of each $F_i(t)$ is highlighted on the right, being (a) for $F_1(t)$ and (b) for $F_2(t)$.

Nonlinear characteristics of the origami wheel robot can provide complex dynamical behavior, and small perturbations can either lead the system to a chaotic behavior or dramatically change its response. In order to explore the influence of these perturbations, a soil interaction is considered and represented by an external mechanical stimulus (external force). Simulations are performed considering $\delta_1 = 10$ N, $\omega_1 = 200$ rad/s and $\omega_2 = 300$ rad/s. The value of the parameter δ_2 is chosen to represent different perturbations, changed on each simulation.

Figure 8-8 presents an analysis of the influence of the perturbation on the origami wheel robot path in four cases, evaluating deviations from the desired path previously defined with a constant velocity, $F(t) = 0$ and the thermal cycle presented in Figure 8-5a.

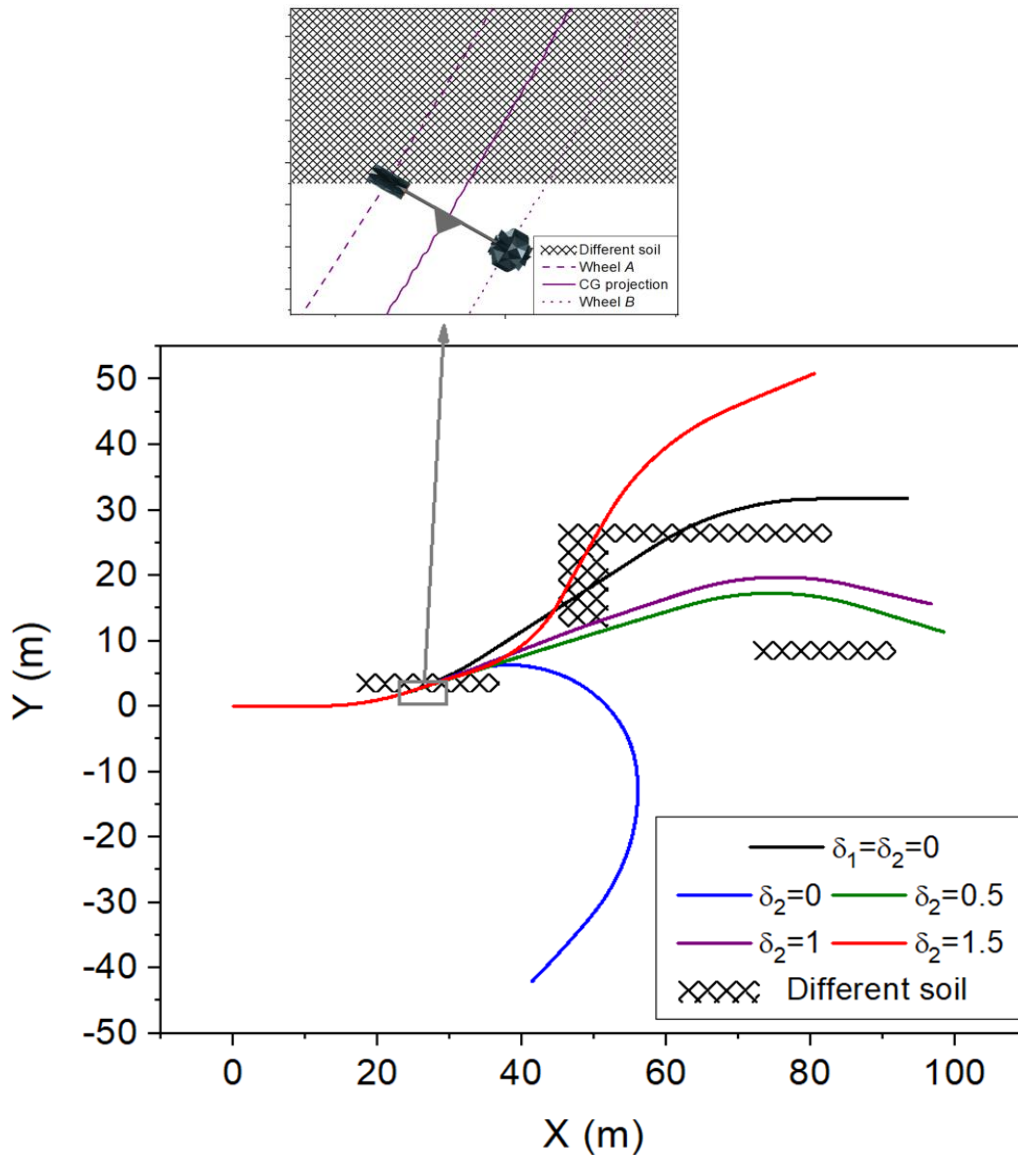


Figure 8-8: Path followed by the origami-wheel robot when passing through different soils, represented by hatched regions and described by an external stimulus. A zoom from the first dashed region is also presented.

The hatched regions on the domain represent perturbation zones related to different soils that excite the wheel with a force $F(t)$. Four situations are treated considering different levels of perturbation: $\delta_2 = 0$ (force is a pure sine, without perturbation), $\delta_2 = 0.5N$, $\delta_2 = 1 N$ and $\delta_2 = 1.5 N$. For all cases, the origami-wheel robot passes through the dashed region at least once, promoting a deviation of the original path. Depending on the angle that the robot enters the dashed region, it can have either one or both wheels over the perturbed soil. Figure 8-8 also shows a zoom that illustrates

an example situation for the case $\delta_2 = 1$ N. Note that initially, only the wheel *A* is subjected to the external force and afterward, both wheels are over the dashed region, being subjected to the same perturbation. When $\delta_2 = 0$ N, after the cooling process of wheel *A*, the wheel *A* stabilizes at an opened configuration, while wheel *B* stabilizes at a closed configuration (see Figure 6-16), which promotes a curved path. A similar behavior occurs for the case $\delta_2 = 1.5$ N, although the origami robot passes through a second dashed region, changing its initial deviation.

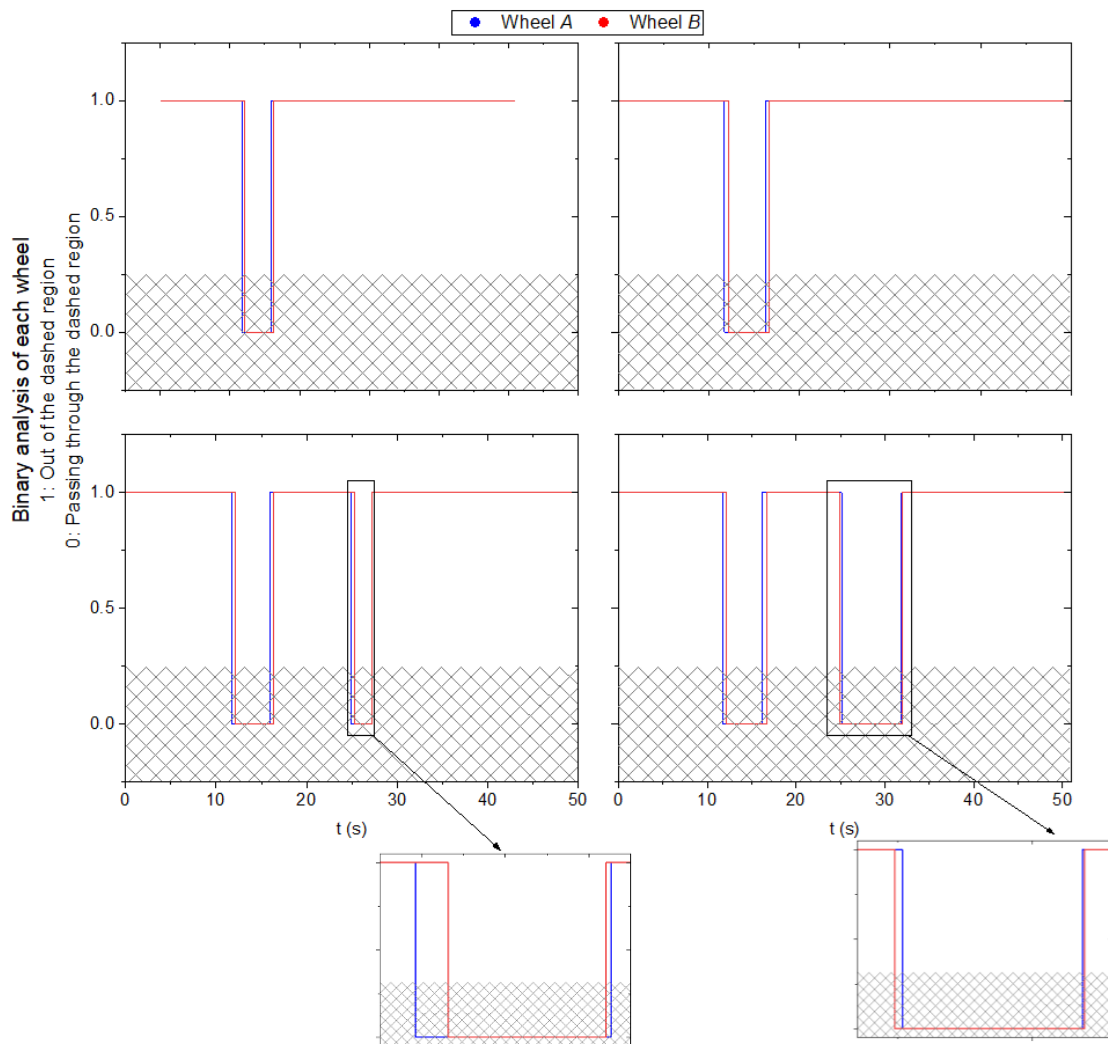


Figure 8-9: Binary representation of the wheels related to the dashed region in Figure 8-8.

Figure 8-9 presents a better idea of the external stimulus considering a binary representation of the wheel with respect to the region. This binary representation

evaluates only if the wheel is contained within a dashed region or not. For all four cases from Figure 8-8, represented respectively in Figure 8-9, the wheel *A* is represented by a blue line, while wheel *B* is represented by a red line. If the wheel is outside the region, it is given a value 1. Otherwise, if the wheel touches the dashed region such that an external force acts on it, it is given a value 0. Note that for all four cases, both wheels reach the dashed region. For the cases $\delta_2 = 0$ N, shown in in Figure 8-9a, and $\delta_2 = 0.5$ N, shown in Figure 8-9b, wheel *A* is the first to reach the dashed region and also the first to leave it. Besides, for these two cases, only one dashed region is reached. For the case $\delta_2 = 1$ N, shown in Figure 8-9c, two dashed regions are reached by the wheels. On the first region, wheel *A* is the first to enter and the first to leave. On the second region, however, wheel *A* is subjected to an external force longer than wheel *B*, once that wheel *A* is the first to enter and the last to leave that region. This second region is highlighted. Finally, for the case $\delta_2 = 1.5$ N, shown in Figure 8-9d, two regions interfere with the car motion. The first one acts similarly to the other three cases, where wheel *A* is the first to enter and the first to leave the dashed region. However, on the second region, wheel *B* is subjected to an external force longer than wheel *A*, once that it stays longer on that dashed region.

The external stimulus acting on the wheels due to the soil interactions promotes oscillations on the wheels, as can be observed in Figure 8-10, that shows time evolution of radius R_A and R_B . The dashed lines indicate regions where the wheel is passing through the perturbation region (hatched regions in Figure 8-8). Note that the largest deviation related to the desired path occurred on cases where the wheels stabilize at different radius after the first cooling process, indicating that a correction on the path can be made by controlling the reverse phase transformation, austenite-martensite.

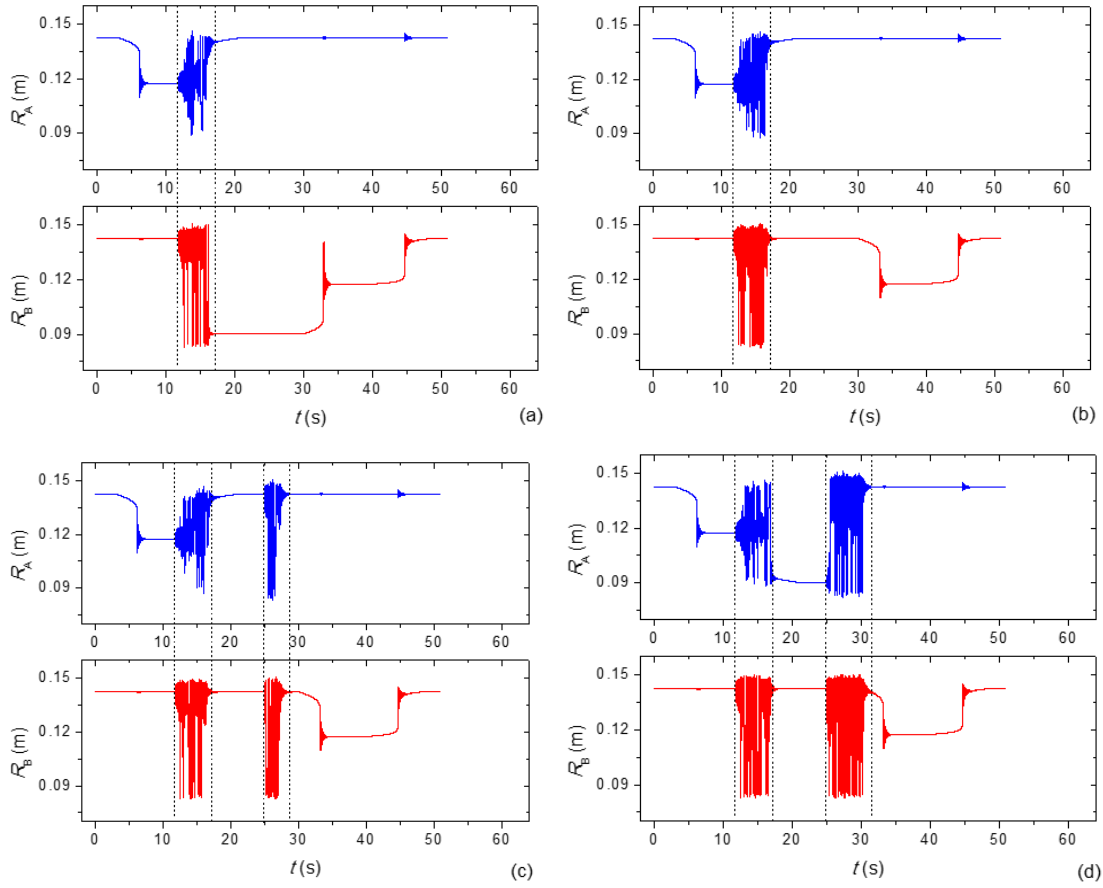


Figure 8-10: Time evolution of the wheels' radius for the cases (a) $\delta_2 = 0$ N; (b) $\delta_2 = 0.5$ N; (c) $\delta_2 = 1$ N and (d) $\delta_2 = 1.5$ N.

The dynamical behavior of the origami wheel A for each one of the cases is represented in Figure 8-11, where the phase portraits and Poincaré sections are taken considering the first region marked in Figure 8-10 (between 12 and 18 seconds). Similarly, the dynamical behavior for the wheel B is presented in Figure 8-12. Note that both wheels have the same qualitative behavior for each case. For $\delta_2 = 0.5$ N, the system has a period-2 response, while the other three cases have a chaotic response. These oscillations can be critical for the origami structure since the creased regions are being continuously bended/released (Francis *et al.*, 2013).

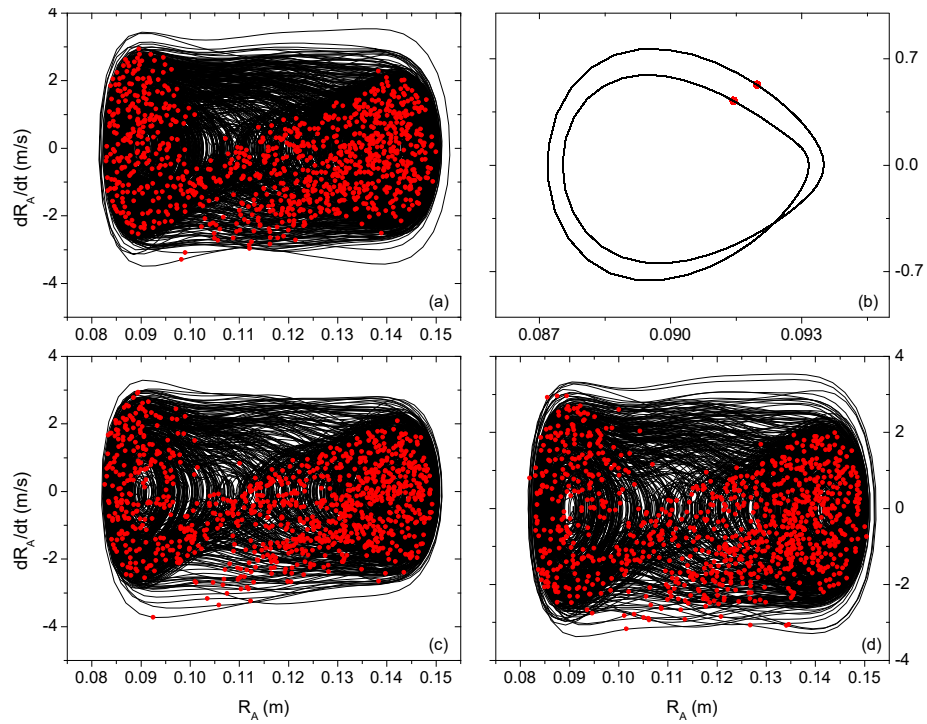


Figure 8-11: Phase portrait and Poincaré section of wheel A for $m_G=0.1$ kg subjected to $F(t)$ for the cases (a) $\delta_2 = 0$ N; (b) $\delta_2 = 0.5$ N; (c) $\delta_2 = 1$ N and (d) $\delta_2 = 1.5$ N.

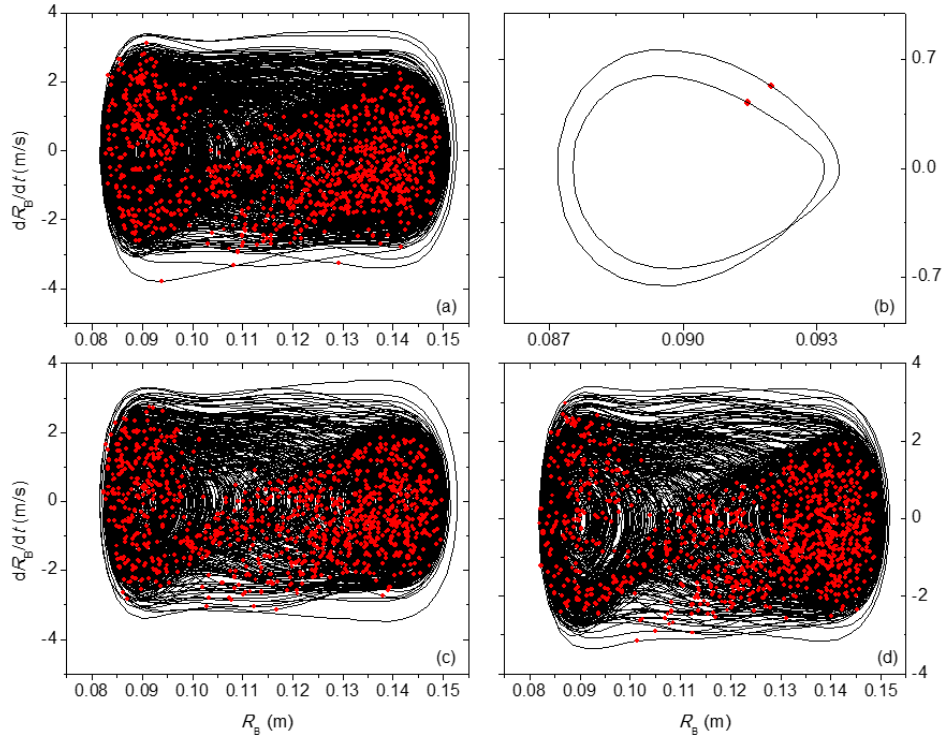


Figure 8-12: Phase portrait and Poincaré section of wheel B for $m_G=0.1$ kg subjected to $F(t)$ for the cases (a) $\delta_2=0$ N; (b) $\delta_2=0.5$ N; (c) $\delta_2=1$ N and (d) $\delta_2=1.5$ N.

It is clear that the origami-wheel robot has a strong sensitivity to parameter change. Based on that, its design needs to be properly developed in order to avoid undesirable behaviors. In this regard, previous simulations in Figure 8-8 are revisited considering a different inertia, $m_G = 0.2$ kg. Under this new condition, the small perturbation case ($\delta_2 = 0.5$ N) presents a deviation on path that is less aggressive than the one presented by the previous case since the change altered the robot stabilization capacity, stabilizing the wheels after the heating/cooling process (Figure 8-13). Besides, the increase on the inertia reduces the sensitivity of the system to external stimulus.

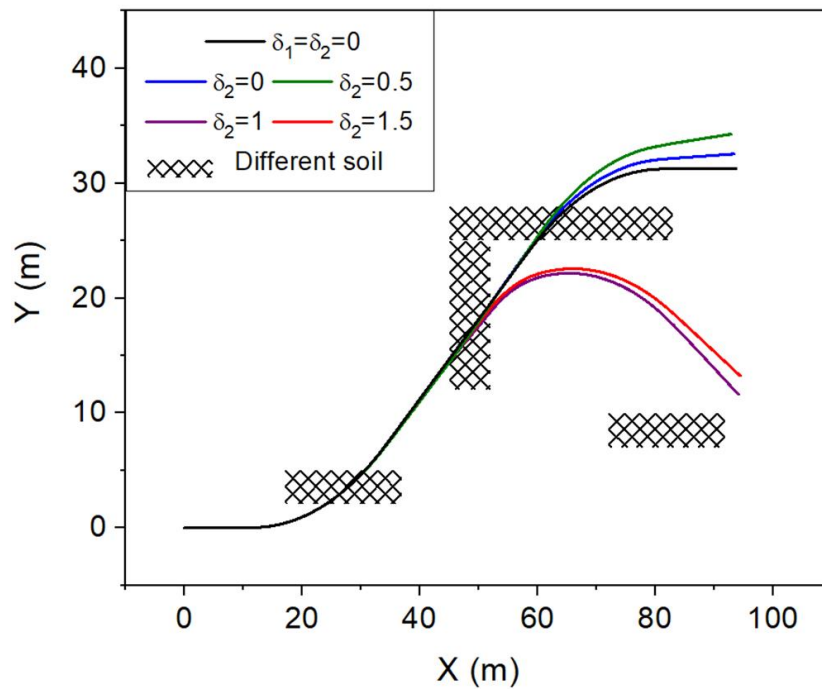


Figure 8-13: Path followed by the origami-wheel robot when passing through different soils considering $m_G=0.2$ kg.

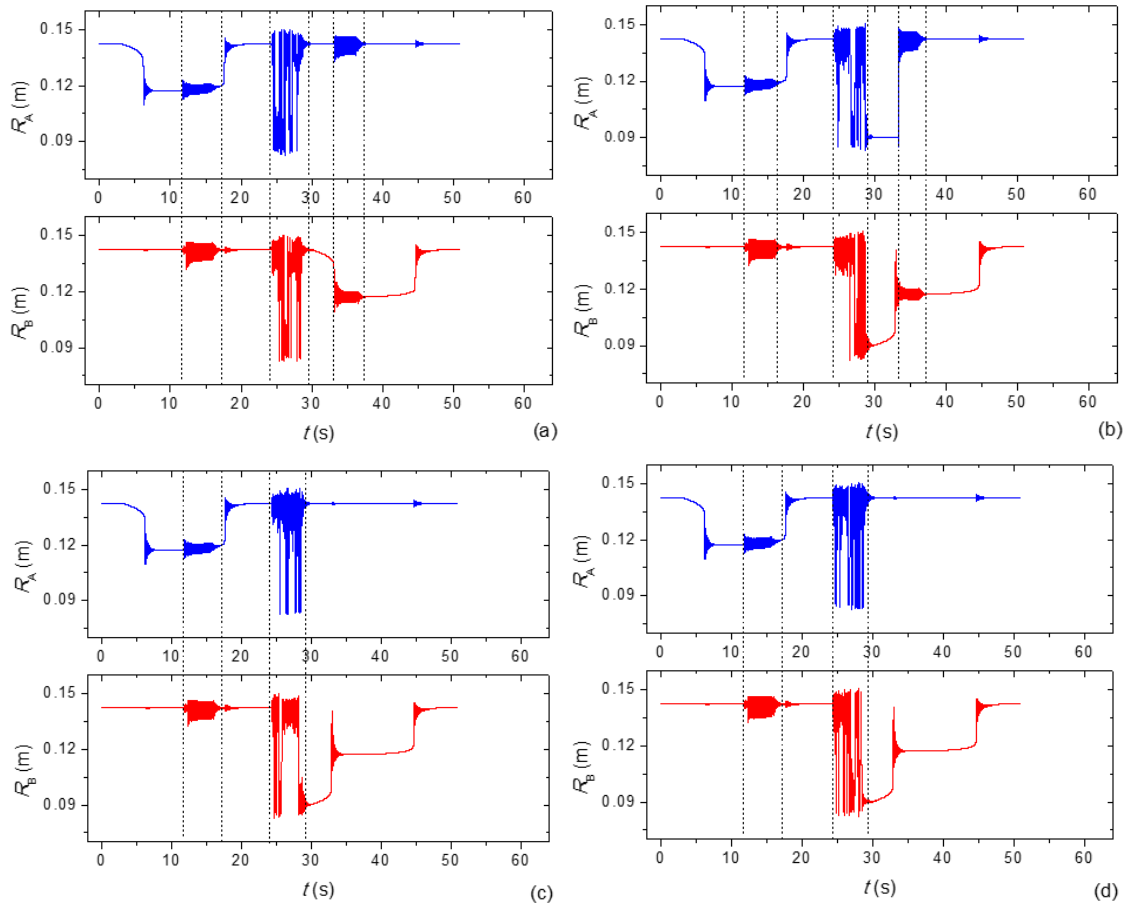


Figure 8-14: Time evolution of the wheels' radius considering $m_G=0.2$ kg for the cases: (a) $\delta_2 = 0$ N; (b) $\delta_2 = 0.5$ N; (c) $\delta_2 = 1$ N and (d) $\delta_2 = 1.5$ N.

For all cases, both wheels stabilize at the same configuration after the first heating/cooling cycle (Figure 8-12a to d), allowing the robot to keep following a straight path. The higher perturbation cases ($\delta_2 = 1$ N and $\delta_2 = 1.5$ N) promote a deviation to the right (clockwise rotation) during the second heating/cooling process, once that wheel *B* stays in an intermediate configuration before stabilizing at an opened one, resulting in a yaw motion clockwise. By changing the inertia, the dynamic response changes from chaotic to period-1 response for the case $\delta_2 = 0$ N and to a period-2 for the other cases. Phase portraits and Poincaré sections for each one of these cases are represented by Figure 8-13 for wheel *A* and Figure 8-14 for wheel *B*.

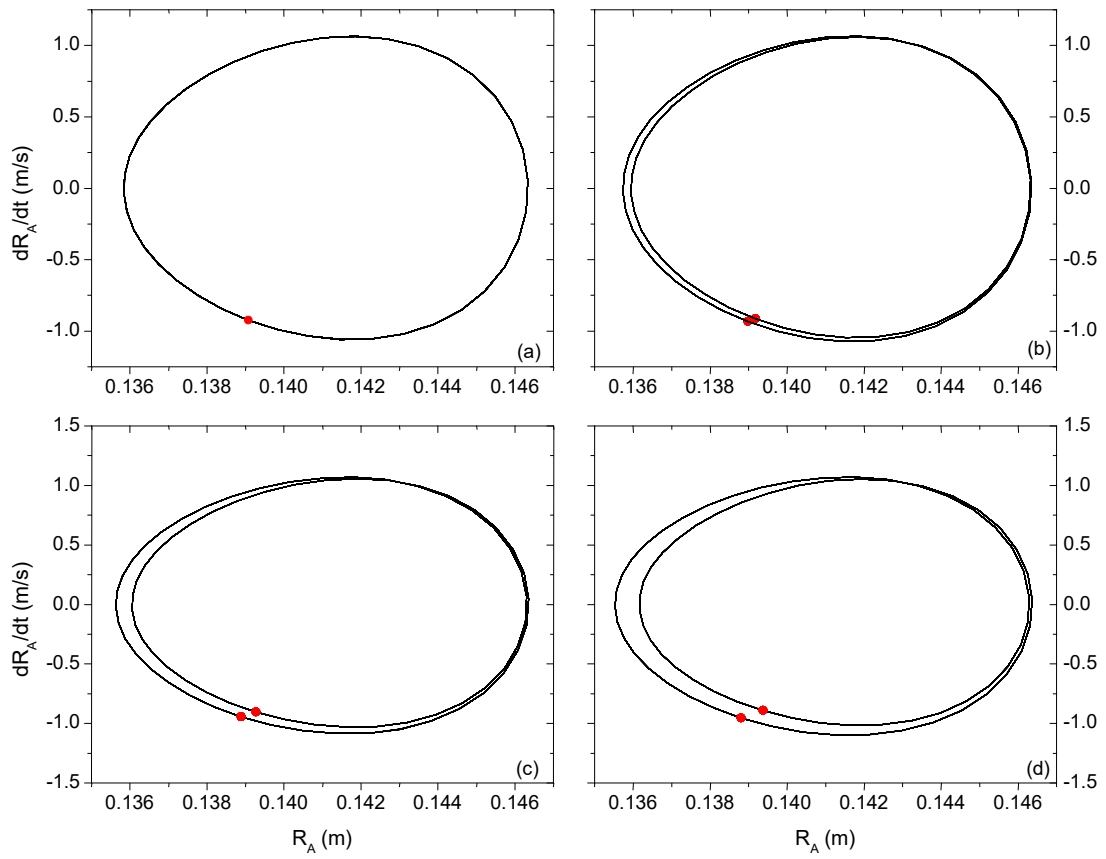


Figure 8-15: Phase portrait and Poincare section of wheel A considering $m_G=0.2$ kg for the cases: (a) $\delta_2 = 0$ N; (b) $\delta_2 = 0.5$ N; (c) $\delta_2 = 1$ N and (d) $\delta_2 = 1.5$ N.

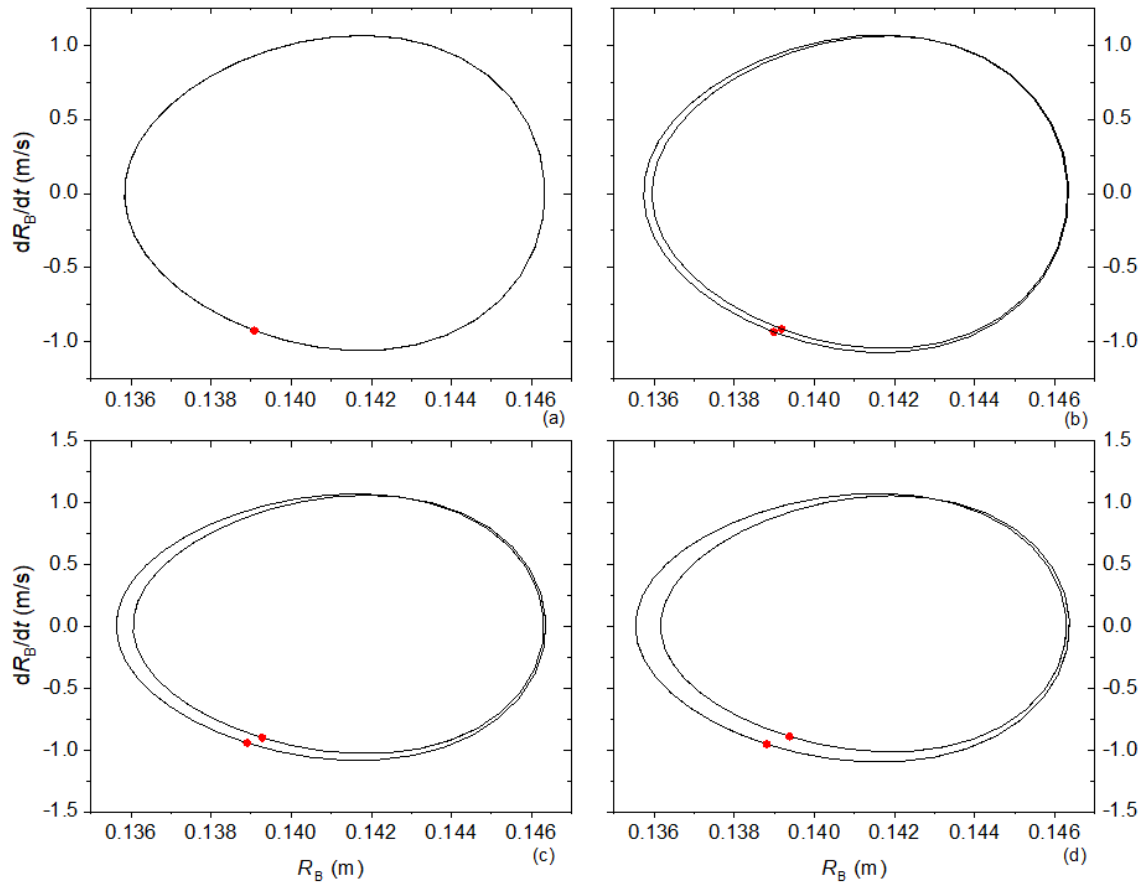


Figure 8-16: Phase portrait and Poincare section of wheel B considering $m_G=0.2$ kg for the cases: (a) $\delta_2 = 0$ N; (b) $\delta_2 = 0.5$ N; (c) $\delta_2 = 1$ N and (d) $\delta_2 = 1.5$ N.

From now on, all simulations are carried out considering that $m_G=0.1$ kg. Chaotic systems present a high sensitivity to initial conditions and, as a result, responses starting at two close initial conditions might develop divergent trajectories. By considering the origami wheel robot, this sensitivity can be represented by small changes at position where the soil interaction starts, leading to drastic changes on the system behavior, influencing the path described by the origami robot. Previously, the soil perturbations are evaluated through the robot path that crosses different soils and, therefore, changes the external stimulus that causes the dynamic behavior of the system. Now, a different situation is of concern, considering that the perturbation is kept constant, a case where the system has a periodic response ($\delta_2 = 0.5$ N), and the phase of the external excitation changes. Under this assumption, consider a situation where both wheels are excited by the same external force: $F(t) = 10 \sin(200t + \rho) + 0.5 \sin(300t + \rho)$, where ρ represents a phase. In order to evaluate the influence of this phase ρ , a spectrum diagram

is generated monitoring a cut along one period of the external force (Figure 8-17-a), starting from the case $\rho = 0$ and increasing the phase until $\rho = 2\pi$. Note that when $\rho = 0$ the system presents a period-2 response (Figure 8-11-b). It should be noted that the increase of the phase causes a change on the system response to a chaotic behavior (Figure 8-17-b). In both conditions no thermal cycle is applied, meaning that the origami robot must follow a straight line. Figure 8-18 shows robot paths by considering two different phases: $\rho \cong 0.765$ rad, associated with a periodic behavior of the wheel; and $\rho \cong 0.558$ rad, associated with a chaotic behavior. For the periodic response, the robot follows a linear path, while it presents a large deviation on the path for the chaotic case. The upper diagrams in Figure 8-17-a are representations of the instant that the wheel enters the perturbed soil, which impacts on the first interaction between the wheels and the soil. On the upper-left diagram, a representation for the chaotic motion, the wheel enters the soil on an instant such that the interaction is similar to an excitation on the wheel starting near the maximum achievable value for the $F(t)$. On the upper-right diagram - a representation for the periodic motion - the wheel enters the soil on an instant such that the interaction between the rough soil and the wheel is similar to an excitation on the wheel starting at the maximum achievable value for $F(t)$, *i.e.*, the peak. This first interaction is important to define the general behavior of the car while rolling over the rough soil.

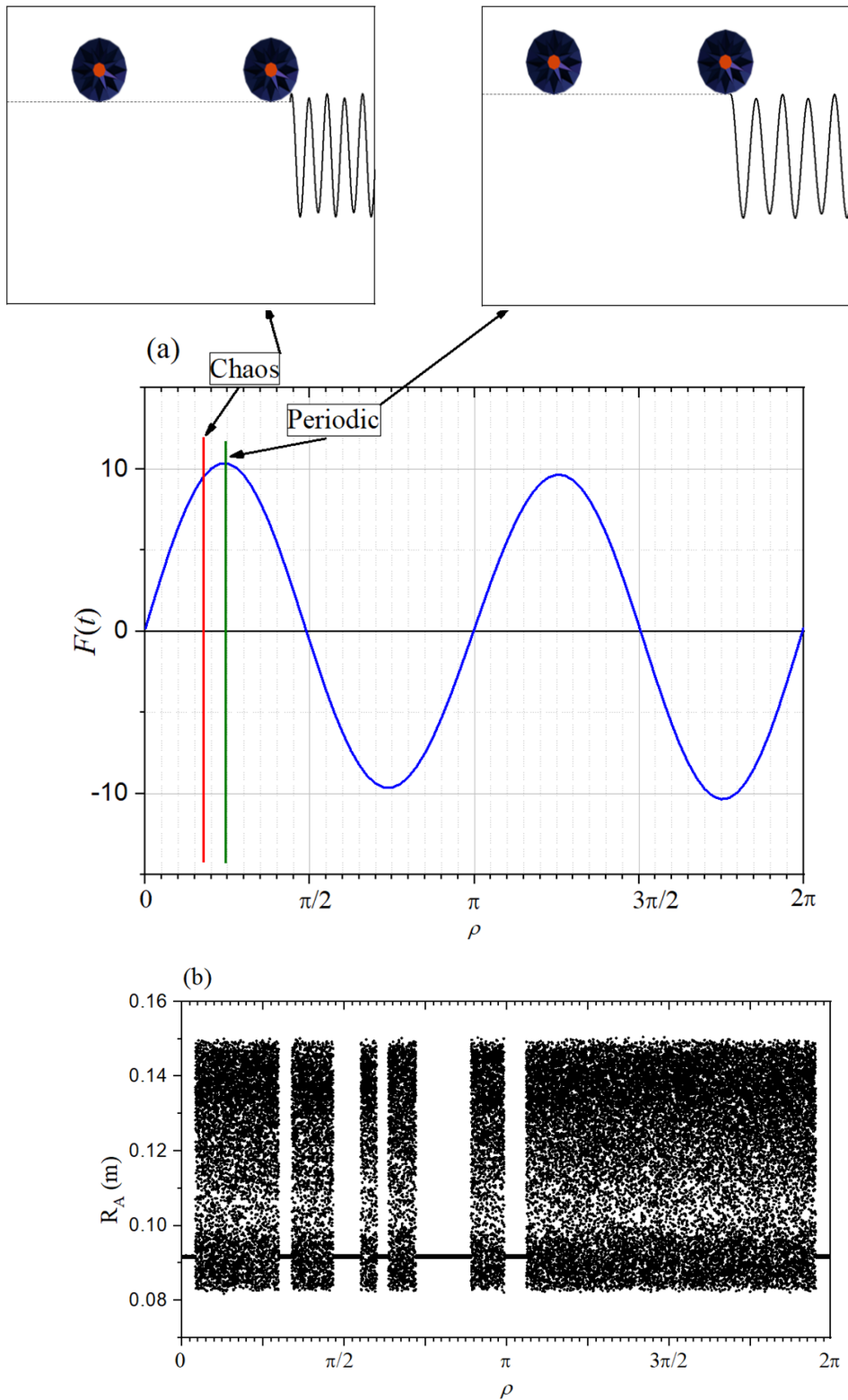


Figure 8-17: Dynamic response of the system when subjected to the force $F(t)$.
 (a) Force on time with a selection of one period (T) with the phase going from 0 to 2π ;
 (b) Spectrum diagram for R_A evaluated on ρ .

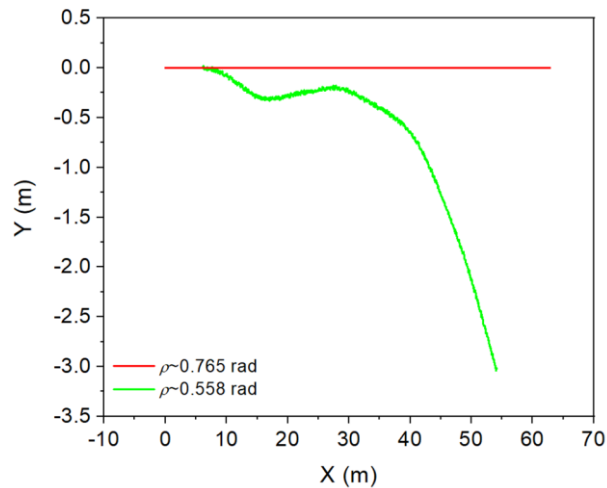


Figure 8-18: Path described by the G point for the chaotic and the periodic responses.

Origami wheel robot has its paths defined by the dynamical behavior of the wheels. Therefore, it is essential to understand their global dynamical behavior. An interesting phenomenon related to the origami dynamics is the synchronization of the wheel behaviors. This means that there is a trend that both wheels have the same qualitative response in steady state. According to the previous simulations, it is concluded that a perturbation of $\delta_2 = 0.5$ N is associated with a periodic behavior of the wheel while a perturbation of $\delta_2 = 1.5$ is related to a chaotic behavior. Now, a situation where each wheel is subjected to a different perturbation is of concern. Under this condition, it is expected that one wheel presents a periodic response, while the other presents a chaotic response. The coupling between the wheels promotes a synchronization of their dynamical behavior, leading to similar responses of both wheels.

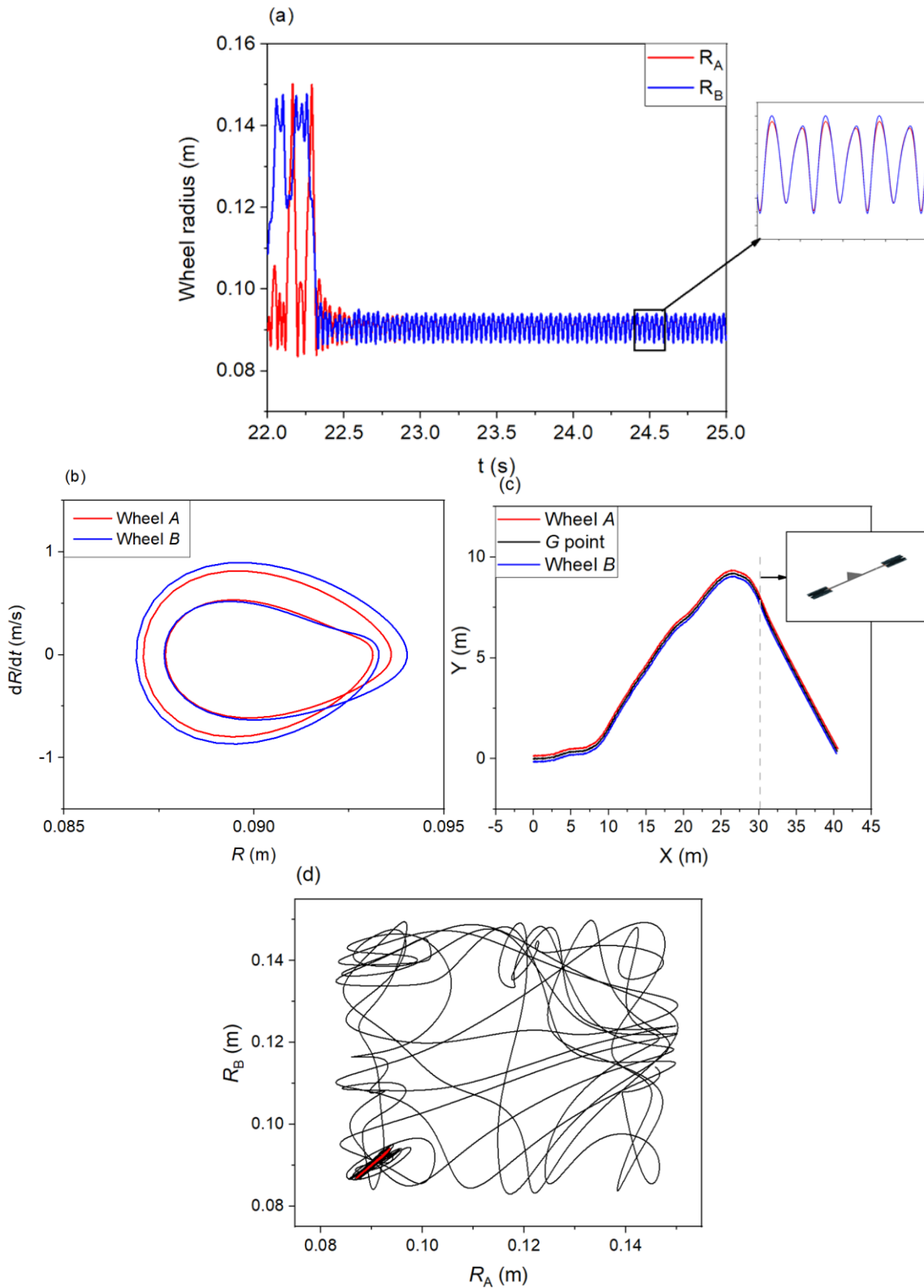


Figure 8-19: Synchronization between wheels *A* and *B*. (a) Time evolution of wheels' radius with a zoom at the permanent regime; (b) phase portrait of wheels *A* and *B* at the synchronized configuration; (c) path described by the origami-wheel robot; (d) radius manifold showing the synchronization.

Therefore, consider a situation where $F_A(t) = 10 \sin(200t) + 0.5 \sin(300t)$ and $F_B(t) = 10 \sin(200t) + 1.5 \sin(300t)$. Thermal effects are not considered which means that a constant temperature is applied to both wheels ($T=288$ K). Figure 8-19 presents results of this simulation showing that the system presents a transient chaos during approximately 22 seconds and, afterwards, the wheels synchronize, presenting a period-2 response (Figure 8-19-a). Through the zoom of the steady state, it is noticeable that the system presents a phase synchronization, which corresponds to a locking of phases of chaotic oscillators (Roseblum *et al.*, 1996). Figure 8-19-b presents phase space of each wheel confirming the differences of both orbits. The path followed by the origami robot is shown at Figure 8-19-c, where the final configuration is highlighted at the dotted line, and, since both wheels stabilize at the same configuration (both closed), the origami-wheel robot follows a straight line after the synchronization. Figure 8-19-d shows the radius space illustrating the transient response (in black) and the synchronization manifold $R_A = R_B$ (in red).

By considering a condition where $F_A(t) = 10 \sin(200t) + 1.0 \sin(300t)$ and $F_B(t) = 10 \sin(200t) + 1.5 \sin(300t)$ with constant temperature to both wheels ($T=288$ K), the system presents a chaotic steady state response (Figure 8-20). Figure 8-20-a shows the radii evolution; Figure 8-20-b presents phase space of each wheel confirming the chaotic-like response. The path followed by the origami robot is shown at Figure 8-20-c, illustrating the difference between this path with the previous one. Figure 8-20-d shows the radius space illustrating the chaotic behavior that tends to occupy all the space.

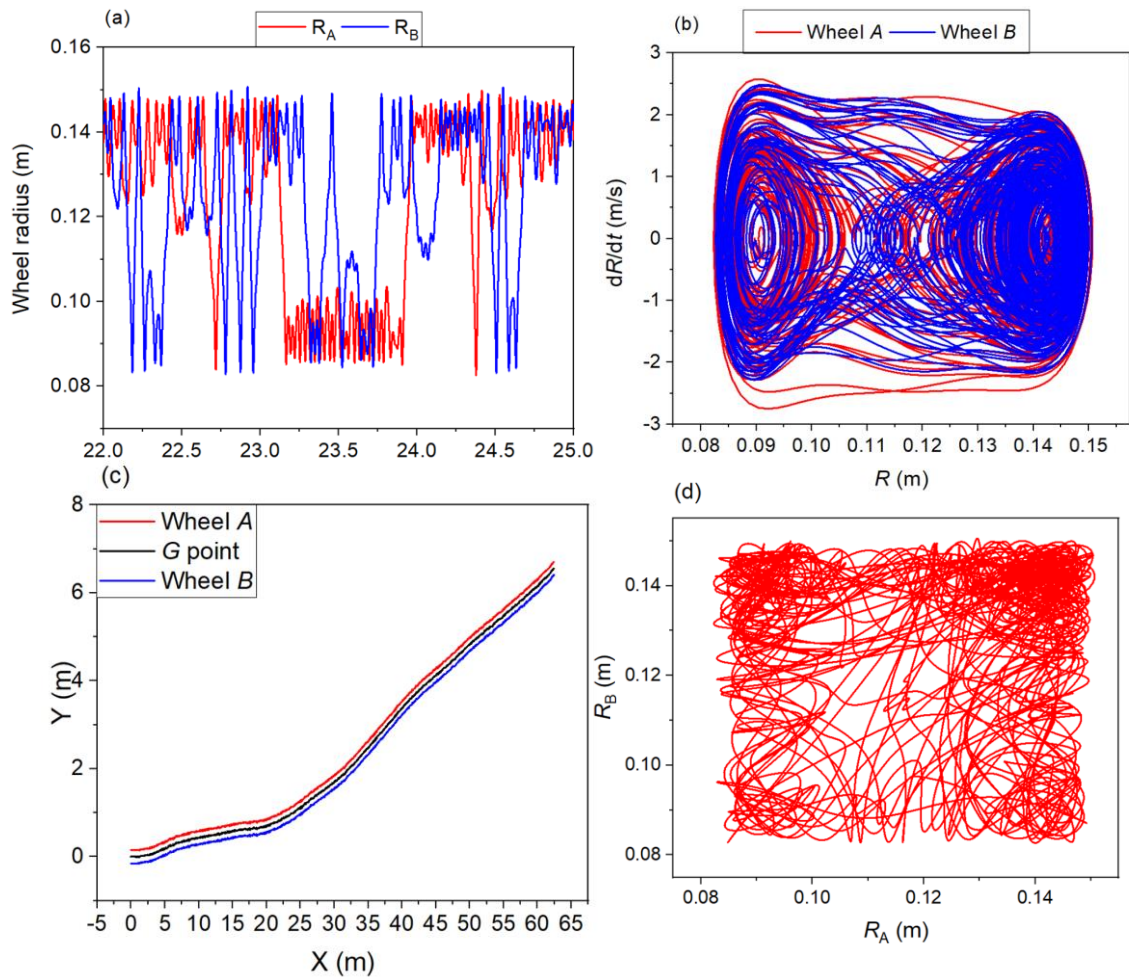


Figure 8-20: Chaotic behavior of wheels *A* and *B*. (a) Time evolution of wheels' radius with a zoom at the permanent regime; (b) phase portrait of wheels *A* and *B* at the synchronized configuration; (c) path described by the origami-wheel robot; (d) radius manifold.

9 Final Remarks and Future Works

This work presents an analysis of the complex behavior of origami structures, with a focus on the waterbomb pattern and related tessellation. It starts with a kinematic formulation of the equivalent mechanism for the 6-creased waterbomb pattern, considering a unit cell. The three dimensional behavior is evaluated through a workspace analysis that provides an interesting approach for the evaluation of the origami configuration and movement during the opening/closing process. This approach allows the identification of necessary actuations and/or restrictions of the folding process to achieve a specific configuration or maintain a specific behavior. It is observed that a no-penetration condition needs a restriction of the vertex movement from a spherical space to a spherical arc, conferring a plane-symmetric condition for the waterbomb configuration. Symmetries reduce the origami behavior complexity and consequently the necessary number of Degrees of Freedom (DoFs).

Finite element analysis allows the evaluation of the rigid foldability hypothesis. It is verified that origamis can present folding process described by a purely kinematic formulation, since the panel deformation does not provide major changes to the origami configuration. In other words, the deviance observed in the inner angles, contained within 1° , can be neglected for the general shape of the structure and actuation design. Using the rigid foldability hypothesis, reduced-order models are able to provide a proper description of the totally symmetric situation, resulting in a single degree of freedom description.

The complex behavior of a waterbomb unit cell provides a rich variety of shapes and folding process for the waterbomb tessellation. It is verified that the tessellation presents hidden degrees of freedom and a complex snap-through behavior, which should be considered on the actuation design. As an example, a closed waterbomb tessellation named origami-wheel is investigated. It takes advantage of the natural strangulation effect

with an additional modification to avoid a negative Gaussian surface (strangulation index less than 1).

The dynamical behavior of the origami-wheel actuated by SMAs is investigated, employing a reduced-order model based on geometric analysis and resulting in a one degree of freedom oscillator. A polynomial constitutive model is employed to describe the thermomechanical behavior of the SMA actuator. Different mechanical and thermal excitations associated with distinct operational conditions are investigated. It is verified the high complexity of such slender structure showing the degree of malleability and the great applicability potential of origami concepts and origami-like structures. The transition between the configurations assumed by the origami is carried out by SMA actuation, and the return to the original configuration is promoted by the linear passive elastic spring. The origami wheel has a rich dynamic behavior, with multiple periods and chaos, and some observations are worth of being highlighted:

- The applied mechanical forcing represents the functioning of the structure under conditions of external stresses, simulating an uneven ground. It appears that this type of effort can promote the closing or opening of the origami, changing its shape. Note that chaotic behaviors are critical, since the structure enters an opening/ closing cycle that can lead to fatigue of the material, promoting even more complex behaviors not contemplated in this work, such as the flexing of the origami panels and asymmetry of efforts due to the edge break.

- The bifurcation diagrams show that the change in the SMA temperature allows the modification of an origami behavior from chaotic to a periodical, desirable one, for the same mechanical effort. In addition, the level of soil irregularity dictates the complexity of the origami wheel behavior.

- Another interesting result observed is the dynamic jump in the resonance curves. Typical of non-linear systems, this behavior can be problematic depending on the application of the structure. Considering that the origami-wheel is in an application that requires opening restriction, the increase in the frequency of external efforts, representing an increasing on soil roughness, can be critical since the contact between the origami-wheel and the restriction contour can produce impacts or dry friction, which can again change the dynamics of the system, culminating even in chaotic behavior or in the flexing of the origami walls.

Finally, this work brings the dynamic analysis of a two-wheeled robot that uses deformable wheels. The origami folding process is driven by alloys with shape memory effect and the robot maneuverability is obtained through the radii change. The origami-robot is interesting since it allows the route control with the use of few actuators. Due to strong nonlinearities involved, it is important a deep nonlinear dynamics analysis that allows a later trajectory control based on the observed effects. The following points can be highlighted:

- The thermal cycle defines the recovery of residual deformation of SMAs, reflecting in the spokes of the origami-wheels. When observing from the point of view of the route, it appears that this cycle defines how open or closed the trajectory of the car will be in relation to a reference trajectory. In addition, the combination of thermal cycle and uneven ground promotes significant path deviations, requiring the use of a controller in these cases.

- Note that uneven ground has a great influence on the trajectory followed by the car, being more prominent in cases where the wheels are on different soils, since the difference in radii promotes the car's camber (left or right curvature). In addition, even if the individual behavior of each wheel is of high periodicity, the car's trajectory only changes if there is a lag between the oscillations of the wheels, that is, if the spokes differ at some point.

- The chaotic behavior is critical in the case of the isolated wheel, in which the focus is on the integrity of the folds, as well as in the analysis of the trajectory. It was observed that when both wheels are subjected to the same mechanical forcing and present chaotic behavior, the path followed by the car undergoes a large deviation, becoming irregular, being necessary in this case to control both wheels.

The dynamic richness presented by origami reinforces the importance of these elements for the increase of engineering applications. Origami inspired elements have a high compaction and spend low energy to move between possible configurations, which makes their use with smart alloys feasible.

Chaotic behavior and shape change make the control analysis relevant in origami applications. In this sense, a continuation for this work is the study of chaos control, aiming to avoid undesirable chaotic dynamics for a controlled periodic response, with the objective of maintaining the determined preferential trajectory. A thermally controlled system is a possible way to control the large deformations presented in chaotic responses, as could be seen in the bifurcation diagrams presented.

Nonlinear dynamics of asymmetric systems is another interesting investigation to be performed. Since high efforts can promote panel bending, non-rigid origami analysis is necessary to be evaluated. This certainly increase the system complexity and accelerates the origami wear. It is also worth mentioning the study of some conditions not covered in this work, such as dry friction in applications with restricted opening of the structure and the effect of origami thickness.

Another interesting investigation is the closer look on the creases on the dynamic application. Since the oscillation induced by mechanical efforts and/or thermal fluctuation promotes a constant and repetitive folding/unfolding process of the creases, they are subjected to failure by fatigue, resulting in a crease breaking or softening. This change on the crease properties might be critical for the structure and its influence on the dynamic behavior should be considered.

10 References

AGUIAR, R. A. A., SAVI, M. A., PACHECO, P. M. C. L., 2010, “Experimental and numerical investigations of shape memory alloy helical springs”, *Smart Materials and Structures*, v. 19, Art. ID 025008.

ALPERIN, R.C., 2000, “A Mathematical Theory of Origami Constructions and Numbers”, *New York Journal of Mathematics*, v. 6, pp. 119-133.

ANDREASS, B., 2011, “Origami art as a means of facilitating learning”, *Procedia - Social and Behavioral Sciences*, v. 11, pp. 32-36, ISSN 1877-0428.

ARGHAVANI, J., AURICCHIO, F., NAGHDABADI, R., REALI, A., SOHRABPOUR, S., 2010b, “A 3-D phenomenological constitutive model for shape memory alloys under multiaxial loadings”, *International Journal of Plasticity*, v. 26, Issue 7, pp. 976-991.

ASHRAFI, M.J., ARGHAVANI, J., NAGHDABADI, R., AURICCHIO, F., 2015a, “A three-dimensional phenomenological constitutive model for porous shape memory alloys including plasticity effects”, *Journal of Intelligent Material Systems and Structures*, v. 42, pp. 1-317.

ASHRAFI, M., ARGHAVANI, J., NAGHDABADI, R., SOHRABPOUR, S., 2015b, “A 3-D constitutive model for pressure-dependent phase transformation of porous shape memory alloys”, *Journal of the Mechanical Behavior of Biomedical Materials*, v. 42, pp. 292-310.

AURICCHIO, F., REALI, A., 2007, “A phenomenological one-dimensional model describing stress-induced solid phase transformation with permanent inelasticity”, *Mechanics of Advanced Materials and Structures*, v. 14, Issue 1, pp. 43-55.

AURICCHIO, F., REALI, A., STEFANELLI, U., 2009, “A macroscopic 1D model for shape memory alloys including asymmetric behaviors and transformation dependent elastic properties”, *Computer Methods in Applied Mechanics and Engineering*, v. 198, Issue 17, pp. 1631-1637.

BAÊTA-NEVES, A.P., SAVI, M.A., PACHECO, P.M.C.L., 2003, “Horizontal Enlargement of the Stress-Strain Loop on a Thermo-Plastic-Phase Transformation Coupled Model for Shape Memory Alloys”. *XVII International Congress of Mechanical Engineering (COBEM)*, São Paulo, Brazil.

BELCASTRO, S.M., HULL, T.C., 2002, “Modeling the Folding of Paper Into Three Dimensions Using Affine Transformations”, *Linear Algebra and its Applications*, v. 348, Issues 1-3, pp. 273–282.

BERNARDINI, D., REGA, G., 2005, “Thermomechanical modelling, nonlinear dynamics and chaos in shape memory oscillators”, *Mathematical and Computer Modelling of Dynamical Systems*, v. 11, Issue 3, pp. 291-314.

BHATTACHARYA, A., LAGOUDAS, D., 1997, “A stochastic thermodynamic model for the gradual thermal transformation of SMA Polycrystals”, *Smart Materials and Structures*, v. 6, Issue 3, pp. 235-250.

BOWEN, L.A., BAXTER, W.L., MAGLEBY, S.P., HOWELL, L.L., 2014, “A position analysis of coupled spherical mechanisms found in action origami”, *Mechanics and Machine Theory*, v. 77, pp. 13-24.

BOYAT, M., KOH, J.-S., WOOD, R.J., 2017, “Addressable wireless actuation for multijoint folding robots and devices”, *Science Robotics*, v. 2, eaan 1544.

BOYD, J.G., LAGOUDAS, D.C., 1996, “Thermodynamic Constitutive Model for the Shape Memory Materials”. *Part I: The Monolithic Shape Memory Alloys*, *International Journal of Plasticity*, v. 12, Issue 6, pp.805-842.

BOYVAT, M., KOHN, J.-S., WOOD, R.J., 2017, “Addressable wireless actuation for multijoint folding robots and devices”, *Science Robotics*, v. 2, Issue 8, Art. ID eaan1544.

BRINSON, L.C., 1993, “One Dimensional Constitutive Behavior of Shape Memory Alloys: thermomechanical derivation with non-constant material functions and redefined martensite internal variable”, *Journal of Intelligent Material Systems and Structures*, v. 4, pp. 229-242.

CHEN, B. G.-g., SANTANGELO, C.D., 2018, “Branches of Triangulated Origami Near the Unfolded State”, *Physical Review X*, v. 8, Art. ID 011034.

CHEN Y., FENG H., MA J., PENG R., YOU Z., 2016, “Symmetric waterbomb origami”, *Proceedings of the Royal Society A: Mathematical, Physical and Engineering Sci*, v. 472, Issue 2190, Art. ID 20150846.

CHEN, Z., GU, J., YANG, X., 2020, “A Novel Rigid Wheel for Agricultural Machinery Applicable to Paddy Field with Muddy Soil”, *Journal of Terramechanics*, v. 87, pp. 21-27.

CHIANG, C. H., 2000, “Kinematics of spherical mechanisms”, Malabar, FL, USA: Krieger Publishing Company.

CHRISTIAN, J. W., 1975, “The Theory of Transformations in Metals and Alloys – Part I: Equilibrium and General Kinetic Theory”, Pergamon Press.

CISSE, C., ZAKI, W., ZINEB, T.B., 2016, “A review of constitutive models and modeling techniques for shape memory alloys”, *International Journal of Plasticity*, v. 76, pp. 244-284, ISSN 0749-6419.

DENAVID, J., HARTENBERG, R., 1955, “A kinematic notation for lower-pair mechanisms based on matrices”, *Journal of Applied Mechanics*, v. 22, pp. 215-221.

DEVONSHIRE, A.F., 1954, “Theory of Ferroelectrics”, *Advances in Physics*, v. 3, Issue 10, pp. 85-130.

ENEMARK, S., SANTOS, I.F., SAVI, M.A., 2016, “Modelling, characterization and uncertainties of stabilized pseudoelastic shape memory alloy helical springs”, *Journal of Intelligent Material Systems and Structures*, v. 27, Issue 20, pp. 2721-2743.

ERINGEN, A. C., 1967, “Mechanics of Continua”, John Wiley & Sons. New York.

EVANS, T.A., LANG, R.J., MAGLEBY, S.P., HOWELL, L.L., 2015, “Rigidly foldable origami twists”, *American Mathematical Society*.

FALK, F., 1980, “Model Free-Energy”, *Mechanics and Thermodynamics of Shape Memory Alloys*, *ACTA Metallurgica*, v. 28, pp. 1773-1780.

FALK, F., 1983, “One-Dimensional Model of Shape Memory Alloys”, *Archives of Mechanics*, n.35, pp. 63-84.

FANG, H., ZHANG, Y., WANG, K.W., 2017, “Origami-Based Earthworm-Like Locomotion Robots”, *Bioinspiration & Biomimetics*, v. 12, Issue 6, Art. ID 065003.

FAVAEDI, Y., PECHEV, A., SCHARRINGHAUSEN, M., RICHTER, L., 2011, “Prediction of Tractive Response for Flexible Wheels with Application to Planetary Rovers”, *Journal of Terramechanics*, v. 48, Issue 3, pp. 199-213.

FEI, L. J., SUJAN, D., 2013, “Origami theory and its applications: a literature review”, *International Journal of Social Behavioral, Educational, Economic and Management Engineering*, v. 7, Issue 1, pp. 113–117.

FELTON, S., LEE, D. Y., CHO, K. J., WOOD, R. J., 2014, “A passive, origami-inspired, continuously variable transmission”, *IEEE International Conference on Robotics and Automation*, pp. 2913–2918.

FIGUEREDO, L.F.C., ADORNO, B.V., ISHIHARA, J.Y., BORGES, G.A., 2013, “Robus kinematic control of manipulator robots using dual quaternion representation”, *IEEE International Conference on Robotics and Automation (ICRA)*, Karlsruhe, Germany.

FINDLEY, T. M., 2013, “An experimental analysis of auxetic folded cores for sandwich structures based on origami tessellations”, PhD thesis, University of Toledo.

FISCHLSCHWEIGER, M., OBERAIGNER, E.R., 2012, “Kinetics and rates of martensitic phase transformation based on statistical physics”, *Computational Material Sciences*, v. 52, Issue 1, pp. 189-192.

FONSECA, L.M., RODRIGUES, G.V., SAVI, M.A., PAIVA, A., 2019, “Nonlinear dynamics of an origami wheel with shape memory alloy actuators”, *Chaos, Solitons and Fractals*, v. 122, pp. 245-261.

FONSECA, L.M., SAVI, M.A., 2020, “Nonlinear dynamics of an autonomous robot with deformable origami wheels”, *International Journal of Non-Linear Mechanics*, v. 125, Art. ID 103533.

FONSECA, L.M., SAVI, M.A., (*in press*), “On the symmetries of the Origami Waterbomb Pattern: Kinematics and Mechanical Investigations”, *Meccanica*.

FRANCIS, K.C., BLANCH, J.E., MAGLEBY, S.P., HOWELL, L.L., 2013, “Origami-like Creases in Sheet Materials for Compliant Mechanism Design”, *Mechanical Sciences*, v. 4, Issue 2, pp. 371-380

FREMOND, M., 1987, “Matériaux à Mémoire de Forme”, *C.R. Acad. Sc. Paris*, Tome 304, s. II, n. 7, pp. 239-244.

FUNAKUBO, H., 1987, “Shape Memory Alloys”, Gordon & Bleach, New York.

GATTAS, J.M., YOU, Z., 2014, “Quasi-Static Impact of Indented Foldcores”, *International Journal of Impact Engineering*, v. 73, pp. 15–29.

GLASSNER, A., 1996, “More Origami Solids”, *IEEE Computer Graphics and Applications*, v. 16, Issue 5, pp. 85-91.

GOGU, G., 2004, “Chebychev–Grübler–Kutzbach's criterion for mobility calculation of multi-loop mechanisms revisited via theory of linear transformations”, *European Journal of Mechanics - A/Solids*, v. 24, Issue 3, pp. 427-441.

- GHYKA, M., 1977, "The Geometry of Art and Life". New York: Dover.
- GREENBERG, H.C., GONG, M.L., MAGLEBY, S.P., HOWELL, L.L., 2011, "Identifying links between origamis and compliant mechanisms", *Mechanical Sciences*, v. 2, pp. 217-225.
- GRIMA, J.N., ALDERSON, A., EVANS, K.E., 2005, "Auxetic Behavior from Rotating Rigid Units", *Physical Status Solidi (b)*, v. 242, Issue 3, pp. 561–575.
- HANNA, B.H., LUND, J.M., LANG, R.J., MAGLEBY, S.P., HOWELL, L.L., 2014, "Waterbomb base: a symmetric single-vertex bistable origami mechanism", *Smart Materials and Structures*, v. 23, Issue 9, Art. ID 094009.
- HARTL, D., LAGOUDAS, D., 2009, "Constitutive modeling and structural analysis considering simultaneous phase transformation and plastic yield in shape memory alloys", *Smart Materials and Structures*, v. 18, Issue 10, Art. ID 104017.
- HARTL, D.J., CHATZIGEORGIOU, G., LAGOUDAS, D.C., 2010, "Three-dimensional modeling and numerical analysis of rate-dependent irrecoverable deformation in shape memory alloys", *International Journal of Plasticity*, v. 26, Issue 10, pp. 1485-1507.
- HELM, D., 2007, "Thermomechanics of martensitic phase transitions in shape memory alloys, I: constitutive theories for small and large deformations", *Journal of Mechanics of Materials and Structures*, v. 2, Issue 1, pp. 87-112.
- HUANG, C., CHEN, C.-M., 1995, "The Linear Representation of the Screw Triangle – A Unification of Finite and Infinitesimal Kinematics", *Journal of Mechanical Design*, v. 117, Issue 4, pp. 554-560.
- HUFFMAN, D. A., 1976. "Curvature and creases: A primer on paper", *IEEE Transactions on Computers*, C-25(10), October, pp. 1010–1019.
- HULL, T., 1994, "On the Mathematics of Flat Origamis", *Congressus Numerantium*, v. 100, pp. 215-224.
- IVSHIN, Y., PENCE, T.J., 1994, "A Constitutive Model for Hysteretic Phase Transition Behavior", *International Journal of Engineering Science*, Issue 32, pp. 681-704, 1994a.
- IVSHIN, Y., PENCE, T.J., 1994, "A Thermomechanical Model for a One Variant Shape Memory Material", *Journal of Intelligent Material Systems and Structures*, Issue 5, pp. 455-473, 1994b.

KRESLING, B., 2008, "Natural Twist Buckling in Shells: From the Hawkmoth's Bellows to the Deployable Kresling-Pattern and Cylindrical Miura Ori," *In Proceedings of the 6th International Conference on Computation of Shell and Spatial Structures*, John F. Abel and J. Robert Cooke, eds., Ithaca, v. 11, pp. 12-32.

KURIBAYASHI K., TSUCHIYA K., YOU Z., TOMUS, D., UMEMOTO, M., ITO, T., SASAKI, M., 2006, "Self-deployable origami *stent* grafts as a biomedical application of Ni-rich TiNi shape memory alloy foil", *Materials Science and Engineering: A*, v. 419, Issue 1, pp. 131–137.

LAGOUDAS, D., HARTL, D.J., CHEMISKY, Y., MACHADO, L., POPOV, P., 2012, "Constitutive model for the numerical analysis of phase transformation in polycrystalline shape memory alloys", *International Journal of Plasticity*, v. 32, pp. 155-183.

LAKES, R., 1987, "Foam Structures with a Negative Poisson's Ratio", *Science* v. 235, Issue 4792, pp. 1038 – 1040.

LANCZOS, C., 1966, "The Variational Principle of Mechanics", Third Edition from the University of Toronto Press, Toronto.

LANG, R.J., 1996, "A Computational Algorithm for Origami Design", *Proceedings of the Twelfth Annual Symposium on Computational Geometry*, Philadelphia, Pennsylvania, USA, pp. 98-105.

LANG, R.J., 2011, "Origami Design Secrets: Mathematical Methods for an Ancient Art", CRC Press, Alamo, ISBN-10 1568814364.

LANG, R.J., 2017. "Twists, Tilings, and Tessellations: Mathematical Methods for Geometric Origami", Taylor & Francis Ltd., ISBN-10 1568812329.

LE P. H., MOLINA, J., HIRAI, S., 2014, "Application of Japanese Origami Ball for Floating Multicopter Aerial Robot", *International Journal of Mechanical, Aerospace, Industrial, Mechatronic and Manufacturing Engineering*, v. 8, Issue 10, pp. 1747– 1750.

LEE D. Y., KIM, J.-S., KIM, S.-R., KOH, J.-S., CHO, K.-J., 2013, "The Deformable Wheel Robot Using Magic-Ball Origami Structure", *International Design Engineering Technical Conferences & Computers and Information in Engineering Conference*, Portland, Oregon.

LEE, J-Y., KANG, B.B., LEE, D-Y., BAEK, S-M., KIM, W-B., CHOI, W-Y., SONG, J-R., JOO, H-J., PARK, D., CHO, K-J., 2016, "Development of a Multi-

functional Soft Robot (SNUMAX) and Performance in RoboSoft Grand Challenge”, *Frontiers Robotics and AI*, Art. ID 201600063.

LEE, K., Wang, Y., Zheng, C., 2020, "TWISTER Hand: Underactuated Robotic Gripper Inspired by Origami Twisted Tower," *IEEE Transactions on Robotics*, v. 36, Issue 2, pp. 488-500.

LEI, C.Y., WU, M.H., 1991, “Thermomechanical Properties of NiTi-Base Shape Memory Alloys”, *Smart Structures and Materials*, ASME, New York, pp. 73-77.

LEMAITRE, J., CHABOCHE, J.L., 1990, “Mechanics of Solid Materials”, Cambridge University Press, Cambridge – England.

LEON, S.E., LAGES, E.N., ARAÚJO, C.N., PAULINO, G.H., 2014, “On the effect of constraint parameters on the generalized displacement control method”, *Mechanics Research Communications*, v. 56, pp. 123-129.

LEON, S.E., PAULINO, G.H., PEREIRA, A., MENEZES, I.F.M., LAGES, E.N., 2011, “A unified library of nonlinear solution schemes”, *Applied Mechanics Reviews*, v. 64, Issue 4, Art. ID 040803.

LIANG, C., ROGERS, C.A., 1990, “One-Dimensional Thermomechanical Constitutive Relations for Shape Memory Materials”, *Journal of Intelligent Material Systems and Structures*, v. 1, pp. 207-234.

LIU, K., PAULINO, G.H., 2017, “Nonlinear mechanics of non-rigid origami: an efficient computational approach”, *Proceedings of Royal Society A: Mathematical, Physical and Engineering Sciences*, v. 473, Issue 2206, Art. ID 20170348.

LV, C., KRISHNARAJU, D., KONJEVOD, G., YU, H., JIANG, H., 2014, “Origami based mechanical metamaterials”, *Scientific Reports*, v. 4, Art. No. 5979.

MA, J., FENG, H., CHEN, Y., HOU, D., YOU, Z., 2020, “Folding of Tubular Waterbomb”, *American Association for the Advancement of Science (AAAS)*, Research, v. 2020, Art. ID 1735081.

MA, J., YOU, Z., 2014, “Modelling of the waterbomb origami pattern and its applications”, *International Design and Engineering Technical Conferences and Computers and Information in Engineering Conference (IDETC/CIE)*, v. 5B: 38th Mechanisms and Robotics Conference, n. DETC2014-35073, pp. V05BT08A047.

MALU, K., MAJUMDAR, J., SANDEEP, 2014, “Kinematics, Localization and Control of Differential Drive Mobile Robot”, *Global Journal of Research In Engineering*, v. 14, Issue 1.

MAVROIDIS, C., ROTH, B., 1997, “On the Geometry of Spatial Polygons and Screw Polygons”, *Journal of Mechanical Design*, v. 119, Issue 2, pp. 246-252.

MIURA K., 1994, “Map fold a la Miura style, its physical characteristics and application to the space science”, *Research of Pattern Formation*, ed R Takaki (Tokyo: KTK), pp. 77–90.

MIYASHITA, S., GUITRON, S., LUDERSDORFER, M., SUNG, C.R., RUS, D., 2015, "An Untethered Miniature Origami Robot that Self-folds, Walks, Swims, and Degrades", *International Conference on Robotics and Automation*, May 2015.

MIYASHITA, S., GUITRON, S., YOSHIDA, K., LI, S., DAMIAN, D.D., RUS, D., 2016, "Ingestible, Controllable, and Degradable Origami Robot for Patching Stomach Wounds", *IEEE International Conference on Robotics and Automation*, May 2016.

MÜLLER, I., 2012, “Pseudo-elastic hysteresis in shape memory alloys”, *Physica B., Condensed Matter*, v. 407, Issue 9, pp. 1314-1315.

NISHIYAMA, Y., 2012, “Miura folding: applying origami to space exploration”, *International Journal of Pure and Applied Mathematics*, v.79, pp. 269-179

NISHIYAMA, K., NAKASHIMA, H., YOSHIDA, T., ONO, T., SHIMIZU, H., MIYASAKA, J., OHDOI, K., 2016, “2d FE–DEM analysis of tractive performance of an elastic wheel for planetary rovers”, *Journal of Terramechanics*, v. 64, pp. 23–35.

OGDEN, R.W., 1997, “Non-linear elastic deformations”, New York, NY: Dover Publications.

OLIVEIRA, H.S., DE PAULA, A.S., SAVI, M.A., 2014, “Dynamical jumps in a shape memory alloys oscillator”, *Shock and Vibration*, v. 2014, Article ID 656212.

OLIVEIRA, S.A., DORNELAS, V.M., SAVI, M.A., PACHECO, P.M.C.L., PAIVA, A., 2018, “A phenomenological description of shape memory alloy transformation induced plasticity”, *Meccanica*, v. 53, pp. 1-21.

OLIVEIRA, S.A., SAVI, M.A., KALAMKAROV, A.L., 2010, “A three-dimensional constitutive model for shape memory alloys”, *Archive of Applied Mechanics*, v. 80, Issue 10, pp.1163–1175.

OLIVEIRA, S.A., SAVI, M.A., ZOUAIN, N., 2016, “A three-dimensional description of shape memory alloy thermomechanical behavior including plasticity”, *Journal of the Brazilian Society of Mechanical Sciences and Engineering*, v. 38, pp. 1451-1472.

PAIVA A., SAVI M.A., 2006, “An overview of constitutive models for shape memory alloys”, *Mathematical Problems in Engineering*, v. 2006, Article ID 56876, pp. 30.

PAN, H., THAMBURAJA, P., CHAU, F., 2007, “Multi-axial behavior of shape-memory alloys undergoing martensitic reorientation and detwinning”, *International Journal of Plasticity*, v. 23, Issue 4, pp. 711-732.

PERAZA-HERNANDEZ, E. A., HARTL, D. J., MALAK Jr, R. J. & LAGOUDAS, D. C., 2014, “Origami-inspired active structures: a synthesis and review”, *Smart Materials and Structures*, v.23, pp. 094001.

PESENTI, M., MASERA, G., FIORITO, F., SAUCHELLI, M., 2015, “Kinetic Solar Skin: A responsive folding technique”, *Energy Procedia*, v. 70, pp. 661-672.

PRALL, D., LAKES, R.S., 1997, “Properties of a Chiral Honeycomb with a Poisson’s ratio of -1”, *International Journal of Mechanical Sciences*, v. 39, Issue 3, pp. 305-307, 309-314.

PROFT, J.L., DUERIG, T.W., 1990, “Mechanical Aspects of constrained recovery and Engineering Aspects of Shape Memory Alloys”, Butterworth-Heinemann, London, pp. 115-129.

REESE, S., CHRIST, D., 2008, “Finite deformation pseudo-elasticity of shape memory alloys e constitutive modelling and finite element implementation”, *International Journal of Plasticity*, v. 24, Issue 3, pp. 455-482.

RODRIGUES, G.V., FONSECA, L.M., SAVI, M.A., PAIVA, A., 2017, “Nonlinear dynamics of an adaptive origami-stent system”, *International Journal of Mechanical Sciences*, v. 133, pp. 303-318.

ROSEMBLUM, M.G., PIKOVSKY, A.S., KURTHS, J., 1996, “Phase synchronization of chaotic oscillators”, *Physical Review Letters*, v. 76, Issue 11, pp. 1804-1807.

SALERNO, M., ZHANG, K., MENCIASSI, A. & DAI, J. S., 2014, “A novel 4-DOFs origami enabled, SMA actuated, robotic end-effector for minimally invasive surgery”, *IEEE International Conference on Robotics and Automation (ICRA)*, pp. 2844-2849.

SAVI, M.A., 2015, “Nonlinear Dynamics and Chaos of Shape Memory Alloy Systems”, *International Journal of Non-linear Mechanics*, v.70, pp.2-19.

SAVI, M.A., PAIVA, A., BAËTA-NEVES, A.P., PACHECO, P.M.C.L., 2002, “Phenomenological Modeling and Numerical Simulation of Shape Memory Alloys: A Thermo-Plastic-Phase Transformation Coupled Model”, *Journal of Intelligent Material Systems and Structures*, v. 3, Issue 5, pp.261-273.

SAVI, M.A., PAIVA, A., DE ARAÚJO, C.J., DE PAULA, A.S., 2016, “Shape Memory Alloys”, *Dynamics of Smart Systems and Structures: Concepts and Applications*, pp.155-188.

SCHEFFER, M., CARPENTER, S., FOLEY, J.A., FOLKE, C., WALKER, B., 2001, “Catastrophic shifts in ecosystems”, *Nature*, v. 413, pp. 591–596.

SCHEFFER, M., CARPENTER, S.R., 2003, “Catastrophic regime shifts in ecosystems: linking theory to observation”. *Trends in Ecology & Evolution*, v. 18, Issue 12, pp. 648–656.

SCHENK M., GUEST, S.D., 2009, "Folded Textured Sheets", *In: Proceedings of the International Association for Shell and Spatial Structures Symposium*, September 28-October 2, Valencia, Spain.

SHARMA, G., TIWARY, S., KUMAR, A., KUMAR, H.N.S., MURTHY, K.A.K., 2018, “Systematic Design and Development of a Flexible Wheel for Low Mass Lunar Rover”, *Journal of Terramechanics*, v. 76, pp. 39-52.

SONG, J., CHEN, Y., LU, G., 2013, “The thin-walled tubes with origami pattern under axial loading”, *JSST International Conference on Simulation Technology*, Tokyo, Japan.

SORGUÇ, A., HAGIWARA, I., SELÇUK, S., 2009, “Origamis in architecture: a medium of inquiry for design in architecture”, *METU Journal of the Faculty of Architecture*, v. 26, Issue 2, pp. 235-247.

SOUZA, A.C., MAMIYA, E., ZOUAIN, N., 1998, “Three-Dimensional Model for Solids Undergoing Stress-Induced Phase Transformations”, *European Journal of Mechanics and Solids*, v. 17, pp. 789-806.

STEINHAUS, H., 1999, “Mathematical Snapshots”, 3rd ed. New York: Dover, pp. 75-76 and 78-82.

STRUIK, D.J., 1961, “Lectures on Classical Differential Geometry”, 2nd Edition, Dover Publications, Inc.

STUPKIEWICZ, S., PETRYK, H., 2013, “A robust model of pseudoelasticity in shape memory alloys”, *International Journal for Numerical Methods in Engineering*, v. 93, Issue 7, pp. 747-769.

TACHI, T., 2009, “Generalization of rigid foldable quadrilateral mesh origami”, *In: Proceedings of the International Association for Shell and Spatial Structures Symposium*.

TACHI T., 2010, “Geometric considerations for the design of rigid origami structures”. *In: Proceedings of the International Association for Shell and Spatial Structures Symposium*, Shanghai, China.

TACHI T., 2011, "Design of Infinitesimally and Finitely Flexible Origami Based on Reciprocal Figures", *Journal for Geometry and Graphics*, v. 16, Issue 2, pp. 223-234.

TACHI, T., 2012, "Freeform origami", Available from: Open Source Repository, <http://www.tsg.ne.jp/TT/software/#ffo>, (10-2-2014).

TACHI T., 2013, "Freeform Origami Tessellations by Generalizing Resch's Patterns", *In: Proceedings of ASME IDETC/CIE (Symposium on Origami-Based Engineering Design)*, DETC2013-12326, Portland, USA, August 4-7.

TANAKA, K., 1985, “A Thermomechanical Sketch of Shape Memory Effect: One -Dimensional Tensile Behavior”, *Materials Science Research International*, v. 18, pp. 251.

TANAKA, K., NAGAKI, S., 1982, “A Thermomechanical Description of Materials with Internal Variables in the Process of Phase Transformation”, *Ingenieur – Archiv.*, v. 51, pp. 287-299.

THAMBURAJA, P., 2010, “A finite-deformation-based phenomenological theory for shape-memory alloys”, *International Journal of Plasticity*, v. 26, Issue 8, pp. 1195-1219.

WASILEVSKI, R.J., 1975, “On the Nature of the Martensitic Transformation”, *Metallurgical Transactions A*, v. 6, Art. No. 1405.

WEBB, D., HIRSCH, B., BRADFORD, C., STEEVES, J., LISMAN, D., SHAKLAN, S., BACH, V., THOMSON, M., 2016, “Advances in starshade technology readiness for an exoplanet characterizing science mission in the 2020’s”, *Proceedings SPIE*, v. 9912, Advances in Optical and Mechanical Technologies for Telescopes and Instrumentation II, 99126H.

WEI, Z.Y., GUO, Z.V., DUDTE, L., LIANG, H.Y., MAHADEVAN, L., 2013, "Geometric mechanics of periodic pleated origami", *Physical Review Letters*, v. 110, Art. ID 215501.

WELLS, D., 1991, "The Penguin Dictionary of Curious and Interesting Geometry" London: Penguin, 229 pp, ISBN 0-14-008029-5.

WILLIAMS, R., 1979, "The Geometrical Foundation of Natural Structure: A Source Book of Design", New York: Dover Publications.

WOLF, A., SWIFT, J. B., SWINNEY, H. L., VASTANO, J. A., 1985, "Determining Lyapunov Exponents from a Times Series", *Physica D: Nonlinear Phenomena*, v. 16, Issue 3, pp. 285–317.

XI, Z., LIEN J. M., 2015, "Continuous unfolding of polyhedra - a motion planning approach," *2015 IEEE/RSJ International Conference on Intelligent Robots and Systems (IROS)*, Hamburg, pp. 3249-3254.

YOSHIMURA Y., 1955, "On the Mechanism of Buckling of a Circular Cylindrical Shell Under Axial Compression", *NACA Technical Memorandums*, T.M. 1390.

ZANG, X., SHEN, C., CHU, Y., LI, B., WEI, M., ZHONG, J., SANGHADASA, M., LIN, L., 2018, "Laser-induced Molybdenum Carbide-Graphene Composites for 3D foldable paper electronics", *Advanced Materials*, v. 30, Issue 26, Art. ID 1800062.

ZHAO, Y., TAYA, M., KANG, Y., KAWASAKI, A., 2005, "Compression behavior of porous NiTi shape memory alloy". *Acta Materialia*, v. 53, Issue 2, pp. 337-343.

ZHAO, Y., ENDO, Y., KANAMORI, Y., MITANI, J., 2018, "Approximating 3D surfaces using generalized waterbomb tessellations", *Journal of Computational Design and Engineering*, v. 5, pp. 442-448.

ZIOLKOWSKI, A., 2007, "Three-dimensional phenomenological thermodynamic model of pseudoelasticity of shape memory alloys at finite strains", *Continuum Mechanics and Thermodynamics*, v. 19, Issue 6, pp. 379-398.

APPENDIX

The appendix brings the constitutive models applied in this work. It starts with a brief explanation about shape memory alloys, followed by thermomechanical aspects, general formulations and the formulation considered in this work. In the sequence, there is a brief explanation regarding the constitutive models used for the mechanical formulation.

A.1. SMA Constitutive Models

Shape memory alloys belong to a class of smart materials, as also piezoelectric, magnetorheological fluids, and electromagnetic materials. These alloys can recover up to 8% of deformation through crystallographic phase transformations induced by thermal, mechanical, or magnetic fields, depending on the alloy.

SMA properties vary according to the microstructure (Lei & Wu, 1991) and chemical compounds. That involves properties such as phase transformation temperatures (Funakubo, 1987). Among the different alloys, it is important to highlight (Proft & Duerig, 1990): Copper-Aluminum-Titanium (CuAlTi) and Copper-Zinc-Aluminum-Manganese (CuZnAlMn). Besides, there is a more commercially popular alloy, Nickel-Titanium (NiTi), that is used in this work.

Phase transformations undertaken by these materials (between phases Austenite – A and Martensite – M) are solid non-diffusive processes, that happens at a high speed, which conceives them an essentially crystallographic feature (Christian, 1975; Wasilevski, 1975). The major characteristics of these transformations are a strong dependency on temperature, an independency on the loading rate and reversibility.

A.1.1. Thermomechanical aspects of SMA

Twinned martensite (M) is a crystallographic phase stable at low temperatures that, under stress free state, has up to 24 variants (Funakubo, 1987), defined by the combination between of habit planes (total of 8) and orientation (total of 3). A mechanical load applied to the alloy starts the process of reorientation of the habit planes along the stress application direction, resulting on the single variant detwinned tractive martensite (M^+), for traction load, and detwinned compressive martensite (M^-), for compression load. Austenite phase (A) is stable on high temperatures in a stress-free state only, and it has a single variant.

These crystallographic transformations can be induced by either temperature or stress, or a combined load, and the thermomechanical coupling propitiates phenomena like pseudo elasticity and shape memory (Figure A-1).

The application of a thermal field on a stress-free state induces the thermoelastic phenomenon (Figure A-1a). A SMA at a high temperature (Austenitic crystallographic phase, $T > A_F$) is cooled down and passes through a crystallographic phase transformation $A \rightarrow M$ (section AB). This process starts at $T = M_S$ and ends at $T = M_F$. For temperatures $T < M_F$, twinned martensite is the stable phase. By heating up again the SMA, an inverse transformation is induced $M \rightarrow A$ (section CD). This second transformation starts at $T = A_S$ and goes until $T = A_F$. For temperatures $T > A_F$, austenite is the stable phase. Note that this process promotes a thermal expansion on the material, associated to a deformation. The inverse transformation recovers this deformation.

Pseudo elasticity and shape memory phenomena are related to the application of stress fields for constant temperatures. The first one, pseudo elasticity (Figure A-1b), happens for samples at $T > A_F$ undergoing mechanical solicitations. The SMA under stress behave as a linear material until a critical tension (mark A) is achieved and the transformation $A \rightarrow M^+$ takes place (section AB). After the completed transformation, the material behaves again as a linear one, where the crystallographic phase is M^+ . Note that A and M^+ have different crystallographic arrangements and, therefore, might have different mechanical properties. By unloading the SMA, it behaves as a linear material until a limit stress is achieved (mark C) and, once that for $T > A_F$ austenite is the stable phase, the material undergoes an inverse transformation (section CD), and all deformation is recovered.

On the other hand, if the sample is at a temperature $A_S < T < A_F$, the total recovery will not be complete, resulting in a residual deformation. This deformation can only be recovered through the application of a stress-free thermal field. This behavior is also called partial pseudo elasticity (Figure A-1c), and is analogous to the shape memory effect, despite of the temperature, that is $T < A_S$ for the shape memory effect (SME).

For the SME, the stable crystallographic phase at a stress-free state is twinned martensite. The mechanical load for this case promotes only a reorientation of the habit planes, going from twinned martensite (M) to detwinned martensite (M^+ or M^-). The unloading process recovers part of the deformation, and a residual deformation associated to the habit planes reorientation can be noticed. This deformation can only be recovered through a thermal cycle for the sample at a stress-free state, once that M^+ is stable for low temperatures (Figure A-2a). Additionally, the SMA can be built as a BIAS system, in opposition to a BIAS spring. In this configuration, the shape memory effect (SME) is described as shown in Figure A-2b. On a BIAS system, the mechanical load applied deforms the shape memory spring at the lower temperature. The SME works against the force from of the bias spring and, when the SMA spring is cooled down, the bias actuator promotes the reorientation process and therefore, the SMA spring changes between two configurations – low and high temperature.

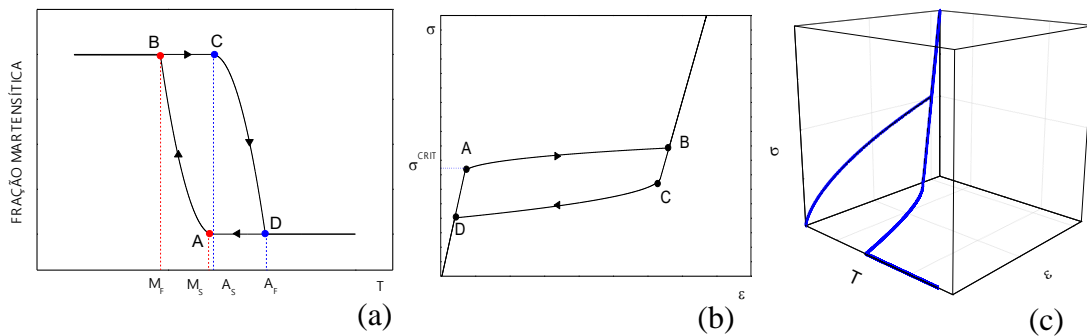


Figure A-1: SMA thermoelastic (a), pseudo elastic (b) and partial pseudo elastic, for $A_S < T < A_F$, or shape memory effect, for $T < A_S$ behavior.

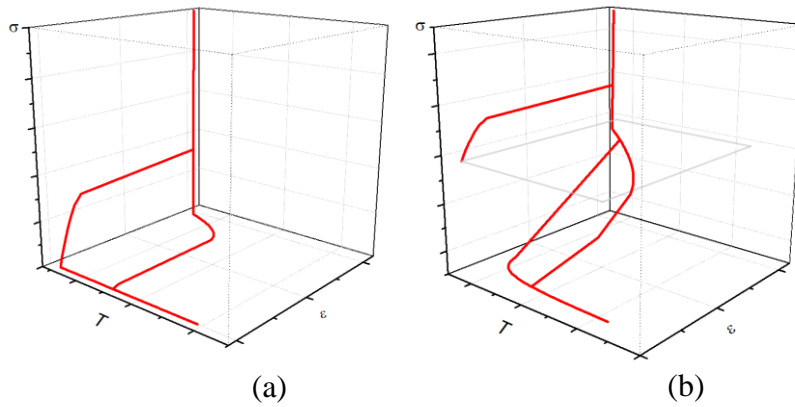


Figure A-2: Typical Stress-Strain-Temperature curves for SMA springs: (a) shape memory effect (SME); (b) SME on a bias system.

A.1.2. Overview of constitutive models

The constitutive model of an alloy with SME depends on the approach chosen to describe the material's behavior observed or expected. The microscopic approach considers metallurgic aspects of the alloys, such as phase nucleation, habit planes organization and the growing function of martensite crystals. Mesoscopic approach uses micromechanics to describe the alloy behavior on micro and meso scales. On the macroscopic approach, the alloy behavior is described according to phenomenological observations, micro-macro simplified thermomechanical analysis or even experimental fitting of parameters.

The thermomechanical state of a material can be fully defined through its state variables, that are subdivided into internal and observable. If the phenomenon allows reversibility, it does not depend on internal variables (Eringen, 1967), once that they are associated to dissipative phenomena, such as plasticity and hysteresis, and depend on the material history (Lemaitre & Chaboche, 1990).

Constitutive models based on plasticity theory assume that phase transformation and detwinning process are ruled by loading functions and flow rules like those from classic plasticity theory (Cisse *et al.*, 2016). Some of the authors that proposed plasticity-based constitutive models are Souza *et al.* (1998), Auricchio & Reali (2007), Auricchio *et al.* (2009) and Arghavani *et al.* (2010b). Ashrafi *et al.* (2015a, b) proposed a

generalization of the work developed by Souza *et al.* (1998) for porous SMA, with validation through experimental data from Zhao *et al.* (2005).

Constitutive models with internal constraints assume that the phase transformation kinetics is described by known mathematical function. The first model with this approach was proposed by Tanaka & Nagaki (1982), and assume, besides observable variables (such as elastic deformation, ε_{EL} , and temperature, T), an internal variable associated to martensite volumetric fraction, β). In view of the non-diffusive nature of martensitic transformations (Tanaka, 1985), the internal variable β is described by a temperature and stress instantaneous function. Different solutions for this function can be found in the literature (Liang & Rogers, 1990; Brinson, 1993; Ivshin & Pence, 1994 a; b; Boyd & Lagoudas, 1996; Hartl & Lagoudas, 2009; Hartl *et al.*, 2010). Lagoudas *et al.* (2012) describes the smooth response of polycrystals of SMA through nonlinear hardening functions.

On the case of elements with high structural rotations (Reese & Christ, 2008) and distortions (Ziolkowski, 2007), some models with formation in finite strain deformation (FSF) were developed to improve the precision of numerical simulations (Helm, 2007; Pan *et al.*, 2007; Ziolkowski, 2007; Thamburaja, 2010; Stupkiewicz & Petryk, 2013).

Models based on statistic physics are developed through local equilibrium considerations for monocrystalline SMAs (Bhattacharya & Lagoudas, 1997; Müller, 2012; Fischlschweiger & Oberaigner, 2012).

One of the simplest macroscopic models is a polynomial based formulation (Falk, 1980; 1983) for the Helmholtz free energy.

The model proposed by Paiva *et al.* (2006) is based on the one developed by Fremond (1987), with the addition of distinct austenite and martensite elastic modules, using the mixing rule through the austenite volumetric fraction, and the addition of a fourth phase related to the twinned martensite (M). This model is studied in other works (Savi *et al.* 2002; Baêta-Neves *et al.*, 2003) and has an alternative tridimensional formulation (Oliveira *et al.*, 2010, 2016, 2018).

A.2. Polynomial constitutive model

The polynomial constitutive model is unidimensional and based on the Landau free energy, applied previously by Devonshire (1954), that defines a free Helmholtz

energy on the polynomial form to describe the behavior of ferroelectric elements. This approach is adopted due to similarity of SMA stress-strain curves to the polarization curves of ferroelectric. Besides, the martensitic transition is of first order (Falk, 1980). The energetic formulation of the unidimensional model is as follows:

$$\rho\Psi(\varepsilon, T) = \frac{c_1}{2}(T - T_M)\varepsilon^2 - \frac{c_2}{4}\varepsilon^4 + \frac{c_3}{6}\varepsilon^6 \quad (\text{A.1})$$

Where ε is the SMA the deformation, T is the temperature, T_M is the temperature below which martensite is the thermodynamically stable, T_A is the temperature above which austenite is thermodynamically stable, and c_1 , c_2 and c_3 are fitting parameters of the model.

The stress, σ , is defined as follows:

$$\sigma = \rho \frac{\partial\Psi(\varepsilon, T)}{\partial\varepsilon} = c_1(T - T_M)\varepsilon - c_2\varepsilon^3 + c_3\varepsilon^5 \quad (\text{A.2})$$

Figure A-3 brings the general behavior described by this constitutive model, including the free energy and the relation stress-deformation for different temperatures.

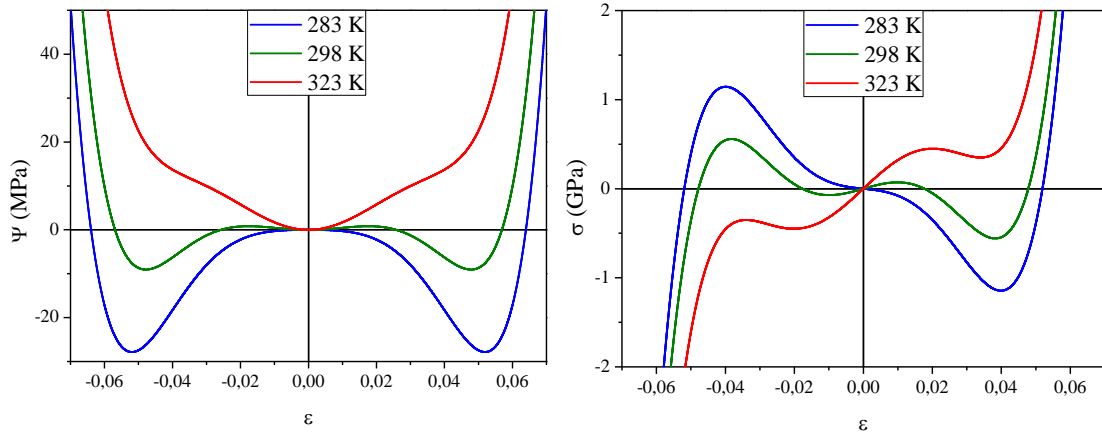


Figure A-3: Polynomial constitutive model describing SMA behavior for $T = 283$ K ($T < T_M$), $T = 298$ K ($T_M < T < T_A$) and $T = 323$ K ($T > T_A$). (a) Free energy; (b) Stress-strain relations

Twinned martensite is not stable on this formulation, and there are only two stable phases for $T < T_M$: detwinned tractive (M^+) or compressive (M) martensite. For

temperatures $T > T_A$, there is one stable crystallographic phase associated to austenite (A). For intermediate temperatures $T_M < T < T_A$ there is one metastable phase associated to austenite (A).

Based on this potential energy for an SMA sample, it is possible to define an analogous expression for an SMA spring, employed as actuator. Aguiar *et al.* (2010) showed that a similar expression $E_{SMA}(u, T)$, where u is the displacement, can be obtained assuming a homogeneous phase transformation on the SMA wire. Therefore, constitutive coefficients are replaced for new parameters that depend on the SMA spring diameter, D_S , the number of spirals, N_S , and the diameter of the SMA wire, d_S . Based on that, three macroscopic phases are treated: austenite, A, stable at elevated temperatures, and two variants of the martensite, M^+ and M^- , induced by tension and compression, respectively.

$$E_{SMA} = E_{SMA}(u, t) = \frac{\bar{c}_1(T-T_M)u^2}{2} - \frac{\bar{c}_2u^4}{4} + \frac{\bar{c}_3u^6}{6} \quad (\text{A.3})$$

where T_M is the temperature below which martensite is stable and \bar{c}_i are defined as follows: $\bar{c}_1 = c_1 \left(\frac{d_S}{\pi D_S^2 N_S} \right)^2$, $\bar{c}_2 = c_2 \left(\frac{d_S}{\pi D_S^2 N_S} \right)^4$ and $\bar{c}_3 = c_3 \left(\frac{d_S}{\pi D_S^2 N_S} \right)^6$, where c_i ($i = 1, 2, 3$) are constitutive model parameters. Another important parameter is the temperature T_A that defines the region where the energy curve has only one minimum, representing the temperature above which only austenitic phase is stable on a stress-free state.

A.3. Hyperelastic constitutive model

A versatile and simple model to describe elastic materials is an hyperelastic formulation (Ogden, 1997), which nonlinear behavior allows to represent different materials. The strain energy density function of the hyperelastic model is defined as a function of the principal stretches λ_j , as follows

$$W(\mathbf{E}) = \widehat{W}(\lambda_1, \lambda_2, \lambda_3) = \sum_{j=1}^{N_{mat}} \frac{\mu_j}{\alpha_j} (\lambda_1^{\alpha_j} + \lambda_2^{\alpha_j} + \lambda_3^{\alpha_j} - 3) \quad (\text{A.4})$$

where α_j , μ_j and N_{mat} denote the material constants. The parameter N_{mat} defines the nonlinearity order assumed to the system, i.e., the number of parameters to be determined. The constitutive parameters μ_j and α_j have to be determined experimentally, but two associated conditions must always be taken into account: the first condition to be obeyed is that the constitutive equation has to reduce to Hooke law for small strains, i.e., it has to be linear. The second condition is related to existence of solutions in finite elasticity.

$$\begin{aligned} \sum_{j=1}^{N_{mat}} \mu_j \alpha_j &= 2\mu \\ \mu_j \alpha_j &> 0 \end{aligned} \quad (\text{A.5})$$

where μ is the shear modulus. A stronger demand for this second condition to fulfill polyconvexity is that either $\mu_j > 0$ and $\alpha_j > 0$ or $\mu_j < 0$ and $\alpha_j < 0$.

It is possible to write the energy density $W(\mathbf{E})$ as a function of the bar stretches instead of deformations by rewriting the Green-Lagrange strain tensor.

$$\mathbf{E} = \frac{1}{2}(\mathbf{C} - \mathbf{I}) = \frac{1}{2}(\mathbf{U}^2 - \mathbf{I}) \quad (\text{A.6})$$

where \mathbf{C} is the right Cauchy-Green tensor and $\mathbf{C} = \mathbf{U}^2$ (the right stretch tensor \mathbf{U} is symmetric by definition). By considering one-dimensional media, the Green-Lagrange strain is reduced to E_x , being possible to rewrite (A.6) as follows

$$E_x = \frac{\lambda_1^2 - 1}{2} \quad (\text{A.7})$$

The one-dimensional form of the second Piola-Kirchhoff (P-K) tensor, S_x , is obtained from the energy density function $W(\mathbf{E})$.

$$\begin{aligned} W(E_x) &= \sum_{j=1}^{N_{mat}} \frac{\mu_j}{\alpha_j} \left[(\sqrt{2E_x + 1})^{\alpha_j} - 3 \right] \\ S_x &= \frac{\partial W}{\partial E_x} = \sum_{j=1}^{N_{mat}} \mu_j (\sqrt{2E_x + 1})^{\alpha_j - 2} \end{aligned} \quad (\text{A.8})$$

The hyper elastic constitutive model also considers a tangent modulus C_t , that represents a tangent stiffness constant. This modulus is obtained from the second P-K tensor as follows.

$$C_t = \frac{\partial S_x}{\partial E_x} = \sum_{j=1}^{N_{mat}} \mu_j (\alpha_j - 2) (\sqrt{2E_x + 1})^{\alpha_j - 4} \quad (\text{A.9})$$

Note that the undeformed state is also a stress-free state, i.e., all bars and springs are free of both stress and strain, and the tangent modulus must attend this condition. The stress-free condition ($S_x = 0$) results in a constraint for μ_j .

$$S_x = 0 \rightarrow \sum_{j=1}^{N_{mat}} \mu_j = 0 \quad (\text{A.10})$$

The constraint (A.10) associated with the conditions (A.5) restrict and conduct the fitting of the model parameters. By considering that $N_{mat} = 2$, the stress S_x is be given by

$$S_x = \frac{C_{t_0}}{\alpha_1 - \alpha_2} \left(\sqrt{2E_x + 1}^{\alpha_1 - 2} - \sqrt{2E_x + 1}^{\alpha_2 - 2} \right) \quad (\text{A.11})$$

where C_{t_0} is the tangent modulus at the initial state (stress-free and undeformed).

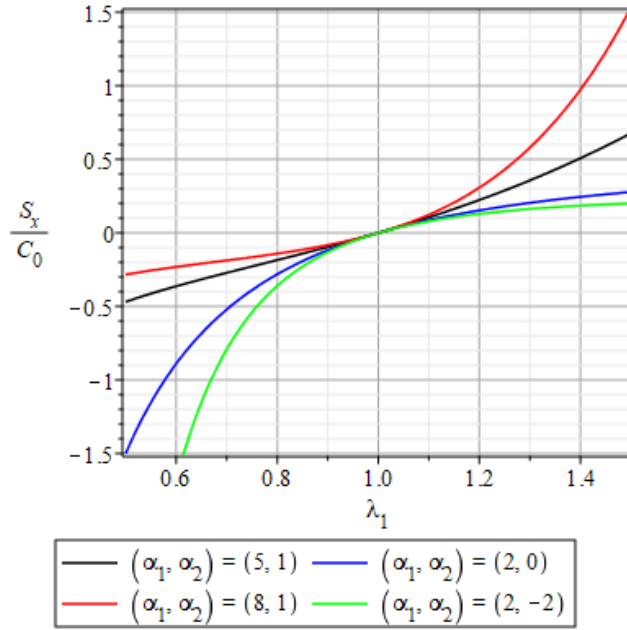


Figure A-4: Four different materials represented by the Ogden model considering different sets of (α_1, α_2) .

Figure A-4 brings an example of four different materials that can be represented by (A.11) if we consider four different sets of (α_1, α_2) , remembering that they must attend the conditions (A.5). Note that the sets $(2, 0)$ and $(8, 1)$ represent materials with opposite behaviors. The first one represents a material that is stiffer under compression than under tension, while the second is stiffer under tension than under compression. The set $(5, 1)$ represents a material that has a quasi-linear behavior, and the set $(2, -2)$ represents the Mooney-Rivlin material.

A.4. Elastic constitutive model

Lv *et al.* (2014) attest that the elastic energy related to the folding process of an origami with N dihedral angles per unit can always be expressed as the sum of the energy of N linear elastic springs. Besides, the linear formulation of the resistive moment of the folding process does not detect local penetration of origami panels and, to avoid that, additional kinematic constraints are considered as an increasing stiffness as the origami reaches limit configurations, defined by limit angles θ_{lim_1} and θ_{lim_2} . So, the constitutive model used to describe the mechanical behavior of the springs from the bar-and-hinge formulation on section 3.3 is as follows:

$$M_{res} = \begin{cases} k(\theta_{lim_1} - \theta_0) + \left(\frac{2k\theta_{lim_1}}{\pi}\right) \tan\left(\frac{\pi(\theta - \theta_{lim_1})}{2\theta_{lim_1}}\right) & , \theta \in]0, \theta_{lim_1}[\\ k(\theta - \theta_0) & , \theta \in [\theta_{lim_1}, \theta_{lim_2}] \\ k(\theta_{lim_2} - \theta_0) + \left[\frac{2k(2\pi - \theta_{lim_2})}{\pi}\right] \tan\left(\frac{\pi(\theta - \theta_{lim_2})}{4\pi - 2\theta_{lim_2}}\right) & , \theta \in]\theta_{lim_2}, 2\pi[\end{cases} \quad (A.12)$$

Figure A-5 shows the relationship moment-angle described in (A.12). Note that as the angle θ gets outside the linear region, being either bigger than the superior limit angle θ_{lim_2} or smaller than the inferior limit angle θ_{lim_1} , the spring gets increasingly stiffer following an asymptotic curve.

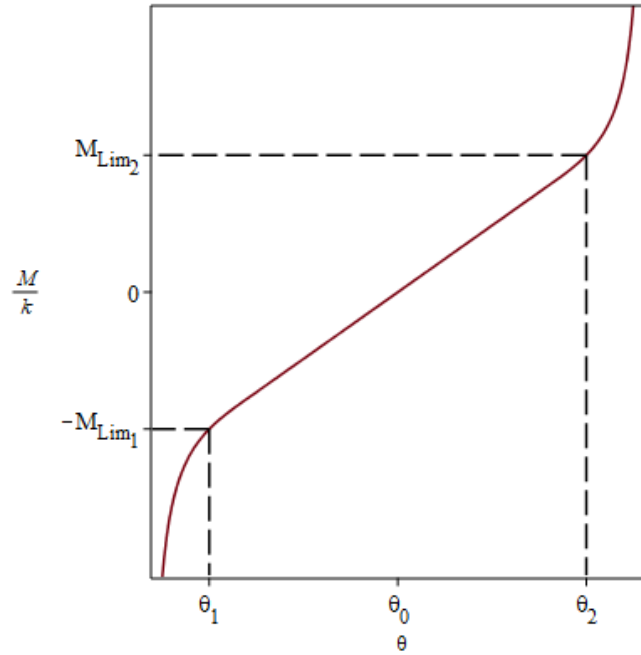


Figure A-5: Relationship between the resisting moment per unit length and the dihedral angle θ , considering the additional kinematic restrictions

Considering now the applied study, the elastic passive spring presented at the origami-wheel has its mechanical behavior also described by a linear elastic constitutive model. The difference is that the non-penetration condition is already contemplated on the geometric formulation and the system geometric parameters, which means that the response is purely elastic linear for the entire folding process. Thus, the passive bias

actuator is considered to be a linear elastic with a quadratic energy, expressed by the following equation

$$E_E = \frac{ku^2}{2} \quad (\text{A.13})$$

where $k = G_E d_E / \pi D_E^2 N_E$ is the stiffness defined by the spring diameter, D_E , the wire diameter, d_E , the number of spirals, N_E , and the tangent coefficient of the material component of the spring, G_E .